# MECHANICAL CHARACTERIZATION OF PORCINE AORTA USING MAGNETIC RESONANCE IMAGING

A dissertation submitted for the degree of Ph.D.

Vittoria Flamini, BEng., MSc.

Dublin City University

Under the supervision of

Dr. Caítriona Lally
Dr. Christian M. Kerskens

School of Mechanical and Manufacturing Engineering

July 2010

# Declaration

I hereby certify that this material, which I now submit for assessment on the program of study leading to the award of Ph.D. is entirely my own work, that I have exercised reasonable care to ensure that the work is original, and does not to the best of my knowledge breach any law of copyright and has not been taken from the work of others save and to the extent that such work has been cited and acknowledged within the text of my work.

Signed:_____ ID No.:_____ Date:_____

# Acknowledgements

Four years ago, while my plane was landing in Dublin airport, little did I know what to expect from this experience. Looking back, I now know that as soon as I left the airport I started an amazing journey in the world of Academia. My main guidance in this journey was my supervisor, Dr. Caítriona Lally. By offering endless encouragement and support, she led me through the depths of learning to the heights of interdisciplinary research. The MRI development of the project was carried out under the supervision of Dr. Christian Kerskens. To him goes my gratitude for the help he provided in pushing the limits of conventional MRI and for the patience he showed with my rigs, not customary in a neuroscience laboratory. I want also to thank Dr. Ciaran Simms and Kevin Moerman in TCD for many precious suggestions in the development of the project.

Many thanks go also to the technicians in DCU that helped in the designing and set up of the rigs and in particular to Liam and Jim.

Luckily I did not embark in this journey alone. From my arrival I met a bunch of great people: Alberto, Debbie, Engin, Irina, Arthur, Houman, Evelyn and Joe. I want to thank them for making enjoyable the trips to the abattoir, the hours in the lab, travelling to conferences. I want also to thank them for sharing many cakes, laughs and knowledge.

I would like to thanks also my flatmates, Huizhong and Daudi, that for three years have been my family. Obviously this adventure could not have started without the support of my real family, my grandad, my parents and my sister, and in particular of Graziano. Words cannot express my gratitude for accepting me leaving, and for showing their support in the highs and lows of the past four years.

Finally, and most unusually, I want to acknowledge that staying here would not have proven possible without the wonderful people that inhabit this island, who made me feel welcome everywhere and everytime.

Lastly, I gratefully acknowledge the Research Frontiers Grant (05/R-F/ENM076), awarded by Science Foundation Ireland, for funding this study.

# Publications and Presentations Resulting from this Study

## Papers

V. Flamini, C. M. Kerskens, C. Lally, Fibre Orientation of Fresh & Forzen Porcine Aorta Determined non-Invasively Using Diffusion Tensor Imaging, Journal of Biomechanics, submitted and in review.

V. Flamini, C. M. Kerskens, K. M. Moerman, C. K. Simms, and C. Lally, Imaging Arterial Fibres Using Diffusion Tensor Imaging - Feasibility Study and Preliminary Results, EURASIP Journal on Advances in Signal Processing, 2010, doi:10.1155/2010/904091.

K. M. Moerman, C. M. Kerskens, C. Lally, V. Flamini, and C. K. Simms, Evaluation of a Validation Method for MR Imaging-Based Motion Tracking Using Image Simulation, EURASIP Journal on Advances in Signal Processing, 2010, doi:10.1155/2010/942131.

## Conferences and Abstracts

V. Flamini, C. M. Kerskens, and C. Lally, Determination of Aortic Tissue Mechanical Properties Combining Magnetic Resonance Imaging and Finite Element Modelling, ISSEC & Irish Mechanics Symposium, University College Dublin, 2010.

V. Flamini, C. M. Kerskens, and C. Lally, Aortic Constitutive Model Determined from Diffusion Tensor Imaging (DTI), IDIG Spring Symposium, 2010.

V. Flamini, C. M. Kerskens, and C. Lally, In Vivo Determination of Aortic Tissue Mechanical Properties Using Magnetic Resonance Imaging (MRI): A Feasibility Study, In Proceedings of the $16^{th}$ Annual Conference of the Section of the Royal Academy of Medicine in Ireland, 2010, 28.

V. Flamini, C. M. Kerskens, and C. Lally, An Anisotropic Structural Model of the Aortic Wall Based on Tensile Tests and Non-Invasive 3D Fibre Analysis Using Diffusion Tensor Imaging, ASME Summer Bioengineering Conference, 2009.

This paper was chosen from more than 180 papers to be among the 18 papers that competed in the PhD Level Best Paper Award Podium competition. It was awarded an Honourable mention in the Tissue and Cell Biomechanics & Imaging category.

V. Flamini, C. M. Kerskens, and C. Lally, An Anisotropic Aortic Constitutive Model Based on 3D Non-Invasive Fibre Analysis and Tensile Testing, In Proceedings of the $15^{th}$ Annual Conference of the Section of the Royal Academy of Medicine in Ireland, 2009, 114.

C. Lally, V. Flamini, C. M. Kerskens, A. Creane, D. Kelly, N. Hynes, and S. Sultan, Preclinical Medical Device Testing and the Potential of Non-Invasive Imaging, 6th Annual Western Vascular Symposium, 2008.

V. Flamini, C. M. Kerskens, and C. Lally, Characterization of the 3D Fibre Distribution in a Porcine Aorta Using Diffusion Tensor Imaging, Journal of Biomechanics, 2008, 41:S69.

V. Flamini, C. M. Kerskens, and C. Lally, Effects of Tractography Parameters on the 3D Fibre Distribution of a Porcine Aorta, Symposium for Mechanical Engineering Research and Practice, Dublin City University, 2008.

This presentation was awarded first place.

V. Flamini, C. M. Kerskens, and C. Lally, 3D Fibre Distribution in a Porcine Aorta Using Diffusion Tensor Imaging (DTI), Sir Bernard Crossland Symposium, University of Limerick, 2008.

This poster was awarded second place at the Sir Bernard Crossland Symposium Postgraduate Workshop.

V. Flamini, C. M. Kerskens, and C. Lally, Determination of the 3D Fibre Distribution as a Function of Radius in a Porcine Aorta Using Diffusion

Tensor Imaging, In Proceedings of the $14^{th}$ Annual Conference of the Section of the Royal Academy of Medicine in Ireland, 2010, 5.

## Invited Talks

V. Flamini, DTI Applied to Porcine Aortas: Analysis of 3D Fibrous Structure, IDIG Research Day 2009, National University of Ireland, Galway, 2009.

# Contents

**Declaration** i

**Publications and Presentations Resulting from this Study** iv

**List of Figures** x

**List of Tables** xvii

**Nomenclature** xviii

**Abstract** xix

**1 Introduction** 1
- 1.1 Cardiovascular Disease . . . 1
- 1.2 Objectives . . . 3

**2 Literature Review** 5
- 2.1 Introduction . . . 5
- 2.2 Aorta: Structure, Function and Diseases . . . 6
  - 2.2.1 Porcine Aortas . . . 13
- 2.3 Constitutive Models for Arterial Tissue . . . 15
  - 2.3.1 Mechanical Tests on Arterial Tissue . . . 24
- 2.4 Medical Imaging . . . 26
  - 2.4.1 Magnetic Resonance Imaging . . . 26
  - 2.4.2 Diffusion Tensor Imaging . . . 27
  - 2.4.3 Fibre Analysis . . . 30
  - 2.4.4 Phase Contrast Magnetic Resonance Imaging . . . 32
- 2.5 Non-invasive Prediction of Aortic Constitutive Behaviour . . . 35
- 2.6 Finite Element Analysis . . . 36
- 2.7 Summary . . . 36

**3 Constitutive Model** **38**
3.1 Methods . . . 39
3.1.1 Uniaxial Tensile Test . . . 41
3.2 Results . . . 43
3.3 Discussion . . . 46
3.3.1 Limitations . . . 51
3.3.2 Conclusions . . . 52

**4 Diffusion Tensor Imaging** **53**
4.1 Methods . . . 54
4.1.1 Preparation of Aortic Sample . . . 54
4.1.2 Imaging Protocol . . . 57
4.1.3 Image Analysis . . . 59
4.1.4 Tensor Analysis . . . 60
4.1.5 Fibre Analysis . . . 60
4.1.6 Extrapolation of Material Parameters . . . 66
4.2 Results . . . 67
4.2.1 Image Analysis . . . 67
4.2.2 Tensor Analysis . . . 67
4.2.3 Fibre Analysis . . . 72
4.2.4 Extrapolation of Material Parameters . . . 82
4.3 Discussion . . . 82
4.3.1 Image Analysis . . . 83
4.3.2 Tensor Analysis . . . 84
4.3.3 Fibre Analysis . . . 85
4.3.4 Optimal $b$ value . . . 87
4.3.5 Extrapolation of Material Parameters . . . 89
4.3.6 Quantification of aortic damage . . . 89
4.3.7 Limitations . . . 94
4.3.8 Conclusions . . . 95

**5 Phase Contrast MRI** **96**
5.1 Methods . . . 96
5.2 Results . . . 104
5.3 Discussion . . . 116
5.3.1 Limitations . . . 121
5.3.2 Conclusions . . . 122

**6 Non-invasive Prediction of Aortic Constitutive Behaviour** **123**
6.1 Methods . . . 124
6.1.1 Evaluation of DTI derived material parameters . . . 124

6.1.2 Finite Element Analysis . . . 124
6.1.3 Constitutive Model Validation . . . 127
6.2 Results . . . 130
6.2.1 Evaluation of DTI derived structural parameters . . . 130
6.2.2 Finite Element Analysis . . . 130
6.2.3 Constitutive Model Validation . . . 131
6.3 Discussion . . . 136
6.3.1 Evaluation of DTI derived structural parameters . . . 136
6.3.2 Finite Element Analysis . . . 138
6.3.3 Aortic Constitutive Behaviour . . . 140
6.3.4 Limitations . . . 144
6.3.5 Conclusions . . . 145

**7 Final Discussion** **146**

**8 Conclusions & Future Work** **154**
8.1 Conclusions . . . 154
8.2 Future Work . . . 155

**A Aortic Chamber** **158**

**B DTI: parameters definition** **160**
B.1 Parametric Analysis . . . 161

**C PC MRI: method** **163**
C.1 Forward/backward integration . . . 163

**D LabVIEW® and MATLAB® scripts** **166**
D.1 LabVIEW® . . . 166
D.1.1 Non-linear Levenberg-Marquardt regression . . . 166
D.1.2 Pressure sensor controller . . . 170
D.2 MATLAB® . . . 173
D.2.1 General image analysis . . . 173
D.2.2 DTI: Tensor analysis . . . 176
D.2.3 DTI: Fibre analysis . . . 181
D.2.4 PC MRI: Definition of elements and deformation velocity 189
D.2.5 PC MRI: Circumferential strains . . . 200
D.2.6 FE: Mesh from MRI data . . . 205
D.2.7 FE: Iterative . . . 214

**E Further data and information** **227**

# List of Figures


1.1 Flow chart describing the main project objectives and the relationship between these objectives. . . . . 4

2.1 Position of the aorta in the body, from [3]. . . . . 7
2.2 Aortic branches, modified from [3]. . . . . 8
2.3 Arterial layers within the aortic wall, modified from [4]. . . . . 9
2.4 Concentrical layers in the arterial fibre orientation, from [5] . . 10
2.5 Abdominal aortic aneurysm, from [18]. . . . . 12
2.6 Anatomy of the aorta in different species: A) Heart and blood blood vessels in a pig, modified from [41]; Heart and blood blood vessels in a human being, modified from [3]. . . . . 14
2.7 Relationship between inflating pressure and arterial behaviour, from [42]. . . . . 16
2.8 How elastin and collagen affect the arterial stress-strain relationship. The broken curve is for an untreated artery from [42]. 17
2.9 Noncoincident loading and unloading, evidence of viscous dissipation, from [6]. . . . . 19
2.10 Example of histomechanical modelling for the coronary artery from [57]: top) fibre angle from histological data; bottom) stress-strain response for every layer. . . . . 22
2.11 Schematic of fibre orientation in different constitutive models: A) one family of fibres [54,58]; B) two families of fibres [49–53]; C) four families of fibres [55, 56]. . . . . 23
2.12 Comparison between FE results for the model described in [54, 59] with experimental data for a adventitia obtained from [60]. . . . . 24
2.13 Example of uniaxial test on aortic tissue; A) longitudinally oriented porcine aorta test specimen; B) representative stress-strain curve for longitudinal vessel distraction, from [65]. . . . 25

3.1 Iliac adventitia stress-stretch curve from [63]. . . . . 42

3.2 Porcine aorta uniaxial tensile test: A) details of the dogbone shape used; B) test set up capture. . . . . 43
3.3 Fibre orientation in the aorta, from [34]. . . . . 44
3.4 Screen capture of the custom-built Levenberg–Marquardt algorithm A)Data from Holzapfel *et al.* [63] ; B) Porcine aorta uniaxial tensile test data. . . . . 45
3.5 Holzapfel *et al.* [63] curves: fit obtained with the custom routine. 46
3.6 Porcine aortas uniaxial tensile tests in the circumferential and in the axial direction. . . . . 47
3.7 Average curves used in the analysis and their standard deviation superimposed on the uniaxial tensile test results. . . . . 48
3.8 Comparison of the interpolated curves with porcine aortas uniaxial tensile test data. . . . . 49
3.9 Effects of changes in the material constants on the interpolated curves, the standard deviation bars are left out for clarity purposes. . . . . 50

4.1 Rendering of the chamber. . . . . 55
4.2 Aorta prepared according to the protocol. . . . . 55
4.3 Aortic segment prior to placement in the chamber. . . . . 56
4.4 RF circular polarised whole body coil, used for scanning. . . . 58
4.5 Convention for the lead fibre angles used in the study: A) reference system for the fibres; B) definition of the fibre angle. 61
4.6 Flow chart indicating the various stages in the image postprocessing sequence. . . . . 62
4.7 Representation of the layers considered for each geometry analysed: A) stored frozen sample; B, C) fresh samples. . . . . 63
4.8 Test helices generated in MATLAB®: the blue and the red one are both left handed but have different leads, the green one is right handed and has a different lead. . . . . 64
4.9 Top row: MRI images of the aortas analysed, A) stored frozen sample; B), C) fresh samples. Second row: fractional anisotropy map of the samples for $b_1$= 200 s/mm$^2$; Third row: fractional anisotropy map of the samples for $b_4$= 800 s/mm$^2$; Bottom row: fractional anisotropy map for $b_6$=1600 s/mm$^2$. In B.1 and C.1 the arrows indicate the presence of lymphatic tissue. . 68

4.10 Steps in the DTI procedure and image postprocessing; (A) MRI anatomical scan, (B) The ROI of the aorta, (C) A map of the angle of the first eigenvector with the ($x$,$y$) plane, (D) A map of the angle of the first eigenvector with the ($x$,$y$) plane with the ROI clearly identified, (E) The results of the tractography process with the fibres superimposed on the reference image, and (F) The aortic fibres within the ROI alone. . . . . 69
4.11 Contour maps of the angle between the first eigenvector and the ($x$,$y$) plane for the central slices of the image data sets for the different $b$ values. . . . . 70
4.12 Contour maps of the angle between the first eigenvector and the ($x$,$y$) plane for the averaged tensors of the image data sets for the different $b$ values. . . . . 71
4.13 Dominant angles for the aortas analysed: A) stored frozen sample; B), C) fresh samples. . . . . 73
4.14 Stored frozen sample of fig.4.9.A.1: A) for $b_1$= 200 s/mm$^2$ MRI image with superimposed fibre plot on the left hand side, distribution of fibres across the different layers of the aorta on the right hand side. B) for $b_4$=800 s/mm$^2$ MRI image with superimposed fibre plot on the left hand side, distribution of fibres across the different layers of the aorta on the right hand side. C) for $b_6$=1600 s/mm$^2$ MRI image with superimposed fibre plot on the left hand side, distribution of fibres across the different layers of the aorta on the right hand side. . . . . 75
4.15 Fresh sample of fig.4.9.B.1: A) for $b_1$= 200 s/mm$^2$ MRI image with superimposed fibre plot on the left hand side, distribution of fibres across the different layers of the aorta on the right hand side. B) for $b_4$=800 s/mm$^2$ MRI image with superimposed fibre plot on the left hand side, distribution of fibres across the different layers of the aorta on the right hand side. C) for $b_6$=1600 s/mm$^2$ MRI image with superimposed fibre plot on the left hand side, distribution of fibres across the different layers of the aorta on the right hand side. . . . . 76

4.16 Fresh sample of fig.4.9.C.1: A) for $b_1$= 200 s/mm$^2$ MRI image with superimposed fibre plot on the left hand side, distribution of fibres across the different layers of the aorta on the right hand side. B) for $b_4$=800 s/mm$^2$ MRI image with superimposed fibre plot on the left hand side, distribution of fibres across the different layers of the aorta on the right hand side. C) for $b_6$=1600 s/mm$^2$ MRI image with superimposed fibre plot on the left hand side, distribution of fibres across the different layers of the aorta on the right hand side. . . . . 77
4.17 Top row: prospective view of the fibres tracked in the sample volumes. In red the fibre bundle corresponding to the first slice, in white the one for the middle slice, and in blue the one for the last slice. Bottom three rows: changes in the fibre distribution according to the ROI chosen for all the samples. 81
4.18 Fibre distribution obtained using nonlinear optical microscopy from [56]: left) sampling of slices from the adventitia to the media where increased undulationcan be noted with decreased pressure, the presence of black voids in the media (which likely indicate where the smooth muscle cells reside) and the dramatic shift in orientation from axial to circumferential fibers; right) fibre angle distribution through wall where 0 marks the outer adventitia, and 1 the inner media; the fiber angle axis is oriented so that 0° is axial and 90° is circumferential. . . . . 86
4.19 Hematoxylin and eosin stained section of fresh (a, b) and frozen (c, d) arteries, with different magnifications: 10× (a, c); 60× (b, d). In the frozen samples condensed nuclei can be seen (c, d), which indicates smooth muscle cell injury, from [140]. 90
4.20 Histological evidence of structural alteration in ascending thoracic aortas. Nonaneurysmal aortas (A, C) and aortic aneurysms (B, D) were stained with elastin-Van Gieson (EVG) (A, B) or an antibody to SM $\alpha$-actin (C, D). Elastin is stained black by EVG and separates the media from the intima (above) and adventitia (below); in the high magnification photomicrographs (C,D) it is possible to see lacerations in the structure for the aortic aneurysm, from [141]. . . . . 92
4.21 Aneurysm induced Alterations in arterial mechanical behaviour: effects of aneurysm on tensile strength of longitudinal (LONG) and circumferential (CIRC) specimens of ascending thoracic aortic aneurysm (black) and nonaneurysmal aortic tissue (white), from [27]. . . . . 93

5.1 Equipment used in the study: A) Pulsatile pump for large animals from Harvard Apparatus; B) Transducer amplifier from CWE Inc.. . . . . 97
5.2 Continuous pulsatile profile produced by the HA553305 pump in the porcine aorta. The pressure recorded at the nine time steps considered in the analysis is highlighted. . . . . 98
5.3 Schematic of equipment connections for the PC MRI experiment: the blue line represents the water connection while the green line represents the electronic connections. . . . . 99
5.4 Top: distribution of values for $V_x$ versus $y$ and $V_y$ versus $x$. This distribution can be fitted by a line whose slope corresponds to $\omega_z$, and whose intercept indicates $A_i$. Bottom: distribution of values for $V_x$ versus $y$ and $V_y$ versus $x$ after the removal of rigid motions effects. Figure adapted from [124]. . 101
5.5 Definition of velocity vectors in a cylindrical coordinate system.103
5.6 Magnitude images of the PC MRI sequence for each slice. . . . 105
5.7 Phase maps of the PC MRI sequence for each slice. . . . . 106
5.8 Components of the image in fig.5.6.A: apart from the connector, these components can also be found on the sub-figures of fig.5.6. . . . . 107
5.9 Organisation of the aortic volume. . . . . 107
5.10 Effect of rigid body motion on the last slice for each time step; black and dark grey lines represent data in the $V_y$, $x$ distribution, green and yellow lines data in the $V_x$, $y$ distribution.108
5.11 Correction of rigid body motion on the last slice for each time step; blue and cyan lines represent data in the $V_y$, $x$ distribution, red and magenta lines data in the $V_y$, $x$ distribution. . . 109
5.12 Cycle trajectories plotted for elements 1 and 11 (blackened) for slices 2, 6, and 9. . . . . 110
5.13 Cycle trajectories plotted for elements 5 and 15 (blackened) for slices 2, 6, and 9. . . . . 111
5.14 Circumferential strains recorded for the second slice over time: the colour map represents the magnitude, the arrows the direction. . . . . 112
5.15 Circumferential strains recorded for the sixth slice over time: the colour map represents the magnitude, the arrows the direction. . . . . 113
5.16 Circumferential strains recorded for the ninth slice over time: the colour map represents the magnitude, the arrows the direction. . . . . 114

5.17 Plots of the circumferential strain for the ninth slice over time; the averages of each quarter of the aorta (5 elements) and over all the elements are also shown. . . . . 115
5.18 Relationship between pressure, flow and circumferential strain: A) pressure ad flow in the abdominal aorta, from [143], where it is shown that pressure increases although flow is decreasing; aortic flow compared to the strains measured by Wedding *et al.*, both flow and strains are measured through MRI, but in two separate acquisitions [120]. . . . . 118
5.19 Comparison of the strains recorded with the results available from literature [120]: The yellow box shows that the strains recorded fall into the average strain range measured in literature (1-4%), while the green box shows that the maxima fall in the range reported for the maximal strains (4-8%). . . . . 121

6.1 Finite element models: loads and boundary conditions. A) uniaxial tensile test; B) aortic geometry. . . . . 125
6.2 Mesh used in the uniaxial tensile test and fibre orientations: A) test in the axial direction; B) test in the circumferential direction. . . . . 126
6.3 Line mesh for the ninth slice in the volume, bullets represent the nodes: A) mesh n.1= 20 elements in the circumference, one element in the thickness; B) mesh n.2= 30 elements in the circumference, 3 elements across the thickness of the aorta. . . 127
6.4 Final ABAQUS® 3D mesh obtained for the meshes of fig.6.3: A) mesh n.1 with no axial divisions; B) mesh n.2 with 3 axial divisions. . . . . 128
6.5 Final ABAQUS® 3D mesh obtained for the meshes of fig.6.3, front view: A) mesh n.1 with no axial divisions; B) mesh n.2 with 3 axial divisions. . . . . 129
6.6 Comparison between the constitutive model fit obtained with the constants defined in ch.3 and with the constants determined non-invasively through DTI. . . . . 131
6.7 Strains in the direction of the load for the uniaxial tensile test: A) axial direction; B) circumferential direction. . . . . 133
6.8 Comparison between the constitutive model fit obtained with the DTI and the stress-strain curve resulting from uniaxial tensile test FE simulation; the axial FE results had to be interrupted at the asterisk due to limit of experimental data. . . 134
6.9 Circumferential strains in the loaded aorta FE simulation: A) side view; B) front view. . . . . 135

6.10 Results from the aortic simulations, The edges of the boxes are the maximum and the minimum strain recorded, while the line represents the average of the strains. . . . . 136
6.11 Effect of the variation of $c$ and $k_1$ on the strains computed from the FE simulation. . . . . 137
6.12 Details of the effect of the variation of the value of $c$ and of the value of $k_1$: A) $k_1$ constant; B) $c$ constant. . . . . 138
6.13 FE model strains for the values resulting from the iterative routine, red box. The blue box represents the average strains in the aorta reported in [109]. . . . . 139
6.14 Effect of the variation of $k_1$ on the amplitude and on the average strain for different values of $c$. . . . . 142

E.1 Plot of the second derivatives of the fibre number versus fibre angle plots for the central slice and $b1$, $b2$ and $b6$. . . . . 228

# List of Tables


3.1 Constitutive parameters used in the model. . . . . 44

4.1 Aortic Measures . . . . . 56
4.2 DTI scanning parameters . . . . . 58
4.3 Details of the fibre analysis step sequence. . . . . 65
4.4 Fibre content per layer; bold characters correspond to the transition layers. . . . . 78
4.5 Fibre percentage per layer; bold characters correspond to the transition layers. . . . . 79
4.6 Values of $\kappa$ obtained for the different fibre distributions of fig.4.13 according to the procedure outlined in 4.1.6. . . . . 82

5.1 PC MRI scanning parameters . . . . . 100
5.2 PC MRI step sequence. . . . . 104

6.1 Mesh convergence study. . . . . 127
6.2 Comparison between the DTI derived parameters and the parameters obtained in ch.3 based on data from literature. In bold are highlighted the changes in $c$ and in $k_1$. . . . . 130
6.3 Material parameters obtained from the changes in $c$ and in $k_1$. 140
6.4 Relevant measures for the strains analysed (%). . . . . 141

B.1 Parametric fibre tracking settings. . . . . 161

E.1 Evaluation of the difference in the eigenvector angles between each repetition and the average over all the repetitions for the central slice of the image. . . . . 229
E.2 Evaluation of the difference in the eigenvector angles between each repetition and the average over all of the repetitions. In this case the measurement is averaged over all of the slices of the volume. . . . . 230

# Nomenclature

| | |
|---|---|
| $\sigma_j$, $j \in \{x, y, z\}$ or $j \in \{r, \theta, z\}$ | Cauchy stresses; |
| $r$ | Radius (variable); |
| $P$ | Pressure; |
| $\delta$ | Thickness; |
| $\lambda_j$, $j \in \{x, y, z\}$ or $j \in \{r, \theta, z\}$ | Stretch; |
| $\Psi$ | Strain energy function; |
| $F$ | Deformation gradient; |
| $E$ | Green strain tensor; |
| $\mathbb{I}$ | Identity tensor; |
| $S$ | Second Piola–Kirchhoff tensor; |
| $J$ | Jacobian; |
| $I_(i)$, $i \in \mathbb{N}$ | Invariants; |
| $C$ | Right Cauchy-Green deformation tensor; |
| $\lambda_i$, $i \in \mathbb{N}$ | Eigenvalues; |
| $a_0$, $a'_0$ | Directions of the fibres; |
| $b$ | Diffusion weighting factor; |
| $D$ | Diffusion tensor; |
| $S_i$ | Signal intensity; |
| $\gamma$ | Gyromagnetic ratio; |
| $G(t)$ | Strength of the gradient pulse; |
| $\phi$ | Phase; |
| $V_j$, $j \in \{x, y, z\}$ or $j \in \{r, \theta, z\}$ | Velocity components; |
| $L$ | Velocity gradient tensor; |
| $W$ | Strain rate tensor; |
| $R$ | Radius (constant); |
| $\epsilon_j$, $j \in \{x, y, z\}$ or $j \in \{r, \theta, z\}$ | Strain; |
| $c, k_1, k_2$ | Anisotropic model constants; |
| $m$ | Angular coefficient; |
| $\omega_j$, $j \in \{x, y, z\}$ | Angular velocity. |

# Abstract

## Mechanical Characterization of Porcine Aorta Using Magnetic Resonance Imaging

**Vittoria Flamini**

Determination of aortic mechanical properties in a non-invasive way would be an important step in predicting the onset and development of one of the most fatal degenerative cardiovascular diseases: abdominal aortic aneurysm (AAA). The approach presented in this work to achieve this goal couples Magnetic Resonance Imaging (MRI) with Finite Element (FE) analysis to define a model of aortic mechanical behaviour. In particular, the aortic fibrous structure was analysed using Diffusion Tensor MRI, the results of which showed that fibres could be tracked in the aortic tissue, and that their angles measured ($\pm$ 15°) are in accordance with the angles reported in literature. DTI was also applied to a frozen aorta, where the structural parameters obtained were different from those for fresh tissue thus indicating the potential of DTI to measure damage in aortic tissue. MRI was also used for characterization of aortic tissue deformation, using Phase Contrast MRI (PC MRI). With this technique circumferential strains were measured in an aorta, which on average ranged between 0.95-4.7%, in accordance with the range found *in vivo* from literature. A mechanical constitutive model was implemented, initially based on the structural information from DTI and uniaxial test data, in a finite element (FE) model. Strains estimated in the model under applied physiological pressure were compared with the strains measured using PC MRI. Material parameters of the constitutive model were changed iteratively until the strains matched, thus obtaining the material constants necessary to characterize the behaviour of the aorta non-invasively. This thesis clearly demonstrates the feasibility of a novel approach to mechanical characteriza-

tion of aortas, based on the use of innovative MRI techniques. Moreover, the application of DTI to both fresh and frozen tissue, which clearly identified differences in the tissues at the fibre level, demonstrates the potential of DTI as a diagnostic tool for degenerative arterial diseases such as AAAs.

*A Graziano*

*ed alla mia Famiglia*

*per avermi accompagnato fin qui*

# Chapter 1

# Introduction

## 1.1 Cardiovascular Disease

Cardiovascular diseases are the main cause of death in Western Countries. They are more prevalent in men over 50s and those exposed to the following risk factors: high lipid diet, smoking and lack of physical activity [1].

The most important characteristic of these diseases is that they can develop symptomless to a large extent for some time. If untreated, cardiovascular diseases may lead to the failure of a major organ such as the heart or brain, an event that in many cases is catastrophic (e. g. infarction, stroke, hemorrhage) [2].

In arteries two cardiovascular diseases that occur frequently are atherosclerosis and aneurysms [1]. Atherosclerosis is a narrowing of the internal lumen of an artery due to the deposition of lipids that form a plaque. The continuous narrowing of the artery may cause a blockage in the blood flow. Aneurysms are a localised failure in the arterial wall structure, such that the vessel becomes thinner and then bulges out. This bulge causes an alteration in the blood flow and can rupture causing internal bleeding. In both diseases the anatomical structure of the arterial wall is affected. In particular, the texture of collagen and elastic fibres that form the arterial wall reinforcement, acting as a buttress may be altered by the progression of these diseases [2].

Currently it is possible to study these diseases by looking at blood flow patterns or using histological techniques. The latter method can give an insight into the cause and the development of the phenomenon, but it has huge limitations. First of all, a histological analysis can evaluate only what happens in a small area of an artery; secondly it requires a surgical procedure, namely the removal of a piece of tissue from inside the body. Such biopsy surgery can cause great discomfort and risk for a patient, with related high costs for the health service. The consequence is that histological techniques cannot be used to perform screenings to evaluate the physiological condition of a vast area of the arterial tree. The disease must therefore be developed enough to cause symptoms and therefore histological analysis cannot be used to perform an early diagnosis of cardiovascular diseases. There is currently no appropriate technique that can infer a diagnosis at an early stage of the disease such that an optimal treatment for the disease can be prescribed.

The absence of an appropriate technology for the study of the composition of arterial walls *in vivo* is also a big limitation to the development of devices for the treatment of cardiovascular diseases. In fact, biomedical engineers cannot rely on histological data only to determine the mechanical behaviour of the arterial wall. Difficulties with this data include: the rapid degradation of tissues excised from the human body and the difficulty with performing these studies on a large statistical sample where both healthy and diseased tissues are represented. The lack of reliable material models for *in vivo* tissue means that numerical analyses performed to improve the design of cardiovascular devices (stents, grafts, filters) are limited. The material models considered are mainly theoretical and due to *ex vivo* analyses.

It is therefore necessary to develop a new method to study the arterial tree and its diseases. This new method should be non-invasive and should allow the different stages of the diseases to be identified and studied. On the one hand, this would lead to a reliable technique for the diagnosis and the screening of patients and on the other hand it would offer an effective means to determine the mechanical properties of the arterial wall, both healthy and diseased.

## 1.2 Objectives

In this study a novel approach is proposed to investigate the structure of arteries, and in particular, of porcine aortas. More specifically, this study focuses on the non-invasive determination of aortic mechanical properties combining Magnetic Resonance Imaging (MRI) and Finite Element Analysis. In order to achieve this goal the following tasks needed to be completed, see also fig. 1.1:

1. **Constitutive Model:**
    - Identification of an appropriate constitutive model to describe the anisotropic fibre structure of an aorta;
    - Implementation of the constitutive model using Finite Element (FE) method;
2. **Structural Static Analysis:**
    - Non-invasive determination of the 3D fibre structure of the aorta using MRI, and in particular Diffusion Tensor Imaging (DTI);
3. **Dynamic Analysis:**
    - Non-invasive determination of aortic deformations under physiologic of blood flow conditions using Phase Contrast MRI (PC MRI);
4. **Determination of Aortic Mechanical Properties:**
    - In an iterative procedure, the constitutive model determined in task 1 needed to be modified using the results from the DT MRI in task 2 and the PC MRI analysis in task 3 to determine the specific mechanical behaviour of the imaged aorta.

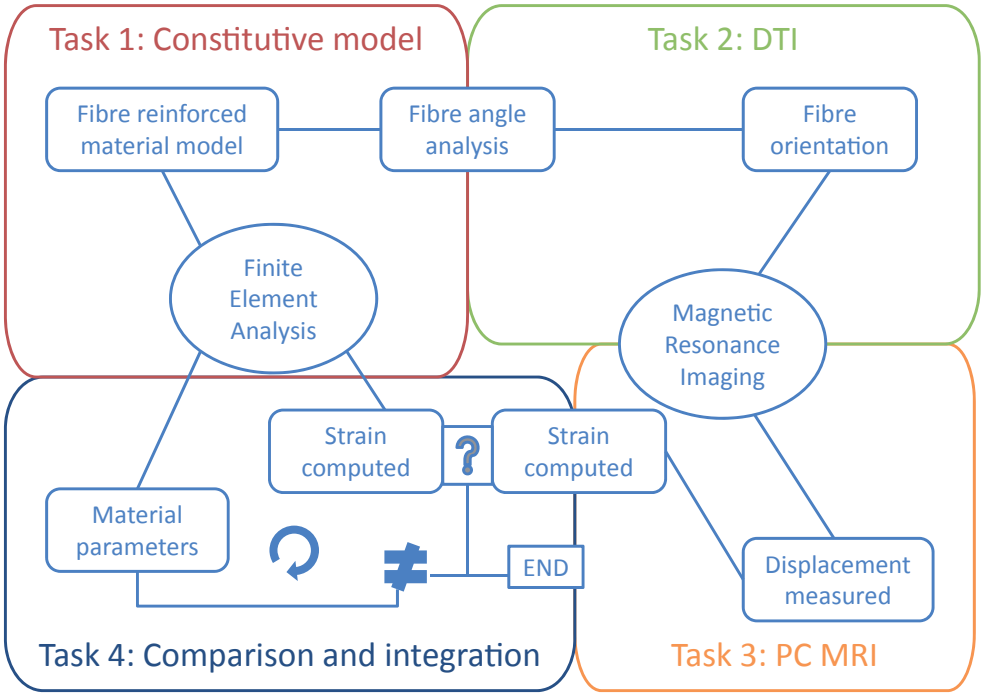


Figure 1.1: Flow chart describing the main project objectives and the relationship between these objectives.

This project shows potential in both the engineering and medical fields. From an engineering point of view, the success of this technique advances preclinical research of vascular devices enabling the development of better medical device designs. From a medical point of view, this methods represents a new means of studying the arterial wall in a non-invasive manner and it could be of great importance for the early diagnosis of many life-threatening vascular diseases, such as aneurysms and the onset of atherosclerosis. In addition, it could offer significant insight into the aetiology of such degenerative disease.

# Chapter 2

# Literature Review

## 2.1 Introduction

The purpose of this study is the *in vivo* determination of the mechanical behaviour of blood vessels and in particular of the aorta. The aorta is the largest blood vessel in the human body, stemming directly from the heart. Due to the closeness of the aorta with the pumping action of the heart, the pressure endured by the aortic wall is the highest in the body, and its shape is pulsatile and both its amplitude and frequency change with different human activities [2]. In order to be able to withstand this continuously changing pulsatile pressure the aortic wall has developed a special structure made of different layers with fibres interwoven. The study of this structure is not only interesting for the characterization of the healthy aortic tissue, but it is of paramount importance in medical practice. In fact, one of the most fatal cardiovascular diseases, the abdominal aortic aneurysm, is related to a change in the structure of the aortic wall.

The aortic wall, like the majority of biological tissues, is a soft tissue whose behaviour can be represented by a constitutive model. Constitutive models are a representation of the real behaviour of the tissue and they are usually determined in a two step process. In the first step the structure of the tissue is analysed and the loading response studied; in the second step the

information about the structure and the loading response are combined and a law that describes the tissue behaviour is derived. A constitutive model for arterial tissue can be implemented into a finite element software, and can be used for representing the tissue behaviour in simulations aimed at improving the design of medical devices or at predicting the outcome of a surgical procedure on a patient.

In order to be deemed suitable a numerical model needs to be validated. In general this validation is achieved by comparing the effects of a realistic loading of the tissue with that obtained from a simulation. In the present work, a constitutive model of the aorta will be defined and validated comparing the deformations obtained from a numerical simulation with these observed in different experiments. Such a constitutive model will be generated using structural information on the aortic wall obtained using a novel technique: the aortic structure will be investigated non-invasively by imaging the vessel using Magnetic Resonance Diffusion Tensor Imaging (MR DTI). MR DTI will be applied to arterial tissue for the first time in the present work.

The procedure outlined and validated in the present work leads the way for the non-invasive characterization of aortic wall structure and has the potential to be implemented as a diagnostic tool for cardiovascular diseases.

## 2.2 Aorta: Structure, Function and Diseases

The aorta is the largest artery of the body. It stems out of the heart's left atrium, and is the 'conduit' that delivers oxygenated blood to all the human body tissues, see fig. 2.1. Immediately after leaving the heart, the aorta forms an arch, from which three main branches leave: the brachiocephalic trunk, the left common carotid artery and the left subclavian arteries, as can be seen in fig. 2.2. These three branches have the role of supplying blood to the upper limbs and the brain. After the arch, the aorta descends into the torso and is then called the descending aorta. Two parts can be

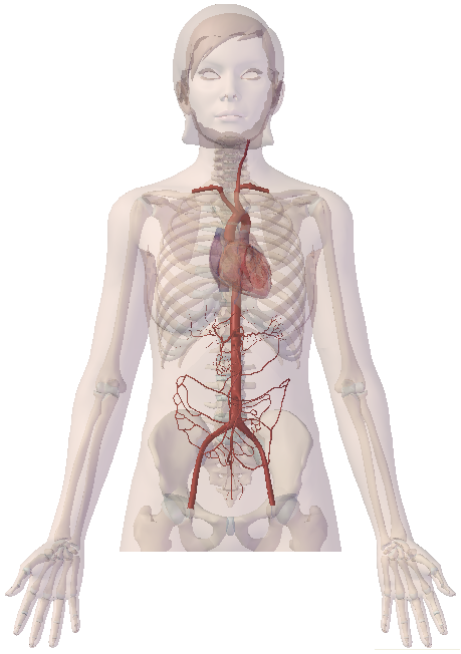

Figure 2.1: Position of the aorta in the body, from [3].

distinguished in the descending aorta: the thoracic aorta and the abdominal aorta. In humans, the transition between the descending aorta and the abdominal aorta is marked by the diaphragm. The thoracic aorta begins at the fourth thoracic vertebra and ends anterior to the twelfth thoracic vertebra, in the diaphragmatic aortic aperture. It provides visceral branches to the pericardium, lungs, bronchi and oesophagus, and parietal branches to the thoracic wall [2, 3].

The abdominal aorta begins at the inferior border of the twelfth thoracic vertebra and descends anterior to the lumbar vertebrae to end at the fourth lumbar vertebra, by dividing into two common iliac arteries. The abdominal aorta branches to supply the viscera and the vertebral column. Its diameter diminishes rapidly in calibre as it descends, because the branches are large, however, with age the diameter increases slightly and the angle at the bifurcation changes [2].

Similar to all arteries the aorta has three layers: the tunica intima (inner layer), the tunica media (intermediate layer) and the tunica adventitia (outer

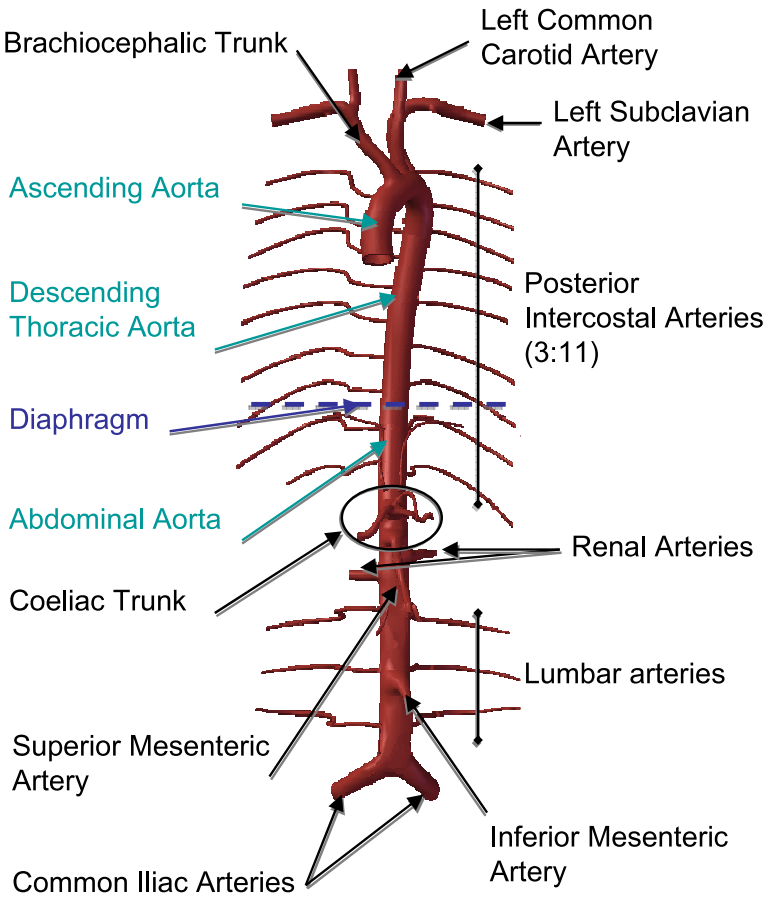


Figure 2.2: Aortic branches, modified from [3].

layer), as can be seen in fig. 2.3. Arteries can be classified as elastic or muscular depending on the composition of these three layers. Elastic arteries are those in which the media contains many elastic laminae and smooth muscle cells. Muscular arteries are those in which the media is mainly composed of smooth muscle cells and the content of elastic laminae has diminished. Large blood vessels are elastic, while small diameter vessels and vessels approaching the periphery are generally classified as muscular [5].

The aortic tunica intima is composed of endothelium and subendothelium. The endothelium is formed by a single layer of cells that is separated from the next layer by a basal lamina. Its role is the protection of the inner structure from plasma lipids and lipoproteins. The subendothelium is composed mainly by smooth muscle cells, that become denser as they ap-

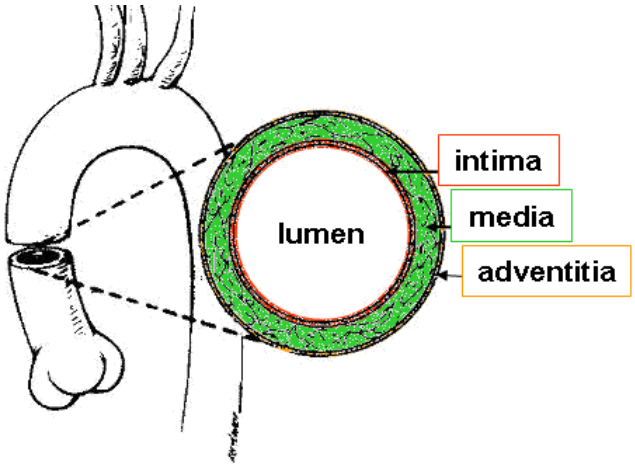


Figure 2.3: Arterial layers within the aortic wall, modified from [4].

proach the tunica media. The tunica media is composed of elastic laminae and smooth muscle cells, as in fig. 2.4. The elastic laminae are concentrically arranged and regularly spaced. The smooth muscle cells are oriented obliquely running diagonally at small angles between the concentric elastic laminae, forming a spiral [5]. Lastly, the tunica adventitia is made up of dense fibroelastic tissue without smooth muscle cells. It can also contain Schwann cells with associated nerve axons.

When excised from the body, the length of the aortic vessel diminishes [6]. The aorta, therefore, like most of arteries, is longitudinally pre-stretched *in situ*. This is a strategy adopted to reduce the load due to the pressure of the blood expelled from the heart. As can be seen in fig. 2.4, fibres within the aorta are helically wound [5]: this means that if stretched along the longitudinal direction, the aortic internal radius diminishes. According to Laplace's law for thin walled vessels[1]:

$$\sigma_\theta = P\frac{r}{\delta}; \tag{2.1}$$

[1]The mean value of $\sigma_\theta$ for thick walled cylindrical vessels equals exactly the universal result for the inflation of a thin walled cylinder, regardless of the material properties or the thickness [6].

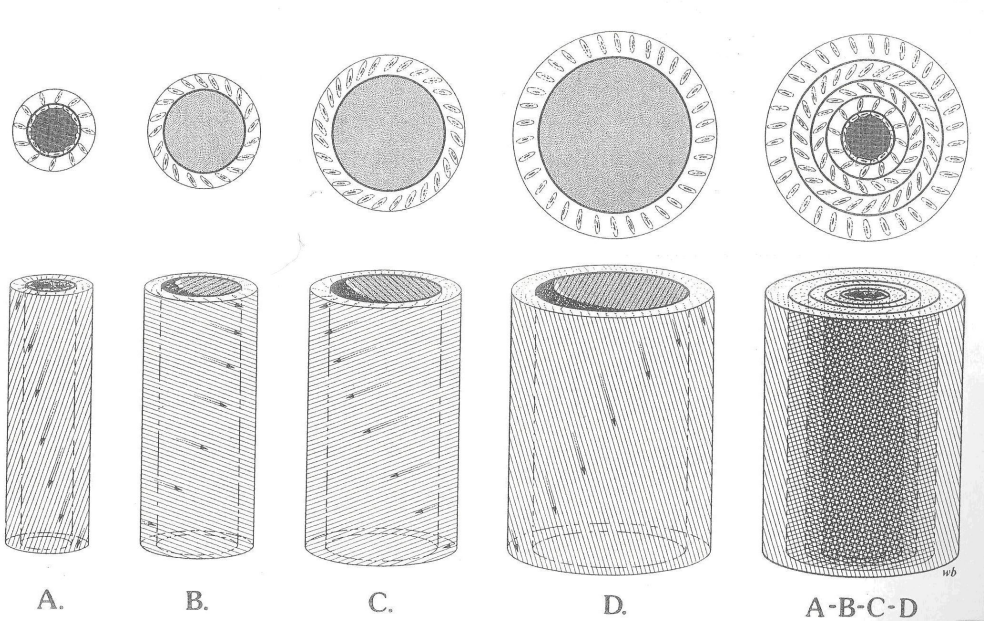


Figure 2.4: Concentrical layers in the arterial fibre orientation, from [5]

where $\sigma_\theta$ is the circumferential stress, $P$ is the internal pressure and $r$ is the internal radius of the vessel when pressurised, and $\delta$ is its thickness. From this it can be deduced that a reduction in the radius due to the longitudinal pre-stretch will consequently reduce the circumferential stress experienced by the aortic wall when pressurised by the blood [7]. The longitudinal pre-stretch can be evaluated from the following:

$$\lambda_z = \frac{z}{Z}; \tag{2.2}$$

which is the ratio of the axial length of the vessel *in situ*, $z$, to that *in vitro*, $Z$ [8]. The parameter $\lambda_z$, axial stretch, has been measured for aortas from different animals and it has been found to increase along the length of the aorta from 1.1 to 1.6 [8].

Another characteristic of arteries that has been observed is that when an arterial ring is cut radially, it springs open [9–11]. This behaviour demonstrates the presence of residual stress in the arteries. Many reasons have been

proposed to explain this phenomenon. From a developmental point of view it has been noted that prior to the first heartbeat residual stress is not present, i.e. the number of cells in the internal and external layers of the vessel are the same [12]. Subsequently, after the first heartbeat, due to the mechanical stimulus of the blood flow the cells in the internal layer grow faster than those in the external layer, causing the residual stress [6]. From a functional point of view, it has been hypothesised that circumferential residual stress is needed to maintain an uniform stress state for the vessel [8]. Residual stress in arteries has been widely studied and it has been found to increase along the aorta away from the heart and to increase with age, demonstrated by an increased opening angle [13]. Moreover, the opening angle was found to be significantly greater in males than in females [13]. Cardiovascular diseases alter the arterial structure of the vascular wall and cause changes in the physiological stress pattern. Usually, this is estimated by measuring the vessel opening angle, whereby it is higher in vessels with visible atheroma [13].

Aortas are susceptible to many different diseases, like aortic atherosclerosis and aneurysms. These diseases are due to or cause an alteration in the mechanical properties of the aortic wall [2].

In aortic atherosclerosis a narrowing of the internal lumen may be observed. This is the result of a chronic inflammatory response in the walls of the aorta. The inflammation is in large part due to the accumulation of macrophage white blood cells. Lacking the adequate removal of fats and cholesterol from the macrophages, which is performed by functional high density lipoproteins (HDL) low density lipoproteins (LDL) accumulate, promoting atherosclerosis [14]. This disease may be implicated in embolic events or strokes. Imaging can be used for the diagnosis of aortic atherosclerosis where it is possible to see a signal loss due to the turbulent flow at the atherosclerotic plaque. Imaging can also enable the narrowing to be observed and the composition of the plaque to be investigated. This can permit the assessment of the risk of plaque rupture and thrombus formation [2].

Aortic atherosclerosis itself may be one of the causes of another disease, the aortic aneurysm [15]. An aneurysm is a dilatation of the aortic wall and may form in any part of the aorta [16]. In the thoracic aorta the medial wall

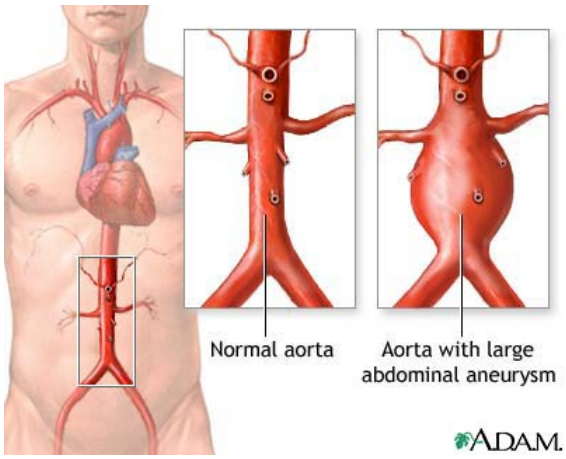


Figure 2.5: Abdominal aortic aneurysm, from [18].

can degenerate and intimal dissection can occur. They can also be result from diseases of the connective tissue such as Marfan's syndrome[2], homocystinuria and Ehlers-Danlos syndrome[3]. Aneurysms in the descending aorta and abdominal aortic aneurysms (AAA), are generally caused by atherosclerosis and in a small percentage of cases by mycotic diseases or trauma, see fig. 2.5. Usually aneurysms grow symptomless. When symptoms are present they include breathlessness, chest pain, back pain, hoarse voice, cough and haemoptysis. An aortic aneurysm can alter the blood flow and give rise to a phenomenon called aortic regurgitation: this altered flow pattern generates murmurs that may be audible on cardiac auscultation. Repair of AAA is generally carried out in patients with symptoms or with a dilatation that exceeds 5 cm in diameter [2, 17]. The treatment consists of a prosthetic-graft replacement of the diseased aorta [19] or in the deployment of a stent graft in the aortic region. The former surgery is quite invasive requiring the abdomen to be opened and may be associated with potential complications like injury to large lymphatic trunks that could lead to chylous ascites [2]. The biggest risk related to aneurysm is the fact that it can grow silently and

[2] `marfan.org`
[3] `ednf.org`

then rupture. Rupture in most cases results in hemorrhage, and is a fatal event. Many studies have been conducted on the factors that lead to aortic aneurysms and aortic aneurysm rupture [20].

Most of the studies done on abdominal aortic aneurysms have analysed the effect that the altered blood flow has on the thin enlarged aneurysmatic wall [17, 21–25] and investigated if a stress concentration in the wall can predict the rupture point [26]. All of these studies investigate the disease once it is clearly manifested, i.e. the aorta is dilated. Further study of the microscopic structure of the aortic wall to assess the disease at an early stage is needed. Many studies have been conducted on the structure and orientation of fibres within the aortic wall. All of them concluded that an aneurysm is the result of a degenerative disease that progressively alters the ratio of aortic wall components, thus weakening its structure [27]. In fact, evidence indicates that AAAs are associated with increased local production of enzymes capable of degrading elastin and interstitial collagen [28]. In particular, it was found that AAAs alter elastin concentration and configuration [28–30], that collagen degradation is caused by an enzyme produced by smooth muscle cells (SMCs) [28,31], and that SMCs content was reduced and SMCs apoptosis was increased in AAAs [30, 32]. Most of the studies that relate aortic wall dilatation with mechanical failure of collagen and elastin were done using histology or special microscopes that require the tissue to be harvested from the body [33–35]. The use of these techniques for the early stage diagnosis of aortic disease is highly impractical due to their invasiveness since removal of a sample of aortic tissue is necessary.

There is a clear need, therefore, to develop a method to study the aortic structure in a non-invasive way, in order to provide a means of early diagnosis of this life-threatening disease.

### 2.2.1 Porcine Aortas

In general, due to limitations in the availability of fresh human tissue, biological studies are carried out on animal tissue. Amongst the many species available, the most popular animal tissue used for modelling the human car-

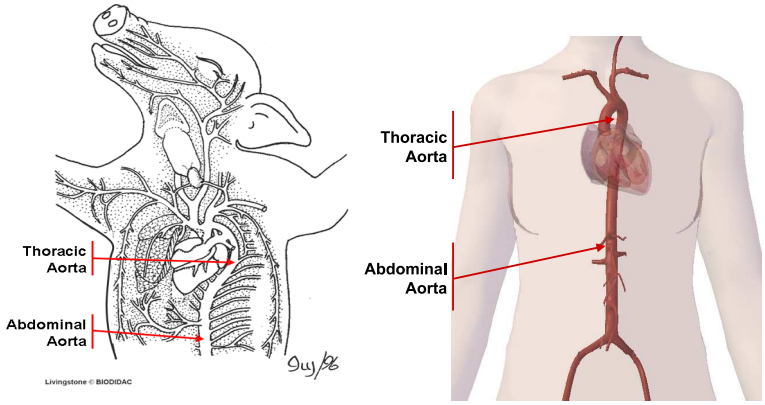


Figure 2.6: Anatomy of the aorta in different species: A) Heart and blood blood vessels in a pig, modified from [41]; Heart and blood blood vessels in a human being, modified from [3].

diovascular system is the porcine one. The similarity between the porcine cardiovascular system and the human cardiovascular system, shown in fig.2.6, stretches so far that porcine aortic valves are used in current clinical practice for xenotransplants on human diseased hearts [36,37]. Porcine arteries can be used to model human arteries not only because of a similar size: it has been demonstrated, in fact, that also the mechanical response and the structure of two systems is particularly close [38, 39]. Early works by Rhodin [5] and Burton [40] used porcine aortas in their histological and mechanical studies of arteries and, more recently, Hughes *et al.* [38] and Johnson *et al.* [39] have used porcine models to mimick the behaviour of human cardiovascular diseases, since also the histopathological proliferative response to arterial disease is similar to that seen in humans [39]. Due to the similarities between human and porcine vascular tissue and due to the large body of literature on the reliability of porcine models, the novel technique described in this work was carried out on porcine aortas.

## 2.3 Constitutive Models for Arterial Tissue

The starting point for the characterization of the mechanical behaviour of the aorta is the choice of a suitable constitutive model. The constitutive model needs to be carefully selected since it will influence the outcome of the whole study, i.e. a poor constitutive model would fail in the characterization of the aorta. Finding a suitable model for aortic tissue is a challenging task, because of the complex three layered structure of the tissue previously described 2.2. This complex structure has implications in the mechanical behaviour of the tissue, which responds non-linearly to loading. Moreover it is noteworthy that *in vivo* the aorta is subjected to a variety of loads: the longitudinal pre-stretch, the circumferential residual stress, the cyclic inflation by blood pressure [6].

### Arterial Mechanical Behaviour

By looking at fig. 2.7 it is possible to see that the behaviour of an artery is non-linear and that it can be represented as a function of the inflating pressure (blood pressure). As outlined previously, the inflation of a cylinder follows the law of Laplace, see eq. 2.1. If Laplace relationships are plotted for different pressures (straight lines through the origin), it can be noted that for each line there is only one point of intersection with the arterial response curve. The radial value where the Laplace line and the artery curve meet, represents the equilibrium radius for the artery at that pressure. For the inflation to be stable, the intersection point has to exist, as it represents an equilibrium condition. This shows that there is a functional reason for the arterial behaviour to be non-linear, as this behaviour will ensure arterial stability for the continuous inflation operated by the heart [42]. The stress-strain relationship for an aortic wall belongs to a particular kind of non-linear material: it can be defined as hyperelastic. Hyperelastic means that the material can undergo large deformations without permanent deformation. This depends on the structure of the three-layered aortic wall and mainly in its composition of elastin and collagen fibres. In the first part of

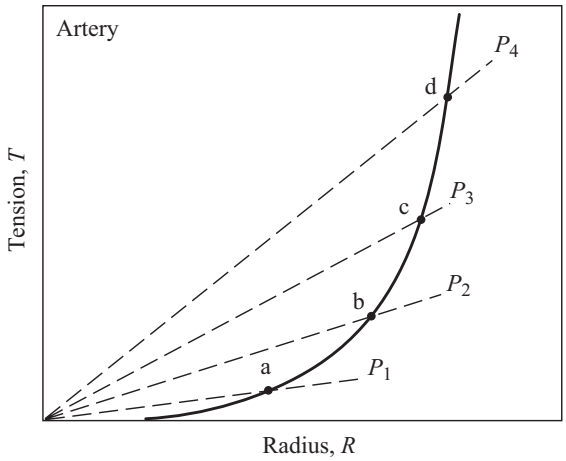


Figure 2.7: Relationship between inflating pressure and arterial behaviour, from [42].

the stress-strain curve of an artery, only elastin is responsible for bearing the load. As the load increases, the collagen fibres, that are stiffer, straighten and start to bear the load; they account for the steep linear part at the end of the curve [42]. This was demonstrated by Burton *et al.* [40] by selectively digesting one of the two components (elastin and collagen) and performing uniaxial tests on the sample. As can be seen from fig. 2.8, when trypsin digestion was used to remove elastin, the remaining tissue demonstrated the properties of collagen (curve with diamonds). Alternatively, when formic acid digestion was used to remove collagen, the remaining tissue had the properties of elastin fibres (curve with open circles). Together with collagen and elastin there is a third component in arteries, that is the matrix on which fibres are laid. This component has a high percentage of water, and gives a very interesting property to the arteries: incompressibility. Water itself is incompressible, and the arterial wall is composed of approximately 70% water. Incompressibility dictates that not all the deformations are allowed simultaneously: stretching in one direction should be accompanied by shrinkage in the other direction to ensure the conservation of volume. This condition is described by equation 2.3, where the product of the stretches in the circumferential, axial, and radial directions, respectively, is equal to one [43].

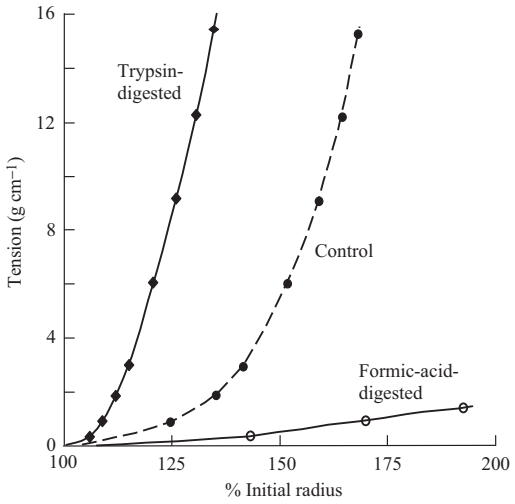


Figure 2.8: How elastin and collagen affect the arterial stress-strain relationship. The broken curve is for an untreated artery from [42].

$$\lambda_\theta \lambda_z \lambda_R = 1; \tag{2.3}$$

### Arterial Constitutive Models

To describe such complex behaviour many constitutive models have been proposed in literature. Due to the hyperelasticity of the aorta, all of them have to be defined for large deformations. Under the assumption of path independence between the initial and final strain states, strain energy functions can be defined to describe these models [44]. The strain energy function is generally a function of the Green strain tensor $E$, see eq. 2.4, which is a function of the deformation gradient $F$, see eq. 2.5 [6, 45]:

$$\Psi = \Psi(E); \tag{2.4}$$

$$E = \frac{1}{2}\left(F^t F - \mathbb{I}\right); \tag{2.5}$$

where $\Psi$ denotes the strain energy function, and $\mathbb{I}$ the identity tensor. The second Piola–Kirchhoff tensor, $S$, and the Cauchy stresses $\sigma$ are closely related to the strain energy function by means of $E$, see eq. 2.6 and 2.7 [44,45]:

$$S = \frac{\partial \Psi(E)}{\partial E}; \tag{2.6}$$

$$\sigma = J^{-1} F \frac{\partial \Psi(E)}{\partial E} F^t; \tag{2.7}$$

where $J$ is the Jacobian determinant of the deformation tensor $J = det(F)$ and represents the ratio of the deformed configuration volume to the reference configuration volume[4] [6]. Expressing a constitutive model through the strain energy function is convenient as it allows the stress–strain relationship to be written as a scalar function rather than a tensor function.

The strain energy functions hitherto proposed in literature are exponential [6,46]; or neo-Hookean [47]; or based on a polynomial interpolation, like the Mooney-Rivlin model, as in [48]. All these works assumed the material model as homogeneous and pseudoelastic. Pseudoelasticity is a concept introduced by Fung [46]. In his studies, he noted that arterial tissue does not have coincident loading and unloading curves, as shown in fig. 2.9. The area enclosed between the two curves represents the amount of dissipated energy. This loss of energy can be regarded as viscous dissipation, that depends not only on the amount of deformation but also on the rate of deformation [6]. Fung [46] observed that soft tissue tends not to depend strongly on strain rate. He suggested that the loading and unloading behaviour could be treated separately as elastic and called such an approach pseudoelasticity. To describe the stress-strain relationship of arterial tissue he proposed an exponential strain function, that in its more general formulation corresponds

[4]The following relationship is also valid: $J^2 = det(C) = I_3 = \lambda_x^2 \lambda_y^2 \lambda_z^2$, where $C$ is the right Cauchy-Green deformation tensor, $I_3$ the third strain invariant and $\lambda$ the stretch in the prescribed direction. For arterial tissue incompressibility is assumed, eq. 2.3, and so it is possible to state that $J = 1$.

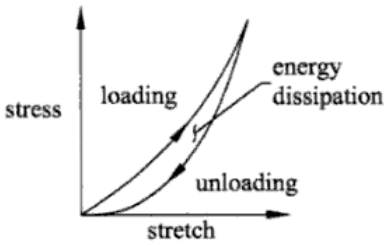


Figure 2.9: Noncoincident loading and unloading, evidence of viscous dissipation, from [6].

to eq. 2.8:

$$\Psi = \frac{1}{2}c\left(e^{Q}-1\right); \tag{2.8}$$

$$\begin{aligned} Q = {} & c_1E_{11}^2 + c_2E_{22}^2 + c_3E_{33}^2 \\ & +2c_4E_{11}E_{22} + 2c_5E_{22}E_{33} + 2c_6E_{33}E_{44} \\ & +c_7\left(E_{12}^2 + E_{21}^2\right) + c_8\left(E_{23}^2 + E_{32}^2\right) + c_9\left(E_{13}^{21} + E_{31}^2\right); \end{aligned} \tag{2.9}$$

where $c$ and $c_1 - c_9$ are material parameters and $E_{11} - E_{33}$ the components of the Green tensor. The number of $c_1 - c_9$ constants changes according to the material symmetries considered: an orthotropic model will need them all; a transverse isotropic model will need five constants; an isotropic model only two [46]. This strain energy function has been applied to a wide variety of biological soft tissues and has proven to be a good description of experimental data [6], although not offering any insight into them. In fact, there is no direct correspondence between the material constants and the structure of the soft tissue analysed. Since this correspondence is key to the aim of this thesis, that is to distinguish and describe the behaviour of the constitutive elements of the aortic tissue, other strain energy function were considered. Another hyperelastic strain energy function is the Mooney–Rivlin model. It is a polynomial function of the strain invariants $I_1$, $I_2$, defined according to eq. 2.11, 2.12. The general formulation of a Mooney–Rivlin strain energy function is the one shown in eq. 2.10:

$$\Psi = \sum_{i=0,j=0}^{\infty} c_{ij}(I_1 - 3)^m (I_2 - 3)^n; \qquad c_{00} = 0; \tag{2.10}$$

where

$$I_1 = tr(C) = \lambda_1^2 + \lambda_2^2 + \lambda_3^2; \tag{2.11}$$

$$I_2 = \frac{1}{2}(C^2 - C^t \cdot C) = \lambda_1^2\lambda_2^2 + \lambda_2^2\lambda_3^2 + \lambda_1^2\lambda_3^2; \tag{2.12}$$

$$I_3 = det(C) = \lambda_1^2\lambda_2^2\lambda_3^2; \tag{2.13}$$

in this case $c_{ij}$ are the material parameters and $C$ is the right Cauchy-Green deformation tensor. Depending on the values assigned to $m$ and $n$ different formulations are possible. For example, with $m = 2$, $n = 1$ the Signiorini model is obtained, while with $m = 3$, $n = 1$ the model used in Lally *et al.* [48] can be reproduced. Note that only when the $c_{10}$ material parameter is present, the constitutive model is called the neo-Hookean model [44]. Unfortunately, with this model it is also difficult to isolate and represent the behavior of collagen fibres, and this is the reason why a different kind of model is needed.

The latest development in the study of arterial tissue is the attempt to study the tissue as a heterogeneous material. Using heterogeneous material elements the constitutive parameters have physiological meanings related to the microstructure, i.e. the model becomes mechanistic. In particular, the arterial wall can be regarded as an anisotropic fibre-reinforced material: a material in which fibres are dispersed in a matrix at a specific angle. Accounting for the presence of fibres results in the addition of a term in the strain energy function that accounts for the anisotropy of the fibres, as shown in the following eq. 2.14.

$$\Psi = \Psi_{iso} + \Psi_{aniso}; \tag{2.14}$$

The isotropic term is often one of the isotropic models presented above, de-

pendent on the strain invariants $I_1$, $I_2$. The anisotropic term depends on the direction (angle) of fibres [43,49–56]. This formulation has led to the determination of new invariants that describe the strain energy function anisotropic term, and are defined by eq. 2.15–2.19 [43]:

$$I_4 = a_0 \cdot C \cdot a_0; \tag{2.15}$$
$$I_5 = a_0 \cdot C^2 \cdot a_0; \tag{2.16}$$
$$I_6 = a_0' \cdot C \cdot a_0'; \tag{2.17}$$
$$I_7 = a_0' \cdot C^2 \cdot a_0'; \tag{2.18}$$
$$I_8 = a_0 \cdot C^2 \cdot a_0'; \tag{2.19}$$

where $a_0$, $a_0'$ are the directions of the fibres present in the material. The fibre orientation within the arterial wall is usually determined through histological analyses, see fig. 2.10, leading to the definition of what can be called a *histomechanical* model [50]. Currently there are models defined for one family of fibres [54, 58], two families of fibres [49–53] and up to four families of fibres [55, 56], see schematic on fig. 2.11.

One of the possible options to model aortic tissue is a fibre reinforced material model, like the one described in [54, 59]. This is a heterogeneous model with one family of fibres, where the isotropic part of the strain energy function has a Mooney-Rivlin formulation and the anisotropic part is a function of $I_4$. One of the characteristics of the model is that it is determined piecewise (e.g. it applies different equations for different portions of the stress-strain curve), hence the determination of the model can be biased by the switch points chosen, making it unsuitable for the present work. Moreover, considering only one family of fibres while producing valid results for the in-fibre direction, does not allow for a correct representation of the cross-fibre directions, [54, 59]. From histological findings, see fig.2.10, it is possible to see that fibres are usually arranged in a symmetrical way, with two opposite directions bearing the load.

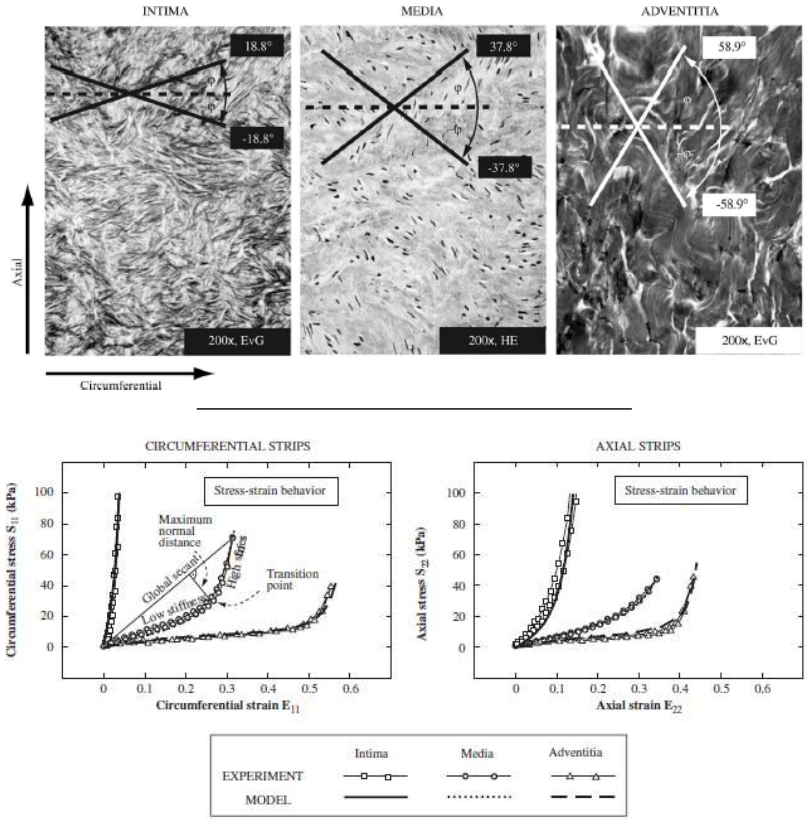


Figure 2.10: Example of histomechanical modelling for the coronary artery from [57]: top) fibre angle from histological data; bottom) stress-strain response for every layer.

In order to give a more complete representation of the variety of fibre distributions observed within the arterial layers, a model considering four families of fibres could be used [55, 56]. The strain energy function defined in this model is the sum of a neo-Hookean term mimicking the elastin isotropic behaviour, an exponential term, function of $I_4$ representing the orientation of each collagen fibre family, and a linear term reproducing the smooth muscle activation. This model, however complete, lacks the possibility of representing fibre distribution variation across the different layers. The absence of a parameter to represent the distribution of each family of fibres weakens the validity of this model: able to represent the arterial wall globally, but unsuitable to represent each arterial layer singularly.

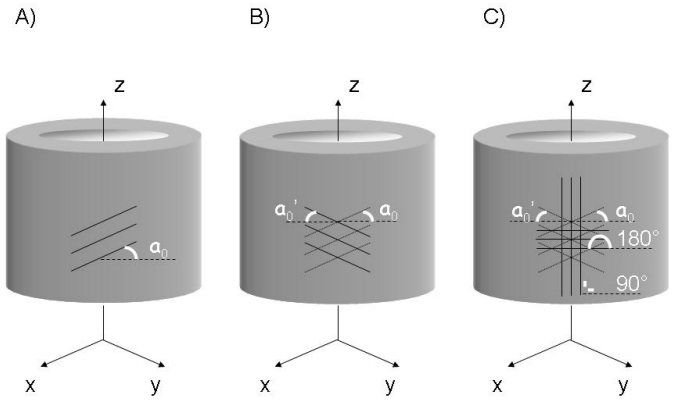


Figure 2.11: Schematic of fibre orientation in different constitutive models: A) one family of fibres [54, 58]; B) two families of fibres [49–53]; C) four families of fibres [55, 56].

Factors that can influence the choice between different structurally motivated models are repeatability, breadth of application, and availability of data for comparison. A model that fits into these requirements is the one defined in [53]. This constitutive relation represents the complex architecture of an arterial layer as a fibre-reinforced composite in which two families of collagen fibres are embedded in an isotropic groundmatrix [53].This model, like the former two analysed, is made up by the sum of an isotropic neo-Hookean term and an anisotropic one. Moreover, like the model by Baek *et al.* [55], the anisotropic term, responsible for representing the collagen response, is an exponential function. However, the biggest advantage of the model developed by Gasser *et al.* [53] is the presence of a fibre dispersion parameter $\kappa$, which, by measuring the distribution of fibres, gives the model a general validity. In fact, such a model can be used to reproduce the behaviour of each single arterial layer, as in fig.2.10, as well as the arterial wall as a whole. This feature, together with the availability of extensive resources on the application of this model to arterial tissue [53, 57, 61, 62], made this constitutive model the most suitable one for the present study.

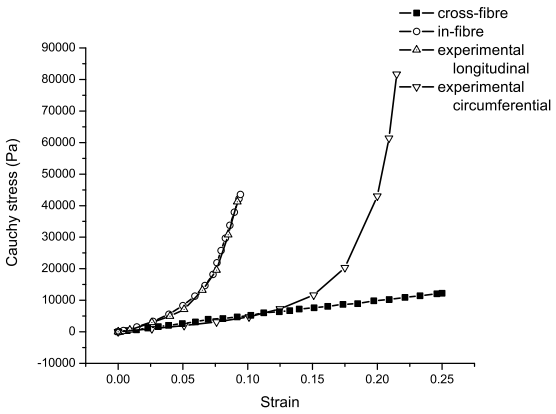


Figure 2.12: Comparison between FE results for the model described in [54, 59] with experimental data for a adventitia obtained from [60].

### 2.3.1 Mechanical Tests on Arterial Tissue

A constitutive model is usually determined from its stress-strain curve, therefore, to study and to determine a characteristic stress-strain curve for the aorta, experimental tests had to be conducted. These tests have demonstrated that the aorta, like most of arteries, has an anisotropic behaviour, i.e. its stress-strain curve depends on the direction of the load. This can be seen in fig. 2.10, where stress-strain curves obtained by testing coronary arteries are shown. From the same figure it is possible to see that this anisotropic behaviour is caused by the orientation of the fibres within the tissue. The anisotropy due to presence of fibres interwoven in the tissue has raised speculations on the most suitable mechanical test for arteries. In literature there are many examples of uniaxial [50, 53] and biaxial [6, 48] tests conducted on arteries. Recently, uniaxial tests on each arterial layer [2], have been reported [57, 60, 63]. In order to account for the anisotropy of the tissue, uniaxial tests on arteries are usually performed in the arterial longitudinal and circumferential direction, see fig. 2.13, and fig. 2.10. Biaxial tests are often used because a biaxial loading is considered closer to the one experienced physiologically by the tissue, that is loaded in two directions simultaneously [17]. While biaxial tests allow for studying the interactions

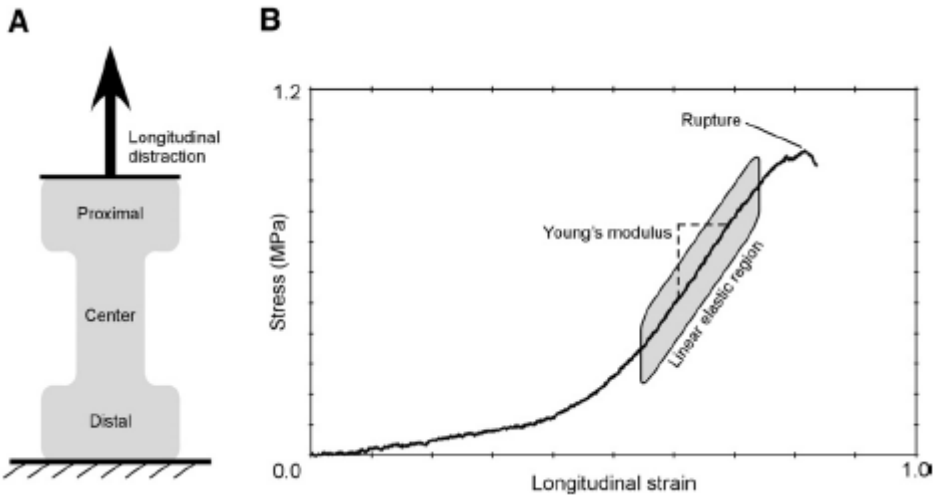


Figure 2.13: Example of uniaxial test on aortic tissue; A) longitudinally oriented porcine aorta test specimen; B) representative stress-strain curve for longitudinal vessel distraction, from [65].

between the fibres and the ground matrix, they make it impossible to determine simultaneously the behaviour of the tissue in each direction, and they need large variations in the stresses and strains applied to the tissue in both directions to obtain a full characterization of the tissue [64]. By contrast, uniaxial tensile tests require the tissue to be tested in each direction of interest and therefore allow the effects of the fibres on each direction to be determined independently. If carried out on each direction of interest, uniaxial tensile tests can then be considered suitable for the determination of the stress response of arterial tissue, since they offer enough information to define an anisotropic behaviour. In the present work, uniaxial tests will be performed in both the longitudinal and the circumferential direction. Since the process of stripping every single arterial layer was considered invasive, the aortic specimens were tested as a whole, and their results used to define the constitutive model.

## 2.4 Medical Imaging

In order to obtain a model representative of the real vascular tissue, its structure and response to stress should be studied *in vivo* and with minimum discomfort for the patient. Currently studies on vascular tissue are conducted mainly using histological techniques. This means that the tissue is studied when it is no longer in the body. In order to perform histological studies, tissue has to be harvested from human bodies by surgery or during autopsy. In the first case the discomfort for the patient is evident, whilst in the second the tissue studied is degraded due to *rigor mortis*. Medical imaging is a non-invasive way to examine what happens inside the body. Non-invasive techniques that are commonly used for the study of arterial diseases include Computed Tomography Angiography (CTA) [66], Magnetic Resonance Angiography (MRA) [67], X-Ray Angiography [68] and colour Doppler Ultrasound [69]. These imaging modalities are limited as they can only image the blood flow and cannot be used to study the mechanics of the arterial wall. They can therefore only provide information on the effect of arterial disease on blood flow and not the underlying cause. Conventional imaging techniques like Computed Tomography (CT) [70] and Magnetic Resonance Imaging (MRI) [71] can be used to image the arterial wall; however they can only provide an anatomical description of a vessel which is insufficient for full mechanical characterization. Finally, disadvantages of techniques such as Ultrasound or Nuclear Medical Imaging (NMI) (like Positron Emission Tomography (PET)) are low penetration through air or bone and the need for radioactive tracer material to be administered to the patient, respectively [72].

### 2.4.1 Magnetic Resonance Imaging

Among the imaging techniques listed above, Magnetic Resonance Imaging is the technique that poses minimal risk for patients who have no ferromagnetic foreign bodies implanted [73]. At the same time, MRI allows the visualisation

of inner human organs: Magnetic Resonance images are characterized by excellent contrast between the various forms of soft tissue within the body [72]. Moreover, MRI offers the possibility of extrapolating information other than geometry of inner organs from the body. Different MRI techniques can evaluate the shear stress on the tissue (Magnetic Resonance Elastography); its motion (Tagged Magnetic Resonance); the velocity of its motion (Phase Contrast Magnetic Resonance or Magnetic Resonance Fluoroscopy [74]); the diffusion of water (Diffusion Tensor Imaging). Due to its versatility and the absence of risks for the patient, Magnetic Resonance Imaging (MRI) is the best technique to determine *in vivo* aortic structure and behaviour.

In particular, to perform the static analyses in this study a special MRI technique was chosen: Diffusion Tensor Imaging. In order to study the aortic wall deformation when subjected to the blood flow cyclic loading another technique was chosen: Phase Contrast Imaging.

### 2.4.2 Diffusion Tensor Imaging

Diffusion Tensor Imaging (DTI) is a particular MRI technique which was introduced in the mid 1990s by Basser *et al.* [75]. With this technique it is possible to study the diffusion of water that is abundant in human tissues. Water molecules move through tissues and this motion is due to the thermal motion of the molecule (Brownian motion). If there are no fibres in the tissue the probability for a molecule of water to move in all the directions is the same. This is the case for isotropic diffusion and the area of probable motion for a water molecule can be represented as a sphere. If there are fibres in the tissue, there is a higher probability for the molecule of water to move along the fibres rather than perpendicular to these fibres, as fibres represent an obstacle. This is the case for anisotropic diffusion and the area of probable motion for a water molecule can be represented as an ellipsoid. This diffusion ellipsoid can be represented mathematically by a tensor. It is therefore possible to determine the anisotropy of a tissue by determining the diffusion tensor of water in the tissue [76, 77].

### Measure of Diffusion

Diffusion is measured using a spin-echo pulse sequence. Every proton ($H^+$), can be represented as a vector with its resonance frequency (Larmor frequency). When a strong magnetic field is applied, all of these vectors align along the direction of the field, say $z$ [78]. When a radio frequency excitation pulse is applied, the vectors are rotated into the transverse plane ($x$,$y$) and start precessing at their Larmor frequency. This frequency is dependent on the magnetic field experienced by the protons, and is dependent on the tissue type. Dephasing is the name given to this process. Subsequently a 180° refocusing pulse is applied, that causes the protons to rephase, but if the Larmor frequencies are changed, the realignment will be imperfect. Applying a magnetic gradient in one direction, the Larmor frequencies are made spatially dependent. Therefore, if spins have not moved, they will realign, but if they have diffused, their frequency will be different and they will not realign [78]. This non-realigning implies a loss in the signal intensity. Then it can be stated that the more a proton moves during this process, the more signal intensity is lost, and this loss depends on the strength and duration of the magnetic field gradient (represented by $b$, the diffusion weighting factor [79]) and on the Diffusion tensor $D$ itself. $D$ is a 3×3 symmetric positive definite tensor. The relationship between the signal intensity and the diffusion tensor can be represented by eq. 2.20:

$$\begin{aligned} \frac{S}{S_0} &= exp^{-\gamma^2 G(t)^2 \delta t^2 (\Delta t - \frac{\delta t}{3}) D} = \\ &= exp^{-bD}; \end{aligned} \tag{2.20}$$

where $S_0$ is the reference signal intensity (i.e. without considering diffusion gradients), $S$ is the signal with the gradient applied, $\gamma$ is the gyromagnetic

ratio[5], $G(t)$ is the strength of the gradient pulse, $\delta t$ is the duration of the pulse, $\Delta t$ is the time between the two pulses, and finally, D is the diffusion constant [78,80]. The $b$ value influences the signal-to-noise ratio of the image and describes the impact that the diffusion has on the image: when the $b$ value increases, water molecular diffusion increases and therefore the signal of the image, $S$, diminishes along the direction of the gradient and the signal-to-noise ratio decreases [81, 82]. In contrast, for low $b$ values the signal-to-noise ratio can be high but diffusion of water molecules along fibres is so low that fibre tracking may be impeded. The $b$ value and the gradient are connected: the $b$ value is proportional to gradient parameters such as amplitude, duration and time spacing and the most suitable value depends on the tissue type being imaged [76, 82].

In order to have a valid result in a three dimensional environment, the gradients are applied in more than one direction simultaneously: diffusion must be measured in at least six directions. This is due to the fact that the orientation of the tensor is not known in advance and that many orientations can be present in a biological sample. This special sequence results in the definition of a diffusion tensor for each voxel of the image.

### Tensor-Derived Quantities Of Diffusion

A Diffusion tensor contains information on water diffusion that may be extrapolated to describe structural characteristics of the material. To study in detail Diffusion Tensor Imaging, tensor-derived quantities have been defined [75,77,79,80,83] that can be used to study the anisotropy of the tissue.

**Diffusion Anisotropy Indices** The diffusion tensor eigenvalues can be evaluated and rotational invariants defined according to the following eq.

[5]When placed in a magnetic field not aligned with its magnetic moment, hydrogen ($H^+$) nuclear spin will precess at a characteristic frequency: the gyromagnetic ratio is the relationship between the precession frequency and the magnetic field strength. It is a property due to proton mass and charge, characteristic of each element rephase [78].

2.21–2.24:

$$I_1 = \lambda_1 + \lambda_2 + \lambda_3; \tag{2.21}$$

$$I_2 = \lambda_1\lambda_2 + \lambda_2\lambda_3 + \lambda_1\lambda_3; \tag{2.22}$$

$$I_3 = \lambda_1\lambda_2\lambda_3; \tag{2.23}$$

$$I_4 = \lambda_1^2 + \lambda_2^2 + \lambda_3^2; \tag{2.24}$$

these quantities can be used to define what are called Diffusion Anisotropy Indices (DAIs) [80], relative quantities that range from zero (isotropy) to one (complete anisotropy) and that can be used to compare different studies. The most used DAI is Fractional Anisotropy (FA) [75, 77, 79, 84]. It is defined according to eq.2.25:

$$FA = \sqrt{1 - \frac{I_2}{I_4}} =$$

$$= \sqrt{\frac{3}{2}}\sqrt{\frac{\left(\lambda_1 - tr(D)\right)^2 + \left(\lambda_2 - tr(D)\right)^2 + \left(\lambda_3 - tr(D)\right)^2}{\lambda_1^2 + \lambda_2^2 + \lambda_3^2}}; \tag{2.25}$$

Fractional Anisotropy[6] is related to the presence of oriented structures within the tissue, and is proportional to the diffusion ellipsoid's eccentricity [85].

### 2.4.3 Fibre Analysis

The quantities evaluated from the Diffusion Tensor are not only related to the motion of water molecules, but can be used to describe the environment in which this motion happens. From the evaluation of the eigenvectors a

[6]It has to be noted that invariant $I_4$ defined by eq. 2.15 for fibre-reinforced materials is different than $I_4$ defined by eq. 2.24 for DTI. In fact, eq. 2.24 corresponds to the trace of a squared tensor, i.e. $I_4 = tr(T^2) = I_1^2 - 2I_2$. Due to the fact that the quantity expressed by eq. 2.24 can be obtained by the sum of two other invariants, $I_4$ will henceforth take the meaning of eq. 2.15.

diffusion ellipsoid can be defined. The first eigenvector will represent the most favoured motion direction. In fact, the first eigenvector of the diffusion tensor can represent the fibre direction. From this idea follows the conclusion that with Diffusion Tensor Imaging it is not only possible to obtain a measure of the degree of anisotropy of a tissue, but it is also possible to determine the position and the orientation of the structures giving rise to such anisotropy within the tissue, i.e. fibres. The study of fibre patterns from DTI is called Fibre Tractography [86].

Many different approaches can be used to interpolate fibre patterns: fluid streamlines theory [86]; probabilistic Monte Carlo methods [87]; simulation of the virtual water diffusion process [88]. The algorithm used in this study is the one available in the software MedINRIA, (Sophia Antipolis, France) [89]. This module uses Log-Euclidean metrics to process tensors, protected by a patent (Filing Number 0503483) [89].

The study of fibres through DTI has found numerous successful applications in the investigation of brain growth [90], structure [83, 91], vascularisation [92], and lesions [77, 79, 93]. It has also been applied to the study of other tissues like myocardium [94–103], skeletal muscle [104, 105], smooth muscle [106] and trabecular bone [85, 107].

In particular, the work done on the myocardium is the closest to that which this study tries to reproduce, as it combines the determination of the fibre pattern with the study of the motion of the tissue. In fact, among the tissues listed above and studied with DTI the myocardium is the only one that undergoes a cyclic deformation whereas brain and trabecular bone are subjected to deformation only in the case of serious, often fatal, injuries, and skeletal muscle experiences different task-targeted deformations. The aortic wall experiences a cyclic deformation, caused by the pumping activity of the blood. Its smooth muscle cells have to cooperate with elastic laminae to contain the blood and at the same time distribute it to the periphery of the body. The aortic wall deforms under the action of blood pressure, and this motion can be studied using other MRI techniques. The MRI techniques that have been used to study the motion of the myocardium are: Tagged MRI [98], and Phase Contrast MRI (PC MRI) [95, 97, 101]. Tagged MRI

cannot be used to study the aortic wall motion *in vivo* due to resolution constraints. To apply Tagged MRI to the aortic wall, a spatial resolution of less than 0.5 mm is required, resolution not achievable with currently available clinical MRI scanners. What can be applied to the aortic wall is the technique called PC MRI.

### 2.4.4 Phase Contrast Magnetic Resonance Imaging

The studies performed with DTI are all static analyses, but arteries are not in a static environment [2]. In fact, arteries are loaded cyclically by the pumping action of the heart. In order to perform a complete study on the arterial structures, their dynamic behaviour has to be evaluated. Using Phase Contrast MRI (PC MRI), it is possible to quantify the velocities generated in each pixel by the cyclic loading of the blood pressure. By the integration of these velocities it is then possible to determine both the pixels trajectories and deformations [108, 109]. In PC MRI, the pixel of the image does not represent the image itself, but the velocity of the pixel, hence the image is said to be velocity encoded. This technique is closely related to DTI, and shares its theoretical formulation. The difference between the two is their focus. PC MRI focuses on the motion of a pixel due to an external stimulus, while DTI focuses on the motion of the water molecules within the pixel. In particular, in PC MRI the application of gradient pulses to moving protons induces phase shifts that are directly proportional to the protons' velocity along the direction of the gradient [110]. PC MRI techniques were firstly applied to the determination of arterial flow (magnetic resonance angiography, MRA). In this case, gradient pulses were used to sensitize the signal to a particular flow velocity and direction through an induced phase shift [111–114]. At the beginning of the nineties the groups of Van Wedeen and Pelc applied PC MRI to the determination of myocardial strains [108, 109]. Over the years, PC MRI has been applied to the study of brain motion [115], skeletal muscle motion [116], muscle contraction [117], and tongue deformation [118]. Finally, the group of Pelc and Taylor worked on vessel wall cyclic strain using porcine aortas [109, 119–122].

**Measurement of Velocity and Strain with PC MRI** When the sensitizing gradient is applied, protons moving at the chosen velocity and direction as well as stationary protons are rephased at the echo time $TE$. Therefore, it is necessary to acquire a reference image (an image with no flow sensitization) and subtract this image from the sensitized image in order to produce images of only the moving protons (the reference image being an image of stationary protons) [111]. In order to acquire a complete characterization of the velocity, sensitized gradients need to be applied in at least three directions. Once the phase images are acquired (images of the moving protons) and under the assumption of approximately constant velocity during the experiment, the velocity component $V_i$ parallel to the imaging gradient $G(t)$ can be considered proportional to the phase shift $\phi_i$ of the moving protons [108]. In particular, the relationship between phase shift and velocity is represented by eq.2.26:

$$\begin{aligned} \phi_i(t) &= \gamma \int_0^{TE} tG(t)V_i(t)\,dt \\ \phi_i &\approx K \cdot V_i; \end{aligned} \tag{2.26}$$

The terms in the integral in eq.2.26 can be considered constant: the term $G(t)$ because the gradient applied is constant; the velocity $V_i(t)$, instead, can be considered approximately constant because the gradient applied for a time interval extremely short. The parameter $K$ is defined as the sensitivity of the phase to the velocity [123]. Local differentiation between neighbouring pixels in each image determines the spatial variation of velocity and leads to the determination of the velocity gradient tensor L:

$$L = \begin{pmatrix} \Delta V_x/\Delta x & \Delta V_x/\Delta y & \Delta V_x/\Delta z \\ \Delta V_y/\Delta x & \Delta V_y/\Delta y & \Delta V_y/\Delta z \\ \Delta V_z/\Delta x & \Delta V_z/\Delta y & \Delta V_z/\Delta z \end{pmatrix}; \tag{2.27}$$

The symmetric part of $L$ is defined as the strain rate tensor and is defined as

$W = \frac{L+L^t}{2}$ [123]. Subsequently, we can consider the following relationship:

$$\Delta V_i/\Delta j = \Delta\phi/K\Delta j; \tag{2.28}$$

Where $\Delta\phi$ refers to the phase difference between adjacent pixels in the $j$-direction. The phase $\phi$ repeats itself every $2k\pi$, $k \in \mathbb{N}$, therefore in order to solve this ambiguity (called "phase wrapping") the MRI experiment should be structured so that the phase difference between adjacent pixels in the tissue satisfies the following equation [108]:

$$\Delta\phi < \pi rad;\ \forall pixel \tag{2.29}$$

Only when this condition is satisfied there is a unique value of the phase difference, and this condition is met in practice by adjusting $K$, the sensitivity of the phase to the velocity, in light of an *a priori* estimate of the maximum values of $\Delta V_i/\Delta j$ present in the tissue [108]. Once the velocities are derived, a further step needs to be taken by removing the effects of rigid body translations and rotations. The procedure for this process is outlined in a patent that describes a method for extracting deformations from PC MRI [124]. Once this step is accomplished the strain-rate tensor can be evaluated, and it is then possible to track the motion of the pixels with the forward/backward integration scheme proposed by Pelc [109]. This is done in order to follow the procedures described in [120–122] for the definition of the strain values.

### Arterial circumferential Strain

Under the assumptions of plane strain (i.e., neglecting through-plane deformation), uniform radial expansion, and approximating the vessel wall as a membrane, the circumferential strain, $\epsilon_{\theta\theta}$, can be expressed in terms of the deformations in cylindrical coordinates [120], as in the following equation:

$$\epsilon_{\theta\theta} = \frac{1}{2}\left[\left(\frac{r}{R_0}\right)^2 - 1\right]; \tag{2.30}$$

in this equation, $R_0$ is the vessel radius at a reference time point, and $r$ is the radius measured at any other time in the cardiac cycle [120]. The reference vessel radius $R_0$ is evaluated from the magnitude image by averaging the distance from the vessel centre to all points in the vessel wall, while the other radii $r$ are calculated from the in-plane velocities measured in the vessel wall [120]. From these analyses on the aortic wall the cyclic strains and the displacements of the tissue can be determined with the aim of using them as a confirmation of the fitness of the constitutive model implemented. Clearly, by defining a constitutive model only on the basis of structural information (obtained by DTI) and uniaxial tensile tests the constitutive model would not necessarily be suitable for describing the tissue behaviour when subjected to physiological pulsatile loading. Hence, a unique constitutive model fit needs to be determined based on the *in vivo* measured strains.

## 2.5 Non-invasive Prediction of Aortic Constitutive Behaviour

Once the constitutive model is established and the structural parameters are evaluated it is possible to compare the circumferential strains predicted by the model with the one measured experimentally by PC MRI. To make this comparison possible, the finite element method (FEM) can be used, since this computational approach allows for the consideration of complex aortic geometry, and of the pulsatile pressure waveform applied during physiological loading.

## 2.6 Finite Element Analysis

Finite Element Models offer a reliable tool for the optimisation of the constitutive parameters. In fact, FEM results and experimental data can be compared and if they match, the constitutive parameters can be defined to be optimised for the description of the mechanical behaviour observed experimentally. This approach has been widely used for the determination of soft tissue constitutive models. In most cases a uniaxial test is performed in both environments and then compared. The tissues analysed with this techniques have included ligament [59], arterial wall [52], and the heart [2]. In the present study, both uniaxial tests and the results from PC MRI will be compared with the results of a finite element simulation to validate the model chosen. The validation through FE simulation has many applications that demonstrate the potential of this work. In fact, a constitutive model which when implemented reproduces physiological arterial behaviour, can be used as an engineering tool for the improvement of surgical devices design, as a diagnostic tool for predicting the rupture of atherosclerotic plaques/aneurysms, and finally as a pre-clinical tool for estimating the outcome of surgical procedures on individual patients, leading to patient-specific solutions.

## 2.7 Summary

The aortic wall is a tissue susceptible to diseases closely related to its structure. Currently, these diseases can be studied only when they reach a final stage, due to their silent progression. Finding a way to study this disease progression means finding a tool able to characterize non-invasively the mechanical behaviour of the aorta and its alterations. The tools available nowadays to detect a change in the aortic structure have many limitations and do not allow for a complete study of the tissue. In fact, some of these tools are invasive, such as histology; others cannot track the early stage of the disease, such as CT scans; still others cannot directly investigate the composition of

the altered arterial wall, such as angiography. In order to find a non-invasive tool for the study of the aortic structure, the first step is the determination of the relevant parameters that need to be measured. In other words, this means defining the model that best describes the mechanical behaviour of the aortic tissue. Details of the model used are given on ch. 3. Next, a state of the art MRI technique (DTI) [75] and magnetic resonance angiography tool (PC MRI) [108] are used to measure both the structural characteristics and the motion of porcine aortas. The application of such techniques to arteries is described in ch. 4 and 5. From the definition of the structural properties of the aorta and from uniaxial tensile tests the constitutive model described in ch. 3 can be completely determined and implemented in a finite element model. Lastly, in ch.6, the aortic deformations predicted by the model are compared with those measured experimentally through PC MRI, in ch. 5. The results of the whole process is the determination of a constitutive model for the physiologically loaded aorta and the definition of a procedure to extract non-invasively relevant aortic structural characteristics from MR imaging.

# Chapter 3

# Constitutive Model

In this chapter the implementation of a suitable constitutive model for porcine aorta will be carried out and discussed. The aortic tissue can be regarded as a fibre reinforced material and its behaviour can be described as the sum of an isotropic behaviour and an anisotropic one. As outlined in ch.2, the model chosen considers two families of fibres and it is widely used to represent arterial tissue [53, 57, 61, 62]. In the following section the method to retrieve the material constants $c$, $k_1$ and $k_2$ will be described and applied to experimental data for porcine aortas, namely uniaxial tensile tests. In order to define these three parameters, two structural parameters are needed, $\gamma$ and $\kappa$. In this chapter the values of these two parameters will be obtained from literature, and in particular from the works by O'Connell *et al.* on aortic medial organisation [34] and by Gasser *et al.* on the implementation of the model [53].

The results of this chapter show that the model can be implemented successfully for representing the loading response of porcine aortas uniaxial tensile tests, but it also shows that its material constants have a precise mechanical meaning and that, by considering alterations in the ground matrix or in the collagen fibres, different mechanical behaviours can be reproduced. The biggest limitation of the constitutive model implementation, however, is that the structural constants are obtained invasively through microscopy [34], using harvested tissue that has therefore lost pre-stretch and residual stresses.

In ch. 4 a novel method to overcome this limitation will be introduced and applied to derive the structural parameters non-invasively without altering the natural loading of the aorta. Inputting these parameters into the constitutive model implemented in the present chapter will generate for the first time a non-invasive structural characterization of arterial tissue.

## 3.1 Methods

The following steps were used to define a constitutive model of aortic wall behaviour that could be implemented in a finite element software and validated by the experimental data found using the MRI procedure described above. The constitutive model chosen is that developed by G. T. Gasser *et al.* [53, 62]. This is a fibre-reinforced mechanistic model based on a neo-Hookean hyperelastic material model and defined in equations 3.1–3.5:

$$\Psi = \Psi_1 + \Psi_2; \tag{3.1}$$

$$\Psi_1 = \frac{c}{2}(\tilde{I}_1 - 3); \tag{3.2}$$

$$\Psi_2 = \frac{k_1}{k_2}\left\{exp\left[k_2\left(\kappa\tilde{I}_1 + (1-3\kappa)\tilde{I}_4 - 1\right)^2\right] - 1\right\}; \tag{3.3}$$

$$\tilde{I}_1 = \lambda_z^2 + \lambda_\theta^2 + (\lambda_z\lambda_\theta)^{-2}; \tag{3.4}$$

$$\tilde{I}_4 = \lambda_z^2 sin^2(\gamma) + \lambda_\theta^2 cos^2(\gamma); \tag{3.5}$$

Where $\Psi$ is the strain energy function, $\Psi_1$ is the behaviour of the ground sub-

stance matrix, $\Psi_2$ is the behaviour of collagen fibres. The ground substance matrix energy function, $\Psi_1$, is described through a neo-Hookean model with $\tilde{I}_1$ the invariant of the right Cauchy stretch tensor, see eq.s 2.11 – 2.13, modified into 3.4 by application of the incompressibility constraint, as shown in the following equation:

$$\lambda_\theta \lambda_z \lambda_R = 1 \rightarrow \lambda_R = \frac{1}{\lambda_\theta \lambda_z}$$

where, by rearranging eq. 2.3, on page 17, the strains to be considered are reduced to the strain in the axial direction $\lambda_z$ and the strain in the circumferential direction $\lambda_\theta$. Instead, the collagen fibres energy function, $\Psi_2$, is a function of $\tilde{I}_4$, see eq.s 2.15 – 2.19, on page 21. In particular, $\tilde{I}_4$ is defined as:

$$\tilde{I}_4 = a_0 \cdot C \cdot a_0;$$

and is modified into eq.3.5 by application of the arguments of symmetry [53]. In this model it is assumed that two families of collagen fibres are embedded symmetrically, with $\gamma$ denoting the angle between the circumference and the mean orientation $a_0$ of the fibre families. The constants $\gamma$ and $\kappa$ represent the structural information, being the fibre angle and the fibre dispersion value, respectively.

In order to fully characterize the material model three material constants need to be defined $c$, $k_1$, and $k_2$, where $c$ is the neo-Hookean parameter, $k_2$ is a dimensionless parameter, and $k_1$ is a stress-like parameter [60]. These constants can be defined from experimental uniaxial tensile test data using non linear regression. In particular, an iterative non linear regression routine was implemented in LabVIEW® to find the value of $c$, $k_1$, and $k_2$ for both curves simultaneously [1]. This routine uses a Levenberg-Marquardt algorithm

[1]While a simple non-linear Levenberg-Marquardt algorythm is already implemented in most curve-fitting tools, a routine able to minimise the objective function in eq.3.6 had to be implemented manually, since it required the minimisation of two exponential curves simultaneously where the variables are in the argument of the exponential function.

to fit the derivatives of the strain energy function defined in eq.s 3.1-3.3 to the experimental stress-stretch curves obtained from uniaxial tensile tests in both the axial and the circumferential direction. Since $c$, $k_1$, and $k_2$ must be the same in the axial and in the circumferential direction, the Levenberg-Marquardt algorithm was modified to fit simultaneously the stress-stretch curve obtained in the axial direction and the one obtained in the circumferential direction. The objective function to minimise is described by the following equation [60, 62]:

$$\chi^2 = \sum_{i=1}^{n} \left[ w_1(\sigma_{\theta\theta} - \sigma_{\theta\theta}^{\Psi})_i^2 + w_1(\sigma_{zz} - \sigma_{zz}^{\Psi})_i^2 \right]; \tag{3.6}$$

$$\sigma_{\theta\theta i}^{\Psi} = \left( \lambda_\theta \frac{\partial \Psi}{\partial \lambda_\theta} \right)_i; \tag{3.7}$$

$$\sigma_{zzi}^{\Psi} = \left( \lambda_z \frac{\partial \Psi}{\partial \lambda_z} \right)_i; \tag{3.8}$$

Where $n$ is the number of data points and $w_1$ and $w_2$ are weighting factors [60]. The equations 3.7 and 3.8 represent the Cauchy stresses in the circumferential and axial directions of the artery. In the objective function $\chi^2$, these values need to be substracted from the experimental Cauchy stresses $\sigma_{\theta\theta}$, $\sigma_{zz}$.

In order to verify the accuracy of the model built, data from Holzapfel *et al.* [63] of the adventitia stress-stretch curve, shown in fig. 3.1, were used to reproduce the corresponding constants presented in [53].

### 3.1.1 Uniaxial Tensile Test

The modified Levenberg-Marquardt algorithm was developed to extrapolate the material constants for the porcine aortic tissue used in the study, and, in order to apply the algorithm, uniaxial tensile tests were performed on fresh

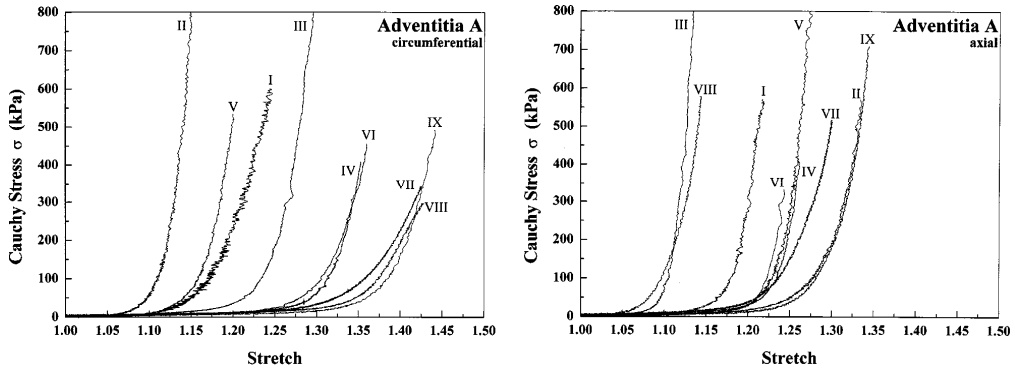


Figure 3.1: Iliac adventitia stress-stretch curve from [63].

porcine aortas. Five aortas, similar to the ones used for the MRI studies, were harvested and tested within 24h of slaughter. Aortic segments were cut in correspondence with the thoraco-abdominal tract and opened along the line of branching small vessels. Using a custom cutter, dogbone samples were cut in the axial and in the circumferential direction in neighbouring areas of the flattened aorta, see fig.3.2.A. This operation resulted in four dogbone samples for each aorta, two in the axial direction and two in the circumferential direction, respectively. On these dogbone samples two horizontal lines were marked with a fine tip marker and two vertical ones, as shown in fig. 3.2.B. The samples were tested using a Zwick/Roell Z005 testing machine with a $20N$ load cell (Zwick GmbH, Ulm, Germany) and custom designed grips also shown in fig.3.2.B. The test were performed using a 0.002 N preload (corresponding to 500 Pa for the average cross-section area) and a test velocity of 12 mm/min. The displacements of the lines were recorded using a video-extensometer camera (MESSPHYSIK Material Testing, Furstenfeld, Austria). The stress-stretch curves obtained were exported into Microsoft Office Excel®, see fig.3.6, and then averaged, see fig.3.7. The two averaged curves obtained for the axial and the circumferential direction were used for the non-linear regression routine. The structural parameters, $\gamma$ and $\kappa$, needed to fit the uniaxial tensile tests routine were determined using confocal miscroscopy data available from literature [34], see fig.3.3, and qualitative considerations derived from the uniaxial tensile tests, as in [53], respectively.

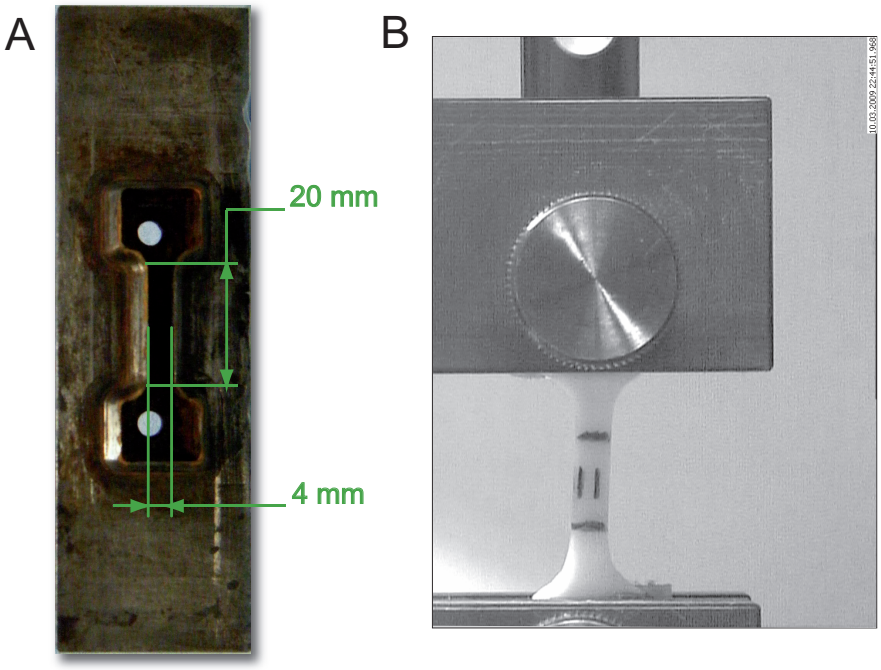


Figure 3.2: Porcine aorta uniaxial tensile test: A) details of the dogbone shape used; B) test set up capture.

## 3.2 Results

In order to verify the fit of the model implemented in LabVIEW®, the data presented in [63] were used and data points retrieved from the image were input into the routine. The structural parameters used, as well as the material constants obtained as a result of the interpolation routine are shown in table 3.1. These constants generated two interpolated curves that fitted the experimental ones for the constants reported in [53], as shown in fig.3.4 and 3.5. In particular, fig.3.4.A shows the LabVIEW® environment where the routine was implemented and details of the user interface. The step following the validation of the Levenberg-Marquardt routine, was the use of such

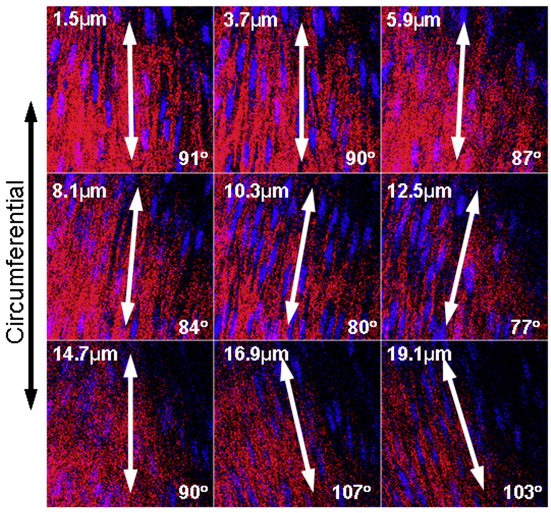


Figure 3.3: Fibre orientation in the aorta, from [34].

a routine to determine the constitutive parameters of the porcine aortas. From the tensile test results, shown in fig. 3.6, it can be seen that porcine aortas tensile tests showed a different directionality from the tests presented in [63], where an iliac artery was used, see fig.3.5. From these uniaxial tests the curves obtained in the circumferential direction as well as the ones in the axial direction can be averaged resulting in an averaged circumferential stress-stretch curve and an averaged axial stress-stretch curve shown in fig. 3.7.

| | Iliac artery [53] | Iliac artery fig.3.4 | Porcine aorta fig.3.8 |
|---|---|---|---|
| $\gamma$ | 49.98° | | 10° |
| $\kappa$ | 0.226 | | 0.326 |
| $c$ | 7.46 kPa | 12.4 kPa | 31.2 kPa |
| $k_1$ | 996.6 kPa | 1 MPa | 1.8 Mpa |
| $k_2$ | 524.6 | 523.6 | 4 |

Table 3.1: Constitutive parameters used in the model.

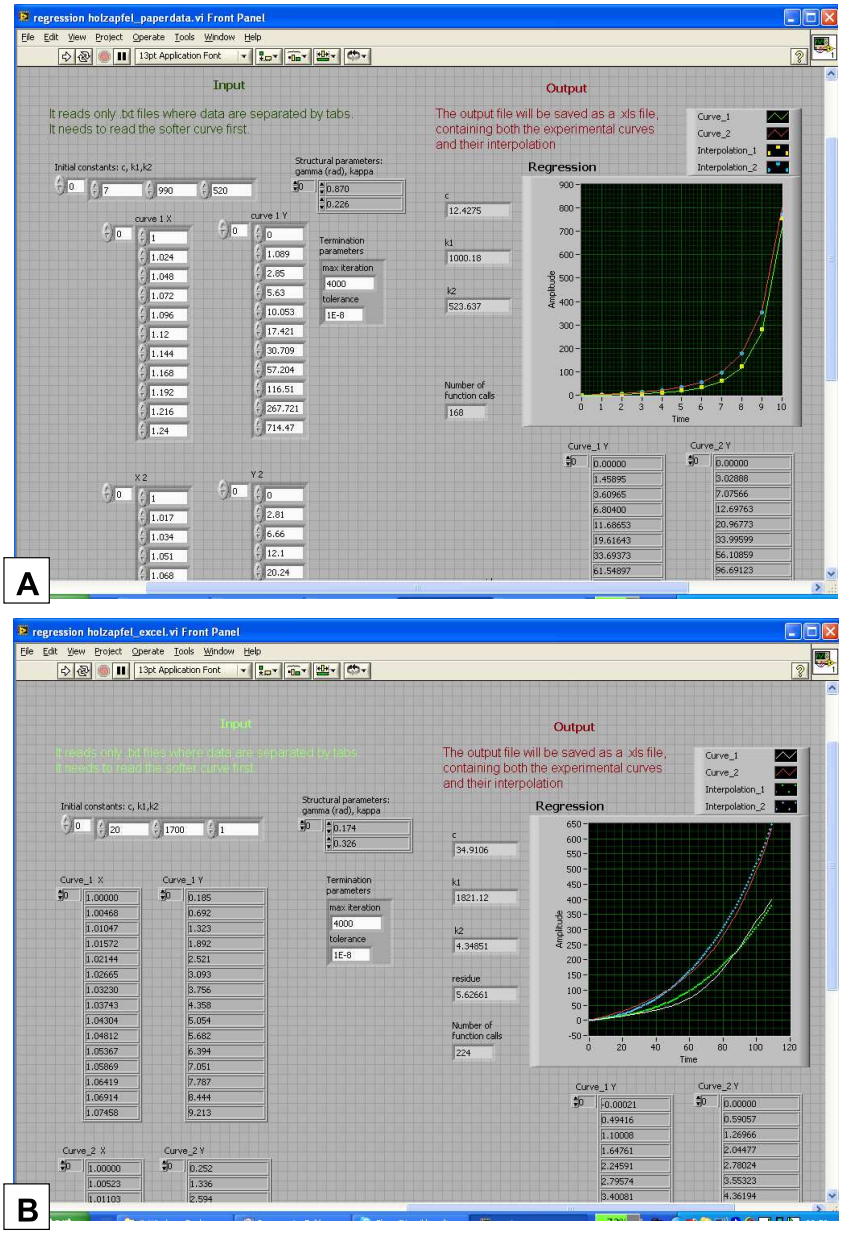


Figure 3.4: Screen capture of the custom-built Levenberg–Marquardt algorithm A)Data from Holzapfel *et al.* [63] ; B) Porcine aorta uniaxial tensile test data.

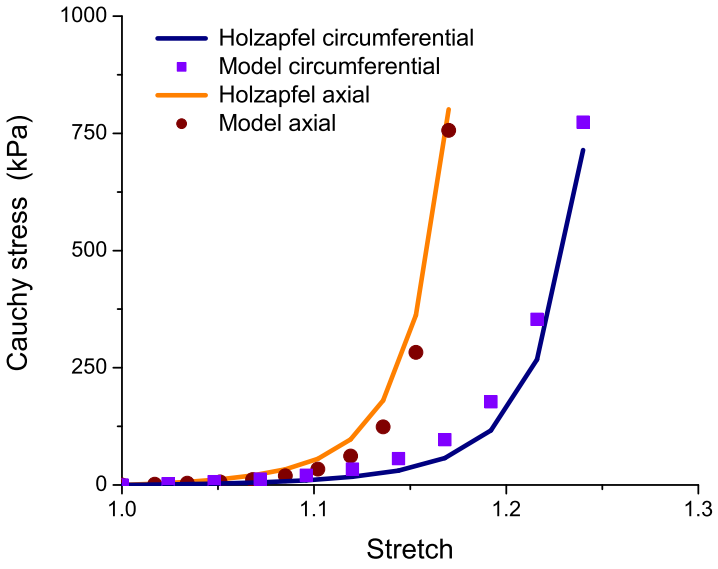


Figure 3.5: Holzapfel *et al.* [63] curves: fit obtained with the custom routine.

These averaged curves can be input into the LabVIEW® routine and the material parameters $c$, $k_1$ and $k_2$ evaluated. The constitutive model curves, shown in fig.3.8, replicated adequately the behaviour of the experimental ones.

Finally, the material parameters were varied in order to analyse how they affect the interpolated stress-stretch curve. The resulting curves are shown in fig.3.9 where it is possible to see that even small changes in the parameters affect the interpolated curve greatly.

## 3.3 Discussion

The search for a suitable model for aortic tissue ended with the identification of the constitutive model described in [53, 62]. This model was deemed suitable because it could represent the anisotropy derived from the fibrous

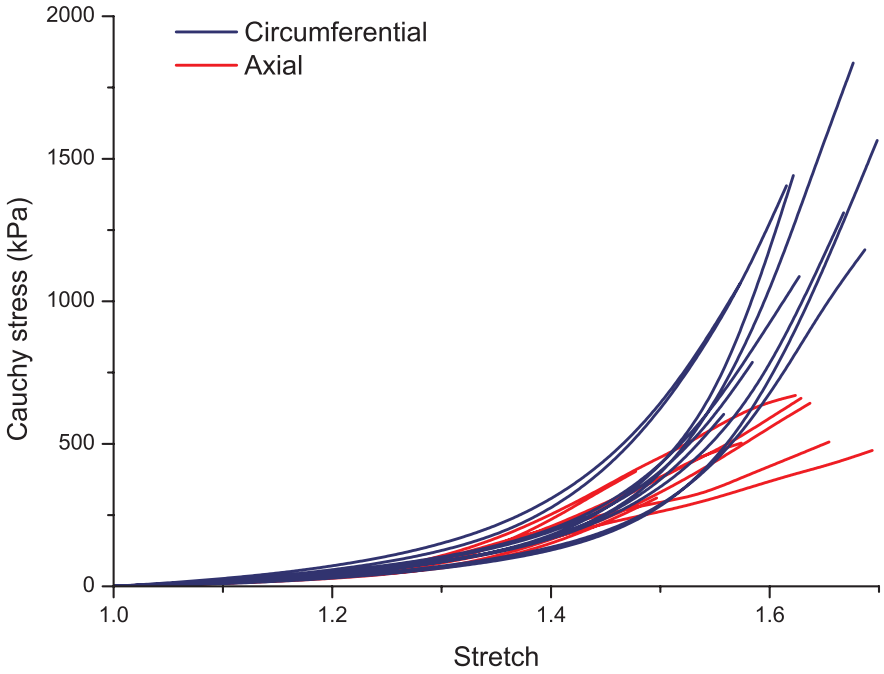


Figure 3.6: Porcine aortas uniaxial tensile tests in the circumferential and in the axial direction.

components in the aorta. This model needs the knowledge of two fibre-related structural parameters $\gamma$ and $\kappa$, and the definition of three material constants, $c$, $k_1$ and $k_2$. The drawback of this model is that the material constants are found by means of a particular non-linear interpolation on the circumferential and on the axial stress-stretch curve [53, 60]. Hence, the non-linear Levenberg-Marquardt interpolation had to be implemented and then validated against published data. In particular, the material constants used in Gasser *et al.* [53] are said to be derived from the stress-stretch curves presented in [63]. Therefore, the validation of the interpolation technique consisted in inputting the data from [63] in order to find the constants used in [53]. The plot shown in fig.3.5, shows that the interpolation routine implemented in LabVIEW, see fig.3.4, was able to derive the same material constants used in [53], as shown in table 3.1. Small differences between the constants published and the ones obtained with our routine have to be ascribed to the fact that the stress-stretch curve data were retrieved from the

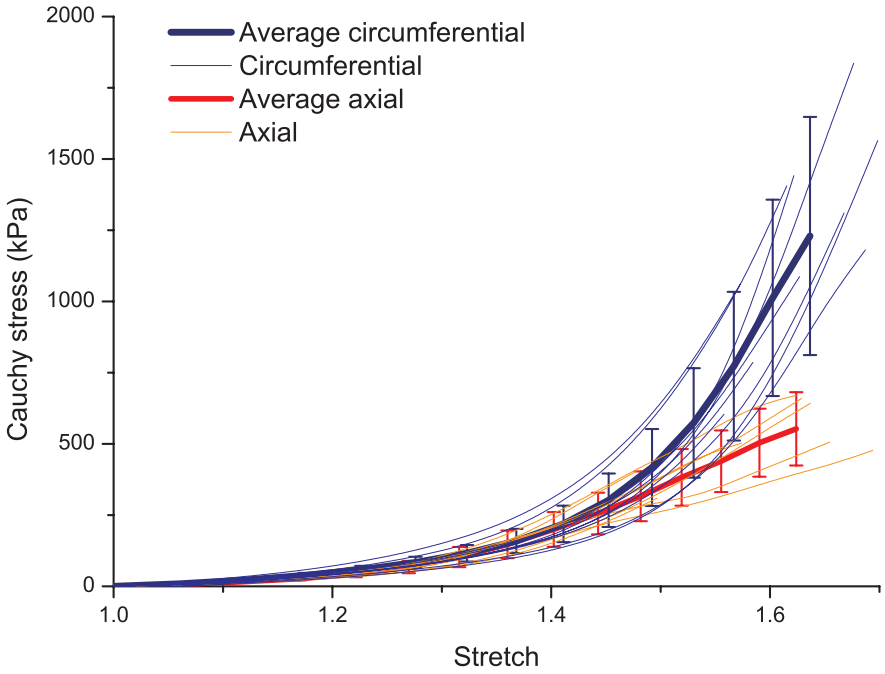


Figure 3.7: Average curves used in the analysis and their standard deviation superimposed on the uniaxial tensile test results.

picture published in the paper and not from the original test result, thus introducing some degree of error. Nevertheless, considering the errors introduced by manually tracking the stress-stretch curve the custom interpolation routine results were validated.

The validated interpolation routine could be then applied to porcine aorta uniaxial tensile tests. The results of the uniaxial tensile tests are shown in fig.3.6. The difference between the porcine aorta and the iliac aorta uniaxial tensile tests is noteworthy by comparing fig.3.4 with fig.3.6. This difference mirrors a difference in the micro-structure of the two arterial tissues: the iliac aorta has fibres oriented at 49.98° [53] and this means that the fibres are acting nearly equally in both directions, although slightly more in the axial directions. Because of such a fibre angle the response is the same in both directions and is characterized by small stretches due to the effect of collagen stiffening in both directions. On the other hand, porcine aorta fibres are oriented in a nearly circumferential orientation at $\sim 10°$ [34]. This results

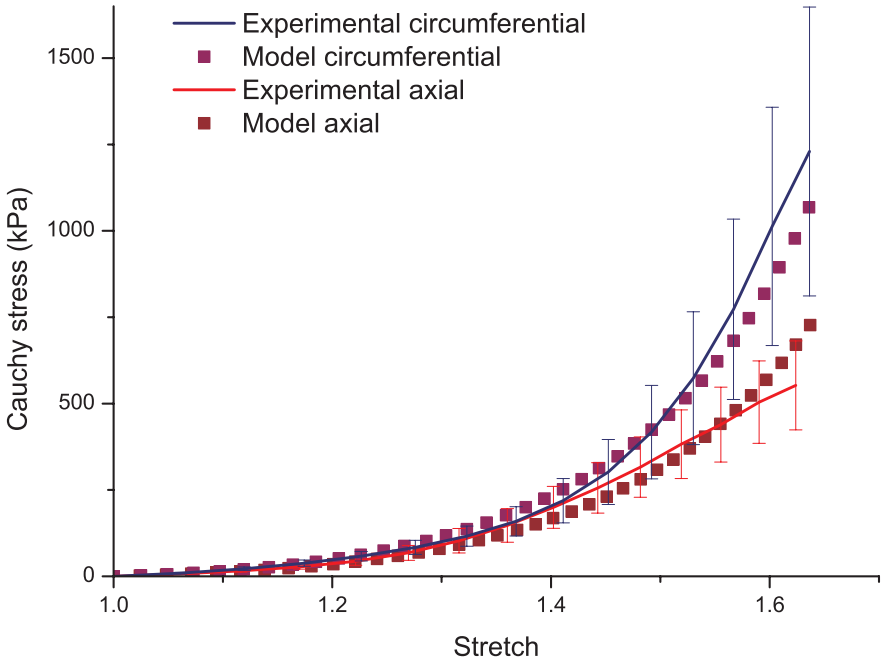


Figure 3.8: Comparison of the interpolated curves with porcine aortas uniaxial tensile test data.

in two completely different curves characterized by a stiffer circumferential response and an axial response where the load bearing capacity of collagen fibres is missing. Moreover, it is interesting to note how different the ground matrix behaviour is, which is responsible for the toe-region of the curves. While in the iliac artery the ground matrix response is nearly absent, fig.3.4, in the porcine aorta it has a role of support and shows an isotropic behaviour, causing the two curves to overlap in the toe-region of the curve.

In order to find the material constants, the value of $\gamma$ used was the one available from literature [34] and corresponded to 10°. In contrast, the value of $\kappa$ used in [63] is chosen as the one for which the best fit is obtained. In the present section, a first approximation of $\kappa$ was obtained using the same criteria used in [63], and this value was further refined by comparing the porcine aorta curves with the iliac artery ones published in [63]. Due to the fact that the porcine aorta stress-stretch curves were closer than the iliac artery ones, and since this 'closeness' is due to the degree of isotropy, the

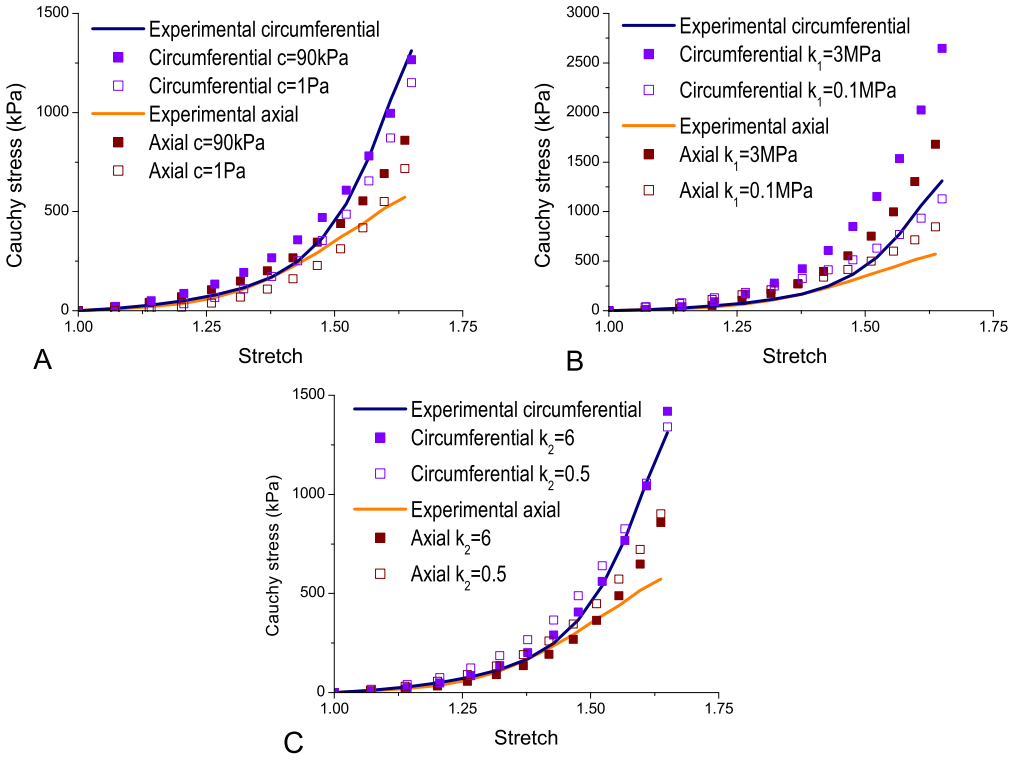


Figure 3.9: Effects of changes in the material constants on the interpolated curves, the standard deviation bars are left out for clarity purposes.

value chosen for $\kappa$ was higher than the one used for the iliac arteries, resulting in a nearly isotropic behaviour, see table 3.1. Further analysis and insights into the value of $\kappa$ will be discussed in ch.4 and in ch.6.

This mechanistic model was developed by assigning a precise mechanical meaning to each constitutive parameter, therefore discussion on the way the different material constants $c$, $k_1$ and $k_2$ affect the interpolated curve is needed. The plots in fig.3.9 show the different curves obtained by changing each material constant separately. The changes in the plots are not large because the changes were made while trying to ensure the convergence of the other material constants wherever possible. An increase in $c$ corresponds to

an increase in the stiffness of the toe-region of the curve, or, in other words, to assigning a higher load bearing capacity to the ground matrix. Since the ground matrix is partially responsible for the loading response, also after the collagen fibres start bearing the load, a change in $c$ corresponds to a change in the overall response, see fig.3.9.A. In contrast, a change in $k_1$, a stress-like parameter [60], corresponds to a change in the stress the collagen fibres can bear. Diminishing $k_1$ corresponds to diminishing such a stress and hence the latter part of the circumferential curve gets closer to the axial curve, which has a reduced collagen response. On the other hand, an increase in $k_1$ corresponds to an increase in the gap between the last part of the two curves, see fig.3.9.B. Finally, $k_2$ is a dimensionless parameter that describes the rate at which the collagen fibres start bearing the load. While in the iliac artery curves the value of $k_2$ is very high because the start of the collagen response is sudden and abrupt resulting in a reverse 'L' shaped curve, shown in fig.3.4, in the porcine aorta curves it is much smaller because the collagen recruitment phase is masked by the ground matrix response; this smoother transition is shown in fig.3.6 and in fig.3.9.C.

### 3.3.1 Limitations

The first limitation to a wide application of this constitutive model is due to the lack of knowledge of the *in vivo* structural parameters $\gamma$ and $\kappa$. Moreover, this model cannot be used to characterize *in vivo* the response of the tissue because uniaxial tensile tests can only be performed on harvested tissue. However, this model represents closely the behaviour of an excised aorta and can be used as a first guess to derive a suitable *in vivo* model.

The second limitation is in the convergence of the line searching algorithm. The interpolated curves converge correctly to the constants prescribed, but only by tuning the first guess material parameters. In other words, finding the convergence starting from numbers distant from the optimal ones is difficult because of restrictive hypothesis made in order to guarantee the convergence for both curves simultaneously. Improving the line searching algorithm and creating an independent LabVIEW® application

will be part of future work.

### 3.3.2 Conclusions

This chapter has demonstrated how the constitutive model described in [53] can be used to model effectively the loading response of porcine aorta uniaxial tensile tests. This model depends on the structural parameters $\gamma$ and $\kappa$ that are characteristics of the tissue analysed. In general, these two parameters are determined invasively by harvesting the aortic tissue, $\gamma$ [5,34,57,63], or qualitatively, based on theoretical considerations, $\kappa$ [53]. The aim of the present work is to determine these constants in a non-invasive way; in particular, in the following chapter it will be demonstrated how these structural constants can be obtained non invasively by using Diffusion Tensor Imaging.

# Chapter 4

# Diffusion Tensor Imaging

The constitutive model illustrated in the previous chapter has the ability to replicate the behaviour of the aortic tissue starting from two structural parameters, $\gamma$, fibre angle, and $\kappa$, fibre distribution. The golden standard for the measurement of these two parameters is histology. A model that is completely based on histology data has many limitations, since histology is an invasive technique that gives insight on the structure of a microscopical bi-dimensional layer of the tissue, as discussed in ch.2. Finding a method to analyse *in vivo* in a non-invasive way the aortic structure is advantageous from both an engineering and a clinical point of view. For biomedical engineers interested in modelling the tissue, analysing a tissue *in vivo* is advantageous because it retains the natural longitudinal pre-stretch and residual stress enabling more realistic models to be created that are closer to the physiological status of the tissue. On the other hand, analysing the tissue *in vivo* in a non-invasive way allows clinicians to understand the underlying biological changes related to alterations in the physiology of the tissue.

In the present chapter it will be demonstrated how Diffusion Tensor Imaging can be used for finding the structural parameters relevant to the constitutive model in a non-invasive way. It will also be clearly demonstrated that this MRI technique can successfully detect alterations in the tissue caused by freezing. It has to be noted that although the potential of DTI in studying the brain structure and its alteration is well established [77, 79, 83, 90–93],

this technique has never been applied to the aorta, or any similar vascular tissue. The results of the present chapter can be seen as an extension of the application of DTI, proving its ability in detecting not only axons, or muscular fibres, but also collagen fibres. Moreover, the results of this chapter suggest that DTI can detect the damage caused by freezing tissue and there may be potential to extend this technique to detect the damage caused by arterial diseases, such as aneurysms. The relevance of this consideration has to be seen in light of its future development: in fact, the results of the present chapter show that DTI has the potential to be developed into a tool for the early diagnosis of degenerative arterial diseases.

## 4.1 Methods

### 4.1.1 Preparation of Aortic Sample

With both MRI techniques the prepared aortic sample had to enter the MRI coil. In order to do so a special chamber was designed where the aorta was placed and immersed in water. This chamber, see appendix A, had a cylindrical geometry, with a diameter of 32 mm and a length of 220 mm. Commercial barbed connectors and cable ties were used to keep the aorta fixed and aligned, see figure 4.1. Tap water was used to fill the chamber as preliminary tests in the MRI with 0.9% saline solution showed noise due to the presence of salt molecules both inside and outside it. In the clinical setting, this limitation will be overcome by the presence of the surrounding tissues that allows for filtering out the noise due to blood solutes. To ensure the chamber was airtight, air was syringed out before closing the chamber.

#### Preparation Protocol

The aortas used for these studies were harvested from pigs provided by Rosderra Meats, Glanbia, Edenderry. All pigs were six months old and came from Irish breeds. The aortas were harvested and all surrounding tissue and

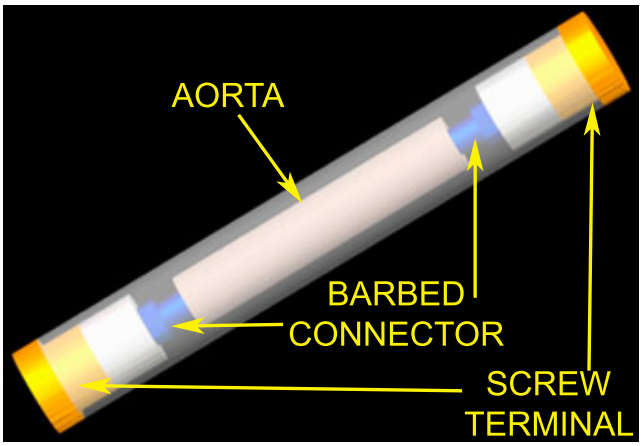


Figure 4.1: Rendering of the chamber.

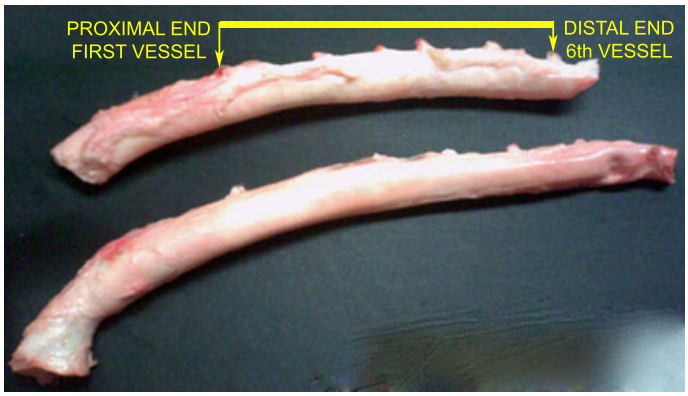


Figure 4.2: Aorta prepared according to the protocol.

lymph nodes were removed. Once prepared, the aortas could either directly undergo scanning (henceforth referred to as 'fresh aortas') or be immersed in water and stored frozen for future scanning (henceforth referred to as 'frozen aortas'). Frozen aortas were fully defrosted on the day of the MRI procedure and then placed in the chamber. Upon completion of the MRI study both kinds of vessels were disposed of through the DCU waste management company. Both frozen samples and fresh[1] samples were tested. The preparation for both samples consisted of finding the line of small branching vessels that

[1]The word fresh refers to an aorta that has not been frozen and that was harvested from an animal killed 24 to 26 hours prior to the MRI procedure.

Figure 4.3: Aortic segment prior to placement in the chamber.

form the thoraco-abdominal tract, taking the first vessel as a reference, six vessels were counted and then the extremities cut, as can be seen in figure 4.2 and 4.3. The resulting vessel segment length was approximately 130 mm. The diameter and the thickness of the vessel were also measured, see table 4.1. The length of the vessel was taken prior to insertion in the chamber and was checked again once within the chamber to ensure it was not over-stretched. In fact, due to the impossibility to measure accurately *in situ* the length of the aorta, the aortic segments were placed in the chamber without considering the axial pre-stretch, thus ensuring conformity and repeatability of the test.

Once the samples were prepared, they were studied using MRI. The scanner used was a 7 T Biospec® (Bruker BioSpin, Germany). This scanner is used for animal studies on rats and mice and provided a high resolution across the thickness of the vessel.

| Aorta | Length | Proximal Internal Diameter | Distal Internal Diameter | Proximal Thickness | Distal Thickness |
|---|---|---|---|---|---|
| frozen | 130±2 mm | 16±1 mm | 13±1 mm | 2.1±0.2 mm | 1.8±0.2 mm |
| fresh | 128 mm | 16.5 mm | 14.5 mm | 2.2 mm | 1.7 mm |

Table 4.1: Aortic Measures

### 4.1.2 Imaging Protocol

As described in ch.2, Diffusion Tensor Imaging enables the anisotropic diffusion of water in a tissue to be studied. In other words DTI is capable of analysing the influence of fibres on the Brownian motion of water molecules. DTI consists of the application of diffusion gradients (i.e. magnetic field linear variations in the MRI magnet) in six or more directions. As a result there is a tensor associated with each voxel that describes the amount of water diffusion over the three directions $x$, $y$ and $z$. The first eigenvector of the diffusion tensor describes the direction of the fibre.

Since this work marked the first time DTI was used for imaging porcine aorta, a great amount of time and effort went into defining the final imaging protocol. For instance, the number of images taken, the optimal imaging parameters and the ideal coil had to be defined. Therefore, many of the samples analysed were used only for preliminary testing and for the definition of the suitable tools and parameters, and could not be used for the definitive analysis of the aortic fibre structure presented in this chapter. This means that although 15 aortic samples were analysed, the results presented in this chapter concentrate on a total of three samples, two fresh and one frozen.

For all three samples, images were taken for different $b$ values, where $b$ is the quantity defined by eq. 2.20, on page 28, and describes the sensitivity to diffusion. Different $b$ values were considered in order to determine the optimal $b$ value for aortic tissue. The values considered were six: 200, 400, 600, 800, 1200 and 1600 s/mm$^2$, indicated in the figures with $b_1$-$b_6$, respectively. The $b$ values in the range 400-1200 s/mm$^2$ correspond to the range of values reported in literature for different tissues [81, 102, 125–127], and this range was extended at the extremities to include 200s/mm$^2$ and 1600s/mm$^2$, thus offering a complete spectrum of possibilities for the determination of the optimal $b$ value for aortic tissue.

Furthermore, for these studies a circular polarised 1H RF whole body coil was used, shown in figure 4.4. The signal obtained with this coil was homogeneous in all directions, thus enabling a throughout study of the aortic geometry. The sequence used was the same for both fresh and frozen


Figure 4.4: RF circular polarised whole body coil, used for scanning.

samples and was characterized by the use of five repetitions of the scanning sequence over 16 slices that were not averaged. It was therefore possible to see the results for each repetition and each of the 16 slices thus ensuring both reproducibility and repeatability of the results and justifying our use of only one frozen sample and two fresh samples. Five repetitions for sixteen slices in the total volume is analogous to taking 16 test samples from an arterial conduit and testing each one five times. Moreover, non-averaged images can easily be transformed to averaged images with a MATLAB® routine. The contrary, however, is not true, i.e. it is not possible to reconstruct from an averaged image all the non-averaged ones.

This approach was chosen to see if there were variations over time in the sample. It was also used to compare the differences due to *post mortem* degradation between the frozen and the fresh sample. The other parameters used are listed in table 4.2.

| Matrix | FOV | N Slices | Slice Distance | Echo Time | Repetition Time |
|---|---|---|---|---|---|
| 128 × 128 | 2.8 × 2.8 cm | 16 | 0.6 mm | 20.3 s | 2400.00 s |

Table 4.2: DTI scanning parameters

### 4.1.3 Image Analysis

The DTI image data-sets were input into a software, MedINRIA (Sophia Antipolis, France), that performed the tensor evaluation [89, 128]. Different interpolation algorithms are available, and in this study the algorithm implemented for the DTI fibre analysis was that available in the software MedINRIA, since this software is optimised for DTI on clinical data sets. In fact, in order to reduce noise common in these kinds of acquisitions, MedINRIA applies a maximum likelihood strategy. The estimation of the tensor, together with the use of Log-Euclidean metrics for tensor processing, improves the quality of the fibres reconstructed, which are tracked by using a streamline algorithm [89]. Following the evaluation of the tensor it was possible to track the fibres within the tissue. This operation was also performed by MedINRIA, whereby the fibres were tracked across the image volume and then exported to FiberViewer (S. Gouttard and M. Jomier; University of North Carolina website) format. FiberViewer format is an ASCII file, readable as a `.txt` file. A MATLAB® routine was created to read the fibre related data contained in the FiberViewer file and to evaluate the fibre angle distribution across the thickness of the aortic wall.

First of all the image data-sets, contained in a unique `.raw` file, were opened using the ImageJ® software. This software allowed the image file to be opened and divided into single `.tiff` files. Once the single files were created (one for each slice) they had to be re-grouped according to the $b$ value they belonged to. This was accomplished using MRIcron®, and converting all `.tiff` files belonging to the same volume to a single 'analyze' file. Once the 'analyze' files were created for the reference $b_0$ value volume and for the other six gradients, all of the seven files were input into MedINRIA. This procedure was repeated for each $b$ value set of images. In the MedINRIA environment a volume was created using the $b_0$ set of images and then from the other six gradients the global tensor was evaluated. Two parameters could be set prior to the tensor evaluation, one regarding the background removal threshold, a filter that removes the noise from the background; and one regarding the tensor smoothing. The background threshold was set to

the maximum and the tensor smoothing was set to high. After the evaluation of the image diffusion tensor, the Region Of Interest (ROI) boundaries were tracked manually. The reference images for the definition of the ROI volume were the $b_0$ ones. The definition of the ROI consisted of the definition of the contours of the vessel, i.e. the inner and outer circumference. The ROI could be saved as a mask, i.e. like a binary file[2] where the white pixels are the aortic wall (ROI) and the black ones are the background. Once the ROI was defined the fibres were tracked. At this point the fibre bundles tracked were selected and exported into the FiberViewer format and the fibre interpolation stage was complete.

### 4.1.4 Tensor Analysis

Diffusion eigenvectors are important for the determination of fibres patterns; the first eigenvector (i.e. the vector corresponding to the largest eigenvalue of the tensor) represents the direction of maximal diffusion and therefore it represents the predominant fibre direction [83, 129]. The tensor analysis was performed using MATLAB® and it consisted of the extrapolation of the first eigenvector from the tensor, and the determination of the angle it formed with the $x, y$ plane, as illustrated in fig. 4.5. This was conducted on a single slice of the image (the central one), following the procedure described by the flowchart in fig. 4.6. In order to study the consistency of the results over the length of the sample, the average of the tensor over all the slices was considered, and the angle of the eigenvector calculated. In both cases the study was focused on the ROI tracked previously in MedINRIA.

### 4.1.5 Fibre Analysis

In MATLAB® a custom routine was implemented that analysed the fibre orientation, the structure of which is shown in fig. 4.6. The first step of this

[2] with all the white pixels equal to one and the black ones equal to zero

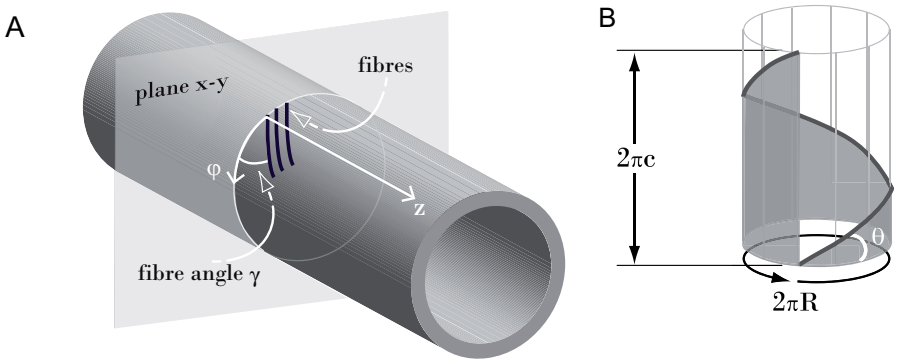


Figure 4.5: Convention for the lead fibre angles used in the study: A) reference system for the fibres; B) definition of the fibre angle.

routine analysed the ROI mask image to define the centre of the vessel and its mean internal and external diameter. This was accomplished studying the position of the non-zero values on the main axes, $x$ and $y$.

Then the file containing the fibre data was opened. In the FiberViewer file for each fibre the coordinates of each voxel composing the fibre expressed in pixels, and the tensor-evaluated quantities, were defined for each voxel.The first action completed in MATLAB® was to scale the coordinates from voxels to mm, using the known resolution of the image, see table 4.2. Then the conversion into a cylindrical coordinate system was performed, using the centre data evaluated from the ROI mask. At this point the fibre angle analysis was performed. To do so, the angle between the fibre and the $x-y$ plane was evaluated using the numerical partial derivatives of each of the points composing the fibre. For each fibre a mean angle and a mean radius were stored.

Each fibre angle and radius value was then post-processed in MATLAB® in order to study the fibre orientation distribution. This part of the analysis required the use of the inner and the outer diameter defined by the ROI mask points and the determination of the vessel thickness in terms of pixels. The thickness value was then converted into mm, as described above, and subdivided to represent equal layers. The number of layers depended upon

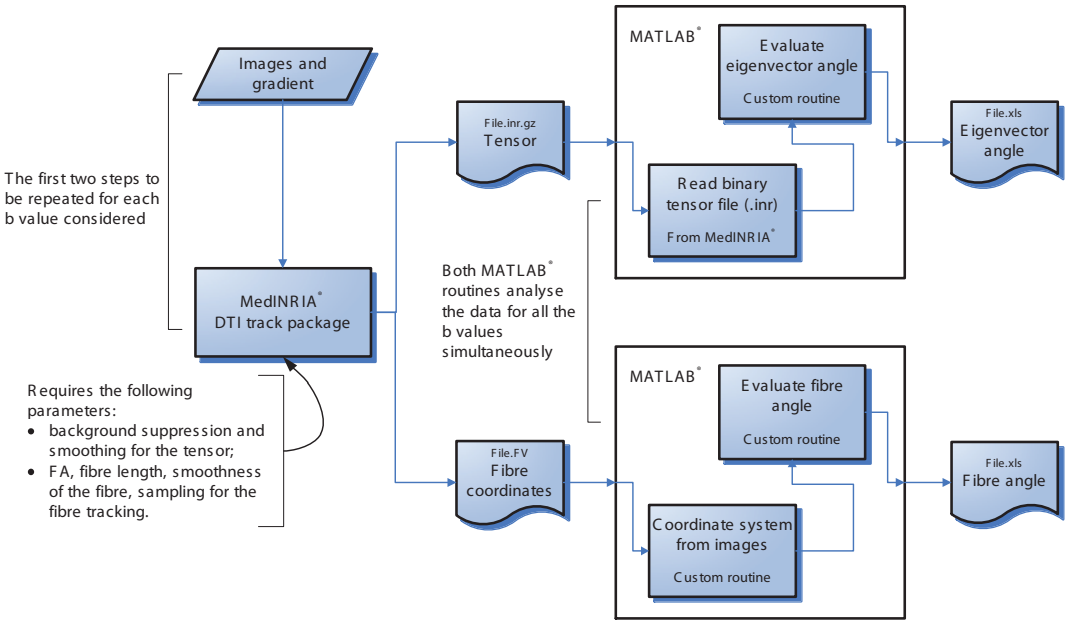


Figure 4.6: Flow chart indicating the various stages in the image postprocessing sequence.

the number of pixels of the ROI. The number of divisions considered was six and corresponded to the average maximum number of pixels in the thickness of the aortic wall defined for all the specimens. The layers obtained are shown in fig.4.7. The mean fibre radii were then determined for each layer and the angle distribution across the thickness evaluated. Finally, two more layers were added in order to consider the fibres whose mean fibre radius fell out of the layers' boundaries shown in fig.4.7.

A sequence description of the different steps involved in the image postprocessing is described in table 4.3.

The MATLAB® angle detection routine was tested creating helices with the same software and inputting them into the angle routine, see fig. 4.8. These 'phantom' helices with known angles were created using the helix equations:

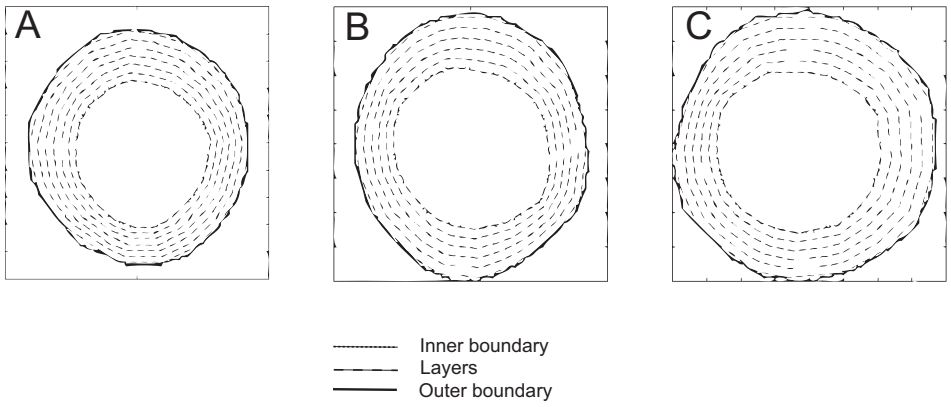


Figure 4.7: Representation of the layers considered for each geometry analysed: A) stored frozen sample; B, C) fresh samples.

$$x = Rcos\,(t)\,; \tag{4.1}$$

$$y = Rsin\,(t)\,; \tag{4.2}$$

$$z = ct; \tag{4.3}$$

Where $t \in (0, 2\pi)$, $c$ is the lead and $R$ is the radius. To have a right handed or a left handed helix the sign of the $x$ or of the $y$ term has to be changed. From these equations the definition of the helix angle used here and in the angle detection routine is given by:

$$\theta = \frac{2\pi c}{2\pi R} = \frac{c}{R}; \tag{4.4}$$

The physical meaning can be easily understood if the surface on which the helices are wrapped is cut and opened flat. In that case it can immediately be seen that $\theta$ corresponds to the tangent of the helix (that becomes a line) on this surface, see fig. 4.5.B.

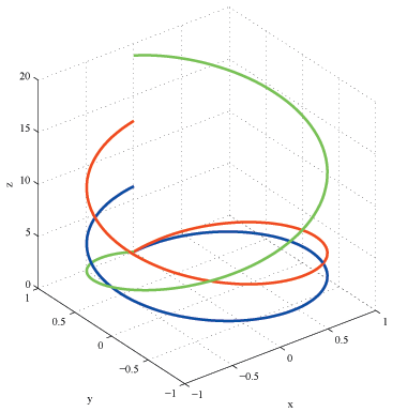


Figure 4.8: Test helices generated in MATLAB®: the blue and the red one are both left handed but have different leads, the green one is right handed and has a different lead.

### Analysis of Different ROIs

The steps illustrated in the previous section were carried out by tracking the ROI from the slice in the middle of the volume. The importance of the position of the ROI can be vital, since it is from the pixels contained in the ROI that the fibre tractography starts. In particular, each pixel's first eigenvector contained in a ROI represents a seed from which the actual fibre can start and develop, assuming complex spatial orientations. This means that the eigenvector indicates the direction of the fibre at the beginning of its path. Along the fibre path this direction may change, thus generating the resulting fibre orientation which is used to evaluate the fibre angle. The difference between the ROI eigenvector angle and the fibre angle can be seen by comparing the tensor values and the fibres plot, which suggest that using a distinct ROI could produce a different fibre distribution.

In order to investigate further the effect of ROIs on fibre angle and overall on the fibre distribution, the fibre tractography procedure was applied to the fibres resulting from a ROI defined on the first slice of the volume (slice 0), and a ROI defined for the last slice in the volume (slice 15).

| **MedINRIA:** |
|---|
| • Analysis of the DTI volume;<br>• Tensor evaluation;<br>• Region Of Interest (ROI) mask manually tracked to define aortic boundaries and volume;<br>• Fibre tracking;<br>• Conversion of fibre bundles into<br>• FiberViewer format. |
| **MATLAB®:** |
| • FiberViewer file opening and reading;<br>• Fibre angle evaluation;<br>• Opening of ROI image mask file;<br>• Aortic wall detection and measure of aortic thickness;<br>• Division of aortic wall into $n$ layers, where $n$ denotes the maximum number of pixels;<br>• Study of fibre angle distribution over the different layers, performed assigning the average fibre radius to each layer. |

Table 4.3: Details of the fibre analysis step sequence.

### 4.1.6 Extrapolation of Material Parameters

DTI was used to study the fibre distribution in the aortic wall. The results of this fibre distribution are the structural parameters $\gamma$ and $\kappa$. The parameter $\gamma$ is the fibre angle while $\kappa$ is a measure of the fibre distribution. These values are necessary inputs for the constitutive model described in ch. 3.

#### Evaluation of fibre angle: $\gamma$

DTI results output a fibre angle distribution for the fresh and for the frozen aortas. These distributions are relevant because they are obtained non-invasively and represent the distribution of fibres across all of the aortic volume analysed. From these distributions it is possible to obtain both a global value of $\gamma$ and a local one, i.e. a value determined for each layer of the aorta. The $\gamma$ resulting as the dominant fibre angle of the fibre angle distribution is the one that will be considered for the definition of the constitutive model.

#### Evaluation of fibre dispersion: $\kappa$

The parameter $\kappa$ describes the way the fibres are distributed around the mean angle. The way to evaluate this parameter is described in [53]. Usually it is nearly impossible to evaluate it because a fibre distribution is needed, and this is difficult to achieve from histological samples.

The present work demonstrates that from DTI it is possible to obtain a global fibre distribution and therefore it is possible to implement the equations described in the work from Gasser *et.al* [53]. The value of $\kappa$ was evaluated using a MATLAB® routine that performed a trapezoidal numerical integration. The angles were analysed using the Von Mises distribution implemented in the `CircStat` package available on the MATLAB® file exchange repository [130]. The $\kappa$ values were evaluated both for fresh and frozen samples and for the fibre distributions obtained for each $b$ value.

## 4.2 Results

In this section the findings obtained from applying DTI to porcine aortas are presented. This section is split in various subsections that mirror the ones in the previous section in order to give a clear representation of the data and of the procedure followed.

### 4.2.1 Image Analysis

The qualitative analysis of the results for the DTI is the first thing that can be done prior to proceeding with the angle detection routine. In the following pages data belonging to both fresh and frozen aortas are presented. Image analysis involved analysing the FA maps generated in MedINRIA, using eq. 2.25. From these maps, qualitative information was noted on the anisotropic content of the sample prior to further investigation, as shown in fig. 4.9. The inspection of FA maps proved a quick verification of DTI's ability to detect aortic anisotropy. In fact, fig.4.9 shows the reference image for the stored frozen and the fresh samples. From these images, it is possible to appreciate the contours of the aortic wall and the presence of some lymphatic tissue around the fresh samples. From the FA maps in fig.4.9, the difference in anisotropy between the aortas and the surrounding water can be seen. Finally, for the fresh samples it is possible to recognise two black areas that correspond to the lymphatic tissue.

### 4.2.2 Tensor Analysis

Once the ability to detect aortic anisotropy was confirmed, the tensor was analysed. The diffusion tensor is 3×3 and is defined for each pixel. Therefore, it was necessary to select the information we needed in order to verify the accuracy and the validity of this information. Since in this work DTI is used to define the structural parameters of the material, and in particular the angle at which the fibres are oriented within the tissue, the information chosen to

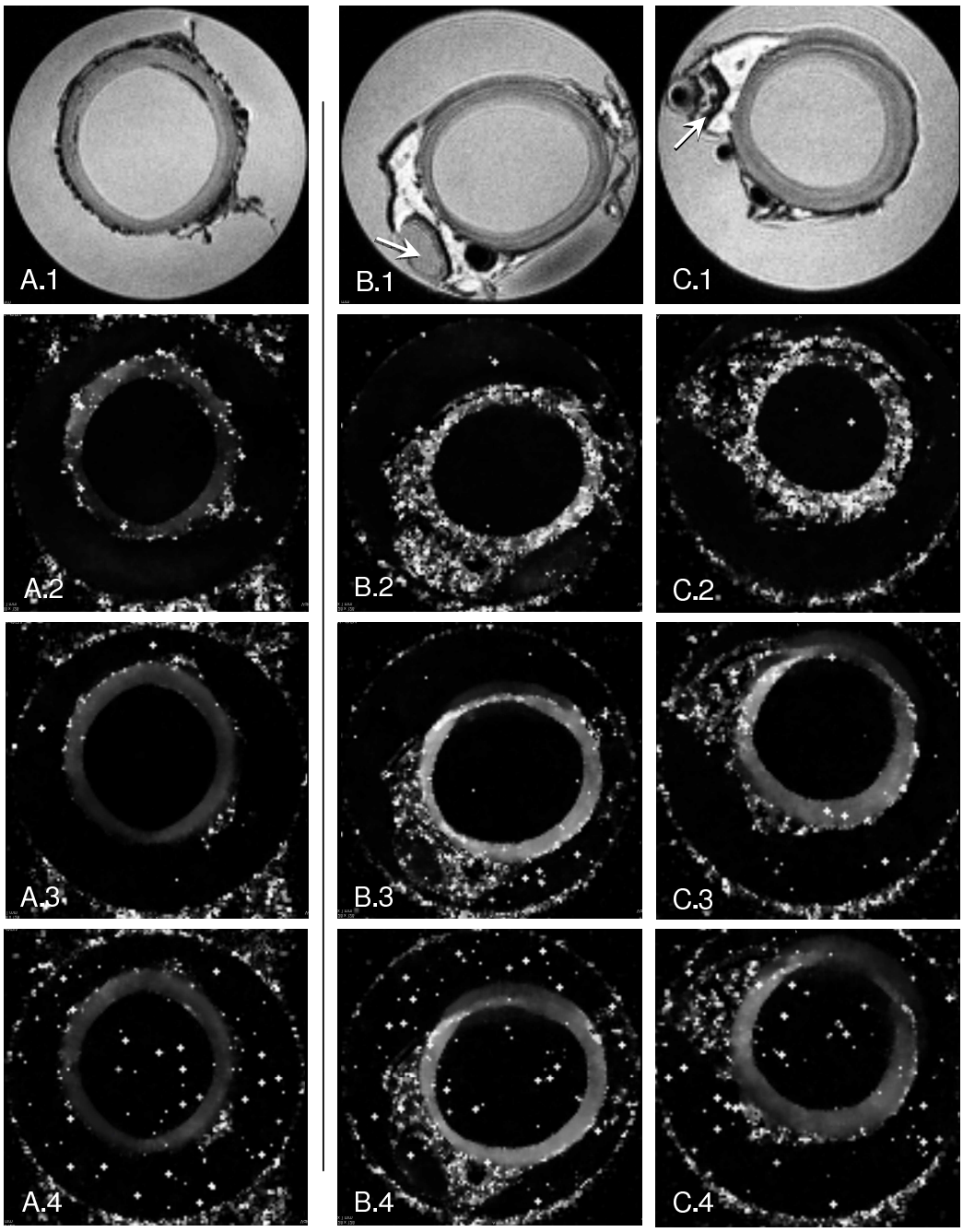


Figure 4.9: Top row: MRI images of the aortas analysed, A) stored frozen sample; B), C) fresh samples. Second row: fractional anisotropy map of the samples for $b_1$= 200 s/mm$^2$; Third row: fractional anisotropy map of the samples for $b_4$= 800 s/mm$^2$; Bottom row: fractional anisotropy map for $b_6$=1600 s/mm$^2$. In B.1 and C.1 the arrows indicate the presence of lymphatic tissue.

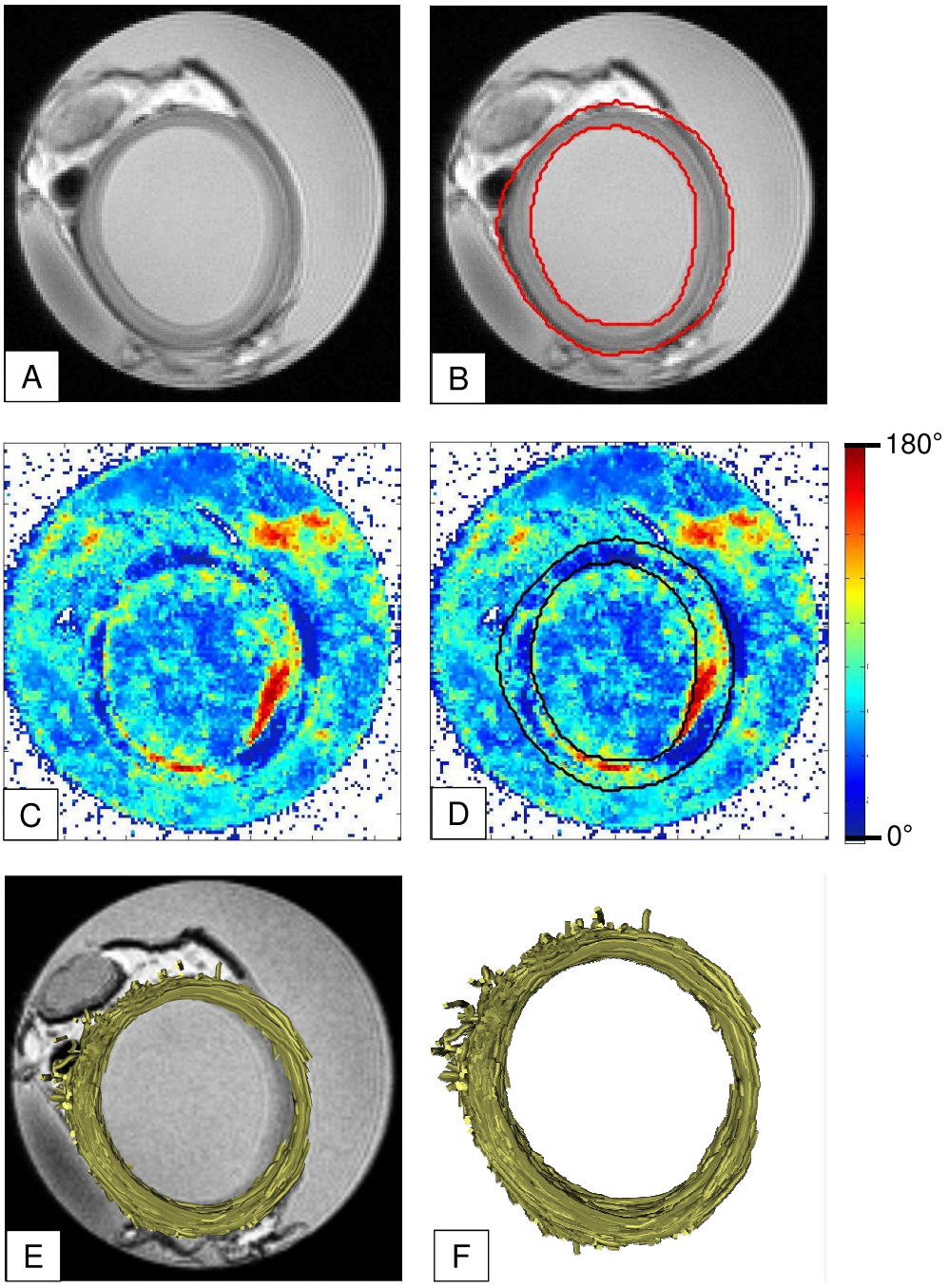


Figure 4.10: Steps in the DTI procedure and image postprocessing; (A) MRI anatomical scan, (B) The ROI of the aorta, (C) A map of the angle of the first eigenvector with the $(x,y)$ plane, (D) A map of the angle of the first eigenvector with the $(x,y)$ plane with the ROI clearly identified, (E) The results of the tractography process with the fibres superimposed on the reference image, and (F) The aortic fibres within the ROI alone.

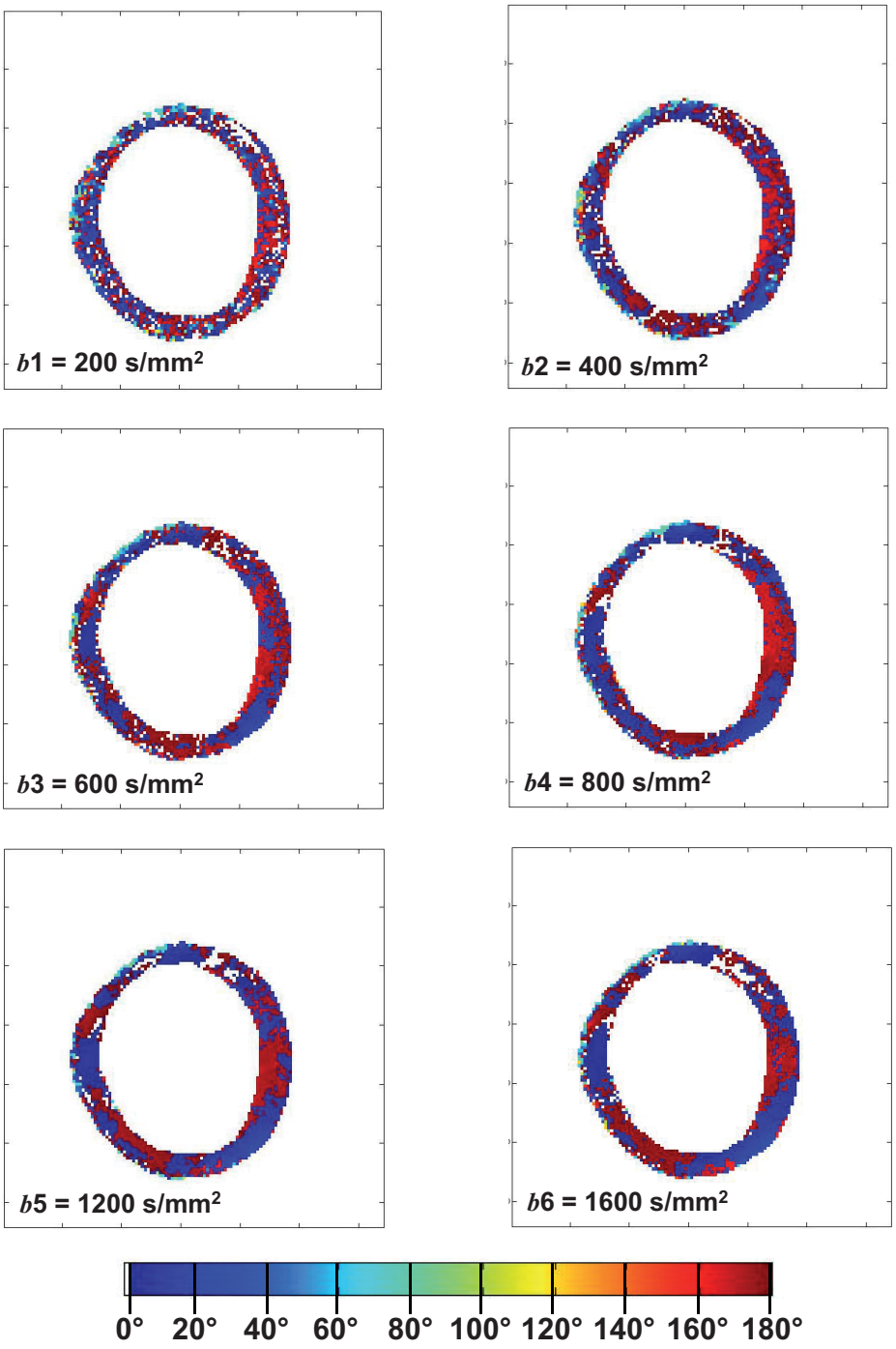


Figure 4.11: Contour maps of the angle between the first eigenvector and the ($x$,$y$) plane for the central slices of the image data sets for the different $b$ values.

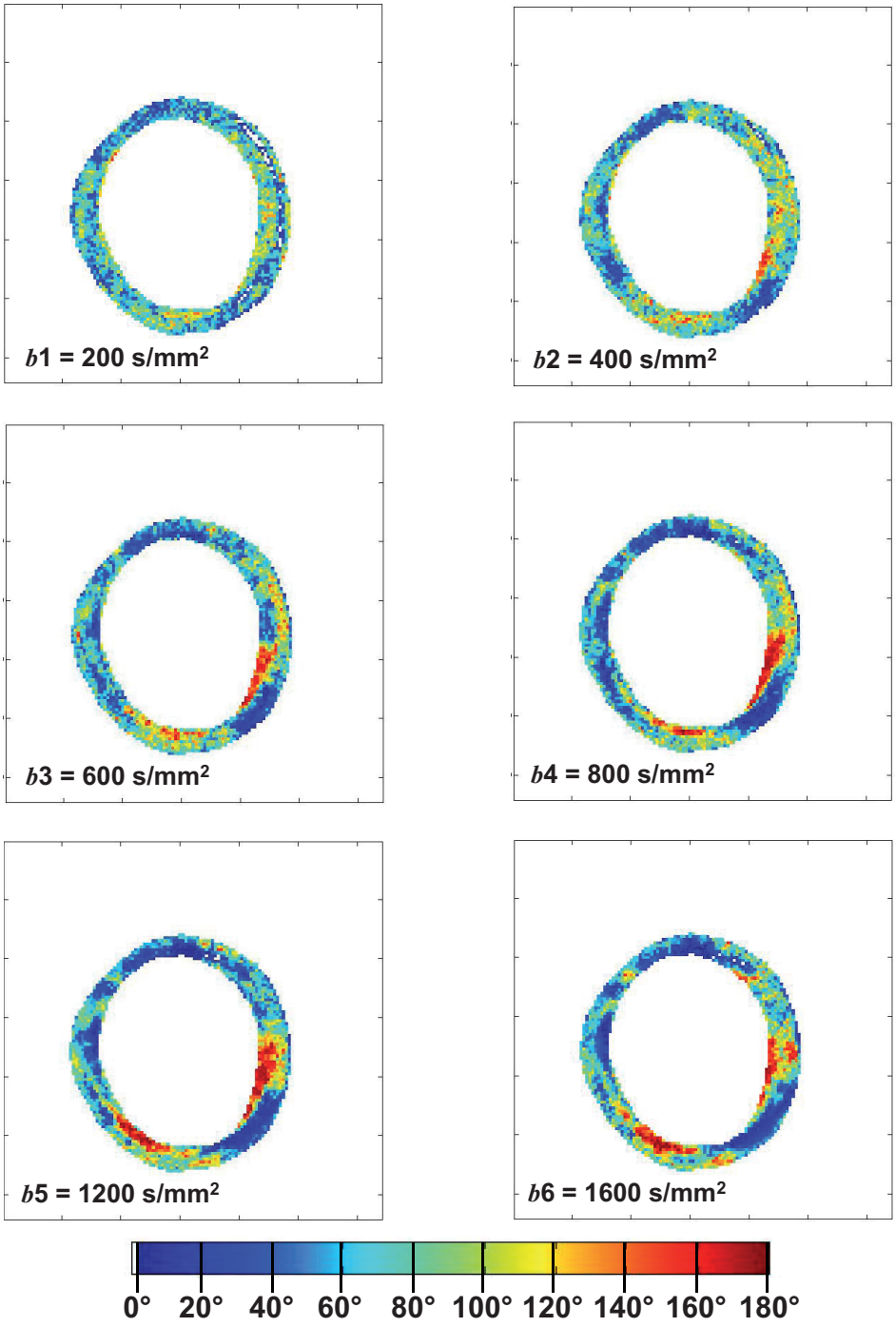


Figure 4.12: Contour maps of the angle between the first eigenvector and the $(x,y)$ plane for the averaged tensors of the image data sets for the different $b$ values.

verify each diffusion tensor was the angle formed by its first eigenvector with the ($x$,$y$) plane. The process of verifying the tensor information is illustrated in fig.4.10, where all of the steps in the postprocessing procedure are shown. Firstly, the anatomical image resulting from the scan was used to determine the ROI, see fig. 4.10(A)-(B). Secondly, the diffusion tensor was analysed in MATLAB and the angle between the first eigenvector and the ($x$,$y$) plane determined and mapped onto the ROI, see fig. 4.10(C)-(D). From both of these images it can be seen that the region of the aorta in the image is still recognisable using the tensor map. This process was carried out only on one fresh sample in order to determine the feasibility of the complete DTI analysis on arterial tissue. The results for the tensor orientation were analysed for different $b$ values to determine the influence of the $b$ value on the tensor angles obtained. For the tensor representing the central slice and the averaged tensor, the angle between the first eigenvector and the ($x$,$y$) plane had greater variability for small $b$ values and became increasingly more consistent at higher $b$ values, see fig.4.11 and 4.12. Two dominant eigenvector angles, close to 0° and 180°, were evident for the analysis of the tensors of the central slice image for all $b$ values (fig.4.11), whilst three, close to 0°, 90° and 180°, were present in the averaged images (fig.4.12).

### 4.2.3 Fibre Analysis

Tracking the fibres passing through a defined ROI of the aorta is the last step in this image post-processing procedure, and some results are shown in fig. 4.10E–F. From these images it can be seen that the fibres plotted are distributed throughout the thickness of the aorta and that they are predominantly oriented circumferentially within the ($x$,$y$) plane of the aorta. Fibre tractography was performed on both fresh and stored frozen aorta images and the fibre angles were evaluated. The distribution measured mean angles $\gamma$, or dominant fibre angles, presented in fig.4.13. For the stored frozen sample, no peaks are clearly visible regardless of the $b$ value used. In contrast, for the fresh samples, two peaks are visible with different amplitudes. In this case, the peaks correspond to 15° ± 2.5° and 175° ± 2.5°, where the fibre

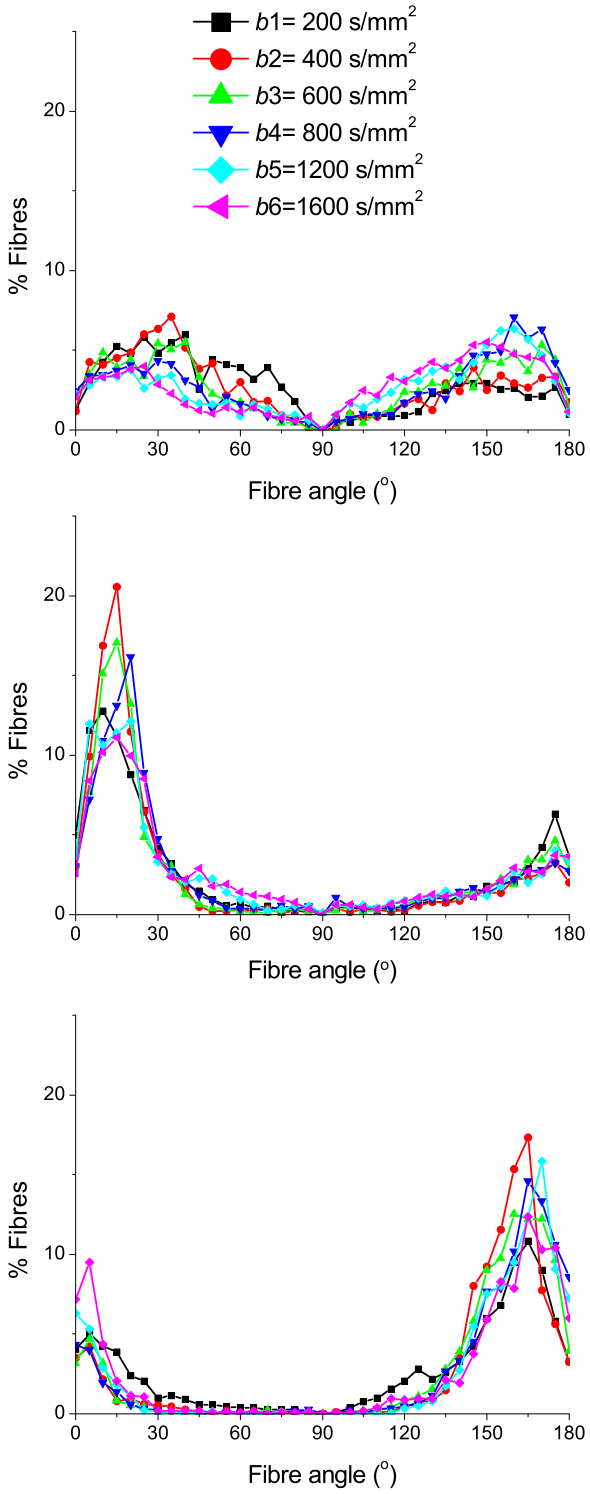


Figure 4.13: Dominant angles for the aortas analysed: A) stored frozen sample; B), C) fresh samples.

angle distribution is evaluated over bands of 5°, and centred in the middle of each band.

The data for the dominant angles, however, does not give any information on the radial distribution, which is presented in fig.4.14, 4.15, and 4.16. From the plots, it is possible to see that the dominant angle prediction is maintained for different $b$ values. The radial distribution is different between the stored frozen and the fresh aortas. In particular, by looking at the images where the fibres tracked for each aorta are superimposed on the MR images, it can be seen that the fibres tracked cover most of the circular profile of the aorta in the fresh samples uniformly, while this is not observed for the frozen one. These observations are confirmed by tables 4.4, 4.5, where the fibre content of each layer is presented. By looking at the data, there are notable differences between the distribution in the frozen aorta and the fresh ones. It can also be seen that the two fresh aortas follow very similar trends.

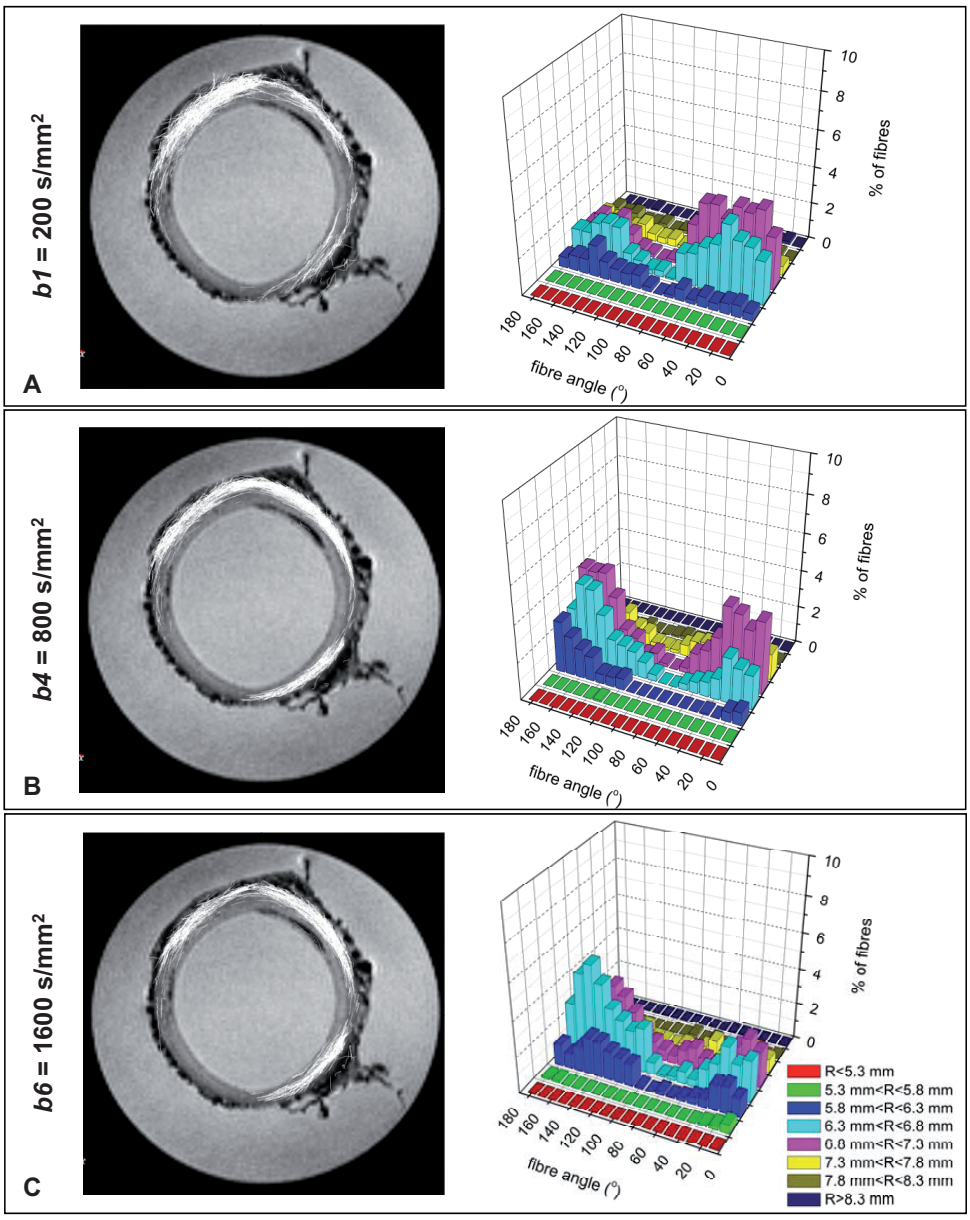


Figure 4.14: Stored frozen sample of fig.4.9.A.1: A) for $b_1$= 200 s/mm$^2$ MRI image with superimposed fibre plot on the left hand side, distribution of fibres across the different layers of the aorta on the right hand side. B) for $b_4$=800 s/mm$^2$ MRI image with superimposed fibre plot on the left hand side, distribution of fibres across the different layers of the aorta on the right hand side. C) for $b_6$=1600 s/mm$^2$ MRI image with superimposed fibre plot on the left hand side, distribution of fibres across the different layers of the aorta on the right hand side.

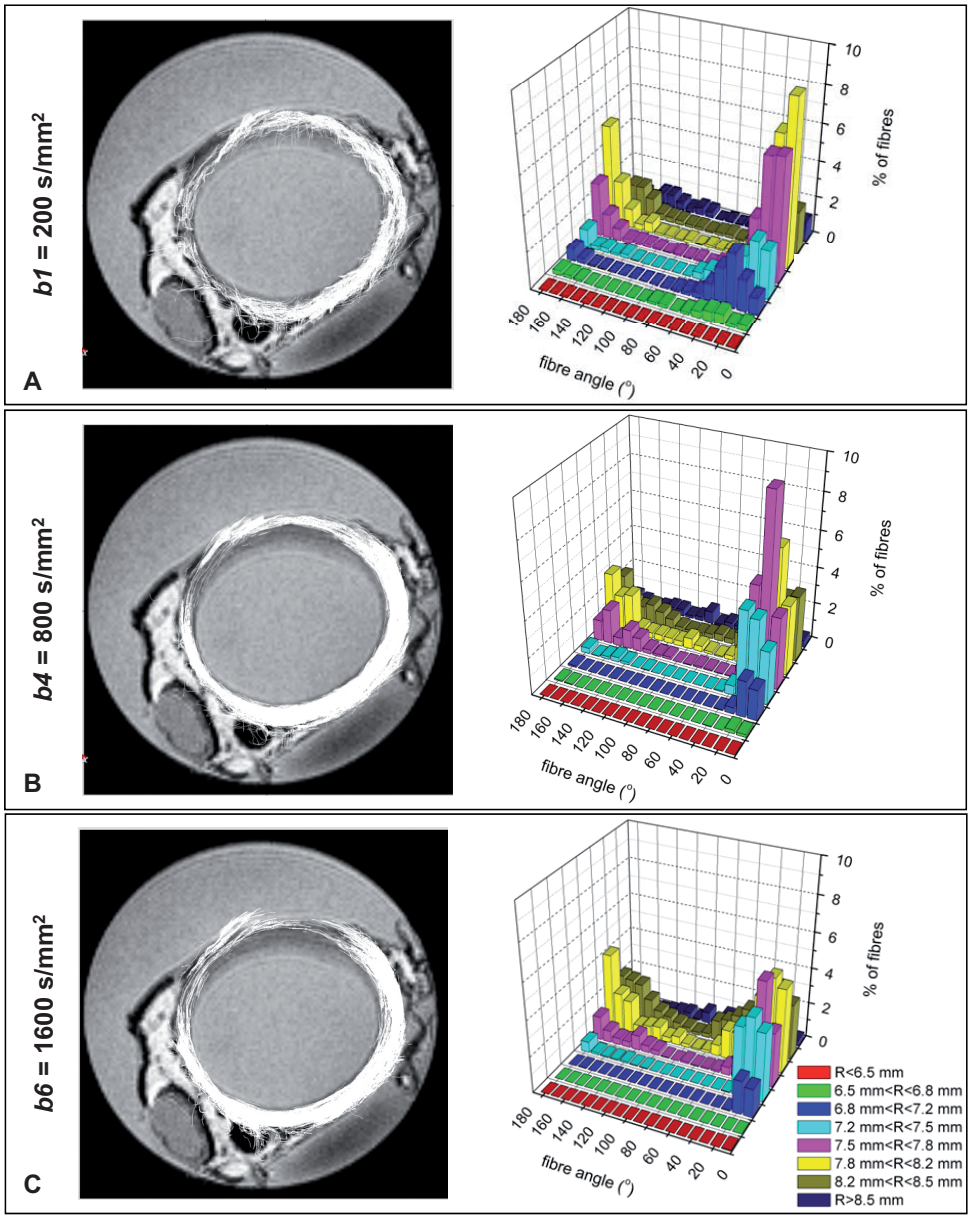


Figure 4.15: Fresh sample of fig.4.9.B.1: A) for $b_1$= 200 s/mm$^2$ MRI image with superimposed fibre plot on the left hand side, distribution of fibres across the different layers of the aorta on the right hand side. B) for $b_4$=800 s/mm$^2$ MRI image with superimposed fibre plot on the left hand side, distribution of fibres across the different layers of the aorta on the right hand side. C) for $b_6$=1600 s/mm$^2$ MRI image with superimposed fibre plot on the left hand side, distribution of fibres across the different layers of the aorta on the right hand side.

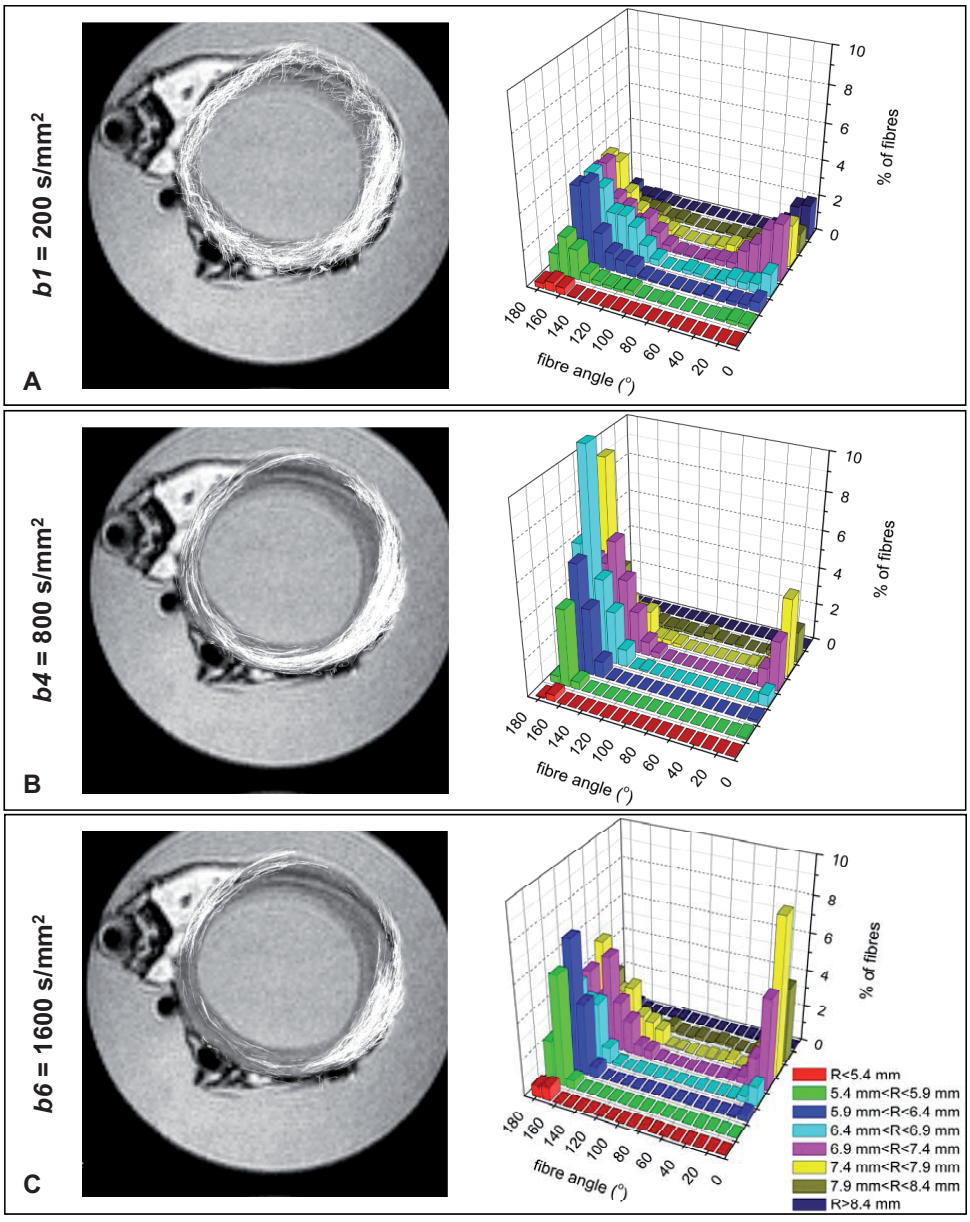


Figure 4.16: Fresh sample of fig.4.9.C.1: A) for $b_1$= 200 s/mm$^2$ MRI image with superimposed fibre plot on the left hand side, distribution of fibres across the different layers of the aorta on the right hand side. B) for $b_4$=800 s/mm$^2$ MRI image with superimposed fibre plot on the left hand side, distribution of fibres across the different layers of the aorta on the right hand side. C) for $b_6$=1600 s/mm$^2$ MRI image with superimposed fibre plot on the left hand side, distribution of fibres across the different layers of the aorta on the right hand side.

| | | content of fibres in each layer | | | | | | | |
|---|---|---|---|---|---|---|---|---|---|
| | | layer 1 | layer 2 | layer 3 | layer 4 | layer 5 | layer 6 | layer 7 | layer 8 |
| | | $R<$ 5.3 mm | 5.3 mm$<R\leq$ 5.8 mm | 5.8 mm$<R\leq$ 6.3 mm | 6.3 mm$<R\leq$ 6.8 mm | 6.8 mm$<R\leq$ 7.3 mm | 7.3 mm$<R\leq$ 7.8 mm | 7.8 mm$<R\leq$ 8.3 mm | $R>$ 8.3 mm |
| | $b1$ | 0 | 0 | 134 | 389 | **438** | **214** | 44 | 4 |
| frozen | $b2$ | 0 | 3 | 166 | 394 | **404** | **205** | 23 | 0 |
| aorta | $b3$ | 0 | 3 | 144 | 334 | **397** | **186** | 24 | 0 |
| | $b4$ | 0 | 1 | 123 | 331 | **469** | **216** | 17 | 0 |
| | $b5$ | 0 | 7 | 138 | 362 | **413** | **201** | 16 | 0 |
| | $b6$ | 0 | 10 | 182 | 414 | **320** | **122** | 5 | 0 |
| | | $R<$ 6.5 mm | 6.5 mm$<R\leq$ 6.8 mm | 6.8 mm$<R\leq$ 7.2 mm | 7.2 mm$<R\leq$ 7.5 mm | 7.5 mm$<R\leq$ 7.8 mm | 7.8 mm$<R\leq$ 8.2 mm | 8.2 mm$<R\leq$ 8.5 mm | $R>$ 8.5 mm |
| | $b1$ | 0 | 64 | 239 | 346 | 712 | **730** | **284** | 110 |
| fresh | $b2$ | 0 | 22 | 178 | 563 | 957 | **1094** | **451** | 57 |
| aorta | $b3$ | 0 | 23 | 263 | 465 | 825 | **1299** | **569** | 49 |
| | $b4$ | 0 | 30 | 202 | 517 | 941 | **1240** | **609** | 68 |
| fig.4.9.B.1 | $b5$ | 0 | 42 | 158 | 584 | 896 | **1212** | **742** | 109 |
| | $b6$ | 1 | 2 | 171 | 450 | 673 | **1258** | **758** | 76 |
| | | $R<$ 5.4 mm | 5.4 mm$<R\leq$ 5.9 mm | 5.9 mm$<R\leq$ 6.4 mm | 6.4 mm$<R\leq$ 6.9 mm | 6.9 mm$<R\leq$ 7.4 mm | 7.4 mm$<R\leq$ 7.9 mm | 7.9 mm$<R\leq$ 8.4 mm | $R>$ 8.4 mm |
| | $b1$ | 32 | 166 | 374 | 502 | **618** | **417** | 138 | 143 |
| fresh | $b2$ | 14 | 138 | 532 | 662 | **651** | **457** | 135 | 14 |
| aorta | $b3$ | 16 | 149 | 328 | 483 | **709** | **446** | 159 | 7 |
| | $b4$ | 9 | 115 | 282 | 595 | **598** | **487** | 188 | 6 |
| fig.4.9.C.1 | $b5$ | 7 | 139 | 222 | 320 | **499** | **428** | 160 | 16 |
| | $b6$ | 22 | 141 | 224 | 206 | **397** | **414** | 183 | 15 |

Table 4.4: Fibre content per layer; bold characters correspond to the transition layers.

| | | percentage of fibres in each layer | | | | | | | |
|---|---|---|---|---|---|---|---|---|---|
| | | layer 1 | layer 2 | layer 3 | layer 4 | layer 5 | layer 6 | layer 7 | layer 8 |
| | | $R<$ 5.3 mm | 5.3 mm$<R\leq$ 5.8 mm | 5.8 mm$<R\leq$ 6.3 mm | 6.3 mm$<R\leq$ 6.8 mm | 6.8 mm$<R\leq$ 7.3 mm | 7.3 mm$<R\leq$ 7.8 mm | 7.8 mm$<R\leq$ 8.3 mm | $R>$ 8.3 mm |
| | $b1$ | 0 | 0 | 10.9 | 31.7 | **35.7** | **17.4** | 3.6 | 0.3 |
| frozen | $b2$ | 0 | 0.2 | 13.8 | 32.9 | **33.7** | **17.1** | 1.9 | 0 |
| aorta | $b3$ | 0 | 0.2 | 13.2 | 30.6 | **36.4** | **17** | 2.2 | 0 |
| | $b4$ | 0 | 0.1 | 10.6 | 28.5 | **40.5** | **18.6** | 1.4 | 0 |
| | $b5$ | 0 | 0.6 | 12.1 | 31.8 | **36.2** | **17.6** | 1.4 | 0 |
| | $b6$ | 0 | 0.9 | 17.2 | 39.2 | **30.3** | **11.5** | 0.4 | 0 |
| | | $R<$ 6.5 mm | 6.5 mm$<R\leq$ 6.8 mm | 6.8 mm$<R\leq$ 7.2 mm | 7.2 mm$<R\leq$ 7.5 mm | 7.5 mm$<R\leq$ 7.8 mm | 7.8 mm$<R\leq$ 8.2 mm | 8.2 mm$<R\leq$ 8.5 mm | $R>$ 8.5 mm |
| | $b1$ | 0 | 2.7 | 9.8 | 12.4 | 23.2 | **30.3** | **14.7** | 6.5 |
| fresh | $b2$ | 0 | 0.2 | 4.7 | 14.5 | 24.7 | **32.2** | **20.4** | 3.2 |
| aorta | $b3$ | 0 | 0.5 | 4.7 | 14.5 | 20.6 | **34.9** | **20.7** | 3.8 |
| | $b4$ | 0 | 0.4 | 4 | 13.3 | 25.8 | **28.4** | **22.7** | 5 |
| fig.4.9.B.1 | $b5$ | 0 | 0.3 | 3.6 | 14.2 | 23.1 | **28.2** | **24.6** | 5.7 |
| | $b6$ | 0.1 | 0 | 3.4 | 13.1 | 17.5 | **30** | **29** | 5.9 |
| | | $R<$ 5.4 mm | 5.4 mm$<R\leq$ 5.9 mm | 5.9 mm$<R\leq$ 6.4 mm | 6.4 mm$<R\leq$ 6.9 mm | 6.9 mm$<R\leq$ 7.4 mm | 7.4 mm$<R\leq$ 7.9 mm | 7.9 mm$<R\leq$ 8.4 mm | $R>$ 8.4 mm |
| | $b1$ | 1.3 | 6.9 | 15.6 | 21 | **25.8** | **17.4** | 5.7 | 5.9 |
| fresh | $b2$ | 0.5 | 5.3 | 20.4 | 25.4 | **25** | **17.5** | 5.2 | 5.3 |
| aorta | $b3$ | 0.7 | 6.4 | 14.2 | 21 | **30.8** | **19.4** | 6.9 | 0.3 |
| | $b4$ | 0.4 | 5 | 12.3 | 26 | **26.2** | **21.3** | 8.2 | 0.2 |
| fig.4.9.C.1 | $b5$ | 0.4 | 7.7 | 12.4 | 17.8 | **27.8** | **23.8** | 8.9 | 0.8 |
| | $b6$ | 1.3 | 8.7 | 14 | 12.8 | **24.7** | **25.8** | 11.4 | 0.9 |

Table 4.5: Fibre percentage per layer; bold characters correspond to the transition layers.

### Different ROIs Analysis

Finally, by looking at fig.4.17 it can be seen that varying the ROI the fibre distribution plots remain the same. There are little changes in the quantity of fibres tracked, as expected because of the ROI different position, but the overall trend is respected.

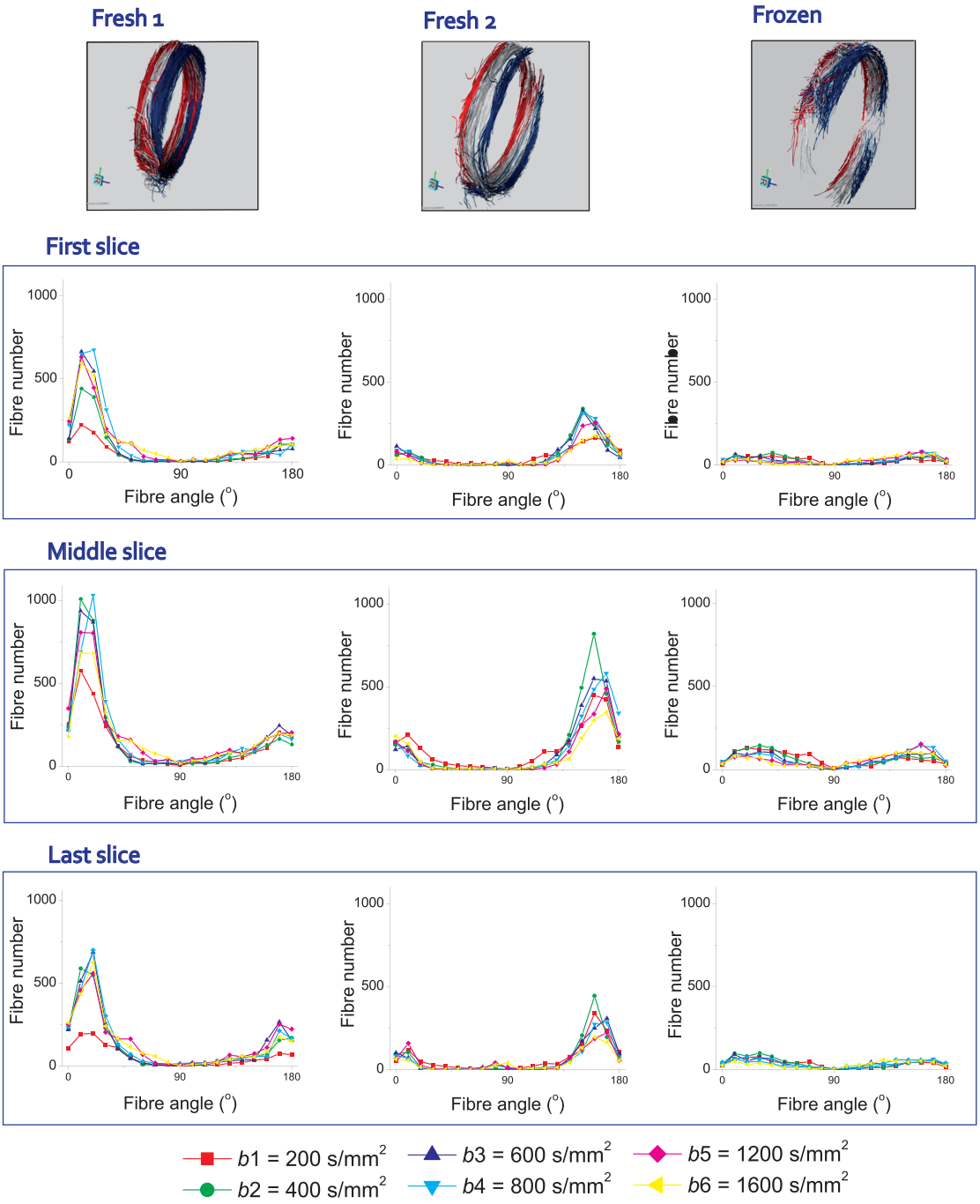


Figure 4.17: Top row: prospective view of the fibres tracked in the sample volumes. In red the fibre bundle corresponding to the first slice, in white the one for the middle slice, and in blue the one for the last slice. Bottom three rows: changes in the fibre distribution according to the ROI chosen for all the samples.

### 4.2.4 Extrapolation of Material Parameters

While the resulting $\gamma$ can be easily extrapolated from the plots, see fig.4.13, $\kappa$ needs to be evaluated through a separate routine described in 4.1.6. The routine results are shown in table 4.6.

## 4.3 Discussion

The arterial wall constitutes a highly organised tissue which must withstand a complex network of forces acting on it, as shown by Burton *et al.* [40] and Peterson *et al.* [131]. The organisation of the tissue is therefore of utmost importance, as it has to offer distensibility and resistance [132]. The arterial tissue mechanical properties are derived from its microstructure which is constituted by collagen, elastin fibres, SMCs and ground substances [5]. The fibrous components reinforce the structure and their distribution generally corresponds to the direction of maximum stress [40, 132].

| values of $\kappa$ | | | | |
|---|---|---|---|---|
| | frozen aorta | fresh aorta fig.4.9.B.1 | fresh aorta fig.4.9.C.1 | fresh aortas average |
| $b_1$ | 0.26 | 0.12 | 0.13 | 0.125±0.05 |
| $b_2$ | 0.22 | 0.09 | 0.09 | 0.090±0 |
| $b_3$ | 0.20 | 0.1 | 0.06 | 0.080±0.02 |
| $b_4$ | 0.21 | 0.12 | 0.07 | 0.095±0.025 |
| $b_5$ | 0.23 | 0.14 | 0.05 | 0.095±0.045 |
| $b_6$ | 0.22 | 0.17 | 0.05 | **0.110±0.06** |

Table 4.6: Values of $\kappa$ obtained for the different fibre distributions of fig.4.13 according to the procedure outlined in 4.1.6.

The orientation of arterial fibrous components has been studied with many different techniques including histology [5], scanning electron microscopy (SEM) [133], confocal electron microscopy [134], and confocal laser scanning microscopy [34]. All of these techniques were consistent in finding that arterial tissue fibres are woven according to a helical pattern with a small pitch. In particular, in the study from O'Connell *et al.* [34], where the three dimensional architecture of arterial fibres was reconstructed by means of microscopy, they demonstrated that all three fibrous constituents of the artery (i.e. collagen, elastin fibres, and SMCs) are aligned predominantly in the circumferential direction and in particular approximately $\pm 10^{\circ}$ from the circumferential direction, as shown in fig.3.3. Moreover, the study by Stergiopulos *et al.* [135] showed that the amount of collagen increases towards the outside of the medial layer of arteries. Finally, the work from Driessen *et al.* [136], analysed the fibre orientation using an indirect approach. This approach consisted in studying the mechanical properties of aorta in order to derive its composition. The model derived described the aorta as a cylinder with helical fibres of very low pitch in the luminal and medial layers (resulting in a near circumferential alignment of fibres), and increasing towards the adventitia. Both direct and indirect analyses of fibres arrangement are in accordance with the findings of the present research, where fibres are found to align nearly circumferentially with a low pitch.

### 4.3.1 Image Analysis

Since this is the first time that DTI has been applied to arterial tissue, the images were analysed qualitatively prior to the numerical interpolation of fibres in order to verify the feasibility of this approach. The qualitative image analysis conducted involved the FA maps. From viewing these maps it is already possible to make two strong statements. The first one is that DTI is capable of identifying the anisotropy of the aortic tissue, as shown in fig. 4.9. In fact, by looking at all of the maps it is possible to distinguish a clear, bright, circular area from the surrounding tissues, and lumps of lymphatic tissue on the surface of the aortas are not as bright as the aortic area. The

second statement is that the anisotropy detected is higher in the fresh tissue than in the frozen one, and this can be clearly seen by comparing the maps in fig.4.9.A.2–4, with the ones in fig.4.9.B.2–4 or fig.4.9.C.2–4. This finding in the latter image implies that there is a difference in the three dimensional fibre distribution of the fresh and the frozen samples which DTI is able to identify. Differences in FA maps intensity are used in clinical practice to diagnose brain damage after a stroke [91, 92]. Therefore, the difference observed in the frozen aorta has the potential to describe an altered tissue structure in the frozen tissue, or one resulting from arterial diseases.

Another interesting feature that can be revealed by a qualitative inspection of the FA maps is that the amount of anisotropy detected changes with the $b$ value used. In fact, by looking at fig.4.9.B–C, the aortic area is noisy for small $b$ values while it is more defined for higher ones. The influence of $b$ values used on the level of anisotropy tracked will be further discussed in section 4.3.4, considering also their influence on the fibre distribution. The insight into the structure of the tissue provided by the qualitative analysis of the FA maps can be further investigated by analysing the diffusion tensor of each pixel.

### 4.3.2 Tensor Analysis

A convenient approach to the study of the diffusion tensors is the use of tensor maps, where selected information extrapolated from each pixel can be represented on the tissue geometry. In particular, tensor maps, where the angle of the first eigenvector with the ($x$,$y$) plane is mapped, show that the main diffusion direction has a small angle. Moreover, by looking at the map for a single slice, it is clear to see that only the angular extremes, 0° and 180°, are evident on the contour map of the artery (fig.4.11). This trend was seen in all individual slices where the eigenvector of the diffusion tensor was determined, however, when considering the overall sample, as in fig.4.11, areas with eigenvectors at 90° to the ($x$,$y$) plane are also present. By comparing the maps of the pixelwise eigenvectors for individual slices (central slices are shown in fig.4.11) to that of the averaged tensor (fig.4.12),

it appears that some changes in the diffusion direction occur in parts of the vessel such that pixels with 0° and 180° eigenvector angles in different slices when averaged result in an angle of 90°. Therefore, analysis of the averaged tensor gives an indication of changes in the diffusion along the length of the vessel whilst individual slices give information on the local diffusion and may be indicators of fibre directions in specific regions of the vessel.

### 4.3.3 Fibre Analysis

In order to establish fibre directions more conclusively, fibre tractography needed to be performed and the fibre tractography on the diffusion tensors in the current study identified dominant fibre angles of ±15° (± 2.5°) over the two fresh samples, as seen in fig.4.13. This is consistent with the fibre direction reported in literature for arterial tissue by O'Connell *et al.* [34]. This result is also in agreement with the eigenvector angles obtained directly from the diffusion tensor. Differences between the eigenvector angles and the fibre angles are to be expected due to the fact that these can be regarded as two different entities. In fact, even though the determination of the fibres is based on eigenvector angles, it is the three dimensional eigenvector arrangement that dictates the fibre together with the constraints imposed by the tractography algorithm, see Appendix B.

From fig.4.15–4.16, it can be seen that the fibre content increases towards the outer radii, as in Stergiopulos *et al.* [135]. This is also confirmed by the data in tables 4.4 and 4.5, where the outermost layers have a higher percentage of fibres. Moreover, for intermediate to high $b$ values, it can be seen that the outermost layers have a less pronounced orientation, with fibres angles as high as ± 60/70°, see fig.4.15.B–C and 4.16.B–C. These results confirm the findings reported in Driessen *et al.* [136]. Finally, the orientation described for intermediate to high $b$ values over the thickness reproduces the pattern observed by Wicker *et al.* [56] for rabbit basal artery. By looking at fig.4.18-right, it is possible to recognise the change in fibre orientation for outer radii plotted in fig.4.15.B–C and 4.16.B–C.

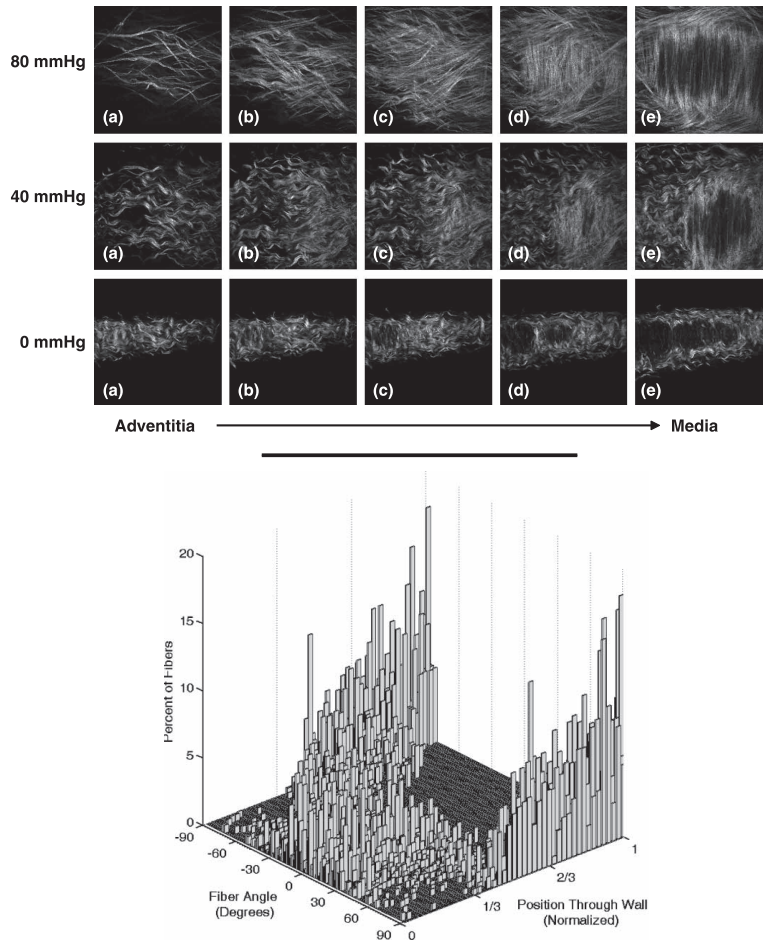


Figure 4.18: Fibre distribution obtained using nonlinear optical microscopy from [56]: left) sampling of slices from the adventitia to the media where increased undulationcan be noted with decreased pressure, the presence of black voids in the media (which likely indicate where the smooth muscle cells reside) and the dramatic shift in orientation from axial to circumferential fibers; right) fibre angle distribution through wall where 0 marks the outer adventitia, and 1 the inner media; the fiber angle axis is oriented so that 0° is axial and 90° is circumferential.

This evidence shows that Diffusion Tensor Imaging can be used successfully to determine the fibre orientation in the aorta. Moreover, this technique could also be used to distinguish different layers. In fact, in fig. 4.15–4.16 it can be seen that there is always a difference in the fibre content among two of the outermost layers. By looking at the data in table 4.4 and 4.5, for both the fresh aortas there is a layer where the fibre content is high (layer 6 for aorta in fig. 4.9.B.1, layer 5 for aorta in fig. 4.9.C.1); while in the subsequent layer the content of fibres markedly diminishes (layer 7 for aorta in fig. 4.9.B.1, layer 6 for aorta in fig. 4.9.C.1). This difference in fibrous content, shown also by the plots in fig. 4.15–4.16, could be used to determine the transition zone that, as reported in Stergiopulos *et al.* [135], exists between the media and adventitia.

All of these results support the use of DTI as a means of obtaining a reliable description of the natural fibre orientation of arterial tissue in a non invasive way, whereas techniques such as histology and microscopy need the tissue to be harvested and fixed. Harvesting the vessel, whilst clearly invasive, also has implications for the structural properties since that it removes any *in situ* longitudinal or circumferential pre-stretches. Moreover, with most of these techniques only small bi-dimensional portions of the arterial wall can be analysed, while with DTI it is possible to obtain the global, three dimensional, fibre orientations.

The fibre angle results obtained for fresh tissue samples are comparable to those obtained from other techniques [5, 57, 135, 136], thus validating the method presented.

### 4.3.4 Optimal $b$ value

Another interesting feature of this study is the determination of the most appropriate $b$ value for the analysis of the fibrous orientation within the arterial wall. The optimal $b$ value in DTI is dependant on the tissue being studied; for example, a value of 1000 s/mm$^2$ has been reported for cartilage [125], whilst 400 s/mm$^2$ has been used for the medial nerve in the human wrist [81, 126], and values between 500 and 800 s/mm$^2$ for the myocardium

[102, 127]. The $b$ value appears to be connected with the composition of the tissue studied and therefore can be used for the diagnosis of diseases that alter such composition [137, 138].

To the best of the authors' knowledge a suitable $b$ value for arterial DTI has not been reported to-date and therefore a range of increasing $b$ values were used in this feasibility study. To find the optimal $b$ value the information in each image set for this range of $b$ values had to be analysed, in particular the amount of significant data obtained in each image had to be quantified. For each $b$ value the tensor maps and the fibre tracts were analysed and these data were compared over the different $b$ values in order to define the optimal one. It is possible to make this comparison by looking at the results shown in fig. 4.11–4.12. For $b$ values less than or equal to 600 s/mm$^2$ it can be seen that while there is agreement with higher $b$ values in terms of the fibre angles plotted, see fig.4.13, the corresponding tensor map is not coherent. It can be seen in fig. 4.11 and 4.12 that for $b1$ and $b2$ a variety of angles are obtained, whereas for higher $b$ values and in particular for $b4$, the angles determined converge on two dominant angles. At the same time, for $b$ values higher than 800 s/mm$^2$, the tensor maps show small changes, especially in fig.4.12. This is confirmed in fig.4.12 where the number of fibres with intermediate angles, especially in the range between 40°-90°, obtained for $b5$ and $b6$ are higher than at $b4$. In addition, the highest number of fibres is tracked for values in the range $b2$ to $b4$ whilst the number reduces from $b2$ to $b1$, and $b4$ to $b6$. These results suggest that the optimal $b$ value for arteries may be around 800 s/mm$^2$ ($b4$), as this is the value for which there is a balance between the eigenvector angles in the tensor maps and the fibre data obtained by the fibre tracking procedure.

The small $b$ values, $b1$-$b2$, can still offer some insights however. By looking at fig. 4.15.A and 4.16.A, and by considering the fact that for these values the fibres are distributed mostly in the internal layers and not in the outer ones, it can be concluded that for small $b$ values a different kind of fibre could be studied. In fact, it is possible to see that for all the other $b$ values the fibre content 'shifts' towards the external radii. The reason for this phenomenon can be explained by fig. 4.9, where it can be seen that in the FA map the

aortic area dilates for higher $b$ values. In particular, it can be postulated that the fibres detected with small $b$ values are elastin fibres that are present in the luminal-medial layers. The verification of this hypothesis however, requires further analyses to be carried out.

### 4.3.5 Extrapolation of Material Parameters

While the evaluation of the structural parameter $\gamma$ was straight forward for the fresh tissue, its determination for the frozen tissue posed more problems, since no clear peaks were detectable, as shown in fig.4.13. A valid measure for $\gamma$ in the frozen tissue would be the average of the distribution measured, and therefore an angle of approximately $\pm$ 30°.The lack of a cohesive fibre organisation was also indicated by the $\kappa$ values calculated from the fibre distribution. In fact, while they are smaller than 0.17 for the fresh samples they are between 0.2 and 0.26 for the frozen ones, with 0.333 being an isotropic distribution, see table 4.6. These values clearly show that there is measurable structural damage due to freezing the aortic tissue. Freezing the tissues generates a rearrangement of the fibres within the tissue that alters the mechanical behaviour of the tissue itself. The origin of this damage and the differences between the fresh and the frozen tissue will be discussed in the following section.

### 4.3.6 Quantification of aortic damage

As stated at the beginning of the present chapter, one of the main aims of this study is to verify the ability of DTI in determining the structure of a healthy aorta as well as a damaged or diseased one. Due to the impossibility of obtaining porcine aneurysmatic tissue, it was necessary to use another kind of damaged tissue and frozen tissue was chosen. In fact, freezing is known to alter the mechanical properties of the soft tissues analysed. Delgadillo, [139] pointed out that the alteration mainly depends on the medium used for the freezing process and the sequence used when defrosting it. In fact, although

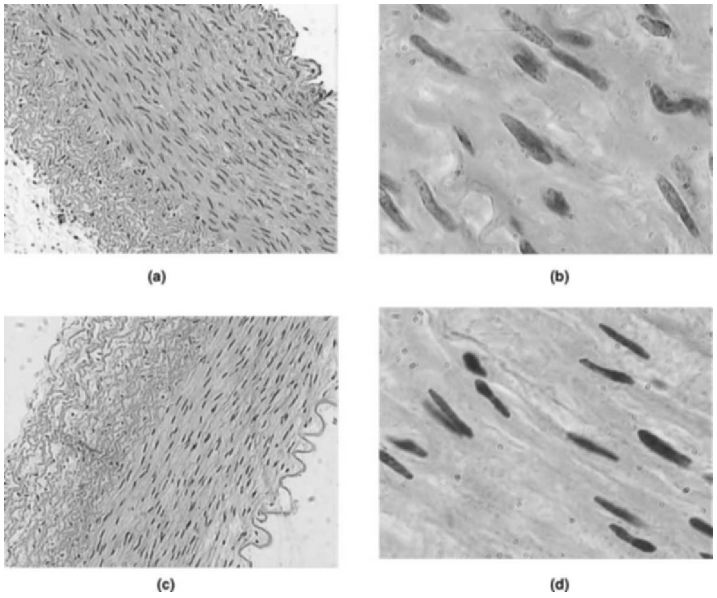


Figure 4.19: Hematoxylin and eosin stained section of fresh (a, b) and frozen (c, d) arteries, with different magnifications: 10× (a, c); 60× (b, d). In the frozen samples condensed nuclei can be seen (c, d), which indicates smooth muscle cell injury, from [140].

some freezing techniques can maintain cell size, the defrosting process can abruptly destroy cells and be much more challenging to control than the freezing process [140]. The result of cells' destruction can be observed by looking at fig.4.19, were arterial frozen cells can clearly be seen to have flattened, like a punctured balloon. As the freezing protocol for this study consisted of simply freezing the aortas in water, cells' structures were altered by the change in volume of the water within them. Water was chosen as it presented minimal noise in the MRI, see section 4.1.1 and as it has been reported to be a freezing media which alters cell structure [139].

Frozen samples obtained by freezing in water produced tissue with an altered fibre pattern. This alteration was so extensive that it could be seen qualitatively by looking at the FA maps, as shown in fig.4.9. In fig.4.9, it can be seen that in the FA maps for the frozen sample the aortic area is darker compared to the fresh samples. This means there is a lower degree of anisotropy and therefore, a different kind of fibre orientation. The confir-

mation of these observations comes from analysing quantitatively the fibre distribution, see fig.4.13, 4.17. In fig.4.13, 4.17 it is possible to see that the fibres in the frozen sample are more scattered than in the fresh ones and also that there is no preferred orientation identifiable by a dominant peak in the fibre angle plot. In fig. 4.14, it can be seen that this inconsistent pattern of fibres continues throughout the layers. These observations are further supported by the data in table 4.4 and 4.5 where the fibre content is arranged across the layers in a different way compared to the fresh aortas. These structural changes give rise to a material with different mechanical properties [140], see fig.4.19, because these properties are influenced by the microscopic changes in the tissue while freezing. The misalignment produced by freezing and shown in fig.4.13.A, corresponds to an overall weakening of the tissue due to the loss of coherence of fibres in the preferred direction. From this it can be inferred that the knowledge of a tissue's structural architecture and relative changes can give an insight into how the damaged tissue will react to different stimuli, such as the physiological blood pressure and or the implantation of a surgical device.

Observing such alterations in the damaged aortic wall is an important result not only in terms of the mechanical characterization of the tissue, but also from a clinical point of view. The profound meaning of this finding is that DTI could be used for detecting changes in the aortic tissue non-invasively, which infers that it has the potential to be further developed as a tool for the diagnosis of early stage AAAs in humans. In fact, in section 2.2, it was described how most of the studies on AAAs development conclude that AAAs are linked to an alteration in the concentration and in the configuration of the protein based constituents of the aortic wall [28–30]. In particular, this modification in the structure is a result of a rearrangement of the medial structure due to a decrease in elastin content and organisation [141], to an alteration in collagen deposition caused by the presence of collagenases [28, 31], and to a significant reduction in smooth muscle cells [31, 32]. All of these changes can be observed by looking at fig.4.20, where histological slices of a non-aneurysmal tissue and of an aneuryms are given for comparison. These histological findings are in accordance with the change in

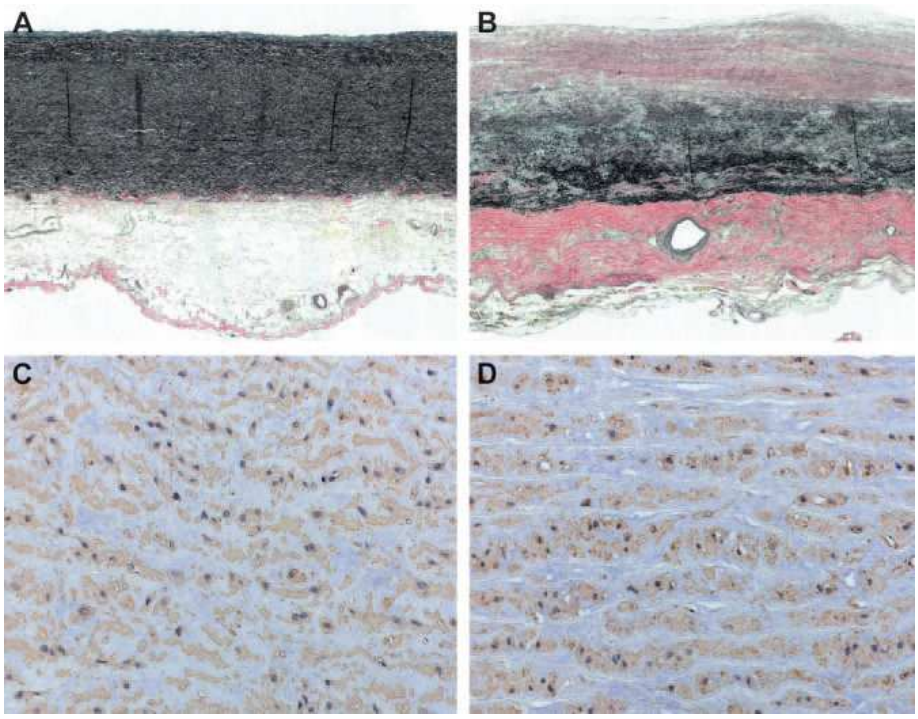


Figure 4.20: Histological evidence of structural alteration in ascending thoracic aortas. Nonaneurysmal aortas (A, C) and aortic aneurysms (B, D) were stained with elastin-Van Gieson (EVG) (A, B) or an antibody to SM $\alpha$-actin (C, D). Elastin is stained black by EVG and separates the media from the intima (above) and adventitia (below); in the high magnification photomicrographs (C,D) it is possible to see lacerations in the structure for the aortic aneurysm, from [141].

the mechanical properties of the tissue reported and in particular with the low tensile strength of AAAs tissue measured by Vorp *et al.* [27], shown in fig.4.21.

By comparing the results obtained from literature for frozen arteries and AAAs arteries, see fig.4.19, and 4.20, it is possible to notice that the damage produced by these phenomena is similar. In both cases there is a global rearrangement of the protein structure of the tissue that is characterized by a global loss of cohesion and fine dispersion. Adding to these observations that DTI is able to pick up alterations in the aortic fibre pattern due to freezing, it is possible to conclude that DTI could have the potential to

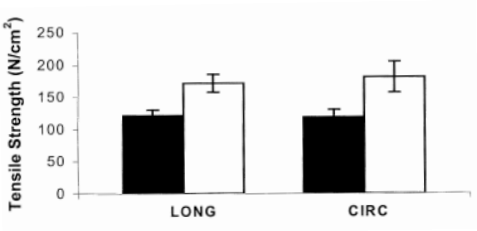


Figure 4.21: Aneurysm induced Alterations in arterial mechanical behaviour: effects of aneurysm on tensile strength of longitudinal (LONG) and circumferential (CIRC) specimens of ascending thoracic aortic aneurysm (black) and nonaneurysmal aortic tissue (white), from [27].

detect alterations in fibre patterns due to AAAs. Besides, the use of DTI for detecting diseased fibre patterns could trigger an even bigger advancement in clinical practice, since it could be used to study the early stage of the disease and thus could give an insight into the aetiology of AAAs, as yet still unknown [142]. Finally, the use of DTI in a clinical setting could produce new criteria for AAA rupture prediction, which would be more scientific and reliable than the current state of the art diameter measurement[3] .

Another relevant aspect of the potential of DTI in identifying altered fibres, is its use in predictive modelling. Determining fibre alteration within the tissue generates new structural parameters for constitutive models which in turn require different material constants. From this interdependence between the structural parameters and the constitutive model, the importance of the structural parameters in determining the overall tissue behaviour can be drawn, which brings to the conclusion that the fibres tracked have a structural significance. Therefore, being able to measure fibre disorganisation with DTI allows for measuring changes in the structural parameters and consequently, for the determination of new constitutive models.

Finally, the biggest advantage of DTI over other tecniques is its non-invasiveness and the possibility of obtaining 3D data. Many of the studies

[3]AAAs smaller that 5 cm are deemed to be unlikely to rupture while AAAs bigger than 5 cm are usually surgically treated. Unfortunately AAAs smaller than 5 cm can rupture and AAAs bigger than 8 cm can keep growing without rupture [17, 23, 25, 26].

on aortic damage are based on 2D histological findings which have been taken from samples harvested *post mortem* following removal of the *in-situ* pre-stretch. By using DTI on fully intact aortic samples there would be two advantages over state of the art histological techniques: first, the alteration in fibre direction measured would be representative of the whole arterial geometry *in situ*; and second, the non-invasive nature of DTI would make large epidemiological studies on humans easier and faster.

In this study a damaged fibre pattern was induced using the effect of water and freezing, so that it could represent diseased aortas with a disrupted fibre pattern. The results presented suggest that DTI can successfully recognise the altered fibre pattern contained in a diseased aorta. From this, it can be concluded that DTI offers a resolution high enough to study patterns in the healthy aorta as well as diseased vessels.

### 4.3.7 Limitations

Regarding the interpretation of the results presented, one of the biggest limitations is in the knowledge of the fibres tracked for the small $b$ values. To determine if they really are elastin fibres further microscopic or histological analyses are required. Such analyses will also be needed to further investigate the transition zone between the media and adventitia and to create a clear correspondence between the aortic tunicae and the layers identified in this study. Three dimensional microscopy analyses such as that performed by O'Connell *et al.* [34] would be the best technique to analyse these phenomena given that it can image fully intact cylindrical samples. Histology could perhaps offer some insights but given that it requires harvesting the tissue and viewing 2D sections where all *in situ* loading has been removed it would not be the optimum exploratory technique.

The aortas were completely immersed in a chamber filled with water as opposed to saline. Imaging the samples with saline solution posed problems in terms of filtering the noise, since the solution was inside and all around the sample. Blood would be inside the samples *in vivo* and there are MRI blood suppression routines available that could be applied so the same issues

would not exist for *in vivo* analyses. Another limitation was the analysis of a vessel in the unloaded configuration, whereby the circumferential stretch was preserved, but the longitudinal stretch was lost. Taking these limitations into account it is still clear that DTI of arterial tissue is feasible and that it can be used to successfully image the fibrous structure of arterial tissue in a non-invasive way.

More generally, a limiting factor in the accuracy of the results was the fibre tracking streamline deterministic algorithm used, i.e. an algorithm that considered only one fibre direction for each voxel. This kind of algorithm is state of the art, but new algorithms are currently under investigation that allow tracking two or more fibres in each voxel. It must be noted that the fibres tracked with this algorithm are not the resultant of the two fibres crossing the voxel, but only one of them. This explains the difference in peak amplitude for different samples: where two fibres cross in a voxel, only one is picked. By taking the nature of the fibre tracking algorithm into consideration it is possible to conclude that there are two families of fibres in the fresh aortic wall which helically criss-cross each other in a symmetrical pattern about the reference central axis, this gives rise to two dominant peaks in the fibre angle plots with equal clockwise and anticlockwise leading angles for helical fibres.

### 4.3.8 Conclusions

DTI can describe the fibre arrangement that was described by other techniques used in literature. Over all the other techniques, DTI has many advantages. Firstly, it has the potential to study fibre orientation in a non invasive way; secondly, it can do so for a large continuous 3D portion of the aorta. This means it can be directly applicable to a living human being and that an extensive portion of the tissue can be studied at the same time. Finally, because a large amount of fibres can be analysed at the same time using a computer based technique, biased and time-consuming results such as those obtained in a manual analysis are avoided.

# Chapter 5

# Phase Contrast MRI

characterizations of the mechanical behaviour of a structure cannot be judged complete without an analysis of the loading response. This analysis can be carried out in many ways like, for example, the tensile tests described in 2.3.1, see page 24. Since the main aim of this paper is to achieve the characterization of aortic tissue non invasively, tensile tests cannot be considered a suitable option, since they require the tissue to be harvested.

Magnetic Resonance Imaging again provides a solution to the problem of determining non invasively the strains resulting from loading of the tissue. In this case, the technique used was Phase Contrast MRI, which is a technique developed for studying arterial flow. Although the application of Phase Contrast MRI to determine circumferential strains in the aortic tissue is already reported in literature [109, 120–122], its expansion to the characterization of the behaviour of the aorta, described in the present work, is novel. In fact, the circumferential strains measured non-invasively with this technique will be used in the final chapter to define suitable parameters for a constitutive model capable of describing aortic mechanical behaviour.

## 5.1 Methods

In contrast with DTI, Phase Contrast MRI is a dynamic technique, producing images that are velocity maps. Therefore, in order to proceed with PC

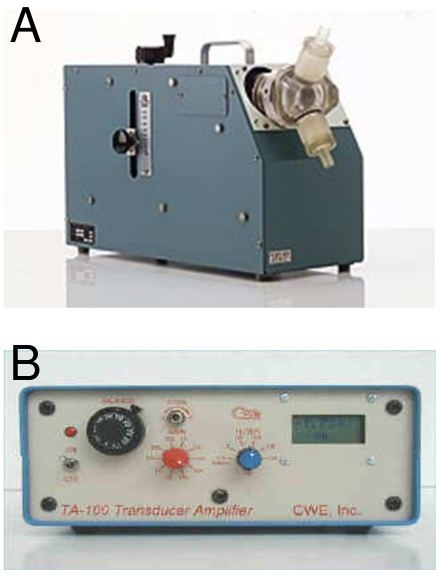


Figure 5.1: Equipment used in the study: A) Pulsatile pump for large animals from Harvard Apparatus; B) Transducer amplifier from CWE Inc..

MRI, the aortas needed to be adequately pressurised. This was achieved by connecting the modified chamber, (page 55), to a pulsatile pump for large animals (HA553305, Harvard Apparatus, MA), see fig.5.1,A. Using this pump the aorta segments were subjected to a pulsatile flow, similar to the one produced by a heartbeat. The pulsatile profile produced lasted for nearly 850 ms and repeated identically each cycle, and is shown in fig.5.2. With dynamic analyses the MRI scanner needs triggering, so that the scan can be taken at the same point in each cycle. This was achieved by using a pressure transducer connected through a probe (DTX-plus, BD Medical Systems, UT). The probe was inserted in the chamber, inside the aorta, and the pressure transducer was connected to a transducer amplifier (TA100, CWE Inc., PA), see fig.5.1,B. The transducer amplifier has two analog outputs. The first output simply reports the pressure from the pressure transducer and is connected into a monitoring laptop where a custom LABVIEW® code was written for control, reported in Appendix D. The second output is a result of an instrument modification conducted in order to trigger the MRI: the transducer

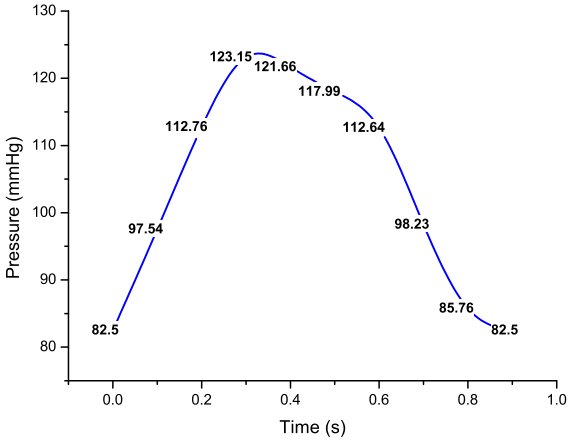


Figure 5.2: Continuous pulsatile profile produced by the HA553305 pump in the porcine aorta. The pressure recorded at the nine time steps considered in the analysis is highlighted.

amplifier was fitted with a transistor-transistor logic trigger (TTL trigger) that could be manually modified to send a trigger signal to the MRI system. The analog output corresponding to the TTL trigger is doubled and feeds both the MRI system and the monitoring laptop. The arrangement of equipment used for this experiment is shown in fig.5.3, where it can be seen how the water flow loop and the electronic feed-back loop communicated through the transducer amplifier. None of the equipment used could stay in the scanner room, due to restrictions on the presence of ferromagnetic metals in the MRI, and therefore all the equipment shown in fig.5.3, was kept in a separate room. Since the chamber used in this study was similar to the one used for the DTI scans, the aortic segments were prepared as described on page 54. Moreover, this imaging technique required extensive preliminary testing and set up, as described on page 57, hence the results obtained for one sample are presented here.

Using the parameters indicated in table 5.1, four images were scanned at 100 ms intervals during the pulsatile cycle (i.e. eight time steps and eight pressure values). The first image was a reference image, with no gradient applied and the remaining three were gradient sensitized images, where the

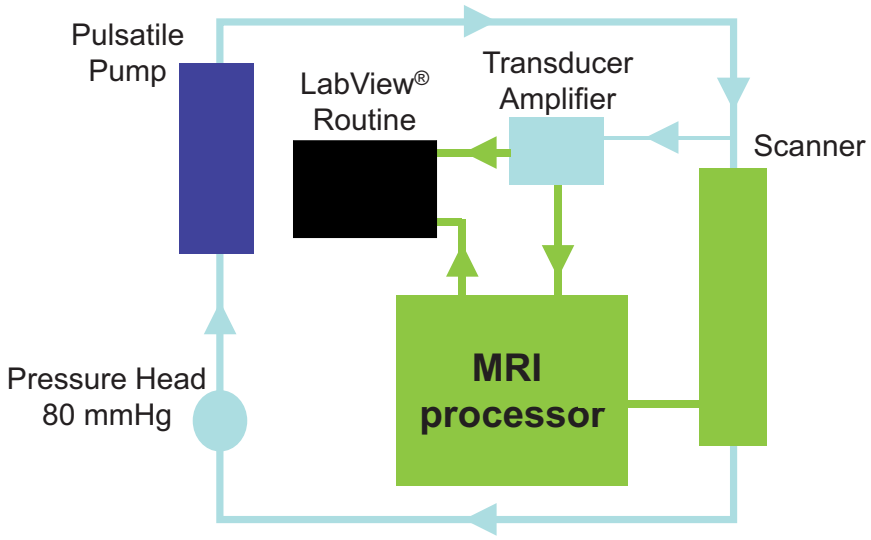


Figure 5.3: Schematic of equipment connections for the PC MRI experiment: the blue line represents the water connection while the green line represents the electronic connections.

gradient was applied each time along a different dimension between $x$, $y$, and $z$. These images were then input into a custom MATLAB® routine where the velocities were analysed together with hand-tracked ROIs of the datasets at each time step.

The first portion of the routine was similar to the DTI routine and analysed the ROIs in order to extrapolate the centre of mass of each image. Then the ROIs were used to select the relevant portion of the image (the aorta). From the images obtained in the $x$, $y$ and $z$ directions, the reference image was subtracted and then the phase pixel values were multiplied by the encoding velocity, as shown in eq. 2.26 (page 33) thus producing velocity encoded images in the three directions. According to the work of Pelc's group [120–122], in order to study the strains in the aorta effects of rigid body translations and rotations on the velocity encoded images need to be removed. Therefore, the images underwent the following procedure to remove the effects of rigid body translations and rotations in accordance with the method described in [124].

### Removal of rigid body translations and rotations

For the removal of rigid body translations and rotations, the centre of the image needs to be calculated first. This was done by tracking manually the ROIs of the first slice of the volume in each dataset and evaluating the ROI's centre of mass using a custom MATLAB® routine. It is then necessary to define the rigid body motion. In three dimensions the rigid body motion can be transformed as a rotation about the centroid of the slice and a translation of the centroid [124]. Rotation velocities are dependent on angular velocity ($V_{rotation} = \omega \times r$; $r$ distance from the centroid), while translation velocities can simply be added, as shown in eq.s 5.1 and 5.2:

$$V_x = z\omega_y - y\omega_z + V_x^{translation} + V_x^{deformation}(x, y) \tag{5.1}$$

$$V_y = x\omega_z - z\omega_y + V_y^{translation} + V_y^{deformation}(x, y) \tag{5.2}$$

Where $V_i$ is the image velocity, $\omega$ is the angular velocity, $r = [x, y, z]$ is the distance from the centroid, $V_i^{translation}$ is the translation velocity component, and finally $V_i^{deformations}(x, y)$ is the velocity of the deforming tissue, i.e. the quantity that needs to be determined [124]. In this approach through-plane velocities ($V_z$) are not considered, however this procedure can be extended to three dimensional motion [124].

Since $\omega$ and the translation velocity can be considered constant during the velocity encoding interval, the eq.s 5.1 and 5.2, can be rewritten as [124]:

| Matrix | FOV | N Slices | Slice Distance | Echo Time | Velocity Encoding |
|---|---|---|---|---|---|
| 256 × 256 | 2.8 × 2.8 cm | 9 | 1.5 mm | 10 ms | 4.6 cm/s |

Table 5.1: PC MRI scanning parameters

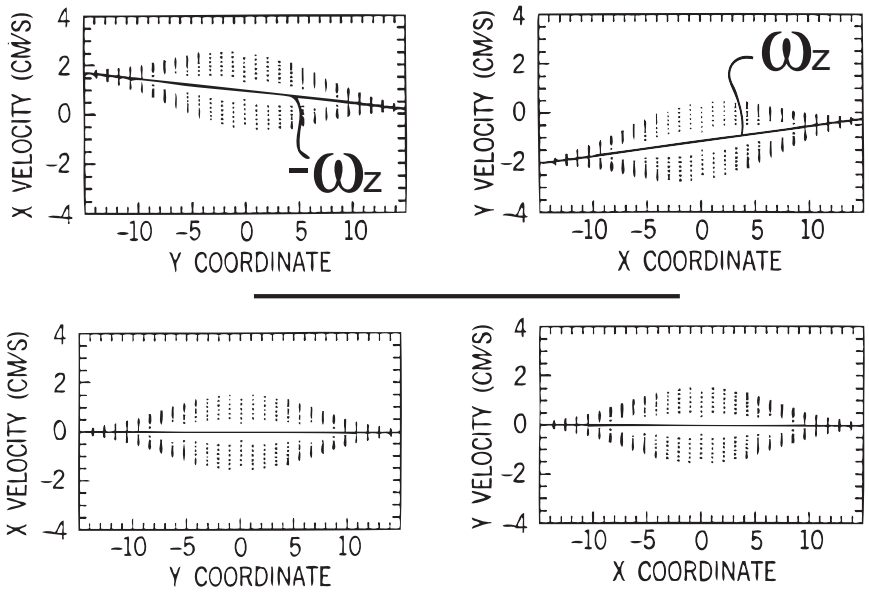


Figure 5.4: Top: distribution of values for $V_x$ versus $y$ and $V_y$ versus $x$. This distribution can be fitted by a line whose slope corresponds to $\omega_z$, and whose intercept indicates $A_i$. Bottom: distribution of values for $V_x$ versus $y$ and $V_y$ versus $x$ after the removal of rigid motions effects. Figure adapted from [124].

$$V_x^{deformation}(x,y) = V_x - A_1 + y\omega_z \tag{5.3}$$

$$V_y^{deformation}(x,y) = V_y - A_2 - x\omega_z \tag{5.4}$$

At this point, the constant values $A_i$ and $\omega_z$ are unknown. From a look at eq.s 5.3 and 5.4 $A_i$ and $\omega_z$ can be regarded as the intercept and the angular coefficient of the line produced by plotting $V_x$ versus $y$ or $V_y$ versus $x$. Then the approach used for evaluating $A_i$ and $\omega_z$ is the following: plotting $V_x$ image velocity values versus $y$ (or $V_y$ versus $x$) a distribution of values is produced that can be fitted by a line, whose slope corresponds to $\omega_z$ [124], and whose intercept indicates $A_i$, as shown in fig.5.4. Finally, $V_i^{deformation}(x,y)$ can be evaluated using eq.s 5.3 and 5.4 and by inputting the average of the two $\omega_z$ and the $A_i$ values for the corresponding direction.

Once the rigid motion was removed from the velocity encoded images and prior to proceeding with the strain determination, the spatial derivative of the deformation velocity was evaluated and thus the gradient velocity tensor was created, as shown by eq. 2.27 (page 33). The final step involved the construction of a mesh of the aorta for each time step. In fact, a division of the aorta into elements was necessary, since it was needed for comparison with Finite Element Models. Therefore, a mesh was created in MATLAB® by using the manually tracked ROIs of all the slices and by stacking them together in order to create a volume. The in-plane division of the mesh depended on the amount of pixels describing the luminal circumference of the aorta, and this allowed for the in-plane density of the mesh to be altered by changing the number of pixels between the nodes of the element. The same convention was applied to the mesh through-plane dimension that was defined by the inter-slice thickness. In this case, one element was used over the in-plane thickness of the aorta, and 20 divisions were applied to the luminal circumference. This resulted in a mesh of 20 elements for each slice of the aorta for each time step of the cycle. The mesh created for the first step of the cycle was exported to ABAQUS® for finite element analysis and strain comparison. The final results of this procedure were the deformation velocity matrices and the gradient velocity tensors for each mesh element and each time step, plus mesh geometrical information (nodes, size of elements, baricentre) for each time step.

**Circumferential strain** For the evaluation of circumferential strains, the results of this MATLAB® routine were exported in a separate file (one for each time step). The data from the files were read iteratively and then the radial component of the resultant velocity vector (the average of the velocity values contained within an element) was evaluated for the $i$, the $i-1$ and the $i+1$ time steps. The extrapolation of the the radial component of velocity was accomplished by using trigonometry and geometrical definitions. In particular, since the radial component of the velocity vector is defined as its projection on the line $s$, see fig. 5.5, it can be described by the equation:

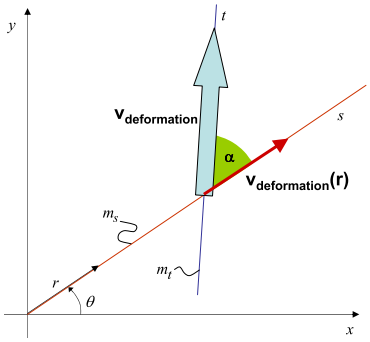


Figure 5.5: Definition of velocity vectors in a cylindrical coordinate system.

$$V_r^{deformation} = V^{deformation} cos(\alpha); \tag{5.5}$$

Where $\alpha$ is the angle between the two lines $t$ and $s$, as shown in fig. 5.5, that can be determined using the slope of the two lines, $m_t$ and $m_s$:

$$tan(\alpha) = \frac{m_t - m_s}{1 + m_t m_s}; \tag{5.6}$$

Then, radial trajectories were evaluated for each mesh element, according to the forward/backward algorithm defined in [109], and described in Appendix C. This method can be applied to cyclic motions and defines the trajectory of an element $r_k$ by combining the trajectory produced by going forward in time $f_{k+1}$ and backward in time $b_{k-1}$, as shown briefly by eq.s 5.7. A more detailed explanation of this integration is reported in Appendix C.

$$\begin{aligned} f_{k+1} &= f_k + \frac{1}{2}\left[V(f_k, t_k) + V(f_{k+1}, t_{k+1})\right]\Delta t; \\ b_{k-1} &= b_k - \frac{1}{2}\left[V(b_k, t_k) + V(b_{k-1}, t_{k-1})\right]\Delta t; \\ r_k &= w_k f_k + (1 - w_k) b_k; \end{aligned} \tag{5.7}$$

Finally, circumferential strains were evaluated using eq. 2.30 (page 35):

| **MATLAB®:** |
| --- |
| • Definition of the centre of mass from ROIs;<br>• Use of the ROIs to select relevant area in the image;<br>• Subtraction of reference image;<br>• Determination of velocity encoded images;<br>• Evaluation of deformation velocity as in [124];<br>• Creation of the velocity gradient tensor $L$;<br>• Mesh definition;<br>• Evaluation of values of interest<br>for each mesh element & for each time step;<br>• Radial trajectories tracked as in [109];<br>• Evaluation of circumferential strain<br>for each mesh element & for each time step as in 2.30; |

Table 5.2: PC MRI step sequence.

$$\epsilon_{\theta\theta} = \frac{1}{2}\left[\left(\frac{r}{R_0}\right)^2 - 1\right];$$

In this case the vessel radius at a reference time point $R_0$ was defined as the radius calculated from the first time step ROI, while $r$ was obtained as the radial component trajectory for each mesh element. A summary of the sequence of the operations performed by the custom MATLAB® routine for PC MRI is illustrated in table 5.2.

## 5.2 Results

The non-invasive determination of circumferential strains was the result of the process described in the previous section. The images obtained from MRI for each time step were obtained in two formats, a magnitude one (standard format in which MRI images are generally produced) shown in fig.5.6, and

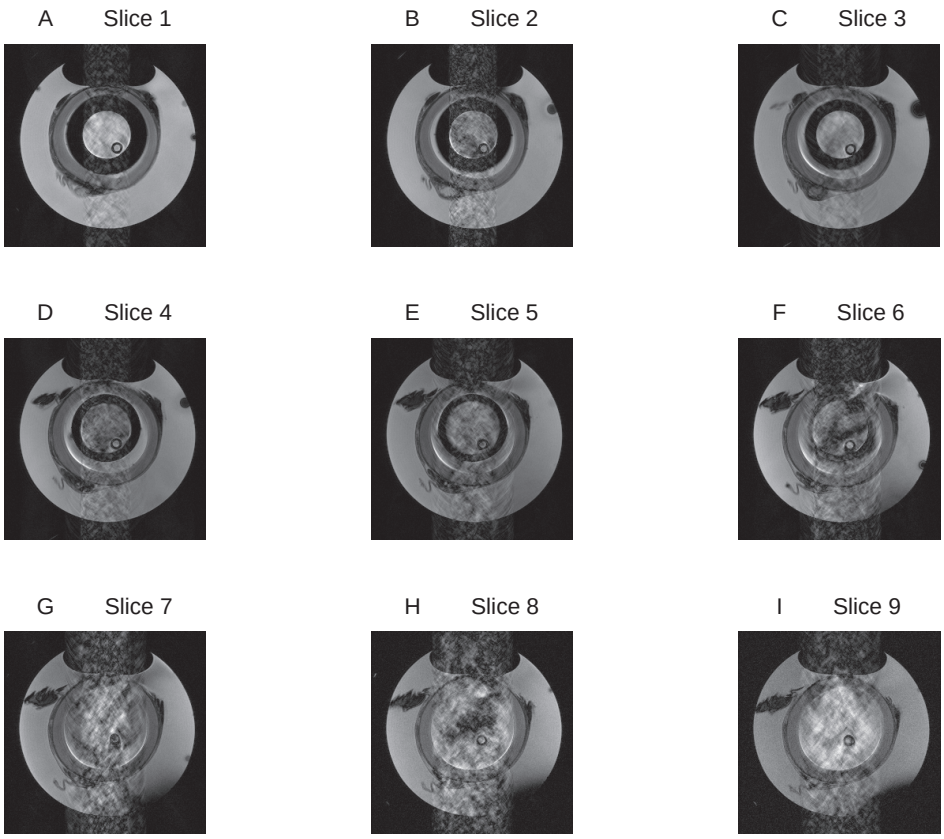


Figure 5.6: Magnitude images of the PC MRI sequence for each slice.

a phase one, shown in fig.5.7, where each pixel represents the phase of the precessing proton and hence, by eq.2.26, the velocity. In these images it is possible to recognise different components: together with the water and the aorta present in the images, in fig.5.6 it is possible to see the pressure transducer, and, for the first slices, the connector which keeps the aorta in place, see fig.5.8 and fig.4.2 (page 55). Moreover, in the images in fig.5.6 it is possible to see a blurring effect created by the noise of the water flowing through the sample. This noise effect is reduced in the phase images in fig.5.7, making them suitable for further analysis.

As described in the previous section, the components of velocities obtained by subtracting the reference image from the directional images, had to be filtered in order to remove the rigid body motions. The results of

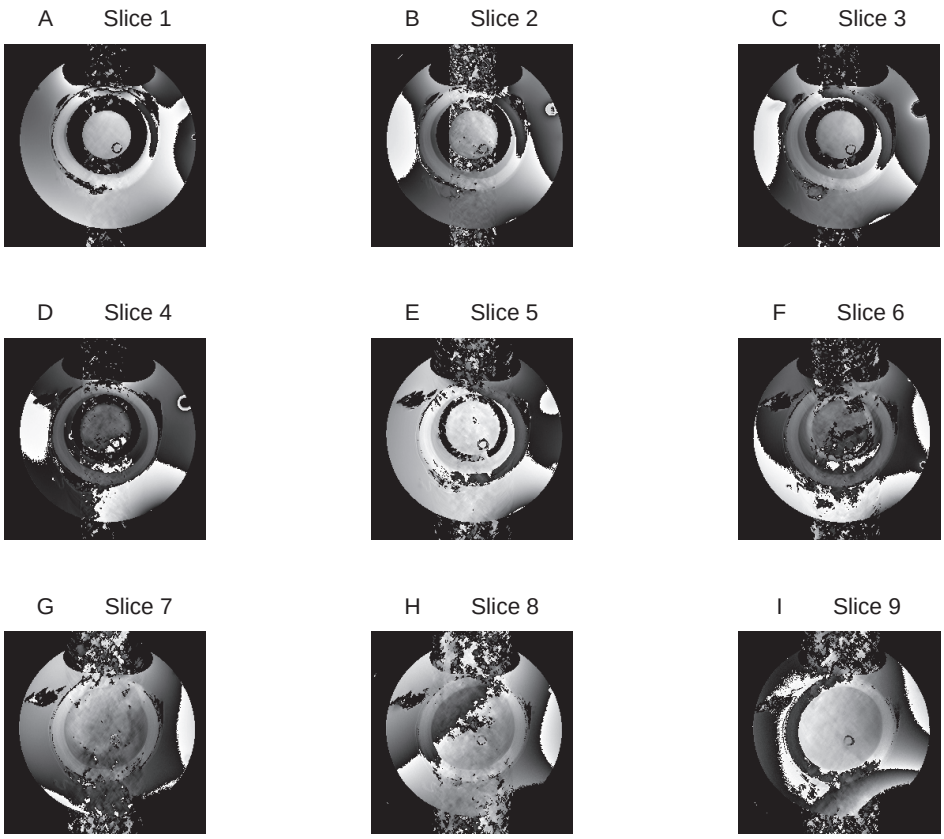


Figure 5.7: Phase maps of the PC MRI sequence for each slice.

this method, reported in section 5.1, are shown here for the last slice of the volume, slice nine, see fig. 5.9. In particular, the distribution of $V_x$ values versus $y$ coordinates and of $V_y$ values versus $x$ coordinates are reported prior to the application of the method, see fig.5.10, and after the application of the method, see fig.5.11. By comparing these two figures it is possible to see the removal of the rigid body motion of the vessel.

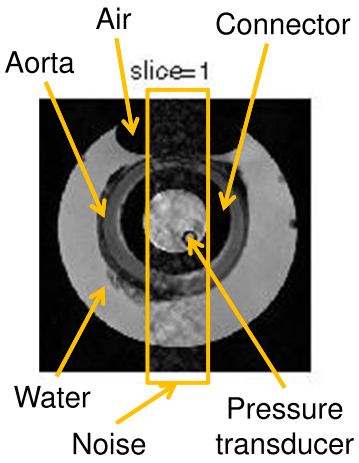


Figure 5.8: Components of the image in fig.5.6.A: apart from the connector, these components can also be found on the sub-figures of fig.5.6.

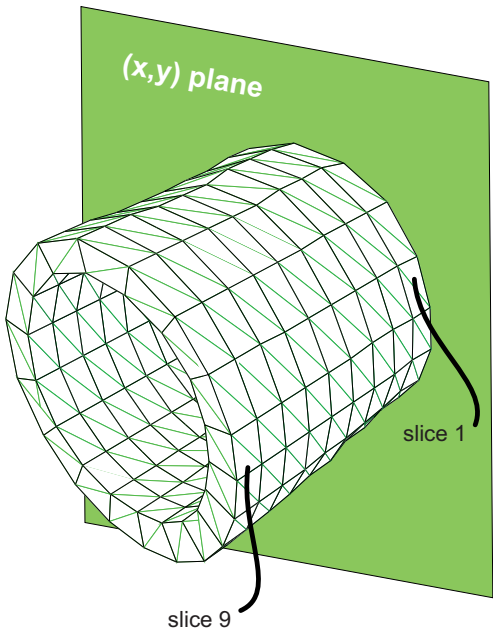


Figure 5.9: Organisation of the aortic volume.

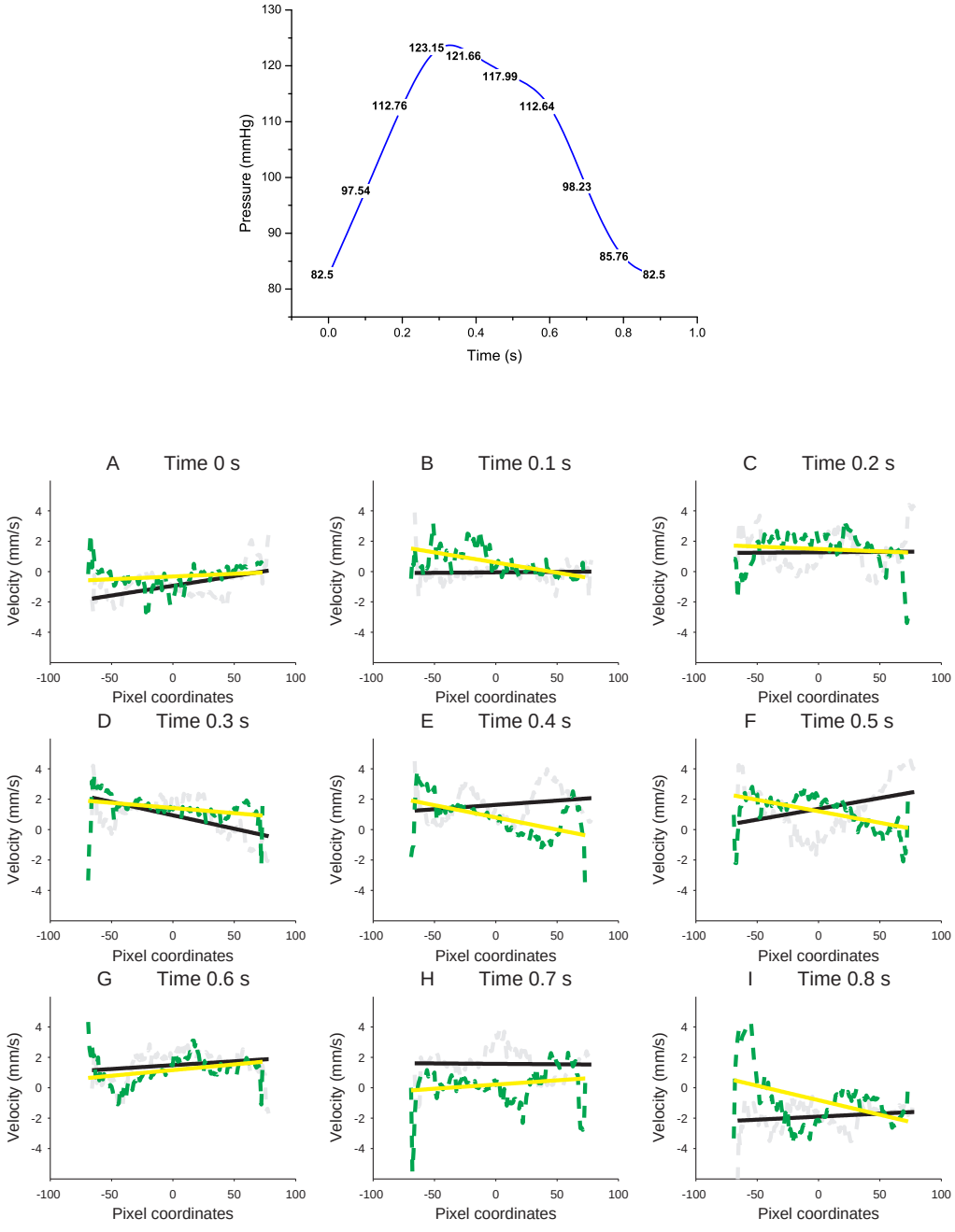


Figure 5.10: Effect of rigid body motion on the last slice for each time step; black and dark grey lines represent data in the $V_y$, $x$ distribution, green and yellow lines data in the $V_x$, $y$ distribution.

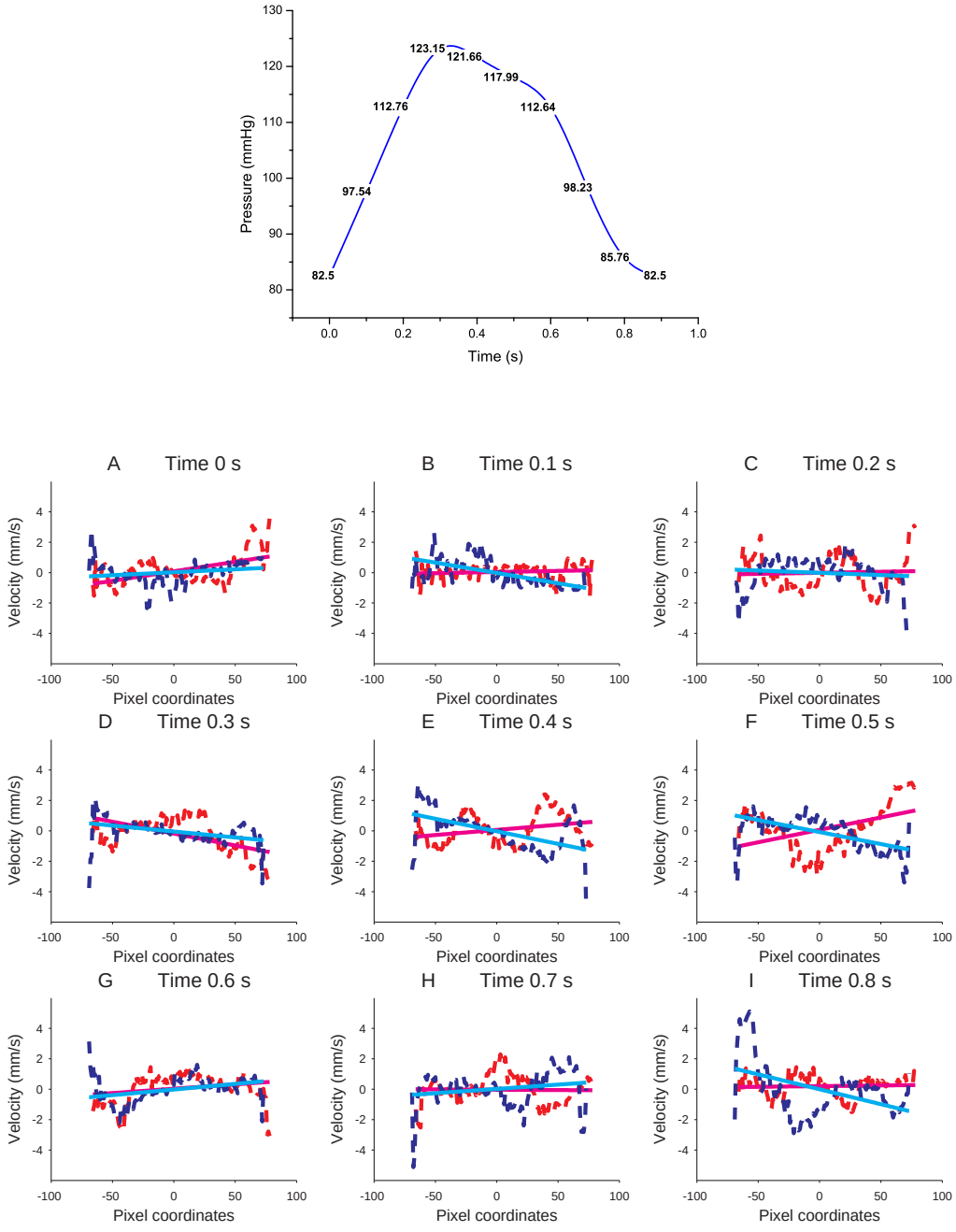


Figure 5.11: Correction of rigid body motion on the last slice for each time step; blue and cyan lines represent data in the $V_y$, $x$ distribution, red and magenta lines data in the $V_y$, $x$ distribution.

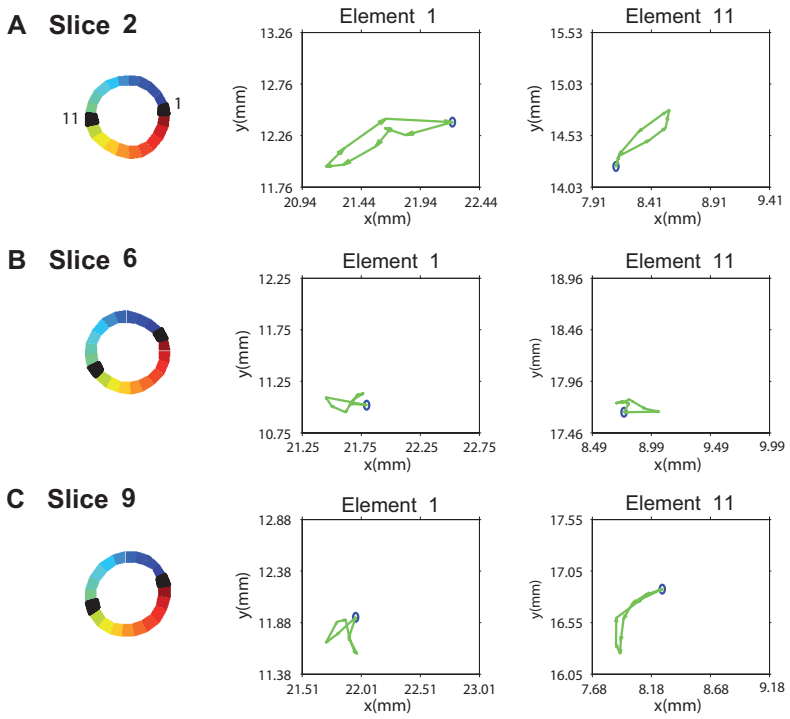


Figure 5.12: Cycle trajectories plotted for elements 1 and 11 (blackened) for slices 2, 6, and 9.

The result of the removal of rigid body motions is a set of directional matrices of velocity representing only the deformation velocity in the three coordinates. From these matrices, where the deformation velocity has been isolated it is possible to measure the aortic trajectories and then the circumferential strains. In order to obtain a distribution of strains comparable with the one resulting from a Finite Element simulation, the aortic volume was divided using the meshing parameters described in the previous section. The trajectories tracked for three sample slices 2, 6 and 9 and for four sample elements, taken every $\pi/2$, are shown in fig.5.12 and 5.13. From these figures it can be seen that the trajectories, although varying in path over the circumference of the aorta, always describe a closing loop due to the interpolation between the forward and the backward integration. On average, the trajectories were smallest for element 5, with an average path of 0.3 mm.

Finally, the circumferential strains over all the cycles are shown for the

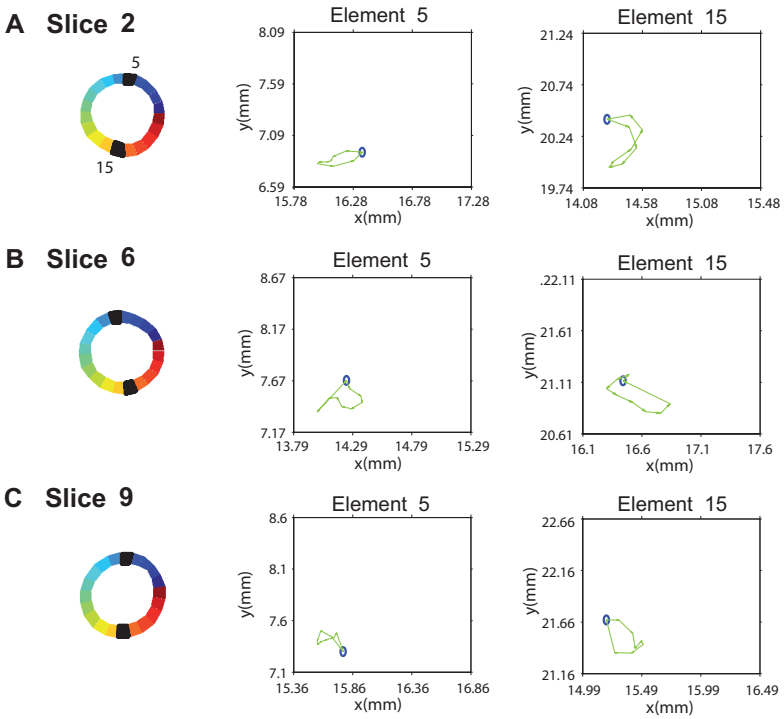


Figure 5.13: Cycle trajectories plotted for elements 5 and 15 (blackened) for slices 2, 6, and 9.

sample slices, 2, 6 and 9 in fig.5.14, 5.15, and 5.16. In these figures the circumferential strain magnitudes are plotted in each element and the strain vector representation is superimposed on the baricentre of each element. Again, by looking at these figures it can be seen that the strains are not uniform throughout the circumference. In particular, it can be noted that for slices 6 and 9 there is a marked reduction in strain for the final time steps.

As shown in fig.5.6 and 5.8, the first slices in the aortic volume are tied to the connector. The presence of this tie and of the connector made it impossible to decipher the behaviour of the first slices, subjected as they are to a variety of loads, including contact and shear. This made it necessary to consider only the last slice (slice 9) for the determination of the strain, given that for this one the end effect could be considered negligible.

The distribution of the circumferential strain for slice 9 is shown in fig.5.17, where the average of the strains over all the elements is plotted.

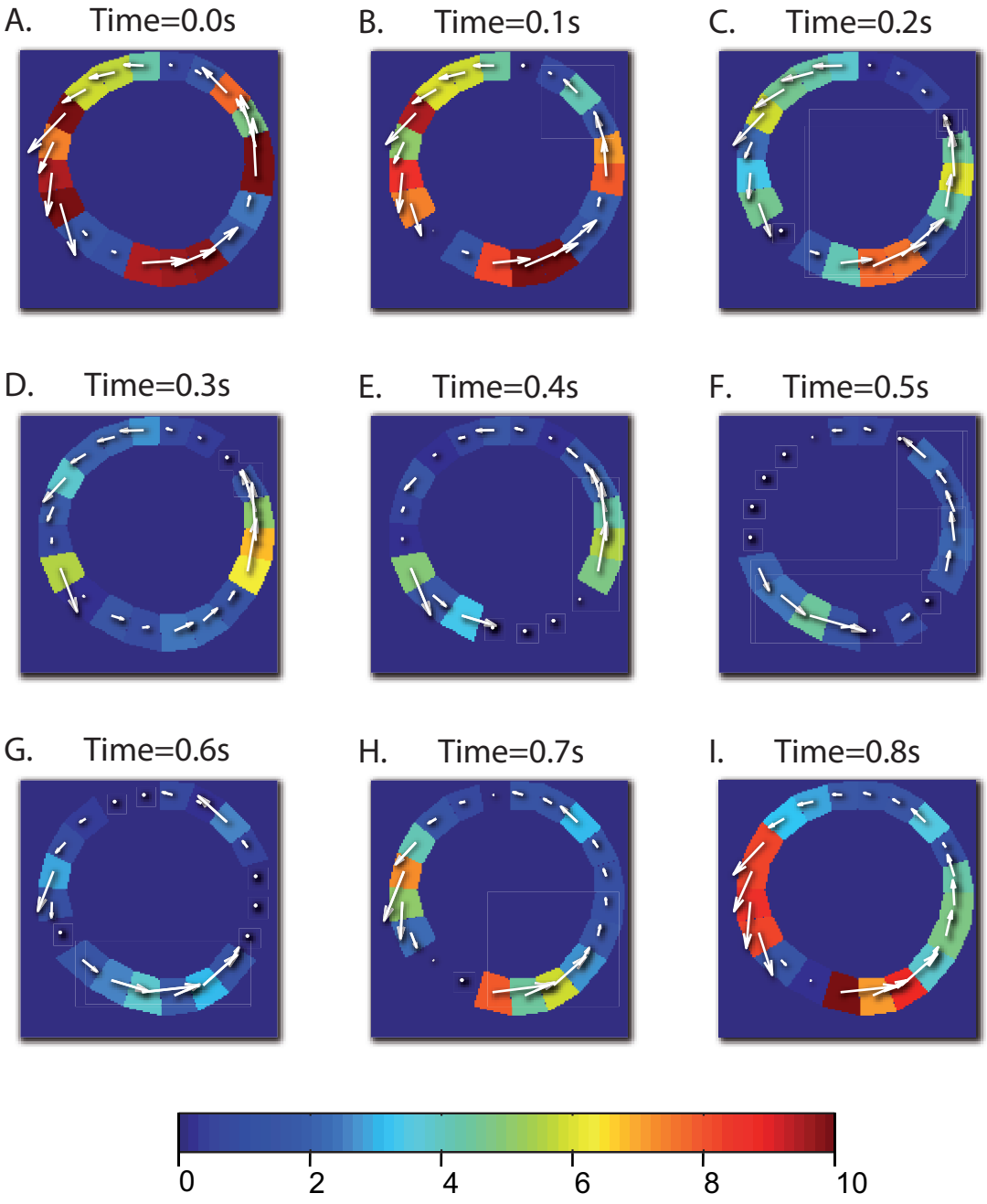


Figure 5.14: Circumferential strains recorded for the second slice over time: the colour map represents the magnitude, the arrows the direction.

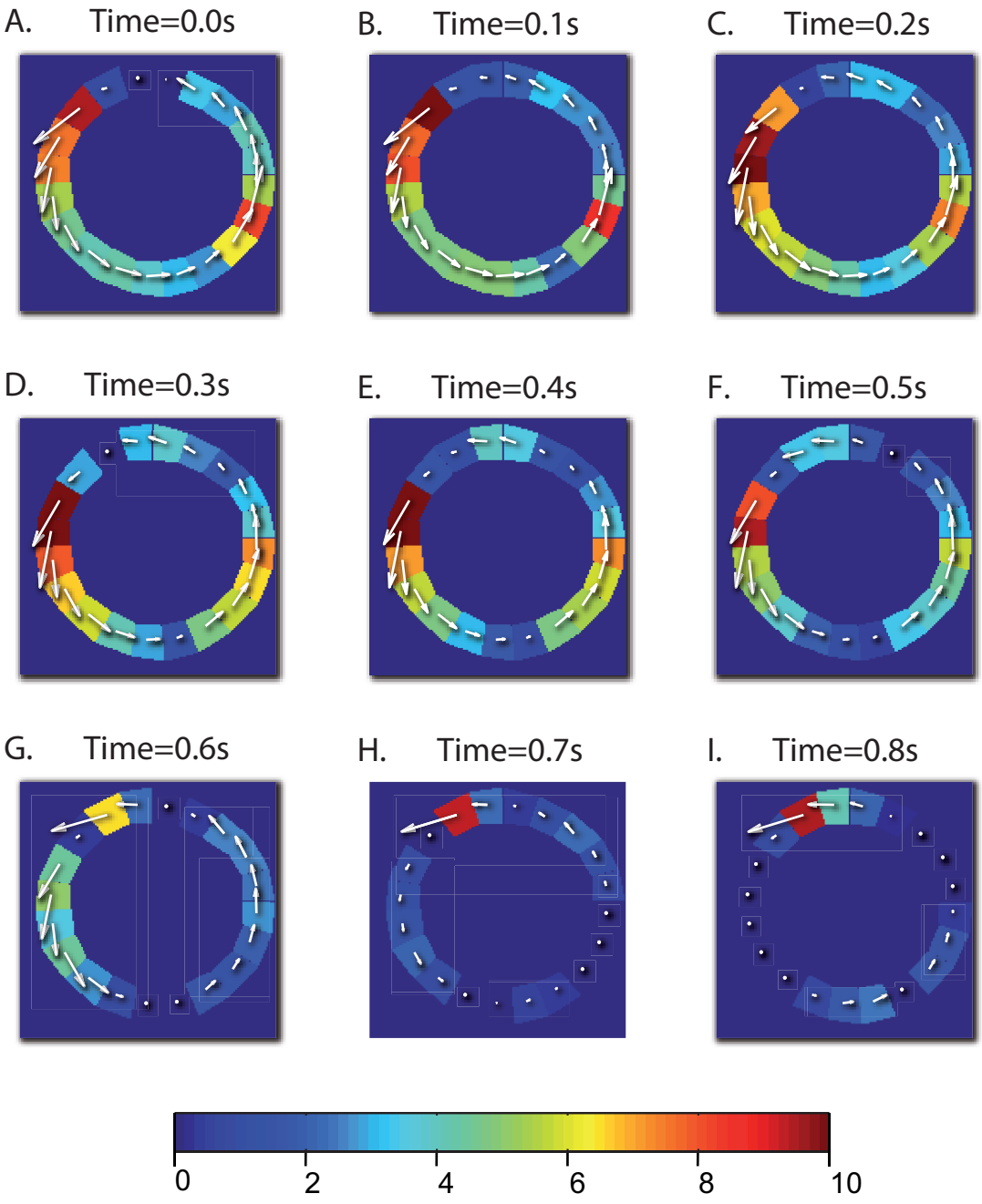


Figure 5.15: Circumferential strains recorded for the sixth slice over time: the colour map represents the magnitude, the arrows the direction.

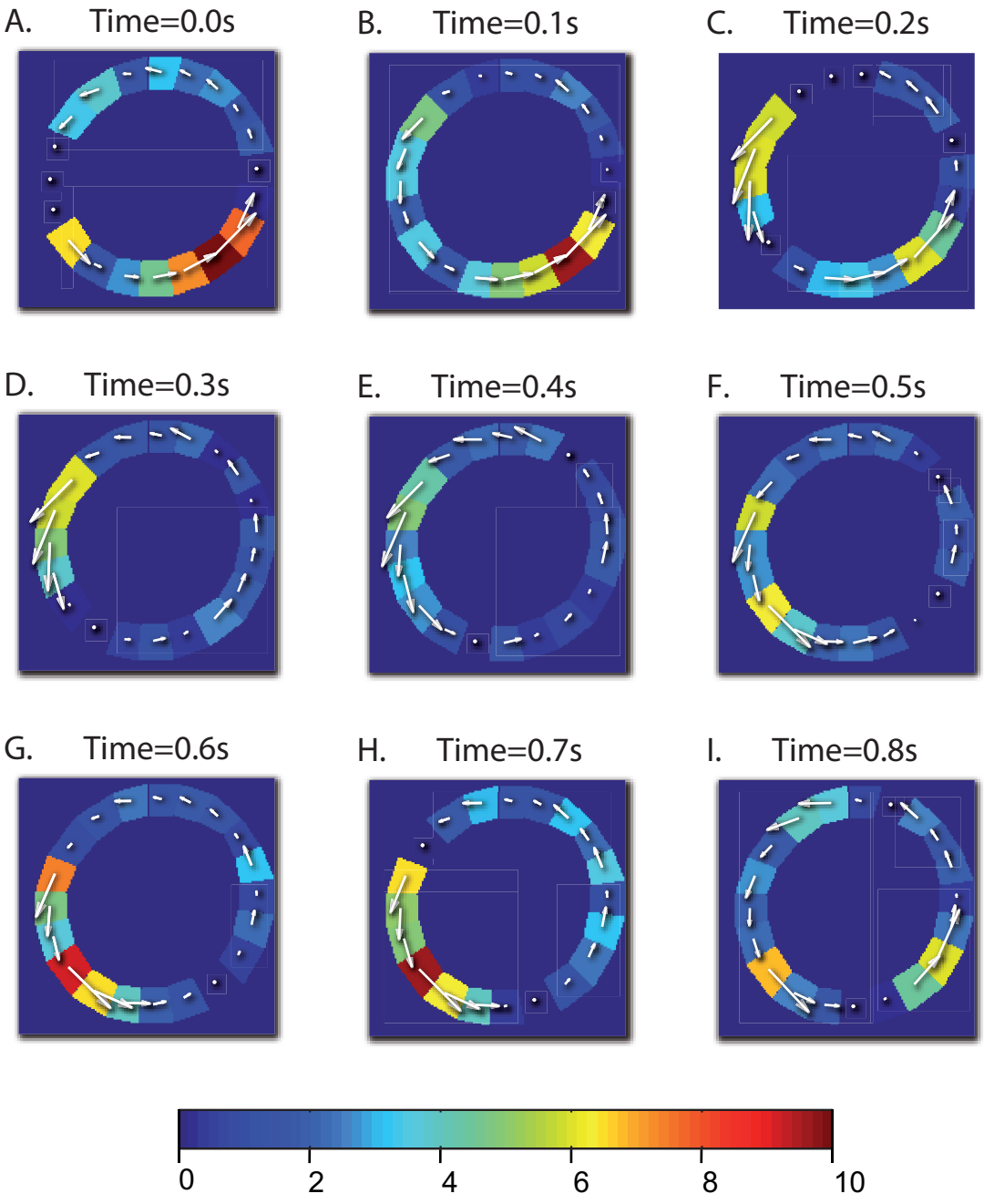


Figure 5.16: Circumferential strains recorded for the ninth slice over time: the colour map represents the magnitude, the arrows the direction.

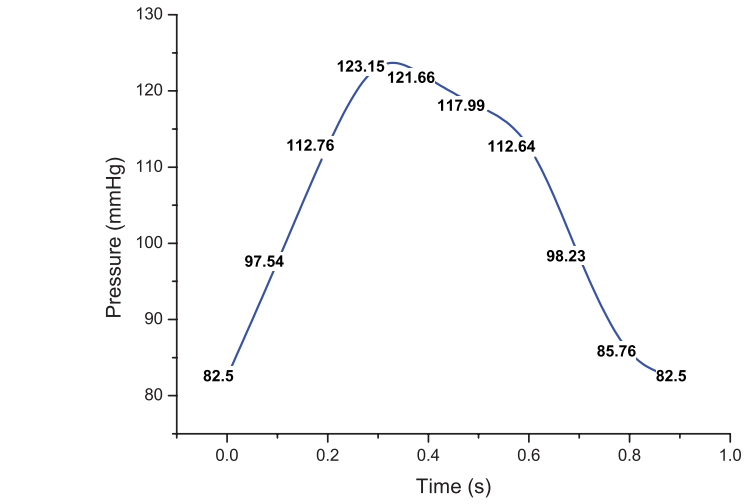


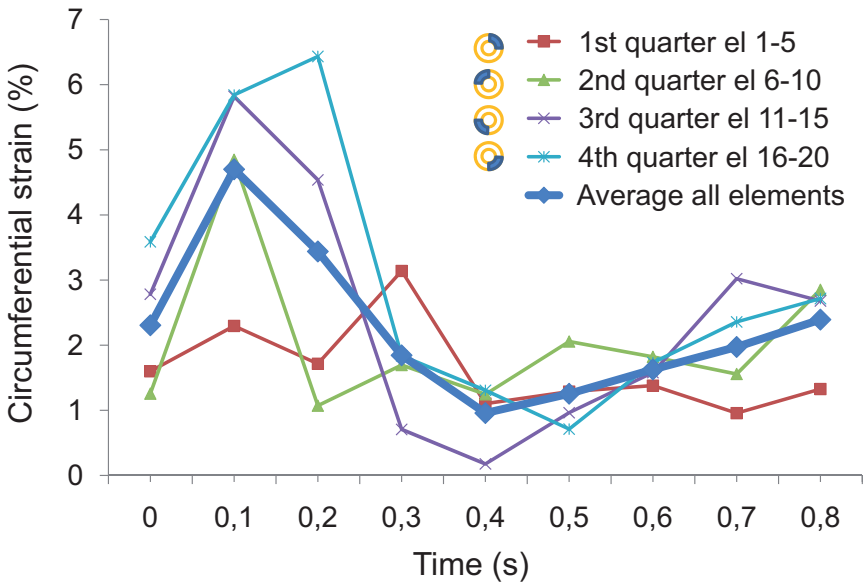


Figure 5.17: Plots of the circumferential strain for the ninth slice over time; the averages of each quarter of the aorta (5 elements) and over all the elements are also shown.

In order to account for the variability in strain observed across the circumference of the aorta, the averages of the circumferential strains over each quarter are also plotted. From fig.5.17, it is possible to see that the pattern of strain observed follows the pattern of the pulsatile waveform applied, increasing rapidly as the pressure rises and then decreasing.

## 5.3 Discussion

The noise in the central part of the images shown in fig.5.6 is representative of the difficulties encountered during the implementation of this technique. Since the PC MRI sequence was not available among the pre-loaded sequences in the Bruker Biospin 7T scanner, it had to be programmed manually, adding the pulse gradients required and reducing the noise created by the pulsatile flow with saturation slices. The saturation slices were particularly useful in reducing the noise, although not able to remove it completely. However, the noise did not affect the phase images as much as the magnitude ones: in the phase images shown in fig.5.7 the noise due to the incoming flow is reduced, although still present. The noise reduction achieved by the saturation slices on the phase images was considered satisfactory for the strain evaluation since it did not affect the aortic wall (see central part of the images) and therefore allowed the analysis of the aortic volume. It has to be noted that the effect of the noise on the phase images rather than magnitude images was important, because in this study only the phase images were used for the evaluation of the strain, while the magnitude images were used for the manual definition of the ROI.

Once the reference image was subtracted from the phase images in the three directions $x$, $y$ and $z$, the velocity of the tissue was evaluated using eq.2.26 [108]. The velocity maps thus obtained needed to be further manipulated in order to extract the deformation velocity. This manipulation consisted of the removal of rigid body translations and rotations. The effectiveness of this method in correcting for rigid body motions is shown by

the comparison of fig.5.10 with fig.5.11. The first figure shows the velocity profile obtained for the last slice (dashed line) and the its linear interpolation (solid line). The second figure shows the same profiles after the application of the correction method. It can be seen that the linear interpolations in the second figure are centered in (0,0) and that their slope is diminished. This showed that the rigid body motion removal was successful, since a reduction in the linear interpolation offset corresponds to the removal of the rigid translation while a reduction in the linear interpolation slope corresponds to the removal of the rigid rotations. This rigid body motion correction was vitally important in this study since the aorta was suspended in the water and the reflection of the pulsatile pressure waveform in the surrounding water caused an increase in the rigid body motion of the tissue. An example of the increase in aortic motion induced by the agitation of surrounding water can be seen in fig.5.10.E-F. In fact, by comparing these figures with the others it is possible to see that the velocities in the aorta are less uniformly distributed and that the rigid body motion algorithm is less efficient in reducing the slope of their linear interpolation, see fig.5.11.E-F. This effect is explained by taking into consideration the flow induced by the pulsatile flow in the aorta. In fact, fig.5.18.A shows that the flow increases with the pressure, but before the pressure reaches its maximum, the flow starts decreasing and creating effects of back-flow into the vessel. By taking into consideration the time steps corresponding to fig.5.11.E-F and the flow pattern shown in fig.5.18, it is possible to determine that for these time steps the flow is decreasing and instability is experienced by the aorta. The presence of water surrounding the vessel and reflecting the flow of the aorta amplifies the effect of this decrease in flow, thus reducing the effectiveness of the rigid body motion removal method. Although less distinct, evidence of the effects of a change in the flow on aortic velocity profile is shown also by fig.5.10.I -5.11.I. In this case, since the change in flow direction happens when the flow is minimal, at the end of the cycle, the removal of the rigid body motion is successful.

As shown in the study by Draney *et al.* [122], the removal of rigid body motion correction is far more successful in *in vivo* PC MRI since the aorta is constrained by the spine and the ligaments, and is surrounded by neigh-

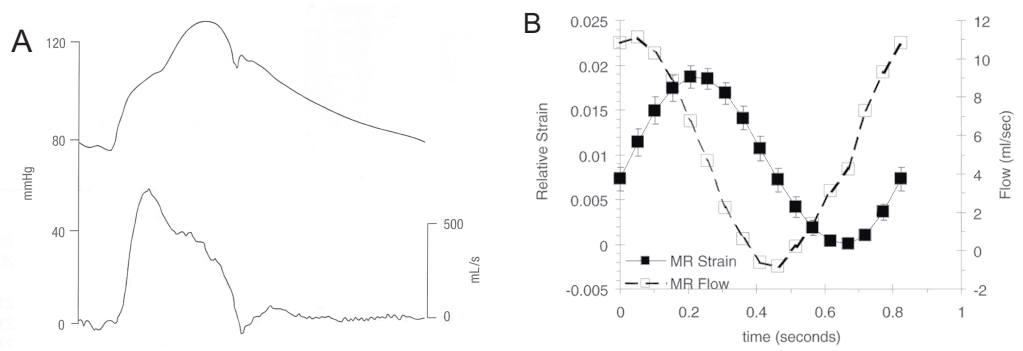


Figure 5.18: Relationship between pressure, flow and circumferential strain: A) pressure ad flow in the abdominal aorta, from [143], where it is shown that pressure increases although flow is decreasing; aortic flow compared to the strains measured by Wedding *et al.*, both flow and strains are measured through MRI, but in two separate acquisitions [120].

bouring internal organs, as opposed to being suspended in water. Therefore, the *in vivo* deformation velocity recorded with this technique will not suffer from a reduction in accuracy for the reverse flow phase of the heartbeat.

Another important consideration that can be drawn from fig.5.10 and 5.11 regards the distribution of the velocities. In fact, from the dashed line plots it can be seen that the amplitude of the deformation velocity is consistent throughout the slice, with some transition effects at the extremities, i.e. at the transition with water. The presence of transition effects at the extremities is caused by the manual tracking of the ROI, which might have led to the inclusion of water pixels. Since the water around and inside the aorta is moving faster and in different directions, noise can be generated in the magnitude images, see fig.5.6, but it is expected that the velocity of such pixels would be different in amplitude from the velocities measured within the aorta.

**Circumferential strain** Once the deformation velocity was isolated, trajectories were tracked using the algorithms proposed in [109, 120–122], and from the trajectories the circumferential strains were evaluated, using eq.2.30. The trajectories found for the different elements into which the aortic vol-

ume was segmented are plotted in fig.5.12 and 5.13. The plots show that these trajectories are consistent, describing paths with an average length of 1.2±0.25 mm. Moreover, these trajectories change across the different slices, as expected, with the first slice constrained and the immediate following ones subjected to the effect of such constraint. The end effect could be considered negligible for the last slice given that it is 1.35 cm distant from the constrained first slice and the radius of the aorta being on average 0.6 cm. Therefore this was the slice where the aortic circumferential strains were measured. The trajectories tracked for the last slice resulted in larger magnitudes than those tracked for the other slices reflecting the different loading condition. Moreover, the trajectories tracked in fig.5.12 and 5.13 for the last slice show a similar path to the paths reported in [120, 122] for the aortic wall.

Lastly, the circumferential strains were measured for the whole volume, although only the strains measured for the last slice were considered representative of the pressure loading on the aortic wall. The method for measurement of strain proposed by [109, 120] and used in this study, uses the radial trajectories in order to define the circumferential strains, see eq.2.30. Since the trajectories tracked describe a motion consistent with that anticipated based on theory and on literature [120, 122], the method proposed by [109, 120] can be used to define the cyclic strains of the porcine aorta in the present study. The measured strains are presented in fig.5.14–5.16 for different slices in the aortic volume. From these maps a precise distribution of the circumferential strains across the aortic volume can be determined and observed, where the sides of the aorta deform more than the top and the bottom. This difference could depend on structural factors: for example the branches of the aorta could be responsible for this variation due to turbulence effects originating at the branches. Another cause of this effect of squeezing of the aorta could be the presence of air bubbles on the top of the aorta, see fig.5.8. Since each element, and the corresponding vector, represents the average response of all the pixels in the area, a sudden change in the magnitude of the strain vector or in the colour of the element could depend on local changes in the distribution of the strains, see fig. 5.14–5.16.

Finally, to evaluate the validity of the profile and the level of strain measured, the strains were compared with aortic strains measured with the same technique reported in literature. From fig.5.17 it can be seen that the circumferential strain profiles in accordance with that reported in literature: the sharp peak of circumferential strains and their subsequent decrease conforms with the observation that the circumferential strains follow the flow profile, see fig.5.18.B, due to the fact that the flow is known to start decreasing while the pulsatile pressure is still increasing, see fig.5.18.A [143]. Moreover, the same behaviour is reported in [120] for both the abdominal and the thoracic aorta.

The level of strains measured by averaging all the elements in the last slice were in the same range as those reported by [109, 120–122] for the porcine aorta, for loadings that were different in shape but always in the physiological range, see fig.5.17. Moreover, the circumferential strains measured agree with those reported by Morrison *et al.* for human aorta in a recent study [144] where the circumferential strains were measured *in vivo* using a CT scan. In particular, by comparing the strains recorded *in vivo* for the human aorta by Wedding *et al.* [120] with the strains measured in this study, fig.5.19, it can be seen that a similar distribution of strains is reported. In fact, in [120], average strains in the aorta are measured between 1-4%, and maximal strains between 4-8%, and fig.5.19 shows that both the average and the maximal strains measured in the current study fall in the same ranges. This validates the strains measured with PC MRI and justifies their use in the following section as a comparison for the strains resulting from the numerical simulation. However, because the reduction in the effectiveness of the rigid body motion removal method for the time steps corresponding to fig.5.11.E-F reduces the accuracy of the strain measurement in the same time step, the strains corresponding to the loading part of the pressure curve can be considered most accurate. Therefore, only the loading of the first four time steps will used for comparison with the numerical model in the following chapter.

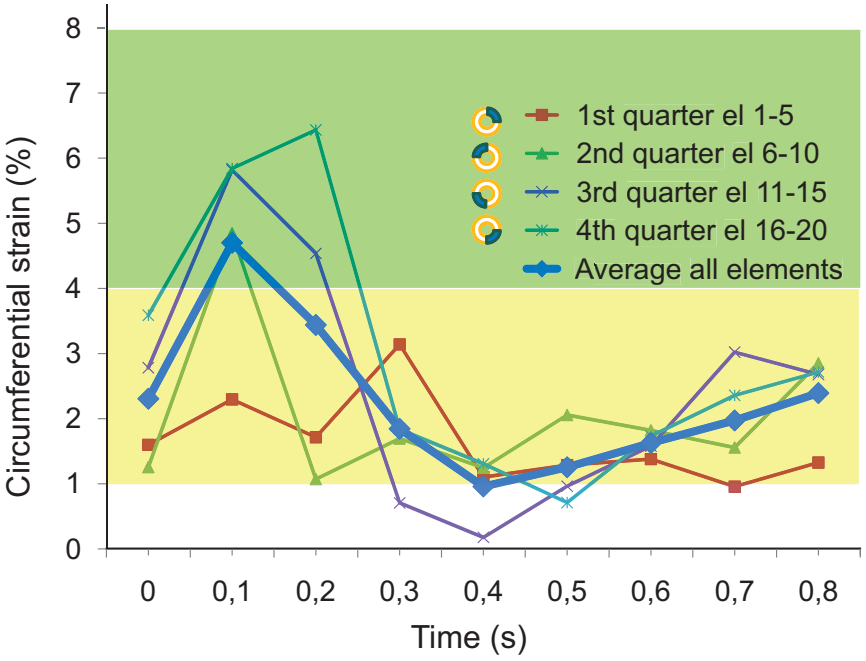


Figure 5.19: Comparison of the strains recorded with the results available from literature [120]: The yellow box shows that the strains recorded fall into the average strain range measured in literature (1-4%), while the green box shows that the maxima fall in the range reported for the maximal strains (4-8%).

### 5.3.1 Limitations

Although the application of PC MRI on just one aortic sample usually can be considered quite limiting, it must be considered that aortic PC MRI is an established technique [109, 120–122], which in this study is applied to nine slices in the aortic volume. The results for these nine slices are consistent and provide a strain pattern that confirms the findings presented in [109,120–122]. In the future, the application of this technique to more samples will give a greater insight into the behaviour of the tissue and into the possibility of using this technique *in vivo* on human patients.

The current study was carried out on a high field experimental scanner for animal studies in order to maximise the resolution of the images. While the use of an experimental scanner was an advantage for the most part, at

the same time it was also the most significant limiting factor in the present PC MRI analysis. In fact, this scanner lacked a PC MRI sequence pre-loaded into the MRI processor and therefore it was not possible to correct all the noise due to the pulsatile flow. These sequences are normally available on human studies MRI scanners [108,109,120–122], and hence this does not pose limitations to the future development of the technique.

Finally, the positioning of the aorta in the scanner was affected by the noise created by the flow of water. In fact, given that water has a higher content of free hydrogen protons than the aorta, the continuous flow of protons caused instability in the signal measured from the scanner that could be reduced only by scanning the aorta at the inflow, where the presence of the connector decreased the effect of the noise. This presented a limitation for the study of the aorta since the measured portion coincided with the constrained part of the aorta, and allowed the determination of the aortic circumferential strains only for the last slice in the volume. However, this limitation does not affect the use of PC MRI for *in vivo* human studies, and hence its future development, since *in vivo* aorta is surrounded by neighbouring organs and by the spine, tissue where the contents of hydrogen protons is comparable to that of the aorta.

### 5.3.2 Conclusions

This chapter demonstrates how, notwithstanding some limitations due to the flow induced noise, PC MRI is able to track the circumferential strains in aortic tissue. The possibility of tracking these strains *in vivo*, as in the work of Morrison *et al.* [144], offers great opportunities for the study of cardiovascular diseases. In particular the advantage of this technique over a CT based one, like the one presented in [144], is that it can be performed together with DTI thus producing a complete mechanical analysis (static and dynamic) with minimum discomfort for the patient.

Coupling DTI and PC MRI opens new opportunities in biomechanical and diagnostic analysis of aortas *in vivo* that will be thoroughly investigated in the next chapter.

# Chapter 6

# Non-invasive Prediction of Aortic Constitutive Behaviour

In this chapter all the findings of the previous chapters will be brought together in order to derive a characterization of the mechanical behaviour of porcine aortas in a non invasive way. This characterization will be the result of three steps: inputting the structural parameters obtained from DTI in ch.4 into the constitutive model defined in ch.3, generating a Finite Element (FE) simulation over the volume of the aorta and modifying iteratively the material parameters until the circumferential strains resulting from the FE simulation are comparable to the ones obtained experimentally from PC MRI in ch.5.

The results of this chapter show that the procedure described in this thesis is successful in determining the characterization of the mechanical behaviour of the porcine aorta since it allows for the evaluation of material constants that can reproduce the behaviour of the tissue in a physiological loading condition. In addition, this characterization is non-invasive, with the structural parameters and the strains being obtained without harvesting the tissue. Finally, by comparing the strains resulting from the iterative procedure with the *in vivo* strains available from literature, it can be seen that this characterization is robust and has the potential to be developed for the *in vivo* characterization of the mechanical behaviour of human aortas.

## 6.1 Methods

### 6.1.1 Evaluation of DTI derived material parameters

In order to create a numerical simulation of the tissue behaviour, the constants to be input into the constitutive model had to be chosen. The structural constants $\gamma$ and $\kappa$ were both obtained non-invasively, as a result of the DTI analyses described in ch.4. These two new structural parameters were input into the Levenberg-Marquardt non-linear regression routine, described in ch. 3, to fit the uniaxial tensile test data reported in the same chapter. The new set of material parameters $c$, $k_1$ and $k_2$, was then used for the definition of the FE model properties.

### 6.1.2 Finite Element Analysis

The constitutive model was implemented in a commercial finite element software environment, ABAQUS®. Both the constants used and the geometry were defined on the basis of the precedent steps: the constants were defined as a results of the DTI analyses, while the geometry was either defined by measurements taken from uniaxial tensile tests or by the definition of the imaged volume. Finite element analyses were used first for the simulation of the uniaxial tensile tests, in order to verify the fit to the material model implemented, and then for the analysis of the loaded aorta, in order to validate the model through the PC MRI results.

**Uniaxial Tensile Test Simulation** To perform the mutual validation between numerical and experimental tests, a finite element model was created representing an eighth of the geometry of a uniaxial test on an aortic sample. The dimensions for the sample were taken from the dog-bone samples used in the experimental uniaxial tensile tests and a brick eighth model was created with symmetry constraints on the $x$, $y$, and $z$ plane. The sample was loaded with a nodal force on the top surface where all the top nodes were constrained

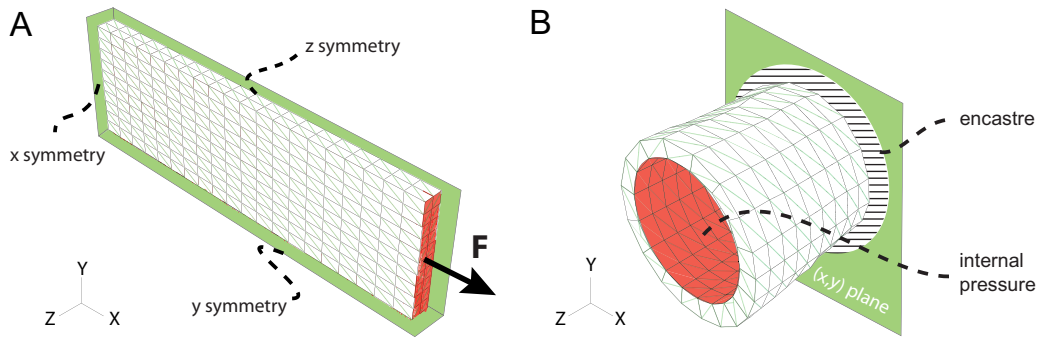


Figure 6.1: Finite element models: loads and boundary conditions. A) uniaxial tensile test; B) aortic geometry.

in order to move together, as described in [53], see fig.6.1. Two separate simulations were performed, one in the axial direction, i.e. with $\gamma$ equal to the value found from DTI studies; and one in the circumferential direction, i.e. with $\gamma$ rotated of $90^o$. The resulting orientations of the model can be seen in fig.6.2, where the red arrows are oriented according to $\gamma$.

**Loaded Aorta Simulation** The aortic model was created from the mesh obtained from PC MRI images. As outlined in section 5.1(page 102) the mesh was created using the ROIs of the aortic volume for the first time step. The boundaries of the aorta were manually tracked and then imported into a custom MATLAB® routine that created nodes across the circumference and in the thickness according to the numbers defined by the user. Examples of two meshes obtained with different parameters are given in figure 6.3. The ROIs obtained from PC MRI were spaced axially according to the MRI interslice resolution, reported in table, 5.1 (page 100), see also fig.6.4.A,. This axial spacing needed refinement for FE meshing and therefore the same MATLAB® routine created axial divisions of the volume by interpolating the $x$-$y$ values between two adjacent slices. Finally, the custom routine grouped all the nodal coordinates and the element connectivities and wrote them into a input file that could be imported into ABAQUS®. The mesh was

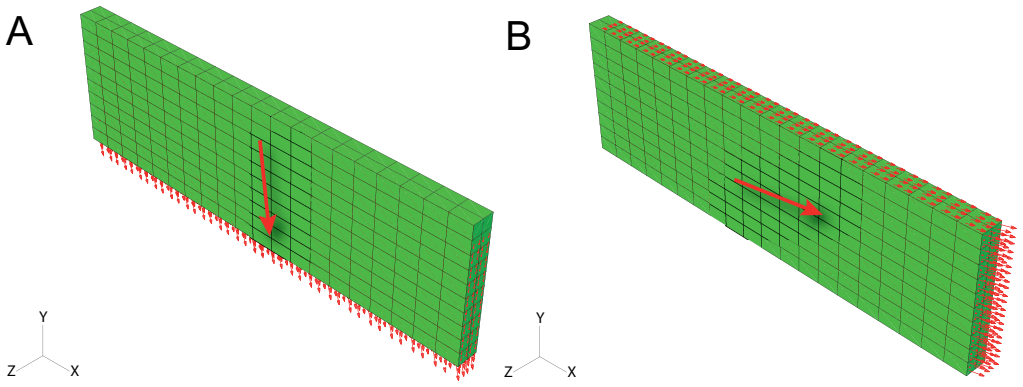


Figure 6.2: Mesh used in the uniaxial tensile test and fibre orientations: A) test in the axial direction; B) test in the circumferential direction.

made up of hexahedral elements with hybrid formulation, the global number of elements dictated by the MATLAB® routine, and is shown in fig.6.4 and fig.6.5. The aortic model was completely constrained on the first slice in order to simulate the constraint the cable tie exerted on the aorta in the MRI setup. The internal area was then loaded with a uniform pressure, changing over four time steps. In fact, due to the limitations in the strain measurement reported for the time steps of fig.5.11.E-F, only the strains resulting from the loading part of the pressure cycle could be compared. This allowed for the creation of a quasi-static model, where the effects of the changing flow could be neglected and pressure could be assumed as the only load applied to the aortic wall. The pressure values applied were the same as those recorded for the equivalent PC MRI time steps, see fig.5.2 time steps between 0 s and 0.4 s (page 98). The material constants used were those defined from DTI. The simulation ran on multiple CPUs and took less than 50 s. The resulting circumferential strains were evaluated in ABAQUS® and exported into Microsoft Office Excel® for further analysis. The mesh convergence was evaluated by increasing the number of elements from 180 to 64,000. From table 6.1 it can be seen that for a mesh density greater than 3,240 elements, there are no significant differences in the results obtained. Consequently, the mesh used for the analysis is the one with 3,240 elements, that is represented

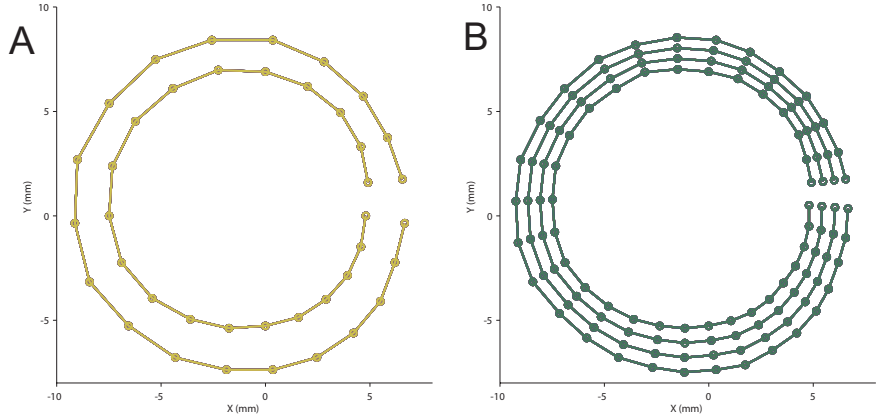


Figure 6.3: Line mesh for the ninth slice in the volume, bullets represent the nodes: A) mesh n.1= 20 elements in the circumference, one element in the thickness; B) mesh n.2= 30 elements in the circumference, 3 elements across the thickness of the aorta.

in fig.6.4.B and 6.5.B.

### 6.1.3 Constitutive Model Validation

The global aim of this work was the comparison of the MRI measured circumferential strains with those obtained from a finite element simulation in order to define an aortic constitutive model through non-invasive techniques. In order to reach this aim, the results of the loaded aorta simulation were

| | Mesh elements | | | |
|---|---|---|---|---|
| | 180 | 3,240 | 26,460 | 61,479 |
| average number of pixels per element | 365±44.5 | **81±9.8** | 17±2.1 | 7±1 |
| max strain (%) | 8.63 | **8.66** | 8.67 | 8.69 |
| min strain(%) | 5.5 | **5.52** | 5.53 | 5.54 |
| average strain(%) | 7.27 | **7.29** | 7.3 | 7.32 |

Table 6.1: Mesh convergence study.

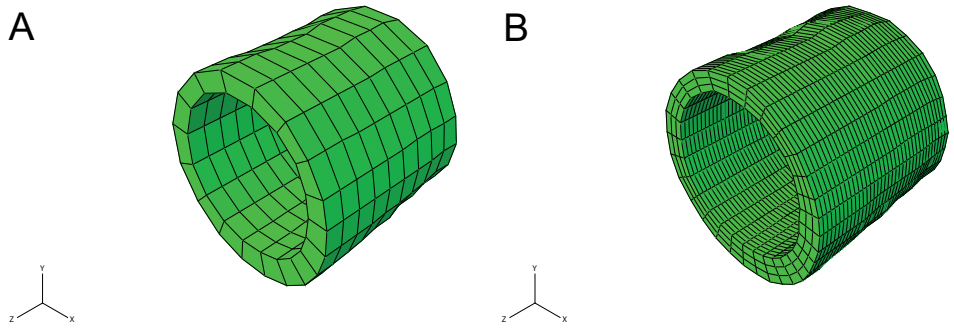


Figure 6.4: Final ABAQUS® 3D mesh obtained for the meshes of fig.6.3: A) mesh n.1 with no axial divisions; B) mesh n.2 with 3 axial divisions.

compared with those recorded from PC MRI and the simulation parameters iteratively changed until there was a good match between the two, i.e. until they fell in the same range. From the work of Wedding *et al.* [120] and from fig.5.17 and 5.19, it can be seen that, although there is variability among the strains that can be recorded in the aorta, average circumferential strains in the aorta are measured between 1-4% [120]. Therefore, to define a set of non-invasively determined material parameters able to simulate the circumferential strains measured *in vivo* for the physiological pressure range, the strains resulting from the FE model must be in the range of the strains recorded by PC MRI, and in particular, their average should be equal to the value of 3.5% that is the average of the strains recorded by PC MRI for the loading phase of the aorta.

Given that the structural parameters $\gamma$ and $\kappa$ represented an intrinsic property of the tissue, only the material parameters $c$, $k_1$, and $k_2$ were modified to reach a match between FE and PC MRI strains. These changes were performed by an iterative custom MATLAB® routine that changed $c$, $k_1$, and $k_2$ recursively until a match was found. To measure the circumferential strains an ABAQUS® simulation started automatically for every change in the parameters, and the average of the strains was compared with the value obtained from PC MRI. The elements considered for comparison between the strains were the elements corresponding to the last slice of the PC MRI

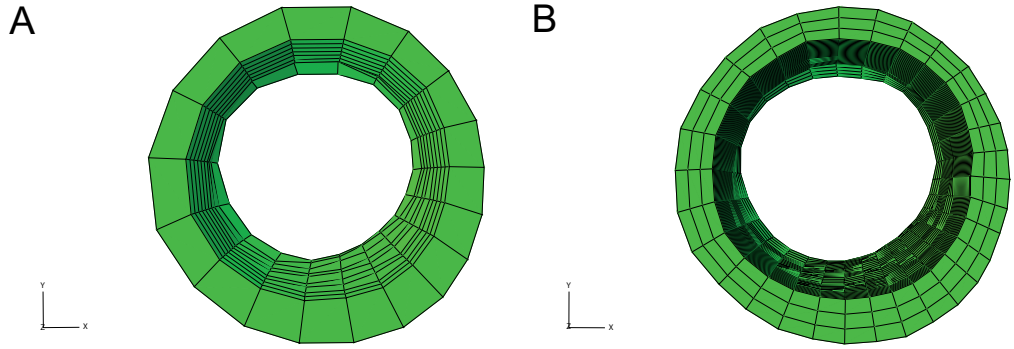


Figure 6.5: Final ABAQUS® 3D mesh obtained for the meshes of fig.6.3, front view: A) mesh n.1 with no axial divisions; B) mesh n.2 with 3 axial divisions.

sample, i.e. the volume defined by the elements in the unconstrained end of the model.

Prior to the determination of the optimal parameters, rules had to be drawn from the way a change in the parameters affected the resulting strains. Initial considerations on the effects of a change in $c$, $k_1$, and $k_2$ were drawn from fig.3.9 (page 50) in ch.3. Since a change in $k_2$ had little impact on the curves, only changes in the parameters $c$ and $k_1$ were considered for the assessment of the optimal parameters. In particular, to study the effect a change in the value of $c$ and $k_1$ had on the strains predicted by FE simulations small changes in $c$ (90% and 150%) and in $k_1$ (85% - 115%) were considered. The ranges of these changes were determined by previous tests (data not shown) that showed that a small change in $k_1$ was sufficient to cause a significant influence on the final strains while $c$ needed a much larger increase and did not converge if reduced by more than 10%.

## 6.2 Results

### 6.2.1 Evaluation of DTI derived structural parameters

Inputting the non-invasively determined values of $\gamma$ and $\kappa$ into the Levenberg-Marquardt routine described on page 39 produced a new fit to the uniaxial tensile data, as shown on fig.6.6. This new constitutive model fit, obtained using DTI data, has a different shape compared to the fit obtained using the literature data reported on table 3.1 (page 44). In fact, from fig.6.6 it can be seen how a change in the DTI constants, and in particular a change in $\kappa$, strengthened the difference between the axial and the circumferential curve by making the stiffening in the circumferential direction and the softening in the axial direction more distinct. In addition, the difference between the fit for DTI and that for literature is highlighted in table 6.2, where it can be seen that the value of $c$ increased by an order of magnitude, and the value of $k_1$ decreased by two orders of magnitude, while $k_2$ showed a smaller decrease.

### 6.2.2 Finite Element Analysis

**Uniaxial Tensile Test Simulation** The FE results for uniaxial tensile test simulations, shown in fig.6.7, demonstrate the effect of the fibres on the

| | Literature, ch. 3 | DTI model |
|---|---|---|
| $\gamma$ | 10° | 15° |
| $\kappa$ | 0.326 | 0.110 |
| $c$ | **34.6 kPa** | **131.575kPa** |
| $k_1$ | **1.2 Mpa** | **12.4kPa** |
| $k_2$ | 4.2 | 1.67 |

Table 6.2: Comparison between the DTI derived parameters and the parameters obtained in ch.3 based on data from literature. In bold are highlighted the changes in $c$ and in $k_1$.

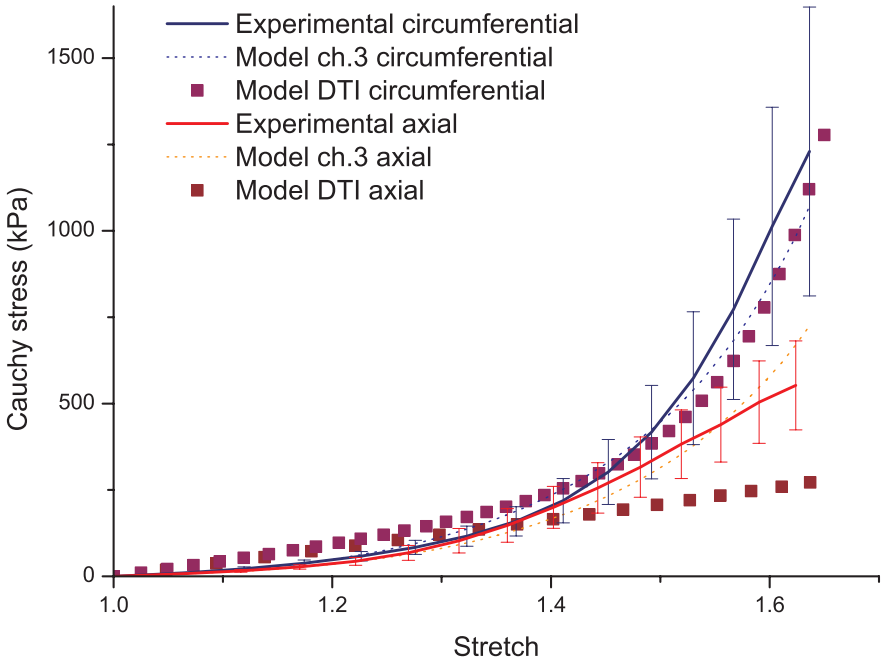


Figure 6.6: Comparison between the constitutive model fit obtained with the constants defined in ch.3 and with the constants determined non-invasively through DTI.

strains. In fact, it can be seen how the axial test deforms more than the circumferential one. Moreover, the stress-strain curves obtained from FE data show good agreement with both the tensile tests and the constitutive model fit resulting from the Levenberg-Marquardt interpolation, see fig.6.8.

**Loaded Aorta Simulation** The results for the loaded aortic geometry show a non-uniform strain distribution that reflects the irregular geometry of the aorta, see fig.6.9. As anticipated, the strain distribution at the constrained end of the aorta is different from the remaining volume.

### 6.2.3 Constitutive Model Validation

By comparing the strains obtained from the FE simulation with those obtained from the PC MRI it is possible to see that the FE strains are far

from those recorded from PC MRI, see fig.6.10. Consequently, the material parameters $c$ and $k_1$ needed to be changed until the strains fell in the appropriate range. The rules for changing the parameters, as mentioned in section 6.1.3 where defined by looking at the effects of changes in the parameters. In particular, by looking at fig. 6.11 and 6.12 it can be seen that an increase in $c$ moved the strain curve downwards while a change in $k_1$ changed the slope in the curve. The optimal parameters were then found by increasing $c$ and decreasing $k_1$. The iterative procedure resulted in the constants reported in table 6.3 and in the strain plotted in fig.6.13. In this figure it can be seen that the strain resulting from the FE simulation is in the range of the PC MRI strains and of the strains reported in literature [120]. The relevant measures of strains, such as minimum strain, average and maximum, are reported in table 6.4.

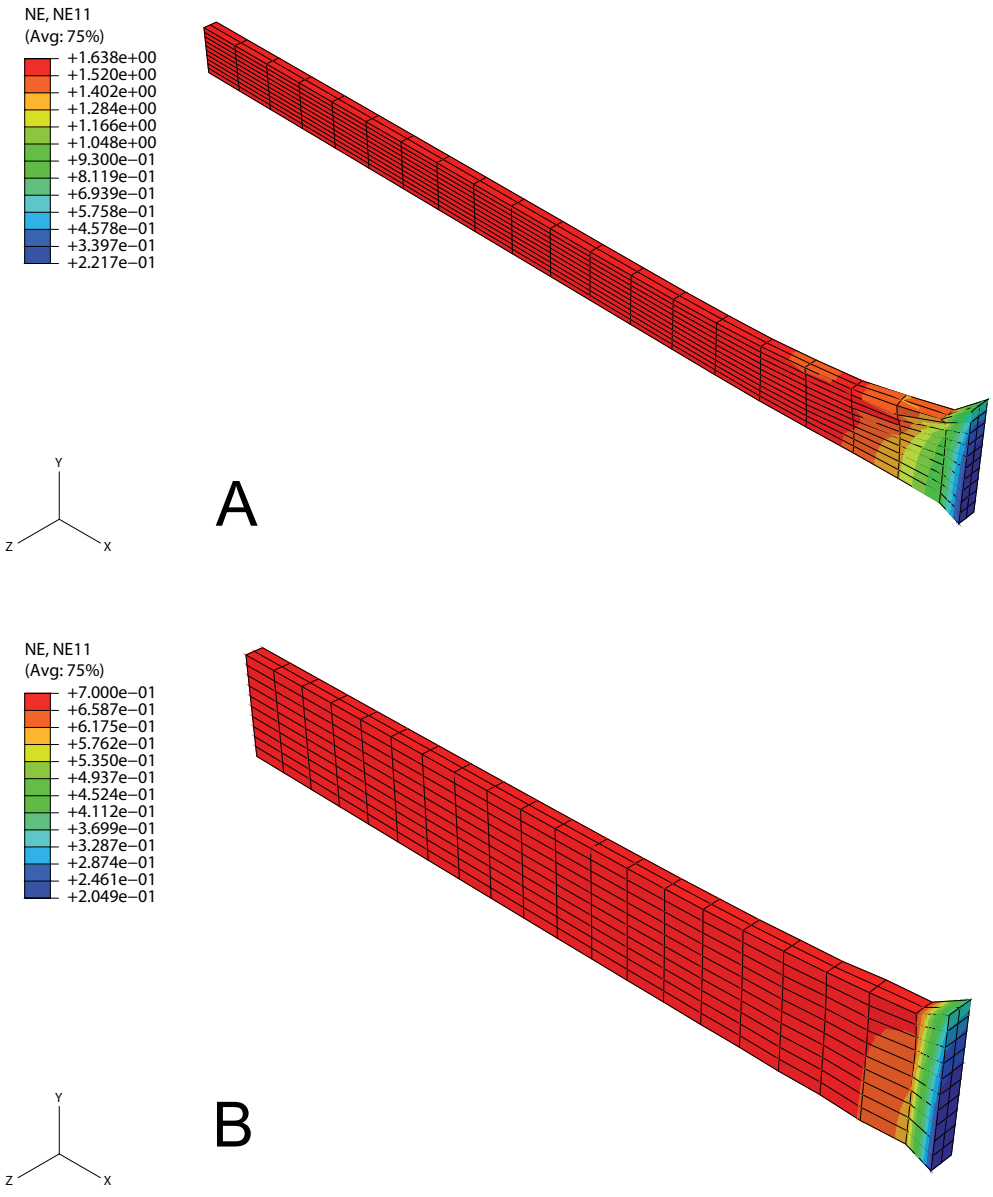


Figure 6.7: Strains in the direction of the load for the uniaxial tensile test: A) axial direction; B) circumferential direction.

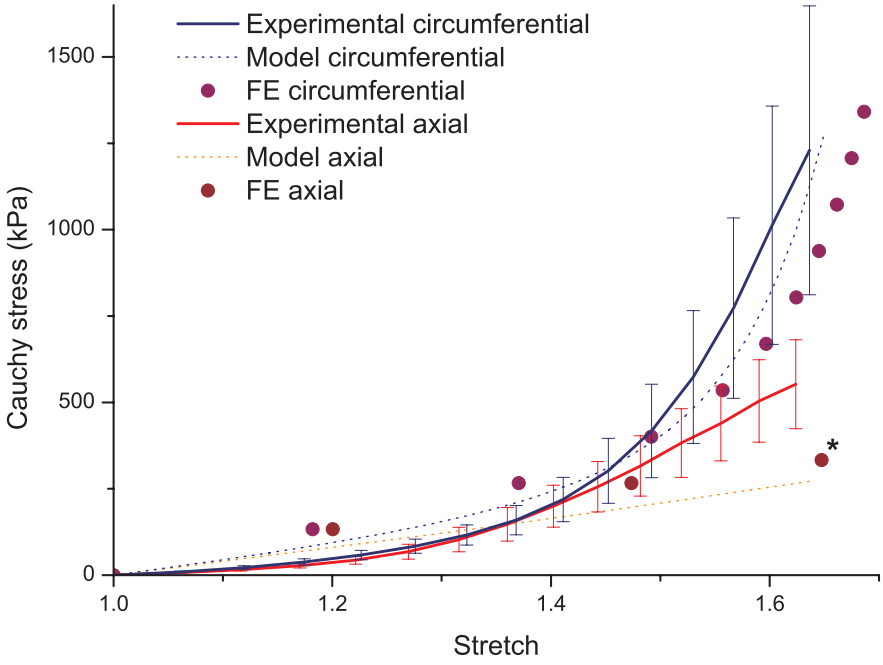


Figure 6.8: Comparison between the constitutive model fit obtained with the DTI and the stress-strain curve resulting from uniaxial tensile test FE simulation; the axial FE results had to be interrupted at the asterisk due to limit of experimental data.

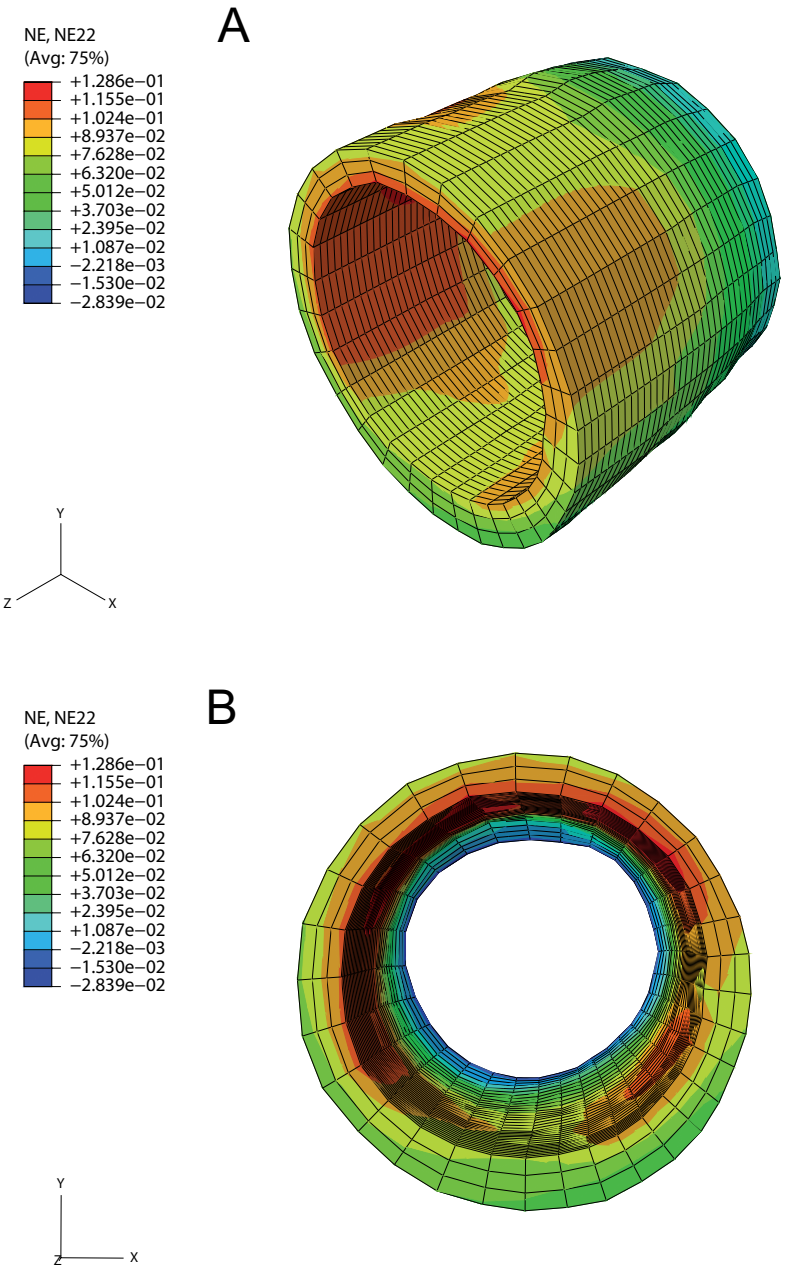


Figure 6.9: Circumferential strains in the loaded aorta FE simulation: A) side view; B) front view.

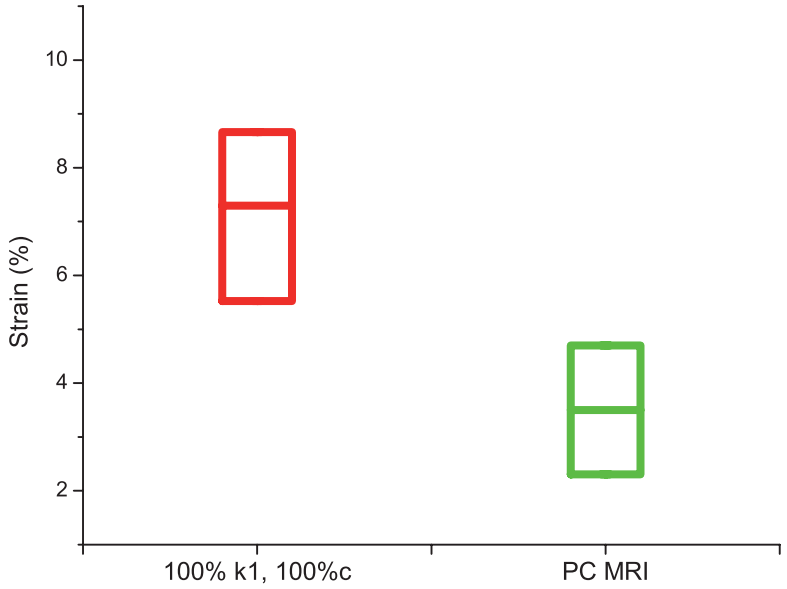


Figure 6.10: Results from the aortic simulations, The edges of the boxes are the maximum and the minimum strain recorded, while the line represents the average of the strains.

## 6.3 Discussion

### 6.3.1 Evaluation of DTI derived structural parameters

The global aim of this chapter was the comparison of the MRI measured circumferential strains with those obtained from a finite element simulation in order to define a constitutive model through non-invasive techniques. To reach this aim, material parameters were defined non-invasively and input in a FE model based on the real aortic geometry measured through MRI.

The structural constants, $\gamma$ and $\kappa$, needed for the definition of the material parameters were obtained from the DTI analyses in ch.4. The value of $\gamma$, $\pm$ 15° found from DTI analyses is in accordance with the nearly circumferential value reported in literature [34] and with experimental uniaxial tests showing distinct stiffening in the circumferential direction, see fig.3.6. By contrast, there is a lack of reference for the value of $\kappa$, since it was determined for the first time in this study from a fibre distribution , and can only be compared

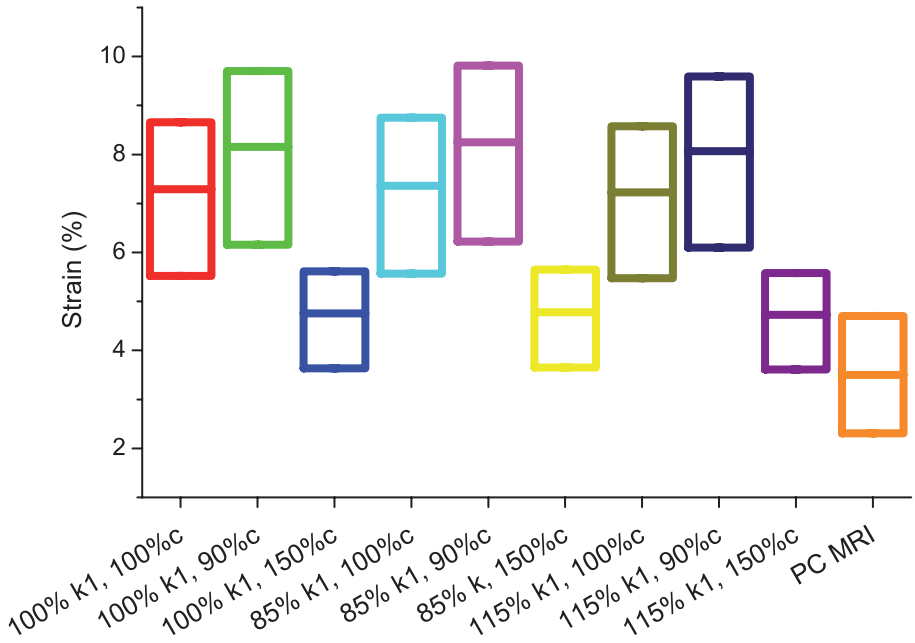


Figure 6.11: Effect of the variation of $c$ and $k_1$ on the strains computed from the FE simulation.

with the values estimated from the tensile test behaviour in ch.3. As shown in table 6.2, the values of $\kappa$ in the two cases are completely different, with the DTI measured $\kappa$ being characteristic of anisotropy and the estimated $\kappa$ being an indication of isotropy. Inputting the DTI derived structural constants into the non-linear Levenberg-Marquardt regression routine, described in ch.3, a new constitutive model fit to the experimental tensile tests was produced, as shown in fig. 6.6. By comparing the new model fit to the one obtained using data from literature, it is possible to see that the DTI derived value of $\kappa$ triggers huge modifications in the curves. In fact, being characteristic of anisotropy, $\kappa$ marks a greater distinction between the behaviour in the circumferential direction and the behaviour in the axial direction. This distinction is marked also in the values of the material parameters $c$, $k_1$ and $k_2$ reported in table 6.2. Here it can be seen that a larger value of $c$ is needed to move the axial response up, and a decrease in the value of $k_1$ is necessary for narrowing the gap between the two responses. According to what was discussed in ch.3, these two changes represent an increase in the stiffness of

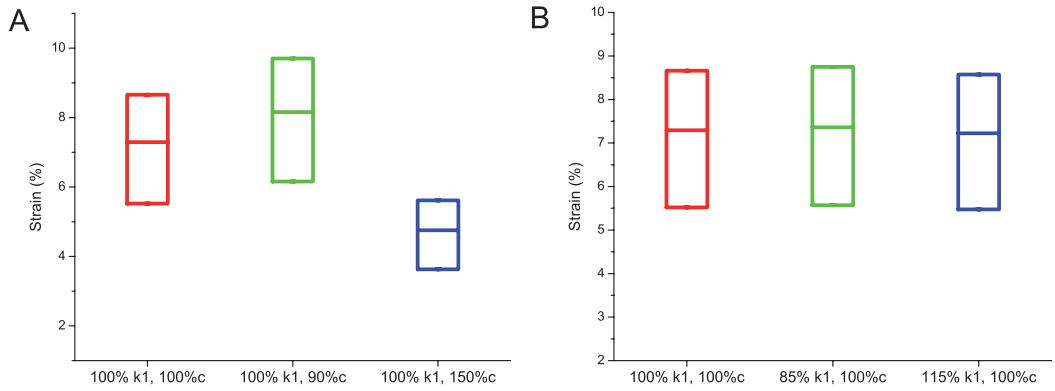


Figure 6.12: Details of the effect of the variation of the value of $c$ and of the value of $k_1$: A) $k_1$ constant; B) $c$ constant.

the ground matrix, larger $c$, that covers also part of the collagen response, therefore reducing the stress-like parameter $k_1$. Finally, the slight decrease in $k_2$ accommodates for a smoother response of the collagen fibres. The increase in the stiffness of the matrix marked by the increase in $c$ and the decrease in $k_1$ is needed to match the experimental data because of the reduction in the stiffness in the axial direction caused by the high degree of anisotropy, i.e. low $\kappa$.

The new constitutive model fit obtained for the non-invasively determined structural parameters differs from the one obtained from the data from literature. In fact the second one, assuming isotropy, could fit the toe region of the experimental tensile test better. This difference in the two model fits demonstrates the necessity for obtaining realistic material parameters as derived from DTI in order to find the most suitable parameters to define the behaviour of the tissue.

### 6.3.2 Finite Element Analysis

Prior to the implementation of a FE aortic model, the stress-strain curve resulting from the FE simulation of a uniaxial tensile test had to be compared with the same curves obtained experimentally, in order to check the validity

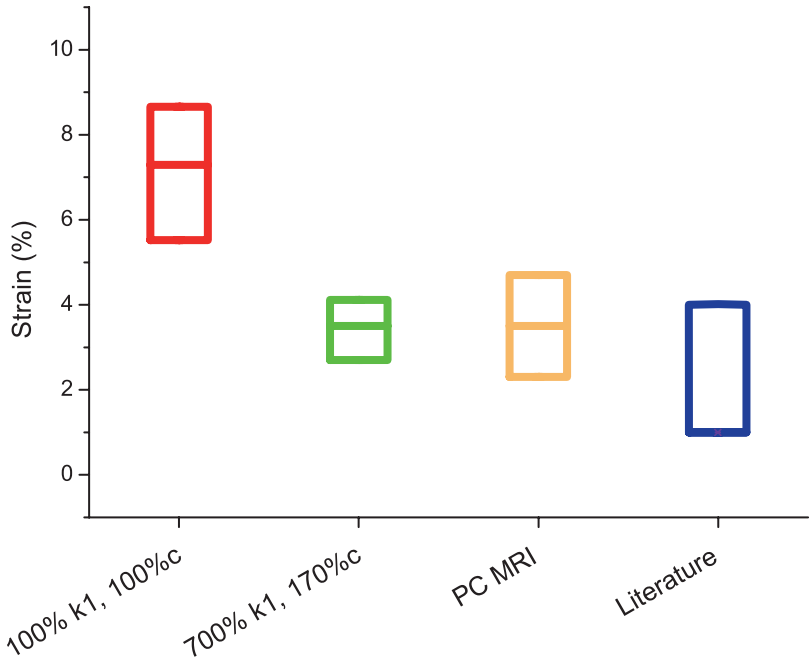


Figure 6.13: FE model strains for the values resulting from the iterative routine, red box. The blue box represents the average strains in the aorta reported in [109].

of the model. Fig. 6.8 shows that the FE stress-strain curves follow the shape of the constitutive model fit, although they are slightly over-estimating the toe-region behaviour. The buckling and the concentration of strains in the first row of elements below the loaded surface, shown in fig.6.7, is due to the particular loading of the sample. In fact, this phenomenon is due to the nodes on the loaded surface being constrained to move together, without changing their spatial relationship, a constraint that was imposed to mimic uniform pulling of the surface.

The FE strains for the geometry of the aorta show a distribution of strains generally uniform throughout the volume, with concentration effects only at the constrained end, in agreement with that anticipated by theory on the end-effect. Local variations on the strain distribution in the aorta are due to the irregularities in the geometry of this biological sample.

### 6.3.3 Aortic Constitutive Behaviour

As can be seen in fig.6.10, the global strains recorded for the loaded aorta using the DTI model are shifted compared to the circumferential strains measured in the previous section. These large strains are due to the decrease of the stress-like parameter $k_1$ reported in table 6.2, and hence to a reduction in the stiffness of the tissue. In order to obtain a better evaluation of the FE computed strains, the material parameters $c$ and $k_1$ needed to be modified according to the observation reported in section 6.1.3. In particular, fig. 6.11 and table 6.4 show that changes in the material parameters can make the strains larger or smaller and can also change the amplitude of the strain response. Moreover, fig. 6.12, shows that a change in $c$ moves the curve, while a change in $k_1$, alters the amplitude of the response. From these considerations, rules were drawn on the modifications that had to be imposed on the curve. In particular, the optimal values of the material parameters were sought by increasing both $c$ and $k_1$.

The optimisation routine then increased both values until the average strain value was reached with the maximal amplitude, see fig.6.13. The values for which this routine converged were $1.7\times c$ and $7\times k_1$, and are reported in table 6.3. In fact, for these two values, an average strain of 3.5% could be reached with an amplitude of 1.45 %. The explanation for why these were the values for which the curve converged can be seen by looking at fig.6.14. In this figure it can be seen how, for increasing values of $k_1$ both the amplitude and

| | DTI model | Iterative procedure |
|---|---|---|
| $\gamma$ | 15° | 15° |
| $\kappa$ | 0.11 | 0.11 |
| $c$ | 131.5 kPa | 223.5 kPa |
| $k_1$ | 12.4 kPa | 87k Pa |
| $k_2$ | 1.67 | 1.67 |

Table 6.3: Material parameters obtained from the changes in $c$ and in $k_1$.

the average strain converge to values characteristic of the value of $c$ used. From fig. 6.14, it can be seen that there are limitations in the behaviour that can be attained, and that the amplitude and the average for strains are linked and depend on the constants chosen. For example, a smaller value of $c$ could increase the amplitude of the strains evaluated, but at the same time it could make them so larger that they would no longer be comparable with the strains measured from PC MRI. On the other hand, a larger value of $c$ could make the minimal strain evaluated from FE coincide with the minimal strain measured from PC MRI, but then the amplitude of the FE strains would be much smaller in comparison. Although strongly influenced by the value of $c$, it is important to note that the routine converged for a marked increase in the value of $k_1$, which stiffens the response of the tissue. The increases in these two constants, $c$ and $k_1$, obviously increase the stiffness of the aorta thus reducing its deformation, but it is important to note that there is a wider meaning to the increases in $c$ and $k_1$ for which the routine converges. First of all, this increase in the stiffness of the aorta is physiologically relevant: in fact, the material parameter $k_1$ was defined as the stress the collagen fibres can bear, see ch. 3, and a change in its magnitude will determine a change in the behaviour of the fibres. By looking at fig. 3.8–3.9 and 6.6–6.8, it can be seen how the $k_1$ value is related to the maximal stress of the curve, which is always of the same order of magnitude. Furthermore, by comparing table 6.2 and 6.3, it can be noted how the use of the DTI defined parameters affects both the values of $c$ and $k_1$, with $k_1$ decreasing of two orders of magnitude. Hence it can be gathered that the increase in both $c$ and $k_1$ prescribed by the optimisation routine describes a compensation mechanism for the stress

| | $100\%k_1$ $100\%c$ | $100\%k_1$ $90\%c$ | $100\%k_1$ $150\%c$ | $85\%k_1$ $100\%c$ | $115\%k_1$ $100\%c$ | $700\%k_1$ $170\%c$ | Literature | PC MRI |
|---|---|---|---|---|---|---|---|---|
| Minimum | 5.52 | 6.15 | 3.63 | 5.57 | 5.47 | **2.70** | – | 2.30 |
| Average | 7.29 | 8.15 | 4.75 | 7.36 | 7.22 | **3.50** | 1-4 | 3.5 |
| Amplitude | 3.14 | 3.55 | 1.98 | 3.17 | 0 | **1.41** | – | 2.4 |

Table 6.4: Relevant measures for the strains analysed (%).

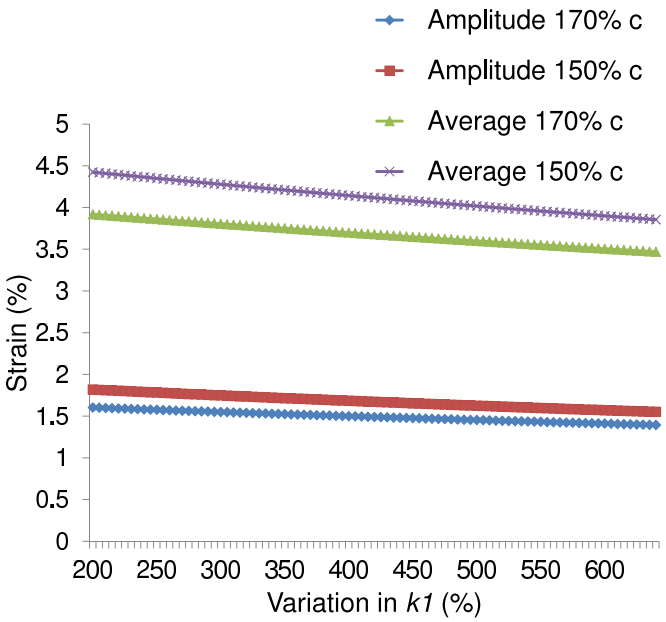


Figure 6.14: Effect of the variation of $k_1$ on the amplitude and on the average strain for different values of $c$.

that can be supported by the collagen fibres which then rises to levels closer to those observed experimentally.

Moreover, these increases can be seen as the effect of considering the whole aorta, as opposed to the samples harvested for uniaxial tests. In these samples the natural residual stresses and the pre-stretch of the tissue, see ch.2.2, are lost and the same happens to the connections between the fibres and the organisation of the ground matrix, severed by cutting. This is the reason why it is expected that the constants obtained by fitting to the uniaxial tensile tests were under-estimated. The same observation applies to the constitutive parameters obtained by other mechanical testing, biaxial testing for example, since it has to do with the invasive action of harvesting the tissue.

The increase in the values of $c$ and $k_1$ estimated by the iterative routine is characteristic of the tissue considered in its integrity, and can be considered as an average of the response of each part of the aorta, i.e. the global response of the tissue. However, the same method could be applied to match the

strains measured by PC MRI in a quarter of the aortic volume to the strains estimated by FE in the same quarter, or even in a smaller portion, thus measuring non-invasively the local properties of the tissue, or even of a single layer. This can be accomplished because the constitutive model chosen, i.e. the model from Gasser *et al.* [53], relies only on the definition of two structural parameters for the determination of the behaviour of the tissue, $\gamma$ and $\kappa$. In fact, as it was discussed in ch.2, by changing the values of these two constants it is possible to characterize each single arterial layer [57].

Moreover, the approach presented in this work is able to generate a mechanistic model of the aortic tissue because it can establish a direct relation between the material parameters estimated and their effect on the behaviour of the tissue. This means that this approach is not only successful in studying the property in a healthy tissue but it has the potential to characterize a diseased tissue as well. In fact, from this close relationship between the biological components of the tissue and the material parameters it can be hypothesised that the characterization for the diseased tissue could be determined solely by knowing the alterations caused by the disease in the fibrous structure, such as the collagen and the elastin matrix disruption in abdominal aortic aneurysms [28–30]. Vice versa, it could be inferred that a change observed in the constitutive model parameters would correspond to a change in size, quantity and orientation of the biological components sustaining the tissue.

Finally, the approach presented in this chapter offers greater potential compared to other techniques currently available for the study of these arterial disease. In fact, in contrast to other techniques that concentrate only on the effects of age and disease on strains [121, 122, 144], or on the tissue geometrical features [21, 24, 144] or even on the local properties of harvested tissue [57, 63], the approach presented can determine global information on the tissue and can put it into context by tying the mechanical properties observed globally to the behaviour of the micro-structural components of the tissue itself.

### 6.3.4 Limitations

The fact that DTI and PC MRI were not carried out on the same aorta can be considered the biggest limitation to this portion of the study. In fact, DTI and PC MRI could not be carried out on the same aorta because of a time conflict: the scanning time would have been in excess of 24 hours, thus invalidating the hypothesis of fresh tissue that holds when the analysis happens within 24h of slaughtering. For the present study, this limitation can be overcome by considering the repeatability of the DTI results. In the future, the use of a DTI sequence optimised for aortic $b$ values will make it possible to obtain both structural parameters and circumferential strains in one scanning session of less than 1h.

Another limitation is represented by the quasi-static analysis. A fluid-structure interaction simulation could have generated a more realistic strain profile for the pulsatile pressure. However, since there was no accurate reference for the strains measured corresponding with the back-flow, only the strains corresponding to the loading part of the pressure profile could be studied. In this phase of the cycle the pressure can be considered the main load acting on the aorta and therefore the assumption of quasi-static loading can be made without loss of generality. Moreover, the analysis of the quasi-static response of the aorta to the loading phase of the pressure can be considered a complete characterization of the aorta since it corresponds to the maximal loading of the tissue.

Finally, having considered the same material properties for all elements can be considered as another limitation of the analysis. In fact, although DTI showed the potential to describe the global arrangement of fibres across the aortic wall thickness, see fig.4.14-4.16, from the uniaxial tensile tests of the aortic wall performed in ch. 3 a homogenised characterization of the aorta was obtained, which was then used in the finite element model. In the future, the knowledge of the stress-strain curves for each layer of the aortic wall might be used to define each layer material properties.

### 6.3.5 Conclusions

In this chapter it was demonstrated that it is possible to determine the mechanical behaviour of the aorta using only non-invasive techniques. This was done by comparing the strains estimated by a FE model to the strains measured by PC MRI, where the constants used in the FE model were determined non-invasively by using DTI. Although a perfect match between the two sets of strains cannot be obtained because of the implementation of a quasi-static analysis and the constraints imposed by the relationship between the constants, by modifying the material parameters $c$ and $k_1$ it is possible to move the strains into the range of the strains measured by PC MRI and described in literature [120]. The modification of the constitutive model parameters conforms with that anticipated from theory and from observations found in literature [5, 7, 8] thus validating this approach.

# Chapter 7

# Final Discussion

Since arteries are the conduits for blood flow in the body, arterial diseases are often characterized by alterations in blood flow patterns although these diseases can also be characterized by structural changes in the arterial wall that give rise to alterations in the blood flow. In fact, histological samples of the two most common arterial diseases, atherosclerosis and aneurysm, have shown alterations in the network of collagen and elastin fibres that sustain the arterial wall [2, 15, 28–30]. At present, most of the knowledge on arterial structure and mechanical properties is based on histological samples [5]. Histological analyses, to date the most powerful technique to investigate the composition of human tissues, have many drawbacks: they are invasive, i.e. a surgical biopsy is needed which poses limitations to their use in clinical practice; they require the tissue to be cut into microscopic pieces, thus removing all the natural pre-load of the tissue [7, 8] and making a global look on the composition of the tissue impossible; they cannot be used for the early diagnosis of a disease, since biopsies are limited to very localised areas. In order to overcome all of these limitations a new technique needs to be established to investigate and define arterial tissue properties, characterized by its non-invasive nature, ability to analyse the global status of the tissue and potential to provide an early diagnosis of arterial diseases.

The importance of an early diagnosis is important for aneurysms, and abdominal aortic aneurysms (AAA), in particular. This disease often pro-

gresses silently until rupture, an event fatal in 95% of cases [2, 17, 20]. Currently AAAs are detected by routine imaging of the abdomen, which is often carried out for patients at high risk of cardiovascular disease. The lack of an early diagnosis of such diseases has generated many hypotheses on its aetiology and on the mechanisms that trigger the enlargement of the aortic tissue, but unfortunately they cannot be verified given the present limitation to studying the onset of the disease.

In this project a novel approach for the mechanical characterization of the aortic behaviour is proposed, based on MR imaging techniques and therefore non-invasive. This novel approach starts with the selection of a suitable histomechanical constitutive model for arterial tissue from those available in literature, and then progresses with the evaluation of the aortic structural parameters through DTI and the measurement of circumferential strains through PC MRI; the constitutive parameters generated by inputting DTI parameters into the constitutive model were optimised to represent the aortic tissue by matching the circumferential strains resulting from a FE model with those measured from PC MRI.

The procedure adopted for the mechanical characterization of the aortic tissue is similar in its organisation to the procedure usually followed for the initial development of a constitutive model, where the estimated output of the model is verified against mechanical testing [53, 57, 61, 62]. In particular, the procedure adopted is similar to the procedure used for the determination of the histomechanical model used in the thesis. In fact, this model uses structural information of the arterial tissue, obtained through histology, and strains measured through mechanical testing to determine the material constants that account for the stiffness of the tissue's biological components, i.e. the fibres and ground matrix [53, 62]. The model has been widely used in literature and was chosen because of the clear mechanical meaning of its constitutive parameters [53,62] and the large availability of data on its implementation [53, 57, 61, 62]. In fact, variations in the constitutive parameters, performed in ch. 3 see fig.3.9 (page 50), demonstrated the link between the stress-strain curves predicted and the mechanical meaning of each of the constitutive parameter. This confirmed that such a mechanistic model was

particularly suited to the approach presented in this thesis since it allowed for an enhanced understanding of the mechanical behaviour, not only of the whole tissue, but also of its structural components.

The model, however, is built starting from information obtained in an invasive way. In fact, both histology and uniaxial tensile tests require the tissue to be harvested and cut in small samples. Since the aim of this thesis was the mechanical characterization of the aorta in a non-invasive way, suitable techniques had to be selected for the non-invasive analysis of aortic structure and the measurement of aortic strains.

The identification of a suitable technique to investigate the structure of the tissue was the biggest challenge, since most of the imaging techniques used in clinical practice can offer only a representation of the geometry of the tissue [66–68] or can detect only very specific alterations in the tissue: for example CT can distinguish calcified arterial tissue [70]. An imaging technique that can analyse accurately many different tissues is MRI, since it detects the water content in the tissues [72], and recently a MRI application was developed to track the motion of hydrogen protons along axon fibres in the brain. This MRI technique, called DTI, is used in literature mainly for studying the structure of the brain [77, 79, 83, 90–93], and has been used for investigating the fibrous structure of the heart [94–103]. However, this technique has never before been applied to the study of arteries, and in particular of the aorta. The novelty of using DTI for the analysis of a tissue, different from the brain or cardiac muscle, introduced many major challenges: finding the appropriate MRI coil for imaging, see fig.4.4 (page 58); determining the optimal imaging parameters such as the $b$ value for the aorta, see fig.4.13 (page 73), and tuning the post-processing parameters, i.e. the tractography parameters from which the fibres could be tracked, see Appendix B. Moreover, since this thesis marked the first application of DTI to aortic tissue, the results obtained had to be verified by comparing them with similar results obtained using microscopic techniques that could provide full 3D information [34, 56], and not with histology, which is limited to a bi-dimensional representation of tissue structure.

The output of the DTI investigations was the analysis of aortic fibrous

structure, see fig.4.10 (page 69) and in particular the evaluation of two fundamental structural parameters for the determination of a histomechanical aortic constitutive model. With DTI, it was possible to measure non-invasively $\gamma$, the fibre angle, and $\kappa$, a parameter that accounts for fibre distribution [53, 62]. The use of DTI marked the first time that $\gamma$ was detected over a complete, three dimensional geometry, and the first time that $\kappa$ was ever measured, see table 4.6 (page 82). In fact, although defined in many papers, $\kappa$ has never been experimentally determined before due to a lack of data regarding the three dimensional arrangement of fibres in the aorta, an arrangement that can be imaged with DTI. The value of $\gamma$, determined by analysing the fibrous structure resulting from DTI, matches the value of aortic fibre angle reported in literature using different techniques [34, 56], and the fibres arrangement across the aortic wall thickness is also in conformity with the arrangement observed in literature [56, 135, 136].

Other than being successful in determining the structural data of a healthy porcine aorta non-invasively, this work aimed at testing if DTI was able to detect alterations in the aortic fibrous structure characteristic of arterial disease. Since it was not possible to obtain diseased porcine aortas for analysis, the alteration in the fibrous structure was created by freezing it, thus producing a damage similar to that found in diseased aortas [27, 139, 140]. The DTI images presented in fig.4.9, 4.13, 4.14, and 4.17 (pages 68, 73, 75, 81), suggests th that this imaging technique has the ability to detect the freezing-induced damage of the aortic structure, thus showing potential to detect structural alterations in the aortic wall. Two fresh and one frozen porcine aorta were analysed, and for each aorta 16 slices of the volume were analysed, and each slice of the volume was scanned five times; this was equivalent to performing five tests on each sample for 16 samples, thus ensuring repeatability and reproducibility of the results, see fig. 4.17 for comparison.

The novel application of DTI to the investigation of aortic structure presented in this work shows the significant potential of this imaging technique. In fact, given that DTI is able to detect the arrangement of fibres in the tissue non-invasively, it could be coupled with standard MR imaging for the creation of patient-specific models, or for the definition of focused surgical

strategies, targeting only the diseased part of the vessel. Moreover, since the present work showed the ability of DTI in detecting damaged aortic tissue, this could be used for the early diagnosis of aneurysms and of arterial diseases. In particular, since there is no currently available tool to study the onset of aneurysms, DTI could be used for early studies on the population at greatest risk of aneurysms, and the results could be used to find new solutions to tackle this disease, thus decreasing the risks connected with open-abdominal surgical procedures currently in use for repairing aneurysms.

In contrast to the lack of suitable imaging techniques for determining non-invasively the structure of aortic tissue, there are many possibilities available for measuring strains in the tissue. Apart from deformation measures obtained by plain imaging [144], that can only give a global estimate of tissue motion, it is worth mentioning tagged MRI, an imaging technique developed in the 90s, consisting of a radio-frequency grid applied to the tissue to study its deformation [98]. Tagged MRI has been used successfully in the heart, but it cannot be applied to arterial tissue due to limitations to its resolution [98]: it is currently not possible to place more than one line (tag) across the aortic tissue. PC MRI is a different imaging technique, able to measure the velocities in the tissue as opposed to the displacements. Although not measuring strains directly, PC MRI has the advantage of not having the same limitations as tagged MRI, and therefore it can be used for every tissue, whatever the thickness, where its main application is in the study of arterial flow [95, 97, 101, 111–114].

The use of PC MRI as an imaging technique that can be used for determining aortic strain is documented in the work by Pelc's group [109,120–122]. In the studies by Pelc *et al.*, PC MRI is only used as a technique to measure the strain but its potential, i.e. the possibility of using the information derived from this technique for the analysis of a diseased vessel, is never exploited. In fact, given that PC MRI can be used for the determination of the local strains in the tissue, it can be used to determine the way arterial disease affects this motion, and therefore its response to the pulsatile loading of the heartbeat.

Apart from the application of PC MRI as an independent diagnostic tool,

in this work the potential of PC MRI was focused on the determination of the circumferential strains generated in a porcine aorta by a pulsatile pressure waveform. The protocol applied for measuring the circumferential strains was the one outlined in [120], and it resulted in strains comparable with those measured in literature with different techniques [120, 144], see fig.5.19 (page 121). Limitations to the implementation of this technique were due to the fact that the scanning was influenced by noise. In fact, in the experimental set up used noise was generated by the water which flowed freely inside and outside the aorta. The noise generated by the flow could not be filtered out by the MRI software because in this case the aorta was suspended in water, as opposed to being surrounded by other tissues. However, the noise affected only a portion of the images taken, see fig.5.10.E-F, 5.11.E-F (pages 108, 109), i.e. the ones taken at the end of the loading phase of the pressure, when the flow diminished to the point where back-flow was generated, see fig.5.18 (page 118). This meant that the strains recorded for the loading part of the pressure waveform were free of noise and, having tested their validity against the circumferential strains measured from literature [120, 144], they could be used for further studies on the mechanical characterization of aortic behaviour.

In the last part of this method, the optimal material parameters were determined by comparing the strains estimated by the constitutive model and the strains measured through PC MRI. Constitutive model strains were generated using a FE model. FE models are widely used in biomedical engineering [52,53,59] as a way to verify theoretical assumptions on the behaviour of biological tissues or as a way to understand the human body and its reactions to different loads and prostheses. Contrary to standard works, where FE models are based on invasive histological analyses, in the present thesis the constants used for this model were generated non-invasively by inputting the values of $\gamma$ and $\kappa$ measured from DTI into the constitutive model established from mechanical tests. The FE analysis performed was a quasi-static analysis of the loading of the tissue. Due to the fact that PC MRI noise did not affect the strains obtained for the initial loading of the tissue, where the pressure is the main load acting, the assumption of quasi-static loading could

be made without loss of generality. The strains obtained by using the original constitutive model with the newly measured $\gamma$ and $\kappa$, were too large when compared to the strains measured with PC MRI, see fig.6.10 (page 136), and alterations to the constitutive model parameters had to be made to achieve strains in the same range as PC MRI. This was achieved by means of an iterative routine, that changed the material parameters. The material constants for which the two sets of strains were comparable, see fig. 6.13 (page 139), showed that the aortic tissue considered as a whole had a stiffer response than strips of the same tissue harvested and tested mechanically. In particular, due to the strong tie between the material constants and the aortic constituents enforced by the model used, it could be concluded that the aortic tissue is characterized by a ground matrix whose stiffness is comparable to the stiffness of the collagenous structure, especially if the values obtained for $c$ and $k_1$ as a result of the present work on the aorta are compared with the same values obtained for the iliac artery in [53].

This result is in agreement with what can be observed by looking at the uniaxial tensile tests of both curves, presented in ch. 3 (pages 42, 47), where it can be seen that the aorta stress-stretch curves are characterized by a large isotropic area which corresponds to the response of the ground matrix. Therefore it can be concluded that the appropriate material parameters were determined for the aorta, and hence its mechanical characterization was successfully obtained non-invasively through imaging techniques.

Overall, this project was successful in defining a novel, non-invasive approach for the determination of aortic mechanical properties. This project involved the use of DTI for the investigation of aortic structure for the first time, and of PC MRI for the studies of aortic strains, two techniques that show a significant potential on their own for the diagnosis of alterations in aortic wall mechanics and kinematics. In particular, coupling the information retrieved from these two techniques with a mechanistic mechanical model such as the one defined in [53], resulted in the determination of the most suitable constants to represent the dynamic behaviour of the aorta. The relevance of this result is not only in the fact that the strains obtained were comparable to the ones reported in literature, but also that the changes

in the constants for which these strains were obtained could be linked to stiffening of the tissue, thus demonstrating that if the aortic strains or the structural constants were altered by a disease, the validity of this approach would still hold.

This work marks the first time where imaging modalities such as DTI and PC MRI are combined with FE to yield information on aortic material behaviour. In particular, from the novel application of DTI to aortic tissue it can be hypothesised that in the future non-invasive analyses of the aortic structure as a whole, or of any part thereof, could be conducted *in vivo* with this technique. Moreover, it can be concluded that this procedure has the potential to be expanded to human arteries where it could become a clinical tool for the diagnosis of arterial disease, or for the estimation of the potential of aneurysms to rupture.

# Chapter 8

# Conclusions & Future Work

## 8.1 Conclusions

The aim of this work was the non-invasive characterization of a porcine aorta constitutive model. This characterization was obtained by using two different MRI techniques, DTI and PC MRI. While PC MRI gave information on the kinematics of aortic tissue, DTI investigated the aortic structure. The main contributions from this work include:

- The determination of a suitable mechanistic constitutive model for aortic tissue. This constitutive model, proposed by Gasser *et al.* [53], allowed for the characterization of the aorta based on the knowledge of two structural parameters, fibre angle and fibre distribution, and the stretches of the tissue. The implementation of this constitutive model could be used for preclinical tests of devices for the aorta.

- The identification of Diffusion Tensor Imaging as a technique for the investigation of aortic fibrous structure *in vivo*; in fact, although DTI had been used before for studies on axonal connections and on cardiac muscle structure, it was never been applied before to arterial tissue and the potential of its application on aortas is explored for the first time in this project.

- The identification of DTI as an effective means of detecting the anisotropy of the aorta and the distribution of the fibres within the tissue by comparison to available literature data [34, 56]; furthermore, the fibre distribution could be post-processed through a custom developed algorithm to determine $\gamma$, the fibre angle, and $\kappa$, the fibre distribution, key structural parameters necessary for the constitutive model.

- The potential of DTI to be used as a diagnostic tool in its own right, demonstrated by differences in fresh and frozen tissue measurements which confirmed that degeneration of aortic fibrous structure can be detected with this novel technique.

- The *in vivo* determination of global and local mechanical properties of aortic tissue using an integrated approach where DTI, PC MRI and FE models were combined. This indirect approach is both non-invasive and low risk and offers a real alternative to invasive and surgical approaches.

- The definition of an effective procedure through which a complete non-invasive characterization of the mechanical behaviour could be obtained in a single MRI session. In fact, this project demonstrates that, by combining DTI and PC MRI, data can be obtained on the structure and the kinematics of the tissue simultaneously. This makes the development of an innovative vascular imaging tool capable of diagnosing arterial diseases based on *in vivo* mechanical characterization of the tissue a real possibility whilst also enabling patient specific models to be generated for preclinical testing of medical devices.

## 8.2 Future Work

Due to the novelty of the technique implemented and to the relevance of non-invasive measurement in clinical practice, the work presented in this thesis has a significant potential to be developed as a clinical tool for diagnosis and for patient-specific modelling. In order to achieve this aim, future work needs to be carried out in the following areas:

- Simultaneous application of DTI and PC MRI: obtaining structural and dynamic information from the same aorta would generate even more accurate characterization of the tissue and of how its fibrous structure changes with physiological motion.

- Testing this approach on healthy and diseased human aortic tissue: the mechanical characterization of healthy and diseased tissue being the first step towards using this technique for clinical diagnosis.

- Combining the structural information obtained from DTI with FE models to study the failure of medical implants, such as peripheral stents, or to improve the outcome of covered stents and grafts, by adapting the polyethylene fibrous structure of the graft to the fibre structure of the aorta analysed with DTI.

- The characterization of the structural changes that occur with age in the aorta using DTI, following what has be done in Morrison *et al.* for the analysis of the circumferential strains with age [144]. This would lead to the definition of the characteristics of healthy aortic tissue and how they change with age.

- The definition of AAA aetiology by analysing the risk population across a time frame and analysing the changes in the aortic structure that lead to the formation of aneurysms with DTI: the same approach could be used to define the factors that determine rupture in AAAs, in order to define a valid criteria for surgical treatment of such disease.

- Extending DTI application to other blood vessels where aneurysms are frequently diagnosed, such as cerebral aneurysms, or to the characterization of atherosclerosis. In sclerotic arteries, DTI has the potential to be used for plaque rupture prediction and for the prevention of ischaemia.

Finally, the extension of the combined approach of DTI, PC MRI and FE to other tissues and other diseases offers the possibility to expand the procedure detailed in this thesis to the non-invasive mechanical characterization of the

arterial tree. This in turn could become a diagnostic tool for cardiovascular diseases enabling the translation of classical engineering principles into routine clinical diagnosis.

# Appendix A

# Aortic Chamber

The drawing of the MRI-safe custom designed aortic chamber is shown below.

| Scale | 1:3 | Designer | Vittoria Flamini | Date | 31-03-2008 |
|---|---|---|---|---|---|
| Material | | Control | / | Date | / |
| Various | | Class | / | Note | / |
| Part Name | | Standard | / | DUBLIN CITY UNIVERSITY SCHOOL OF MECHANICAL & MANUFACTURING ENGINEERING | |
| Aorta chamber assembly | | Project | / | | |
| | | Type | / | | |
| | | Part No. | / | | |

# Appendix B

# DTI: parameters definition

The appropriate tensor and tractography parameters were defined by means of a number of sensitivity tests. In order to obtain the most suitable value for each parameter, a range of values were applied and the difference observed between the results obtained was considered to establish the most suitable parameter for this particular application. For the tensor parameters, the background suppression and the tensor smoothing had to be set. The background suppression consists in setting a threshold on the signal of the image under which no tensor will be estimated, based on the reference image $S_0$. This value was set to 1000 compared to a maximum of 32766, in order not to interfere with the fibre tracking due to the fact that some areas of the arterial tissue were nearly as dark as the background. Regarding the tensor smoothing, a feature available in MedINRIA to reduce the noise of the tensor, it was set to 'high'because, by analysing the different FA maps, this was found to be the only value that would suppress the effect of surrounding water. Then the fibre tractography to be determined where: the FA threshold, the minimum length and the smoothness of the fibres and finally the sampling parameters. The FA value was analysed first. Fractional anisotropy can be regarded as a tool to erase the noise and therefore the threshold value of FA influenced the amount of fibres tracked in the total image volume. The optimum FA should track fibres predominantly in the region of interest. For the aorta encased in fluid, extremely low FA threshold values ($<0.15$) resulted in large amounts

of fibres being tracked in the water volume, while high FA threshold values (>0.3) resulted in very few fibres being tracked even in the aortic volume. Empirically we found that for a FA threshold value of 0.2 most of the fibres were tracked in the aortic volume and almost none in the water. Following the establishment of a suitable FA value, the effect of the minimum length of the fibre tracked was considered by means of a parametric analysis.

## B.1 Parametric Analysis

For the fibre bundles detected using the angle detection routine a parametric analysis was performed to determine the dependence of the fibre tracking algorithm on the tracking parameters. The parameters considered are described on table B.1. Over two different sets of images, three different fibre lengths were considered, 5, 10 and 15 mm. For 5 mm many fragmented fibres were tracked while for 15 mm only a few fibres, albeit extremely long fibres, were tracked. By comparison to available histological data on aortic tissue, a minimum fibre length of 10 mm showed an optimal trade-off between the number of fibres and their length for all the different b values and enabled a suitable sample from which average fibre directions could be ascertained. The value of 10 mm corresponds to one third of the planar resolution of the image. The influence of the smoothness parameter on the fibres tracked was also addressed. This parameter defines the smoothness of the curvature of the final fibre and ensures that large discontinuities in curvature from pixel

| | FA threshold | Sampling | Fibre Minimal Length | Fibre Smoothness |
|---|---|---|---|---|
| Small ROI | 0.2 | 1 pixel | 5 pixels<br>10 pixels<br>15 pixels | 20%<br>50%<br>80% |
| Wide ROI | 0.2 | 1 pixel | 5 pixels<br>10 pixels<br>15 pixels | 20%<br>20%<br>80% |

Table B.1: Parametric fibre tracking settings.

to pixel of the image are identified such that they cannot be considered one fibre. For the chosen fibre length of 10 mm, variations in the smoothness value over a large range (20%-80%) showed that the fibre number tracked is relatively insensitive to this parameter. Finally, the sampling parameter was investigated. The sampling parameter accounts for the number of pixels used for the determination of the fibre. A sampling parameter of one pixel, although extremely accurate, is computationally expensive. Empirically we found that a sampling parameter of three, where fibre tracking is only performed in one voxel out of each three, yields very good accuracy by comparison to a sampling of one pixel and reduces the computational time considerably [128].

# Appendix C

# PC MRI: method

The evaluation of PC MRI circumferential strains was performed using a method available from literature: the forward/backward integration of velocities according to the algorithm defined in [109].

## C.1 Forward/backward integration

This approach is based on the assumption that the trajectory of a region can be computed by integrating its velocity as a function of time. The structure of the algorithm can be divided into three phases: forward integration, backward integration and combined integration [109].

**Forward integration** First, the relevant parameters have to be defined: $V(s,t)$, the velocity at a spatial position $s$ and time $t$; $f$ the forward integrated trajectory; $f_k$ location of the region to be tracked at time $t_k$, where $k$ is the frame number. Using these parameters it is possible to define the simplest estimate of the location of the region at a time $t_{k+1} = t_k + \Delta t$:

$$f_{k+1} = f_k + V(f_k, t_k)\Delta t; \tag{C.1}$$

This equation assumes $V(f_k, t_k)$ as the constant velocity for all the interval and then suddenly becomes $V(f_{k+1}, t_{k+1})$. A better approach would consider

the velocity varying linearly over the interval between the two values, thus resulting in [109]:

$$f_{k+1} = f_k + \frac{1}{2}\left[V(f_k, t_k) + V(f_{k+1}, t_{k+1})\right]\Delta t; \tag{C.2}$$

The difficulty with eq. C.2 is that it requires the knowledge of $V(f_{k+1}, t_{k+1})$ in order to compute $f_{k+1}$. This problem can be avoided using an estimate of $f_{k+1}$ obtained through C.1 to determine $V(f_{k+1}, t_{k+1})$, and then eq. C.2 can be used for evaluating the 'optimal' $f_{k+1}$ [109]. In the practical application of this algorithm $f_k$ corresponds to the centre of the region to be tracked, i.e. the centre of a pixel or the centre of an element.

**Backward integration** Since the motion of an artery is periodic, for each time frame it is possible to track the motion of the region also going backward in time. In this case $b_k$ will be the trajectory resulting from the backward integration [109]. Again, the estimate of $b_{k-1}$ can be obtained as:

$$b_{k-1} = b_k - V(b_k, t_k)\Delta t; \tag{C.3}$$

Also in this case eq. C.3 will give only a first estimate of $b_{k-1}$ that will be used to determine $V(b_{k-1}, t_{k-1})$ in order to evaluate the 'optimal' $b_{k-1}$ using the following equation:

$$b_{k-1} = b_k - \frac{1}{2}\left[V(b_k, t_k) + V(b_{k-1}, t_{k-1})\right]\Delta t; \tag{C.4}$$

Finally, it is important to note that in this integration the same definition of a region to be tracked is used as the forward integration [109].

**Combined integration** Each of the two integrations illustrated in the previous paragraphs provides an estimated trajectory. Since both trajectories are computed from different time frames, they will have different velocity offsets and different noise [109]. It is important then, to combine both trajectories into a single estimate. This is done by defining $r_k$ a trajectory that

is a linear combination of the previous two, defined by:

$$r_k = w_k f_k + (1 - w_k) b_k; \tag{C.5}$$

Where $w_k$ is a weighting factor obtained by minimising the variance of the combined trajectory. This weighting factor can be expressed as:

$$w_k = \frac{N - k + 1}{N}; \tag{C.6}$$

In the eq. C.6 $N$ is the number of frames produced per cycle, and it can be seen that $w_k$ changes in each time frame. Details on the advantages of this technique in terms of minimisation of the error and of the noise can be found in [109].

# Appendix D

# LabVIEW® and MATLAB® scripts

## D.1 LabVIEW®

### D.1.1 Non-linear Levenberg-Marquardt regression

The non-linear Levenberg-Marquardt regression is made up of several nested routines. The main one is Regression_Holzapfel_excel, that calls simultaneously the comparison and convergence check routine and the function that the regression should fit. Many other sub-functions are already defined in LabVIEW®, and therefore are not given in this thesis.

# Regression_Holzapfel_excel

**regression holzapfel_excel.vi**

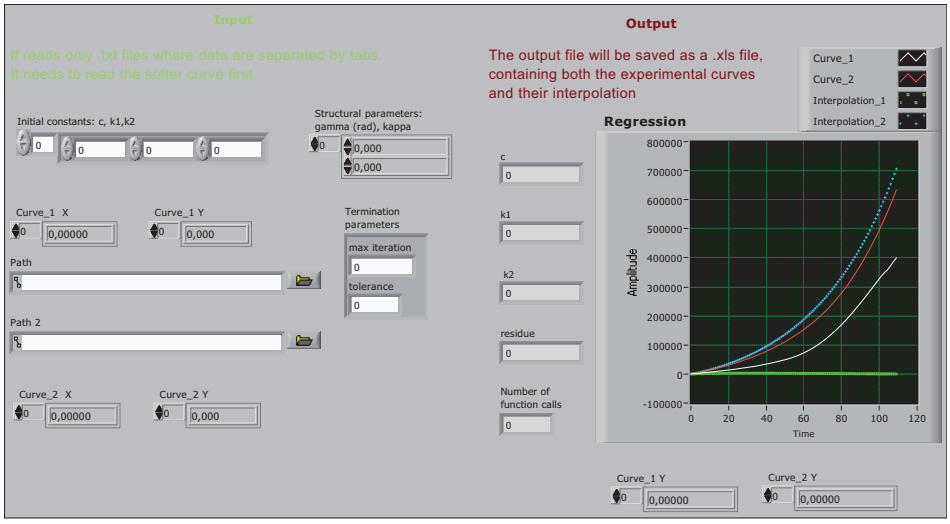


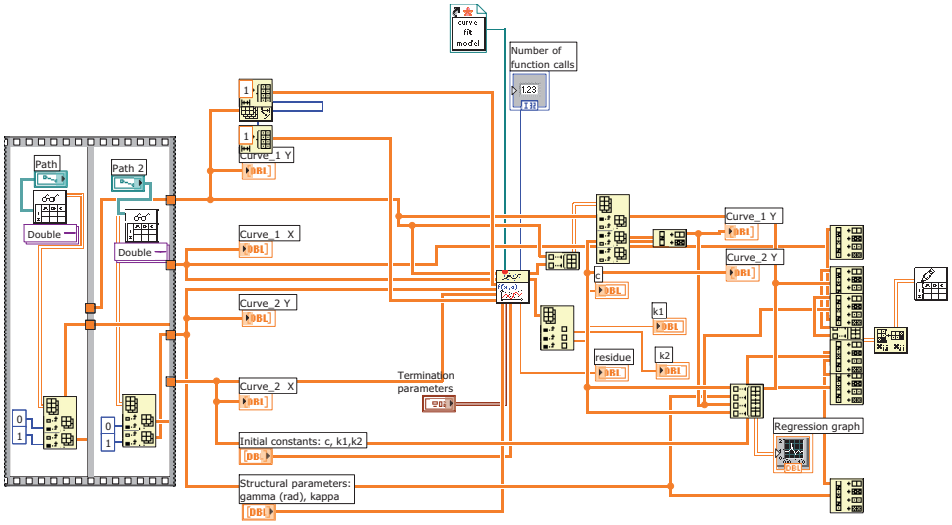

# Comparison e convergence check

Connector Pane

**Nonlinear Curve Fit VF.vi**

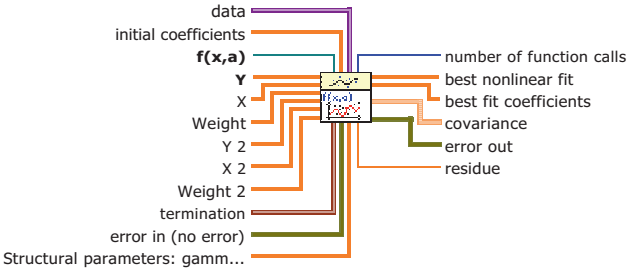


Uses the Levenberg-Marquardt algorithm to determine the least squares set of coefficients that best fit the set of input data points (<B>X</B>, <B>Y</B>) as expressed by a nonlinear function y = <B>f(x,a)</B>, where a is the set of coefficients. You must manually select the polymorphic instance to use.

Front Panel

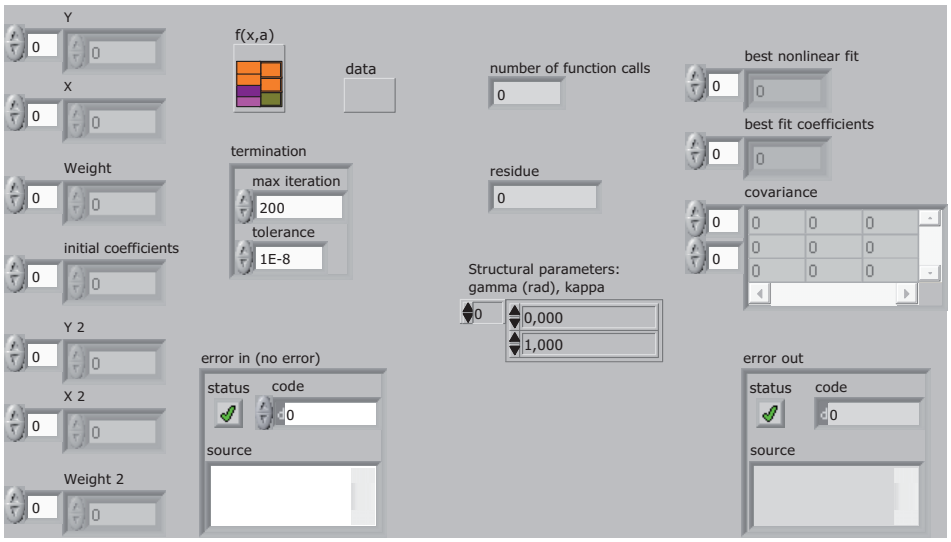

# Holzapfel function

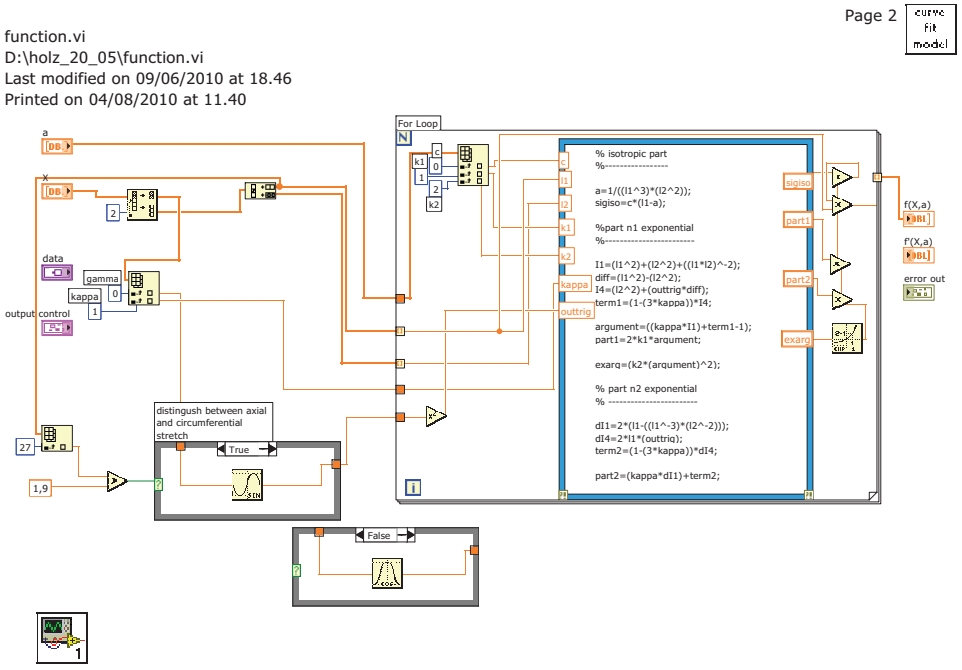

## D.1.2 Pressure sensor controller



pressure sensor.vi
D:\pressure sensor\pressure sensor.vi
Last modified on 19/11/2009 at 17.27
Printed on 03/08/2010 at 8.52

**pressure sensor.vi**

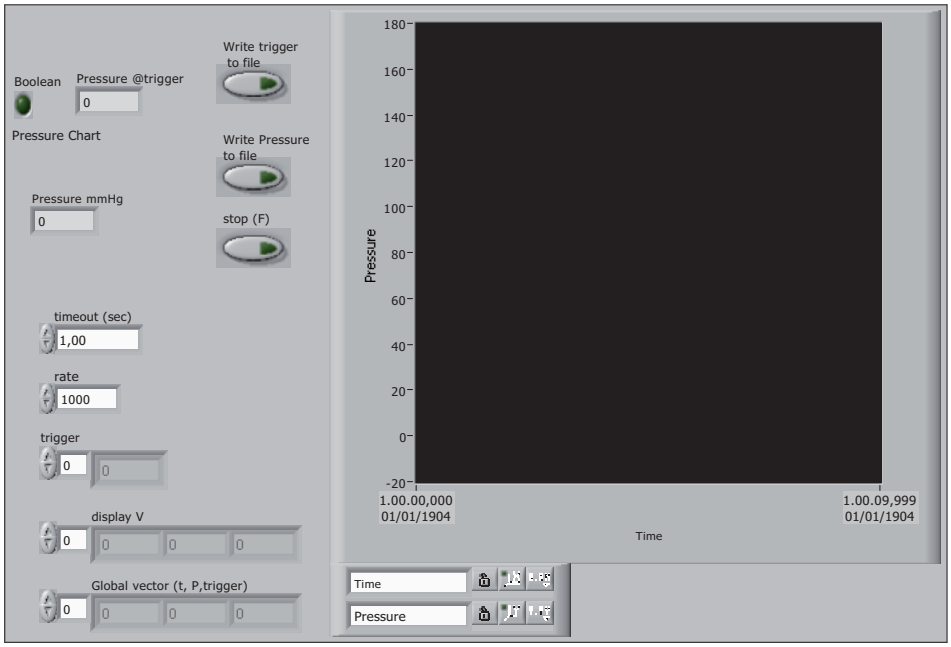

pressure sensor.vi
D:\pressure sensor\pressure sensor.vi
Last modified on 19/11/2009 at 17.27
Printed on 03/08/2010 at 8.52

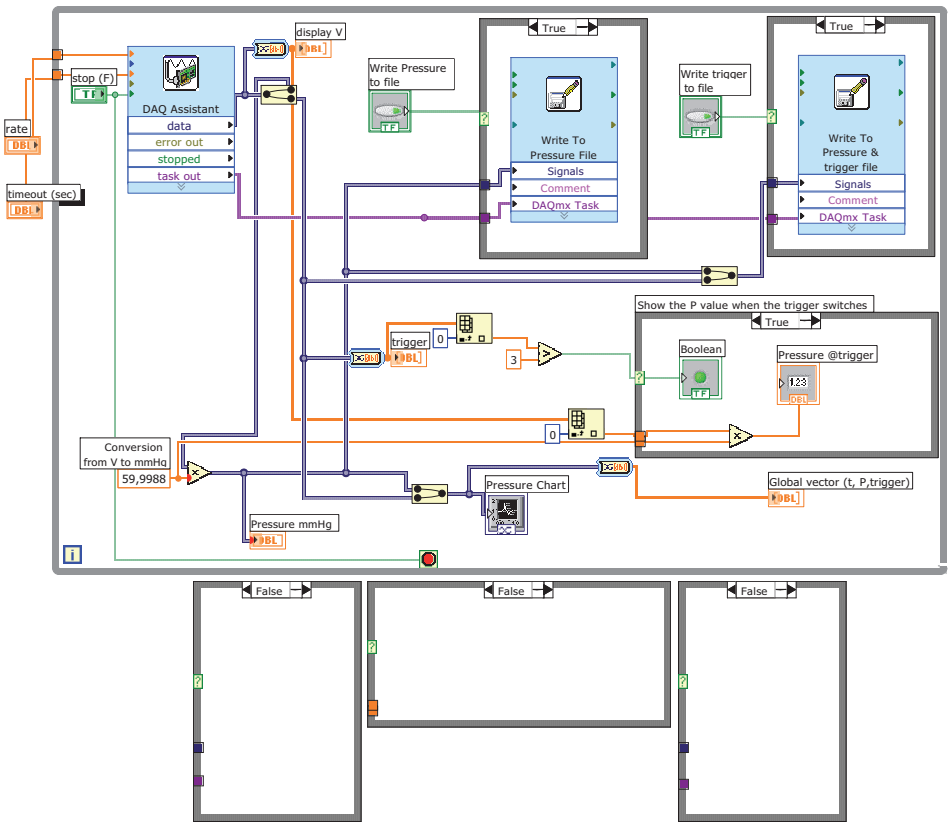


**Write To Pressure File**
Write To Measurement File
Writes data to a text-based measurement file (.lvm) or binary measurement file (.tdm).
---

This Express VI is configured as follows:

Mode: Save to one file
Filename: C:\Documents and Settings\Vittoria Flamini\My Documents\pressure sensor\pressure_meas.lvm
Ask Operator to choose file
If a file already exists: Rename and keep existing file
Description:

**Convert from Dynamic Data3**
Convert from Dynamic Data
Converts the dynamic data type to numeric, Boolean, waveform, and array data types for use with other VIs and functions.

pressure sensor.vi
D:\pressure sensor\pressure sensor.vi
Last modified on 19/11/2009 at 17.27
Printed on 03/08/2010 at 8.52

**Convert from Dynamic Data2**
Convert from Dynamic Data
Converts the dynamic data type to numeric, Boolean, waveform, and array data types for use with other VIs and functions.

**Convert from Dynamic Data**
Convert from Dynamic Data
Converts the dynamic data type to numeric, Boolean, waveform, and array data types for use with other VIs and functions.

Creates, edits, and runs tasks using NI-DAQmx. Refer to the DAQ Quick Start Guide for information on devices supported by NI-DAQmx.

When you place this Express VI on the block diagram, the DAQ Assistant launches to create a new task. After you create a task, you can double-click the DAQ Assistant Express VI in order to edit that task. For continuous measurement or generation, place a loop around the DAQ Assistant Express VI.

For continuous single-point input or output, the DAQ Assistant Express VI might not provide satisfactory performance. Refer to examples\DAQmx\Analog In\Measure Voltage.llb\Cont Acq&Graph Voltage-Single Point Optimization.vi for techniques to create higher-performance, single-point I/O applications.

**Write To Pressure & trigger file**
Write To Measurement File
Writes data to a text-based measurement file (.lvm) or binary measurement file (.tdm).
---

This Express VI is configured as follows:

Mode: Save to one file
Filename: C:\Documents and Settings\Vittoria Flamini\My Documents\pressure sensor\pressure_meas.lvm
Ask Operator to choose file
If a file already exists: Rename and keep existing file
Description:

## D.2 MATLAB®

### D.2.1 General image analysis

For both DTI and PC MRI techniques, image data from ROIs were obtained by using the following routine, although sometimes with small changes and different names (eg. masking in PC MRI routine).

```
function [cxo,cyo,circles_2,angles,Out,In]=figure_data_mod(mask)
%+++++++++++++++++++++++++++++++++++++++++++++++++++++++++++++++++++++++++
% In this function the geometrical data of the ROI are defined
%+++++++++++++++++++++++++++++++++++++++++++++++++++++++++++++++++++++++++
% define the mask
I= mask;

%number of layers & spacing
lay=5;
spacing=18;

%image resolution
resolution=[256 256 10];

% ======================================
% Define boundaries and parameters
% ======================================

% dilate the image
se = strel('disk', 1, 0);
BW1 = imdilate(I(:,:,1),se);

% find perimeter
BW2 = bwperim(BW1,8);

% get boundaries
Boundary=bwboundaries(BW2(:,:));
Out = Boundary{1};
In = Boundary{2};

% create points in the inner circumference
```

```
inner=In(round(linspace(1,length(In),spacing)),:);
inner(length(inner),:)=[]; % avoids the first and the last point being
                           % the same
% create corresponding points in the outer circumference
index=closest(inner, Out);
outer=Out(index,:);

%find centre of mass
L = bwlabel(I(:,:,1));
stats = regionprops(L,'all');
prop=[stats.Centroid];
cxo=round(prop(2));
cyo=round(prop(1));

% find radius
z=BW1([1:cyo],cxo,1);
rady=find(z);

% define vector angles equivalent to inner points
angles=zeros(length(inner(:,1)));

% translate inner points to center of mass
circ=[-(inner(:,2)-cyo) (inner(:,1)-cxo)];

% find ROI angles
angles=atan2(circ(:,2,1), circ(:,1,1));
ROI_angles=[angles inner outer];
ROI_matrix=sortrows(ROI_angles);

% =========================================================
% Create intermediate points
%=========================================================

inner_ord=[-(ROI_matrix(:,3)-cyo) -(ROI_matrix(:,2)-cxo)];
outer_ord=[-(ROI_matrix(:,5)-cyo) -(ROI_matrix(:,4)-cxo)];

for i=1:size(inner,1)

    for j=1:size(inner,2)
```

```
        nodes(i,j,:)=linspace(inner_ord(i,j),outer_ord(i,j),lay);

    end

end

circles=nodes([1:length(nodes),1],:,:);
ang=atan2(nodes(:,2,1),nodes(:,1,1));
circles_2=zeros(length(nodes),lay);

for i=1:lay

    circles_2(:,i)=resolution(1)*sqrt((nodes(:,2,i).^2)+...
        (nodes(:,1,i).^2));

end

%=============================================================
% Output vectors
%=============================================================
Out=[Out(:,2) Out(:,1)];
In=[In(:,2) In(:,1)];
```

### D.2.2 DTI: Tensor analysis

The routine that analysed tensor read the MedINRIA tensor using a Matlab® available on MedINRIA website.

```
function Tensor_analysis(bvalues,image_size,mask)%image_filename

% performs the analysis of the eigenvectors of the diffusion tensor
%% definition of the variables

eigenvalues=zeros(image_size(1),image_size(2),image_size(3),bvalues);
eigenvector_x=zeros(image_size(1),image_size(2),image_size(3),bvalues);
eigenvector_y=zeros(image_size(1),image_size(2),image_size(3),bvalues);
eigenvector_z=zeros(image_size(1),image_size(2),image_size(3),bvalues);
eigenv_angle_xy=zeros(image_size(1),image_size(2),image_size(3),...
    bvalues);

average=zeros(image_size(1),image_size(2),bvalues);
central_slice=zeros(image_size(1),image_size(2),bvalues);
mask_tens=ones(image_size(1),image_size(2),bvalues).*-30;

% definition of the files to be read
stock = char('18_08_b1.inr','18_08_b2.inr','18_08_b3.inr',...
    '18_08_b4.inr','18_08_b5.inr','18_08_b6.inr');

%% Read tensors and extrapolate eigenvectors
for i=1:bvalues

    [T,sp,origin] = ReadInrTensorData(stock(i,:));

    for j=1:image_size(1)

        for h= 1:image_size(2)

            for m=1:image_size(3)

                [VV,D]=eig(T{j,h,m});

                einval=[D(1,1) D(2,2) D(3,3)];
                value=(max(einval));
```

```
        if isempty(find(einval))==0

            index=find(einval==max(einval));

            eigenvalues(j,h,m,i)=D(index,index);
            eigenvector_x(j,h,m,i)=VV(1,index);
            eigenvector_y(j,h,m,i)=VV(2,index);
            eigenvector_z(j,h,m,i)=VV(3,index);

            plane=sqrt(((eigenvalues(j,h,m,i)*...
                VV(1,index))^2)+((eigenvalues(j,h,m,i)*...
                VV(2,index))^2));

            eigenv_angle_xy(j,h,m,i)=(atan2(...
                eigenvalues(j,h,m,i)*VV(3,index),plane))*...
                (180/pi);

            if eigenv_angle_xy(j,h,m,i)<0

                eigenv_angle_xy(j,h,m,i)=...
                    eigenv_angle_xy(j,h,m,i)+180;

            end

        else

            % eigenvectors of pixels
            % non belonging to the aorta,
            % i.e. with 0 eigenvalues, were given an out of
            % boundary value in order to filter them out
            eigenv_angle_xy(j,h,m,i)=-110;

        end

    end

end
```

```
    end

    average(:,:,i)=sum(eigenv_angle_xy(:,:,:,i),3)/16;
    central_slice(:,:,i)=eigenv_angle_xy(:,:,8,i);

end
%% Read start image

img=zeros(image_size(1),image_size(2),image_size(3));

file_name=[50 100 115 101 113 48 48 48 48]; % 2dseq0000 %

extension=char([116 105 102]); % tif

tic
for i=0:(image_size(3)-1)

    % definition of the sequential file name
    file_name(6:9)=[48+fix(i/1000) 48+fix(rem(i,1000)/100) 48+fix(...
        rem(rem(i,1000),100)/10) ...
        48+fix(rem(rem(rem(i,1000),100),10)/1)];

    % storage of the image in the matrix
    img(:,:,i+1)=imread(char(file_name),extension);

end
toc

%% Masking

E= imread(mask,'png');

I=flipud(fliplr(E(:,:,1)));

% dilate the image

se = strel('disk', 1, 0);
BW1 = imdilate(I(:,:,1),se);
```

```
BW2 = bwperim(BW1,8);

%find centre of mass
L = bwlabel(I(:,:,1));

Boundary=bwboundaries(BW2(:,:));
Out = Boundary{1};
In = Boundary{2};

%% Angle Distribution Evaluation

ind= find(base);
size(ind)
edges_1=[0:1:180];
normal_domain=zeros(length(edges_1),image_size(3),bvalues);
inverted_domain=zeros(length(edges_1),image_size(3),bvalues);
%invert angles

edges_2=[-90:1:90];

for j=1:bvalues

    for k=1:image_size(3)

        usematrix=eigenv_angle_xy(:,:,k,j);
        size(usematrix(ind))
        normal_domain(:,k,j)= ((hist(usematrix(ind),edges_1)));%

        dd=find(usematrix>90);

        usematrix(dd)=usematrix(dd)-180;

        inverted_domain(:,k,j)= ((hist(usematrix(ind),edges_2)));%

    end

end

M=[edges_1' normal_domain(:,8,4) edges_2' inverted_domain(:,8,4)];
```

```
xlswrite('angle_distribution',M)
```

### D.2.3 DTI: Fibre analysis

The function that estimates angles is made up of two functions with the following hierarchy:

- Fibres study
  - Fibre analysis: this function opens the .fib file where fibres are stored and evaluates $\gamma$

#### Fibres study

```
function fibres_study(resolution,imagefilename)
%
%
% This function reads the .fib files obtained from MedInria, computes
% the fibres and extracts the relevant data information such as fibre
% angle $\gamma$ and fibre distribution (evaluation of $\kappa$ in a
% separate routine). The resulting fibre angles are printed in a .xls
% file.
%
%
% This function require as input a vector of the resolution in the
% x,y,z directions and the name of the ROI file for which the fibres
% were tracked. The ROI file must be in a .png format.
%
%
%% read the mask and defines the layers
% ======================================
lay=6; % number of layers considered across the thickness of the tissue

[cxo1,cyo1,circles,angles]=figure_data_var(resolution,imagefilename,lay);


% definition of the center of mass (due to the different conventions
% between images coordinates they need to be inverted
cxo=128-cyo1;
cyo=128-cxo1;
%% read the fibres
```

```
% ========================================

% 6=number of fibres files (number of b values)

%--------------------------------------------------------------------------
% Grouping fibre angles

edges=[0.0:10:180.0];
langle=length(edges);
angle_distribution=zeros(langle,6); %angles across whole tissue
singlelayer=zeros(langle,(lay*d)+2,6); %angles on each layer
%--------------------------------------------------------------------------

%--------------------------------------------------------------------------
% Storage

dti_fibres = char('b1_3s_FV.fib','b2_3s_FV.fib','b3_3s_FV.fib',...
    'b4_3s_FV.fib','b5_3s_FV.fib','b6_3s_FV.fib'); % files containing
                                                   % the fibres
                                                   % coordinates for
                                                   % each b value
savefile = double('angles000.txt'); % storage of fibre angle
                                    % distribution  for the evaluation
                                    % of $\kappa$
%--------------------------------------------------------------------------


%% Find angles

for i=1:6 % b values

%--------------------------------------------------------------------------
% Fibre angle evaluation
%
% Function that evaluates the fibre angles and returns a variety of
% parameters. Since the fibre angle is defined as the tangent of the
% helix formed by the fibre, 'tangent' is the name of the vector
% containing the fibre angles
[nfibers,tangent,layer_data]=fibrenumberread(dti_fibres(i,:),cxo,...
```

```
    cyo,resolution,i,circles,angles,lay,edges);
%-------------------------------------------------------------------------


%-------------------------------------------------------------------------
% Output

angle_distribution(:,i)= ((hist(tangent,edges))'); %distribution over
                                                    % the whole aorta

singlelayer(:,:,i)=layer_data./nfibers; % distribution over the layers

% Write file for the evaluation of $\kappa$.

savefile(7:9)=[48+i 48 48]; % change file name to angles00x.txt
save(char(savefile), 'mtang','-ASCII') % write file
%-------------------------------------------------------------------------

end
%% Write data
% Dominant angles
size(angle_distribution);
size(edges);
superM=[ edges' angle_distribution];

xlswrite('fibres_at_10_deg', superM)
%% Write data
% Distribution over thickness

Layers=[ edges' singlelayer(:,:,1)...
    edges' singlelayer(:,:,2)...
    edges' singlelayer(:,:,3)...
    edges' singlelayer(:,:,4)...
    edges' singlelayer(:,:,5)...
    edges' singlelayer(:,:,6)];

xlswrite('layer_distribution_at_10_deg', Layers)
```

### Fibre analysis

```
function [nfibers,mtang,mstdtang,mvartang,mradius,mangle,fibertang]=
fibre_read(filename,Xo,Yo,resolution,num)

%funtion that reads the .fib file and analysies the fibres outputting
%the mean angle of each fibre

%--------------------------------------------------------------------
% open .fib file
fid=fopen(filename,'r');

%look for number of iteration
status = fseek(fid,40,'bof');
[A,count] = fread(fid,5,'char');

% look for number of fibres
nfibers=((A(1)-48)*10000)+((A(2)-48)*1000)+((A(3)-48)*100)+...
    ((A(4)-48)*10)+(A(5)-48);% char from 48 to 57 are numbers

%--------------------------------------------------------------------
%--------------------------------------------------------------------
% defining storing vectors
%--------------------------------------------------------------------
mtang=zeros(nfibers,1); %FIBRE MEAN ANGLE!
mstdtang=zeros(nfibers,1); %standard variation
mvartang=zeros(nfibers,1);

mradius=zeros(nfibers,1); % FIBRE MEAN RADIUS
mstdrad=zeros(nfibers,1); % standard deviation

mangle=zeros(nfibers,1); % position of the fibre in radians

fiberradii=zeros(200,(nfibers-1)); % fibre radius for each point
fiberx=zeros(200,(nfibers-1)); % fibre x coordinate
fiberangles=zeros(200,(nfibers-1)); %fibre angle for each point
fibery=zeros(200,(nfibers-1));% fibre y coordinate
fiberz=zeros(200,(nfibers-1));% fibre z coordinate
%--------------------------------------------------------------------
```

```
status = fseek(fid,618,'bof'); % read the file
index=1;

%=========================================================================
%Reads fibers from file and stores them in matrices.
%=========================================================================
for i=1:(nfibers-1)

    % read number of points of the fiber
    [A,count] = fread(fid,3,'char');

    if A(3)≥48 && A(3)≤58                                    % >10 fibres

        npoints=((A(1)-48)*100)+((A(2)-48)*10)+(A(3)-48);

        % read parameters of the fiber
        status = fseek(fid,11,'cof');

    elseif A(1)==32

        break

    else                                                     % <10 fibres

        npoints=((A(1)-48)*10)+(A(2)-48);

        % read parameters of the fiber
        status = fseek(fid,10,'cof');

    end

    %+++++++++++++++++++++++++++++++++++++++++++++++++++++++++++++++++++++++
    % read from file:
    % x y z tensor1 tensor2 tensor3 tensor4 tensor5 tensor6 fa ga i
    l1 l2 l3 xevmin yevmin zevmin xevmed yevmed zevmed xevmax yevmax
    zevmax md r red green blue
    [A,count] = fscanf(fid,'%f %f %f %f %f %f %f %f %f %f %f %f %f '
    '%f %f %f %f %f %f %f %f %f %f %f %f %f %f %f %f %f',[29 npoints]);
```

```
Points=A';


%+++++++++++++++++++++++++++++++++++++++++++++++++++++++++++++++++++++++
% transform from pixel to mm
Points(:,1)=Points(:,1)*resolution(1);
Points(:,2)=Points(:,2)*resolution(2);
Points(:,3)=Points(:,3)*resolution(3);


%+++++++++++++++++++++++++++++++++++++++++++++++++++++++++++++++++++++++
% shift to center
cpoint1=Points(:,1)-(Xo*resolution(1));
cpoint2=Points(:,2)-(Yo*resolution(2));


%+++++++++++++++++++++++++++++++++++++++++++++++++++++++++++++++++++++++
% define cylindrical coordinates
THETA=zeros(npoints,1);
RHO=zeros(npoints,1);
Z=zeros(npoints,1);

[THETA,RHO,Z] = cart2pol(cpoint1,cpoint2,Points(:,3));

THETA2=unwrap(THETA); %puts in order theta!


%+++++++++++++++++++++++++++++++++++++++++++++++++++++++++++++++++++++++
% assign quantities to storing vectors
fiberradii([1:npoints],i)=RHO;
fiberx([1:npoints],i)=Points(:,1);
fiberangles([1:npoints],i)=THETA2;
fibery([1:npoints],i)=Points(:,2);
fiberz([1:npoints],i)=Z;

mradius(i)=median(RHO);
mstdrad(i)=std(RHO);

mangle(i)=median(THETA2);
```

```
    mstdand(i)=std(THETA2);


    %+++++++++++++++++++++++++++++++++++++++++++++++++++++++++++++++++++
    % EVALUATE FIBRE ANGLE
    C=-diff(Points(:,3))./diff(THETA2); %derivative

    tang=(atan2(C,RHO(1:(npoints-1))))*180/pi;

    fibertang([1:(npoints-1)],i)=tang;

    mtang(i)=median(tang); %!!!

    %move from [-pi/2 pi/2] to [0 180]
    if mtang(i)<0

        mtang(i)=mtang(i)+180;

    end

    mstdtang(i)=std(tang);
    mvartang(i)=var(tang);


    %+++++++++++++++++++++++++++++++++++++++++++++++++++++++++++++++++++
    % end
    if i==(nfibers-1)
        %exit
        break

    else
        %move to next fibre
        status = fseek(fid,392,'cof');
        index=index+1;

    end

end
```

```
fclose(fid);
```

### D.2.4 PC MRI: Definition of elements and deformation velocity

The function that estimates deformation velocities from PC MRI images as the following hierarchy:

- Phase mesh
  - Masking (similar to the routine reported in section D.2.1)
  - Application of the method described in [124]
  - Evaluation of deformation velocity
  - Assign values to elements

#### Phase mesh

```
function phase_mesh
%%
%This function creates the matrices containing the deformation
%velocity and
%the geometry for each slice acquired during PC MRI

% PC MRI acquisition images
magnitude=double('mag0000.tif');
file=double('phase0000.tif');
destination=double('time000');
strain=double('strain000');
save_image=double('seig000risultante');
extension=double('tif');

%storage matrices
translation=ones(256,256,10);
images=zeros(256,256,10,4);
venc_im=zeros(256,256,30);

%storage file
savefile = double('data0006.txt');
eingfile = double('eing0006.txt');
```

```
mapfile=double('map0006.txt');

%define mesh parameters
layers=2;
lines=20;%eq to elements per slice

index=1;
%%
% ================================================================
% define centre of mass from first slice

mask(:,:)=imread(char(double('roi0000.bmp')));
[cxo,cyo,circles_2,angles,Out,In]=figure_data_mod(mask(:,:));

translation_x=translation;
translation_y=translation;

translation_x(:,1:cyo,:)=translation_x(:,1:cyo,:)*-1;
translation_y(1:cxo,:,:)=translation_y(1:cxo,:,:)*-1;
% ================================================================
%%
%================================================================
% read images
for j=0:8

    count=1;

    for i=0:3 % directions

        for h=0:9 % slices

            file(6:9)=[48+j 48+i 48 48+h];

            images(:,:,h+1,count) = imread(char(file));

        end

        count=count+1;
```

```
end

count2=2+(j*4);

% centering & masking with ROI
[volume,nodes_x,nodes_y,Coord]=masking...
    (j+1,layers,lines,cxo,cyo,angles);

% vectors for rigid translation and rotations
A=zeros(10,3); %A1 A2
omegaz=zeros(10,3);%omegaz>0 omegaz<0

for k=1:3

    % subtraction of reference image
    phase_im=images(:,:,:,k+1)-images(:,:,:,1);

    start=(10*(k-1));stop=10*k;

    % conversion from pixel value to angle -->
    % angle=pixel*pi/maxpixel
    phase_im_ang=(pi/65536)*phase_im;

    % VEnc=(2*pi/(42.58*(10^6)*(360*(10^-3))*((7.5*(10^-3))^2)))
    % (m/s)
    % VEnc 7.5 ms 0.0023
    venc_im_unmask=0.0023*phase_im_ang;

    % mask with ROIs
    artery=venc_im_unmask.*volume;

    % define deformation velocity according to patent
    [A(:,k),omegaz(:,k)]=patent(Coord,artery,k,j+1);

    % create a unique array of the velocity in the different
    % directions
    venc_im(:,:,[1+start:stop])=artery;

    count2=count2+1;
```

```
        index=index+1;

    end

    % evaluate V deformation
    [Vdef]=defvdef(A,omegaz,venc_im,volume,cxo,cyo,j+1);

    % evaluate spatial derivative
    [dVdx,dVdy]=derivativesxy(Vdef);
    [dVdz]=derivativesz(Vdef);

    % average on elements
    % assign values to elements defined in the mesh
    [map,element_dVvalue,eig_quantities,geometry]=meshing(nodes_x,...
        nodes_y,dVdx,dVdy,dVdz,Vdef);

    eig=cell2mat(eig_quantities);
    supermap=vertcat(map(:,:,1),map(:,:,2),map(:,:,3),map(:,:,4),...
        map(:,:,5),map(:,:,6),map(:,:,7),map(:,:,8),map(:,:,9),...
        map(:,:,10));

    % write output files
    mapfile(4:6)=[48+j 48 48];
    save(char(mapfile), 'supermap','-ASCII')

    data=horzcat(element_dVvalue,geometry);
    savefile(5:7)=[48+j 48 48];
    save(char(savefile), 'data','-ASCII')

    eingfile(5:7)=[48+j 48 48];
    save(char(eingfile), 'eig','-ASCII')

    save_image(5:7)=[49+j 48 48];

end
```

### Patent method [124]

```
function [A,omegaz,fig]=patent(Coord,Artery,k,w)
% Definition of patent parameters

A=zeros(10,1); %A1 A2
omegaz=zeros(10,1);%omegaz>0 omegaz<0

fig=zeros(2,1);

if k==1 %y, Vx

    for h=1:10

        D=Artery(:,:,h);
        [i,j]=find(D);

        points=[min(i):1:max(i)];

        vx=zeros(length(points),1);

        y=Coord{2,h}';

        a=length(y)-length(points);

        if a≥1

            %linear interpolation of Vy distribution
            y=y(1+fix(a/2):length(y)-rem(a,2)-fix(a/2));

        end

        for r=1:length(points)

            vx(r)=mean(nonzeros(D(points(r),:)));

        end

        b=polyfit(y,vx,1);
```

```
        A(h,1)=b(2); %rigid translation
        omegaz(h,1)=b(1); %rigid rotation

    end

elseif k==2 %x, Vy

    for h=1:10

        [i,j]=find(Artery(:,:,h));

        points=[min(j):1:max(j)];

        vy=zeros(length(points),1);

        x=Coord{1,h}';

        a=length(x)-length(points);

        if a≥1

            %linear interpolation of Vx distribution
            x=x(1+fix(a/2):length(x)-rem(a,2)-fix(a/2));

        end

        for r=1:length(points)

            vy(r)=mean(nonzeros(Artery(:,points(r),h)));

        end

        p=polyfit(x,vy,1);

        A(h,1)=p(2); %rigid translation
        omegaz(h,1)=p(1); %rigid rotation

    end
```

```
else % z, Vz

    A(:,1)=ones(10,1);
    omegaz(:,1)=ones(10,1);

end
```

### Evaluation of Velocity deformation

```
function [Vdef]=defvdef(Aa,omegaz,Venc,volume,cxo,cyo,index)
% Definition of deformation velocity according to patent

[a,b,c]=size(Venc);
Vdef=zeros(a,b,c);

% average of rigid rotations
Wz(1:10,1)=(abs(omegaz(:,1))+abs(omegaz(:,2)))/2;

for h=1:10

    [i,j]=find(volume(:,:,h));

    for s=1:length(i)

        Vdef(i(s),j(s),h)=Venc(i(s),j(s),h)-Aa(h,1)+((j(s)-cxo)
        .*Wz(h).*sign(omegaz(h,1)));
        Vdef(i(s),j(s),h+10)=Venc(i(s),j(s),h+10)-Aa(h,2)-((i(s)-cyo)
        .*Wz(h).*sign(omegaz(h,2)));
        Vdef(i(s),j(s),h+20)=Venc(i(s),j(s),h+20);

    end

    if h==10

        i=sort(i);
        j=sort(j);

    end
end
```

### Assign values to elements

```
function [map,element_dVvalue,eig_quantities,geometry]=
meshing(nodes_x,nodes_y,dVdx,dVdy,dVdz,venc_im)

% ========================================================================
% function that reads the nodes and the velocity gradients and gives
% back
% the average of the velocity gradient over the element and the
% eigenvectors
% ========================================================================
[a,b,c]=size(dVdx);

map=zeros(a,b,10);
points=zeros(a,b);
geometry=zeros(length(nodes_x),5); % center of mass x center of mass y
%width height position
element_dVvalue=zeros(length(nodes_x),12); % dVxdx dVydx dVzdx dVxdy
%dVydy dVzdy dVxdz dVydz dVzdz Vx Vy Vz
eig_quantities=cell(length(nodes_x),2); % cells containing eigenvalues
%& eigenvectors (D & V)
% ::::::::::::::::::::::::::::::::::::::::::::::::::::::::::::::::::::::::
% definition of the X Y vectors that will create the grid
% ::::::::::::::::::::::::::::::::::::::::::::::::::::::::::::::::::::::::

for i=1:256

    X((i*256)-255:i*256)=i*ones(256,1);
    Y((i*256)-255:i*256)=[1:1:256]';

end

terminal=length(nonzeros(nodes_x(:,9)));

for j=1:terminal % for every element

    slice=nonzeros(nodes_x(j,9));
      %   j, length(nodes_x)
    element_1_x=[nodes_x(j,1:4) nodes_x(j,1)];
```

```
element_1_y=[nodes_y(j,1:4) nodes_y(j,1)];
IN_1=inpolygon(X,Y,element_1_x,element_1_y);

element_2_x=[nodes_x(j,5:8) nodes_x(j,1)];
element_2_y=[nodes_y(j,5:8) nodes_y(j,1)];
IN_2=inpolygon(X,Y,element_2_x,element_2_y);

points(IN_1)=j;

map(:,:,slice)=map(:,:,slice)+points;

points_BW=bwlabel(points);

% define element geometry parameters
stats = regionprops(points_BW,'all');
prop=[stats.Centroid];
bx=round(prop(2));
by=round(prop(1));
width=[stats.MajorAxisLength];
height=[stats.MinorAxisLength];

geometry(j,:)=[bx by width height nodes_x(j,9)];

for u=1:3

    dX=dVdx(:,:,slice*u);
    dY=dVdy(:,:,slice*u);
    dZ=dVdz(:,:,slice*u);

    % assign value to starting points
    element_dVvalue(j,(u*3-2):(u*3))=[(mean(dX(IN_1))+mean...
        (dX(IN_2)))*0.5 (mean(dY(IN_1))+mean(dY(IN_2)))*0.5 ...
        (mean(dZ(IN_1))+mean(dZ(IN_2)))*0.5];

end

    Vx=venc_im(:,:,slice);
    Vy=venc_im(:,:,slice+10);
    Vz=venc_im(:,:,slice+20);
```

```
        element_dVvalue(j,10:12)=[median(Vx(IN_1))  ...
            median(Vy(IN_1)) median(Vz(IN_1))];

    % 0.1=time step ==> transforms strain rate into strain
    tensor=0.1*[element_dVvalue(j,3) 0.5*(element_dVvalue(j,2)+...
        element_dVvalue(j,4)); ...
        0.5*(element_dVvalue(j,2)+element_dVvalue(j,4)) ...
        element_dVvalue(j,5)];

    [VV,D]=eig(tensor);

    eig_quantities{j,1}=D;
    eig_quantities{j,2}=VV;

    points=zeros(a,b);

end
```

### D.2.5 PC MRI: Circumferential strains

```
function circumferential_strain

% This function evaluates circumferential strains starting from the
PC MRI
% data stored in the files for each time step

% Output form phase_mesh.m (maps concatenated vertically)
savefile = double('data0004.txt');
eingfile = double('eing0004.txt');
mapfile=double('map0004.txt');

% Storage vectors
translation=ones(256,256,10);
Trajectory_f=zeros(180,6,9);%ten points, three coordinates, nine time
%steps %225
Trajectory_b=zeros(180,6,9);%ten points, three coordinates, nine time
%steps
Trajectory_r=zeros(180,6,9);%ten points, three coordinates, nine time
%steps
strain=zeros(180,9);
% ================================================================
% define centre of mass from first slice

mask(:,:)=imread(char(double('roi0000.bmp')));
[cxo,cyo,circles_2,ang,Out,In]=figure_data_var(mask(:,:,1,1));

translation_x=translation;
translation_y=translation;

translation_x(:,1:cyo,:)=translation_x(:,1:cyo,:)*-1;
translation_y(1:cxo,:,:)=translation_y(1:cxo,:,:)*-1;
% ================================================================

% ================================================================
for j=0:8

    %-------------------------------------------------------------
```

```
% open files
mapfile(4:6)=[48+j 48 48];
savefile(5:7)=[48+j 48 48];
eingfile(5:7)=[48+j 48 48];

dataf1 = load(char(savefile));
eigenf1 = load(char(eingfile));
mapsf1 = load(char(mapfile));

num_nodes=max(mapsf1(256,:));
%-------------------------------------------------------------

iterations=[1:num_nodes:length(dataf1(:,1))];

%-------------------------------------------------------------

step=[0.000117*dataf1(:,15) 0.000117*dataf1(:,16) 0.0015*
    ones(length(dataf1(:,1)),1)];

count=9-j;
index=1+j;

L=length(dataf1(:,1));

if j==0

    % ================================================================
    % determine starting points

    pointfy=dataf1(:,14);
    pointfx=dataf1(:,13);
    [thetaf, radiusf] = cart2pol(pointfx-cyo,pointfy-cxo);
    pointfz=ones(L,1);

    pointby=dataf1(:,14);
    pointbx=dataf1(:,13);
    [thetab, radiusb] = cart2pol(pointbx-cyo,pointby-cxo);
    pointbz=ones(L,1);
    % ================================================================
```

```
    Trajectory_r(:,1:3,1)=[pointfx pointfy pointfz];
    Trajectory_f(:,1:3,1)=Trajectory_r(:,1:3,1);
    Trajectory_b(:,1:3,end)=Trajectory_r(:,1:3,1);

    index=1;
    %   forward integration starting points=element centre
    [theta, radius] = cart2pol((0.000117)*(pointfx-cyo),(0.000117)
    *(pointfy-cxo));
    fkx=0.000117*pointfx;
    fky=0.000117*pointfy;
    fkr=radius;
    fkt=theta;
    fkz=0.0015*ones(L,1);

    %   backward integration starting points=element centre
    bkx=0.000117*pointbx;
    bky=0.000117*pointby;
    bkr=radius;
    bkt=theta;
    bkz=0.0015*ones(L,1);

    step=[(0.000117*dataf1(:,15))/2 (0.000117*dataf1(:,16))/2
        (0.0015*ones(length(dataf1(:,1)),1))/2];

    count=0;

elseif j==8

    index=1;

end

% Forward velocity
savefile(5:7)=[48+index 48 48];
dataf2 = load(char(savefile));

venc_im_f1=[dataf1(:,10) dataf1(:,11) dataf1(:,12)];
venc_im_f2=[dataf2(:,10) dataf2(:,11) dataf2(:,12)];
```

```
    % Backward velocity
    savefile(5:7)=[48+count 48 48];
    datab1 = load(char(savefile));

    savefile(5:7)=[48+8-j 48 48];
    datab2 = load(char(savefile));

    venc_im_b1=[datab1(:,10) datab1(:,11) datab1(:,12)];
    venc_im_b2=[datab2(:,10) datab2(:,11) datab2(:,12)];

    %   forward integration
    [fkx,fky,fkz,pointfx,pointfy,pointfz]=
    forward_integration_g(venc_im_f1, venc_im_f2, fkx,fky,fkz,
    pointfx,pointfy,pointfz,step);

    Trajectory_f(:,:,j+1)=[pointfx pointfy pointfz fkx fky fkz]; % j+2

    %   backward integration
    [bkx,bky,bkz,pointbx,pointby,pointbz]=
    backward_integration_g(venc_im_b1, venc_im_b2, bkx,bky,bkz,
    pointbx,pointby,pointbz,step);

    Trajectory_b(:,:,(end)-j)=[pointbx pointby pointbz bkx bky bkz];
    %(end-1)-j

    % assign output
    fkx=fkx;
    fky=fky;
    fkz=fkz;

    bkx=bkx;
    bky=bky;
    bkz=bkz;

end

%=============================================================
% Determine global trajectory
```

```
for k=0:8

    wk=(9-(k+1)+1)/9;
    Trajectory_r(:,:,k+1)=(wk*Trajectory_f(:,:,k+1))+
    ((1-wk)*Trajectory_b(:,:,k+1));

    [th(:,k+1),r(:,k+1)]=cart2pol(Trajectory_r(:,4,k+1)-
    (cyo*0.000117),Trajectory_r(:,5,k+1)-(cxo*0.000117));

end

%=================================================================
% Determine circumferential strain
for k=0:8

    strain_angle=th(:,k+1)+(pi/2);

    radial=((r(:,k+1)./Ro).^2);

    strain(:,k+1)=0.5*(radial-1);

    components_circum_strain(:,:,k+1)=[strain(:,k+1).*
        cos(strain_angle) strain(:,k+1).*sin(strain_angle)];

end
```

### D.2.6 FE: Mesh from MRI data

This routine is based on the general image analysis routine, and it is extended to the definition of nodes, of the element, and of the surface to which the pressure will be applied.

```
function initialmesh
% This function defines a mesh of the aorta starting from PC MRI images

% define starting ROIs
file_mask=double('2roi000.png');

% storage vectors
mask=zeros(257,257,10);
nodes_x=zeros(135, 9);
nodes_y=zeros(135, 9);
Coord=cell(2,10);

% mesh parameters
layers=8;
lines=60; %max number of lines=69 (limit due to the number of the
          %pixels)
interslices=4;
% =================================================================
%% define centre of mass from first slice

mask1=imread(char(double('2roi000.png')));
[cxo,cyo,circles_2,angles,Out,In]=figure_data_mod(mask1(:,:,1));
% =================================================================

n_count=1;
count=0;
points=[1:lines:(lines*layers*10)+1];

for h=0:9

    file_mask(5:7)=[48 48 48+h];
    prova=imread(char(file_mask));
```

```
mask(:,:,h+1)=prova(:,:,1);

AA=mask(:,:,h+1);
[i,j]=find(AA);
Coord{1,h+1}=[-cyo+min(j):1:257-cyo-(257-max(j))];
Coord{2,h+1}=[-cxo+min(i):1:257-cxo-(257-max(i))];
% ======================================
% Define boundaries and parameters
% ======================================

% dilate the image
se = strel('disk', 1, 0);
BW1 = imdilate(mask(:,:,h+1),se);

% find perimeter
BW2 = bwperim(BW1,8);

% get boundaries
Boundary=bwboundaries(BW2(:,:));
Out = Boundary{1};
In = Boundary{2};

inner=inner_spacing(In,lines,cxo,cyo);

index=closest_v(inner,Out,cxo,cyo);
outer=Out(index,:);

% translate inner points to center of mass
circ=[-(inner(:,2)-cyo) (inner(:,1)-cxo)];

% find ROI angles
angles3=atan2(circ(:,2,1), circ(:,1,1));
ROI_angles=[angles3 inner outer];
ROI_matrix=sortrows(ROI_angles);

inner_ord=[(ROI_matrix(:,3)) (ROI_matrix(:,2))];
outer_ord=[(ROI_matrix(:,5)) (ROI_matrix(:,4))];

% ======================================================
```

```
% Create intermediate points in the boundaries
% ========================================================

for i=1:size(inner,1)

    for j=1:size(inner,2)

        nodes_prov(i,j,:)=linspace(inner_ord(i,j),...
            outer_ord(i,j),layers);

        n_count=n_count+1;
    end

end

for t=1:layers

    % assign nodes coordinates
    nodes(points(count+t):points(count+t+1)-1,:)=[...
        [points(count+t):1:points(count+t+1)-1]' ...
        (nodes_prov(:,1,t)-cxo)*0.000117 ...
        (nodes_prov(:,2,t)-cyo)*0.000117  0.0015*h*ones(lines,1)];

end

count=count+layers;

for u=1:layers-1

    in=(u*size(nodes_prov,1))-(size(nodes_prov,1)-1);
    nod_reord(in:in-1+size(nodes_prov,1),1:8)=[...
        nodes_prov(:,:,u) nodes_prov(:,:,u+1) ...
        circshift(nodes_prov(:,:,u),-1) ...
        circshift(nodes_prov(:,:,u+1),-1)];

end

Out=[Out(:,2) Out(:,1)];
In=[In(:,2) In(:,1)];
```

```
% ================================================================
% Save nodes
% ================================================================

slice=(h+1)*ones(length(nod_reord(:,1)),1); % slice pointer

if h==0

    nodes_x(1:length(nod_reord),1:4)=([nod_reord(:,1) ...
        nod_reord(:,3) nod_reord(:,7) nod_reord(:,5)]-cyo)*0.117;
    nodes_y(1:length(nod_reord),1:4)=([nod_reord(:,2) ...
        nod_reord(:,4) nod_reord(:,8) nod_reord(:,6)]-cxo)*0.117;

elseif h==9

    nodes_x((length(nod_reord)*8)+1:(length(nod_reord)*9),5:8)...
        =([nod_reord(:,1) nod_reord(:,3) nod_reord(:,7) ...
        nod_reord(:,5)]-cyo)*0.117;
    nodes_x((length(nod_reord)*8)+1:(length(nod_reord)*9),9)=...
        0.0015*[slice];
    nodes_y((length(nod_reord)*8)+1:(length(nod_reord)*9),5:8)...
        =([nod_reord(:,2) nod_reord(:,4) nod_reord(:,8) ...
        nod_reord(:,6)]-cxo)*0.117;
    nodes_y((length(nod_reord)*8)+1:(length(nod_reord)*9),9)=...
        0.0015*[slice];

else

    nodes_x((length(nod_reord)*(h-1))+...
        1:(length(nod_reord)*(h)),5:8)=([nod_reord(:,1) ...
        nod_reord(:,3) nod_reord(:,7) nod_reord(:,5)]-cyo)*0.117;
    nodes_x((length(nod_reord)*8)+1:(length(nod_reord)*9),9)=...
        0.0015*[slice];
    nodes_x((length(nod_reord)*(h))+...
        1:(length(nod_reord)*(h+1)),1:4)=([nod_reord(:,1) ...
        nod_reord(:,3) nod_reord(:,7) nod_reord(:,5)]-cyo)*0.117;

    nodes_y((length(nod_reord)*(h-1))+...
```

```
            1:(length(nod_reord)*(h)),5:8)=([nod_reord(:,2) ...
            nod_reord(:,4) nod_reord(:,8) nod_reord(:,6)]-cxo)*0.117;
        nodes_y((length(nod_reord)*8)+1:(length(nod_reord)*9),9)=...
            0.0015*[slice];
        nodes_y((length(nod_reord)*(h))+...
            1:(length(nod_reord)*(h+1)),1:4)=([nod_reord(:,2) ...
            nod_reord(:,4) nod_reord(:,8) nod_reord(:,6)]-cxo)*0.117;

    end


end
%% Create interslices (axial divisions)

if interslices≥1

    % storage vectors
    points_is=[1:lines*(layers):...
        (lines*(layers)*(10+(interslices*9)))+1];

    position=[1:lines*(layers):lines*(layers)*(interslices+1)+1];

    place=[1:lines*(layers):lines*(layers)*10];

    nodes_is=zeros((lines*(layers)*(10+(interslices*9))),4);

    for h=1:9 %slices-1

        for u=1:lines*layers

            nodes_is_size=length(position);

            % linear interpolation of the points belonging to two
            % PC MRI slices
            vector=[linspace(nodes(place(1),2),nodes(place(2),2),...
                (interslices+2))' ...
                linspace(nodes(place(1),3),nodes(place(2),3),...
                (interslices+2))' linspace(nodes(place(1),4),...
                nodes(place(2),4),(interslices+2))'];
```

```
            for t=1:nodes_is_size

                nodes_is(position(t),:)=[position(t) vector(t,:)];

            end
            position=position+1;
            place=place+1;

        end

        position=[lines*(layers)*(interslices+1)*h+1:lines*...
            (layers):lines*(layers)*(interslices+1)*(h+1)+1];

    end

end

%*******ELEMENTS*****************************************************

sizc = lines;%circumferential size(c_nodes,2);
sizr = layers; %radial, 1 less element than nodes in radial direction
               %size(c_nodes,3);
siza = 10+(9*interslices); %axial, 1 less element than nodes in axial
               % direction size(c_nodes,4);

c_elements = zeros( sizc + (sizr-2)*sizc + (siza-2)*sizc*(sizr-1) ,8);

c_count = [];

for k = 1:siza-1

    for j = 1:sizr-1


        for i = 1:sizc

            c_elements( i + (j-1)*sizc + (k-1)*sizc*(sizr-1) ,1) =...
                i + (j-1)*sizc + (k-1)*sizc*sizr;
```

```
            c_elements( i + (j-1)*sizc + (k-1)*sizc*(sizr-1) ,2) = ...
                i + 1 + (j-1)*sizc + (k-1)*sizc*sizr;

            c_elements( i + (j-1)*sizc + (k-1)*sizc*(sizr-1) ,3) =...
                i + 1 + (j)*sizc + (k-1)*sizc*sizr;

            c_elements( i + (j-1)*sizc + (k-1)*sizc*(sizr-1) ,4) =...
                i + (j)*sizc + (k-1)*sizc*sizr;

            c_elements( i + (j-1)*sizc + (k-1)*sizc*(sizr-1) ,5) =...
                i + (j-1)*sizc + (k)*sizc*sizr;

            c_elements( i + (j-1)*sizc + (k-1)*sizc*(sizr-1) ,6) =...
                i + 1 + (j-1)*sizc + (k)*sizc*sizr;

            c_elements( i + (j-1)*sizc + (k-1)*sizc*(sizr-1) ,7) =...
                i + 1 + (j)*sizc + (k)*sizc*sizr;

            c_elements( i + (j-1)*sizc + (k-1)*sizc*(sizr-1) ,8) =...
                i + (j)*sizc + (k)*sizc*sizr;

            if i == sizc % as there are as many circumferential nodes
                         % and elements


                c_elements( i + (j-1)*sizc + ...
                    (k-1)*sizc*(sizr-1) ,2) = c_elements...
                    ( i + (j-1)*sizc + (k-1)*sizc*(sizr-1) ,2) -
sizc;
                c_elements( i + (j-1)*sizc + ...
                    (k-1)*sizc*(sizr-1) ,3) = c_elements...
                    ( i + (j-1)*sizc + (k-1)*sizc*(sizr-1) ,3) -
sizc;
                c_elements( i + (j-1)*sizc + ...
                    (k-1)*sizc*(sizr-1) ,6) = c_elements...
                    ( i + (j-1)*sizc + (k-1)*sizc*(sizr-1) ,6) -
sizc;
                c_elements( i + (j-1)*sizc + ...
                    (k-1)*sizc*(sizr-1) ,7) = c_elements...
```

```
                    ( i + (j-1)*sizc + (k-1)*sizc*(sizr-1) ,7) -
sizc;

            end

            if j == 1; c_count = [c_count, i + (j-1)*sizc + ...
                    (k-1)*sizc*(sizr-1)]; end;

        end
    end
end

for j = 2:sizr-1; c_count(j,:) = c_count(1,:) + (j-1)*sizc; end

nel=[1:length(c_elements)]';
elements=[nel c_elements];
%*********************************************************************
%*******ELSET*********************************************************
% this set define the internal area of the aorta where the pressure is
% applies
thickness=lines*(layers-1);
elemensets=zeros(1,lines*9);
count=0;
count2=0;

for h=1:9+9*interslices

    elemensets(count+1:count+lines)=[count2+1:count2+lines];

    count=count+lines;
    count2=count2+thickness;

end

division=1:16:length(elemensets);
el_set=zeros(length(division),16);

for j=1:length(division)-1
```

```
    el_set(j,:)=elemensets(division(j):1:division(j+1)-1);

end
odds=length(elemensets(division(end):end));
el_set(end,1:odds)=elemensets(division(end):end);
% ****************************************************************

Writefile(nodes_is,elements,el_set,'vitto_mesh')
```

### D.2.7 FE: Iterative

The iterative routine follows this hierarchy:

- Abaqus iteration
  - Abaqus routine call
  - Phyton script:

#### Abaqus iteration

```
function initialmesh
% This function defines a mesh of the aorta starting from PC MRI images

% define starting ROIs
file_mask=double('2roi000.png');

% storage vectors
mask=zeros(257,257,10);
nodes_x=zeros(135, 9);
nodes_y=zeros(135, 9);
Coord=cell(2,10);

% mesh parameters
layers=8;
lines=60; %max number of lines=69 (limit due to the number of the
          %pixels)
interslices=4;
% =================================================================
%% define centre of mass from first slice

mask1=imread(char(double('2roi000.png')));
[cxo,cyo,circles_2,angles,Out,In]=figure_data_mod(mask1(:,:,1));
% =================================================================

n_count=1;
count=0;
points=[1:lines:(lines*layers*10)+1];
```

```
for h=0:9

    file_mask(5:7)=[48 48 48+h];
    prova=imread(char(file_mask));

    mask(:,:,h+1)=prova(:,:,1);

    AA=mask(:,:,h+1);
    [i,j]=find(AA);
    Coord{1,h+1}=[-cyo+min(j):1:257-cyo-(257-max(j))];
    Coord{2,h+1}=[-cxo+min(i):1:257-cxo-(257-max(i))];
    % ======================================
    % Define boundaries and parameters
    % ======================================

    % dilate the image
    se = strel('disk', 1, 0);
    BW1 = imdilate(mask(:,:,h+1),se);

    % find perimeter
    BW2 = bwperim(BW1,8);

    % get boundaries
    Boundary=bwboundaries(BW2(:,:));
    Out = Boundary{1};
    In = Boundary{2};

    inner=inner_spacing(In,lines,cxo,cyo);

    index=closest_v(inner,Out,cxo,cyo);
    outer=Out(index,:);

    % translate inner points to center of mass
    circ=[-(inner(:,2)-cyo) (inner(:,1)-cxo)];

    % find ROI angles
    angles3=atan2(circ(:,2,1), circ(:,1,1));
    ROI_angles=[angles3 inner outer];
    ROI_matrix=sortrows(ROI_angles);
```

```
inner_ord=[(ROI_matrix(:,3)) (ROI_matrix(:,2))];
outer_ord=[(ROI_matrix(:,5)) (ROI_matrix(:,4))];

% =========================================================
% Create intermediate points in the boundaries
% =========================================================

for i=1:size(inner,1)

    for j=1:size(inner,2)

        nodes_prov(i,j,:)=linspace(inner_ord(i,j),...
            outer_ord(i,j),layers);

        n_count=n_count+1;
    end

end

for t=1:layers

    % assign nodes coordinates
    nodes(points(count+t):points(count+t+1)-1,:)=[...
        [points(count+t):1:points(count+t+1)-1]' ...
        (nodes_prov(:,1,t)-cxo)*0.000117 ...
        (nodes_prov(:,2,t)-cyo)*0.000117  0.0015*h*ones(lines,1)];

end

count=count+layers;

for u=1:layers-1

    in=(u*size(nodes_prov,1))-(size(nodes_prov,1)-1);
    nod_reord(in:in-1+size(nodes_prov,1),1:8)=[...
        nodes_prov(:,:,u) nodes_prov(:,:,u+1) ...
        circshift(nodes_prov(:,:,u),-1) ...
        circshift(nodes_prov(:,:,u+1),-1)];
```

```
end

Out=[Out(:,2) Out(:,1)];
In=[In(:,2) In(:,1)];

% ================================================================
% Save nodes
% ================================================================

slice=(h+1)*ones(length(nod_reord(:,1)),1); % slice pointer

if h==0

    nodes_x(1:length(nod_reord),1:4)=([nod_reord(:,1) ...
        nod_reord(:,3) nod_reord(:,7) nod_reord(:,5)]-cyo)*0.117;
    nodes_y(1:length(nod_reord),1:4)=([nod_reord(:,2) ...
        nod_reord(:,4) nod_reord(:,8) nod_reord(:,6)]-cxo)*0.117;

elseif h==9

    nodes_x((length(nod_reord)*8)+1:(length(nod_reord)*9),5:8)...
        =([nod_reord(:,1) nod_reord(:,3) nod_reord(:,7) ...
        nod_reord(:,5)]-cyo)*0.117;
    nodes_x((length(nod_reord)*8)+1:(length(nod_reord)*9),9)=...
        0.0015*[slice];
    nodes_y((length(nod_reord)*8)+1:(length(nod_reord)*9),5:8)...
        =([nod_reord(:,2) nod_reord(:,4) nod_reord(:,8) ...
        nod_reord(:,6)]-cxo)*0.117;
    nodes_y((length(nod_reord)*8)+1:(length(nod_reord)*9),9)=...
        0.0015*[slice];

else

    nodes_x((length(nod_reord)*(h-1))+...
        1:(length(nod_reord)*(h)),5:8)=([nod_reord(:,1) ...
        nod_reord(:,3) nod_reord(:,7) nod_reord(:,5)]-cyo)*0.117;
    nodes_x((length(nod_reord)*8)+1:(length(nod_reord)*9),9)=...
        0.0015*[slice];
```

```
        nodes_x((length(nod_reord)*(h))+...
            1:(length(nod_reord)*(h+1)),1:4)=([nod_reord(:,1) ...
            nod_reord(:,3) nod_reord(:,7) nod_reord(:,5)]-cyo)*0.117;

        nodes_y((length(nod_reord)*(h-1))+...
            1:(length(nod_reord)*(h)),5:8)=([nod_reord(:,2) ...
            nod_reord(:,4) nod_reord(:,8) nod_reord(:,6)]-cxo)*0.117;
        nodes_y((length(nod_reord)*8)+1:(length(nod_reord)*9),9)=...
            0.0015*[slice];
        nodes_y((length(nod_reord)*(h))+...
            1:(length(nod_reord)*(h+1)),1:4)=([nod_reord(:,2) ...
            nod_reord(:,4) nod_reord(:,8) nod_reord(:,6)]-cxo)*0.117;

    end


end
%% Create interslices (axial divisions)

if interslices≥1

    % storage vectors
    points_is=[1:lines*(layers):...
        (lines*(layers)*(10+(interslices*9)))+1];

    position=[1:lines*(layers):lines*(layers)*(interslices+1)+1];

    place=[1:lines*(layers):lines*(layers)*10];

    nodes_is=zeros((lines*(layers)*(10+(interslices*9))),4);

    for h=1:9 %slices-1

        for u=1:lines*layers

            nodes_is_size=length(position);

            % linear interpolation of the points belonging to two
            % PC MRI slices
```

```
            vector=[linspace(nodes(place(1),2),nodes(place(2),2),...
                (interslices+2))' ...
                linspace(nodes(place(1),3),nodes(place(2),3),...
                (interslices+2))' linspace(nodes(place(1),4),...
                nodes(place(2),4),(interslices+2))'];

            for t=1:nodes_is_size

                nodes_is(position(t),:)=[position(t) vector(t,:)];

            end
            position=position+1;
            place=place+1;

        end

        position=[lines*(layers)*(interslices+1)*h+1:lines*...
            (layers):lines*(layers)*(interslices+1)*(h+1)+1];

    end

end

%*******ELEMENTS*****************************************************

sizc = lines;%circumferential size(c_nodes,2);
sizr = layers; %radial, 1 less element than nodes in radial direction
               %size(c_nodes,3);
siza = 10+(9*interslices); %axial, 1 less element than nodes in axial
               % direction size(c_nodes,4);

c_elements = zeros( sizc + (sizr-2)*sizc + (siza-2)*sizc*(sizr-1) ,8);

c_count = [];

for k = 1:siza-1

    for j = 1:sizr-1
```

```
        for i = 1:sizc

            c_elements( i + (j-1)*sizc + (k-1)*sizc*(sizr-1) ,1) =...
                i + (j-1)*sizc + (k-1)*sizc*sizr;

            c_elements( i + (j-1)*sizc + (k-1)*sizc*(sizr-1) ,2) = ...
                i + 1 + (j-1)*sizc + (k-1)*sizc*sizr;

            c_elements( i + (j-1)*sizc + (k-1)*sizc*(sizr-1) ,3) =...
                i + 1 + (j)*sizc + (k-1)*sizc*sizr;

            c_elements( i + (j-1)*sizc + (k-1)*sizc*(sizr-1) ,4) =...
                i + (j)*sizc + (k-1)*sizc*sizr;

            c_elements( i + (j-1)*sizc + (k-1)*sizc*(sizr-1) ,5) =...
                i + (j-1)*sizc + (k)*sizc*sizr;

            c_elements( i + (j-1)*sizc + (k-1)*sizc*(sizr-1) ,6) =...
                i + 1 + (j-1)*sizc + (k)*sizc*sizr;

            c_elements( i + (j-1)*sizc + (k-1)*sizc*(sizr-1) ,7) =...
                i + 1 + (j)*sizc + (k)*sizc*sizr;

            c_elements( i + (j-1)*sizc + (k-1)*sizc*(sizr-1) ,8) =...
                i + (j)*sizc + (k)*sizc*sizr;

            if i == sizc % as there are as many circumferential nodes
                         % and elements


                c_elements( i + (j-1)*sizc + ...
                    (k-1)*sizc*(sizr-1) ,2) = c_elements...
                    ( i + (j-1)*sizc + (k-1)*sizc*(sizr-1) ,2) -
sizc;
                c_elements( i + (j-1)*sizc + ...
                    (k-1)*sizc*(sizr-1) ,3) = c_elements...
                    ( i + (j-1)*sizc + (k-1)*sizc*(sizr-1) ,3) -
sizc;
                c_elements( i + (j-1)*sizc + ...
```

```
                    (k-1)*sizc*(sizr-1) ,6) = c_elements...
                    ( i + (j-1)*sizc + (k-1)*sizc*(sizr-1) ,6) -
sizc;
                c_elements( i + (j-1)*sizc + ...
                    (k-1)*sizc*(sizr-1) ,7) = c_elements...
                    ( i + (j-1)*sizc + (k-1)*sizc*(sizr-1) ,7) -
sizc;

            end

            if j == 1; c_count = [c_count, i + (j-1)*sizc + ...
                    (k-1)*sizc*(sizr-1)]; end;

        end
    end
end

for j = 2:sizr-1; c_count(j,:) = c_count(1,:) + (j-1)*sizc; end

nel=[1:length(c_elements)]';
elements=[nel c_elements];
%*************************************************************************
%*******ELSET*************************************************************
% this set define the internal area of the aorta where the pressure is
% applies
thickness=lines*(layers-1);
elemensets=zeros(1,lines*9);
count=0;
count2=0;

for h=1:9+9*interslices

    elemensets(count+1:count+lines)=[count2+1:count2+lines];

    count=count+lines;
    count2=count2+thickness;

end
```

```
division=1:16:length(elemensets);
el_set=zeros(length(division),16);

for j=1:length(division)-1

    el_set(j,:)=elemensets(division(j):1:division(j+1)-1);

end
odds=length(elemensets(division(end):end));
el_set(end,1:odds)=elemensets(division(end):end);
% ********************************************************************

Writefile(nodes_is,elements,el_set,'vitto_mesh')
```

### Abaqus routine call

```
function averages=ab_rout(c,k11,k22,file, command)

%import old .inp file
%*********************************************************************

fid = fopen('vitto_new.inp');
C = textscan(fid, '%q', 'Whitespace', '');
fclose(fid);

C = C{1};

ind1 = [];


% find line of material properties in .inp file
%*********************************************************************

for i = 1:length(C)
    if length(C{i}) == length('*anisotropic hyperelastic,holzapfel,
        local directions=2');
        if C{i} == '*anisotropic hyperelastic,holzapfel,
            local directions=2'
            ind1 = i;
            break;
        end;
    end
end


ind1 = ind1+1;

C{ind1};


%change properties
%*********************************************************************
```

```
c10 = c;
k1 = k11;
k2 = k22;

material_str = [' ',num2str(c10),', 0, ',num2str(k1),', ',num2str(k2),
    ', 0.11 '];


%*********************************************************************
%write new file


fid = fopen(char(file),'w+');

D = [ C(1:ind1-1); cellstr(material_str); C(ind1+1:end) ];

for i = 1:length(D)

    fprintf(fid,[D{i}, '\n']);

end

fclose(fid);

%*********************************************************************
%run new file


[sta, string_out] = system(char(command));

pause(50)
% average value from last simulation
%*********************************************************************

name=double('abaqus python extract_NE22_step0.py');
averages=zeros(9,1);

for j=1:9
```

```
    name(32)=48+j;

    [sta, string_out] = system(char(name));

    s_out = str2num(string_out); % average s22

    averages(j)=s_out;

end
```

### Phyton script

```
from odbAccess import *

odb = openOdb('uniaxial.odb');

field = odb.steps['Step-1'].frames[-1].fieldOutputs['NE'];

field = field.getSubset(position=CENTROID);


i = 0;

s11 = [];
s22 = [];
s33 = [];
s12 = [];
s13 = [];
s23 = [];

while i < len(field.values):

    s11.append(field.values[i].data[0]);
    s22.append(field.values[i].data[1]);
    s33.append(field.values[i].data[2]);
    s12.append(field.values[i].data[3]);
    s13.append(field.values[i].data[4]);
    s23.append(field.values[i].data[5]);

    i = i+1;


print s11[1]
```

# Appendix E

# Further data and information

In the following pages additional DTI plots and information on repetitions are reported.

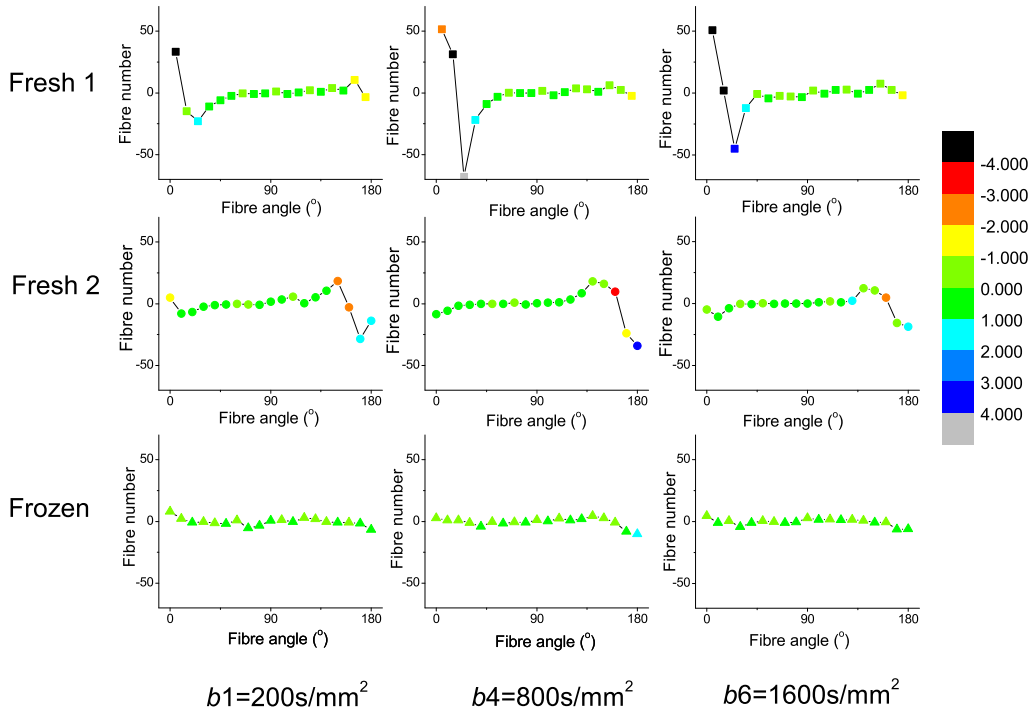


Figure E.1: Plot of the second derivatives of the fibre number versus fibre angle plots for the central slice and $b1$, $b2$ and $b6$.

| | | Angles between 0°–90° | | Angles between 90°–180° | |
|---|---|---|---|---|---|
| | | Most prevalent angle range (°) | % of occurrence | Most prevalent angle range (°) | % of occurrence |
| Repetition n.1 | $b1$ | 5 ± 2.5 | 7.29 | 175 ± 2.5 | 4.19 |
| | $b2$ | 5 ± 2.5 | 9.12 | 175 ± 2.5 | 6.50 |
| | $b3$ | 5 ± 2.5 | 12.35 | 175 ± 2.5 | 8.42 |
| | $b4$ | 5 ± 2.5 | 13.49 | 175 ± 2.5 | 11.00 |
| | $b5$ | 5 ± 2.5 | 15.76 | 175 ± 2.5 | 10.87 |
| | $b6$ | 5 ± 2.5 | 17.50 | 175 ± 2.5 | 10.87 |
| Repetition n.2 | $b1$ | 5 ± 2.5 | 8.64 | 175 ± 2.5 | 5.94 |
| | $b2$ | 5 ± 2.5 | 10.74 | 175 ± 2.5 | 8.77 |
| | $b3$ | 5 ± 2.5 | 13.23 | 175 ± 2.5 | 12.31 |
| | $b4$ | 5 ± 2.5 | 15.58 | 175 ± 2.5 | 12.13 |
| | $b5$ | 5 ± 2.5 | 17.29 | 175 ± 2.5 | 13.66 |
| | $b6$ | 5 ± 2.5 | 18.33 | 175 ± 2.5 | 15.28 |
| Repetition n.3 | $b1$ | 5 ± 2.5 | 9.04 | 175 ± 2.5 | 6.90 |
| | $b2$ | 5 ± 2.5 | 14.14 | 175 ± 2.5 | 10.13 |
| | $b3$ | 5 ± 2.5 | 13.71 | 175 ± 2.5 | 11.39 |
| | $b4$ | 5 ± 2.5 | 17.63 | 175 ± 2.5 | 11.39 |
| | $b5$ | 5 ± 2.5 | 19.21 | 175 ± 2.5 | 10.43 |
| | $b6$ | 5 ± 2.5 | 19.07 | 175 ± 2.5 | 14.01 |
| Repetition n.4 | $b1$ | 5 ± 2.5 | 8.77 | 175 ± 2.5 | 5.46 |
| | $b2$ | 5 ± 2.5 | 13.18 | 175 ± 2.5 | 8.90 |
| | $b3$ | 5 ± 2.5 | 13.05 | 175 ± 2.5 | 10.91 |
| | $b4$ | 5 ± 2.5 | 14.80 | 175 ± 2.5 | 11.65 |
| | $b5$ | 5 ± 2.5 | 18.07 | 175 ± 2.5 | 12.75 |
| | $b6$ | 5 ± 2.5 | 16.89 | 175 ± 2.5 | 11.48 |
| Repetition n.5 | $b1$ | 5 ± 2.5 | 8.47 | 175 ± 2.5 | 6.11 |
| | $b2$ | 5 ± 2.5 | 10.30 | 175 ± 2.5 | 8.77 |
| | $b3$ | 5 ± 2.5 | 14.80 | 175 ± 2.5 | 11.48 |
| | $b4$ | 5 ± 2.5 | 16.06 | 175 ± 2.5 | 12.13 |
| | $b5$ | 5 ± 2.5 | 19.82 | 175 ± 2.5 | 13.09 |
| | $b6$ | 5 ± 2.5 | 19.82 | 175 ± 2.5 | 13.09 |
| Averaged repetitions | $b1$ | 20 ± 2.5 | 9.15 | 160 ± 2.5 | 8.77 |
| | $b2$ | 5 ± 2.5 | 11.41 | 175 ± 2.5 | 10.88 |
| | $b3$ | 5 ± 2.5 | 15.28 | 175 ± 2.5 | 12.39 |
| | $b4$ | 5 ± 2.5 | 17.92 | 175 ± 2.5 | 11.62 |
| | $b5$ | 5 ± 2.5 | 19.01 | 175 ± 2.5 | 15.14 |
| | $b6$ | 5 ± 2.5 | 18.56 | 175 ± 2.5 | 15.14 |

Table E.1: Evaluation of the difference in the eigenvector angles between each repetition and the average over all the repetitions for the central slice of the image.

| | | Angles between 0°–90° | | Angles between 90°–180° | |
|---|---|---|---|---|---|
| | | Most prevalent angle range (°) | % of occurrence | Most prevalent angle range(°) | % of occurrence |
| Repetition n.1 | *b*1 | 5 ± 2.5 | 7.09 | 175 ± 2.5 | 4.36 |
| | *b*2 | 5 ± 2.5 | 9.76 | 175 ± 2.5 | 6.72 |
| | *b*3 | 5 ± 2.5 | 11.33 | 175 ± 2.5 | 8.42 |
| | *b*4 | 5 ± 2.5 | 12.55 | 175 ± 2.5 | 10.06 |
| | *b*5 | 5 ± 2.5 | 15.08 | 175 ± 2.5 | 10.72 |
| | *b*6 | 5 ± 2.5 | 14.99 | 175 ± 2.5 | 10.43 |
| Repetition n.2 | *b*1 | 5 ± 2.5 | 8.69 | 175 ± 2.5 | 5.50 |
| | *b*2 | 5 ± 2.5 | 10.85 | 175 ± 2.5 | 8.34 |
| | *b*3 | 5 ± 2.5 | 12.70 | 175 ± 2.5 | 10.13 |
| | *b*4 | 5 ± 2.5 | 14.21 | 175 ± 2.5 | 11.15 |
| | *b*5 | 5 ± 2.5 | 16.28 | 175 ± 2.5 | 11.37 |
| | *b*6 | 5 ± 2.5 | 15.63 | 175 ± 2.5 | 12.48 |
| Repetition n.3 | *b*1 | 5 ± 2.5 | 8.18 | 175 ± 2.5 | 6.35 |
| | *b*2 | 5 ± 2.5 | 11.59 | 175 ± 2.5 | 9.21 |
| | *b*3 | 5 ± 2.5 | 12.96 | 175 ± 2.5 | 10.72 |
| | *b*4 | 5 ± 2.5 | 15.93 | 175 ± 2.5 | 11.24 |
| | *b*5 | 5 ± 2.5 | 16.19 | 175 ± 2.5 | 11.48 |
| | *b*6 | 5 ± 2.5 | 17.59 | 175 ± 2.5 | 12.72 |
| Repetition n.4 | *b*1 | 5 ± 2.5 | 8.12 | 175 ± 2.5 | 5.52 |
| | *b*2 | 5 ± 2.5 | 11.48 | 175 ± 2.5 | 9.54 |
| | *b*3 | 5 ± 2.5 | 12.85 | 175 ± 2.5 | 10.32 |
| | *b*4 | 5 ± 2.5 | 14.45 | 175 ± 2.5 | 11.04 |
| | *b*5 | 5 ± 2.5 | 16.17 | 175 ± 2.5 | 11.11 |
| | *b*6 | 5 ± 2.5 | 16.80 | 175 ± 2.5 | 11.26 |
| Repetition n.5 | *b*1 | 5 ± 2.5 | 7.42 | 175 ± 2.5 | 5.63 |
| | *b*2 | 5 ± 2.5 | 11.46 | 175 ± 2.5 | 8.36 |
| | *b*3 | 5 ± 2.5 | 12.44 | 175 ± 2.5 | 10.10 |
| | *b*4 | 5 ± 2.5 | 13.29 | 175 ± 2.5 | 12.00 |
| | *b*5 | 5 ± 2.5 | 16.24 | 175 ± 2.5 | 12.31 |
| | *b*6 | 5 ± 2.5 | 16.24 | 175 ± 2.5 | 12.31 |
| Averaged repetition | *b*1 | 20 ± 2.5 | 9.14 | 175 ± 2.5 | 7.45 |
| | *b*2 | 5 ± 2.5 | 10.28 | 175 ± 2.5 | 9.35 |
| | *b*3 | 5 ± 2.5 | 12.57 | 175 ± 2.5 | 10.14 |
| | *b*4 | 5 ± 2.5 | 14.65 | 175 ± 2.5 | 10.48 |
| | *b*5 | 5 ± 2.5 | 13.45 | 175 ± 2.5 | 13.20 |
| | *b*6 | 5 ± 2.5 | 14.03 | 175 ± 2.5 | 13.31 |

Table E.2: Evaluation of the difference in the eigenvector angles between each repetition and the average over all of the repetitions. In this case the measurement is averaged over all of the slices of the volume.

# Bibliography


[1] Mackay J, Mensah GA. The Atlas of Heart Disease and Stroke. World Health Organization; 2004.

[2] Standring S, Ellis H. Gray's anatomy. Elsevier Churchill Livingstone; 2005.

[3] Publishing A. (USA), [online];. (Accessed 9 April 2010). `http://www.visiblebody.com`.

[4] National MF. (USA), [online];. (Accessed 9 March 2008). `http://www.marfan.org/nmf/GetSubContentRequestHandler.do?sub_menu_item_content_id=16&menu_item_id=4`.

[5] Rhodin JAG. Architecture of the vessel wall. In: Bohr DF, Somlyo AP, V SH, editors. Handbook of Physiology Sec. II. vol. 2. Am. Physiol. Soc., Bethesda, MD; 1980. p. 1–31.

[6] Humphrey JD, Delange SL. An Introduction to Biomechanics: Solids and Fluids, Analysis and Design. Springer; 2004.

[7] Learoyd BM, Taylor MG. Alterations with Age in the Viscoelastic Properties of Human Arterial Walls. Circulation Research. 1966;18(3):278–292.

[8] Zhang W, Herrera C, Atluri SN, Kassab GS. The effect of longitudinal pre-stretch and radial constraint on the stress distribution in the vessel wall: a new hypothesis. Mech Chem Biosystems. 2005;2:41–52.

[9] Rachev A, Greenwald S. Residual strains in conduit arteries. Journal of Biomechanics. 2003;36(5):661–670.

[10] Rachev A, Hayashi K. Theoretical Study of the Effects of Vascular Smooth Muscle Contraction on Strain and Stress Distributions in Arteries. Annals of Biomedical Engineering. 1999;27(4):459–468.

[11] Taber LA, Eggers DW. Theoretical Study of Stress-Modulated Growth in the Aorta. Journal of Theoretical Biology. 1996;180(4):343–357.

[12] Taber LA, Humphrey JD. Stress-Modulated Growth, Residual Stress, and Vascular Heterogeneity. Journal of Biomechanical Engineering. 2001;123:528.

[13] Saini A, Berry C, Greenwald S. Effect of age and sex on residual stress in the aorta. J Vasc Res. 1995;32(6):398–405.

[14] Ross R. Atherosclerosis–An Inflammatory Disease. New England Journal of Medicine. 1999;340(2):115.

[15] Reed D, Reed C, Stemmermann G, Hayashi T. Are aortic aneurysms caused by atherosclerosis? Circulation. 1992;85(1):205–211.

[16] Isselbacher EM. Thoracic and Abdominal Aortic Aneurysms. Am Heart Assoc; 2005.

[17] Vorp DA. Biomechanics of abdominal aortic aneurysm. Journal of Biomechanics. 2007;40(9):1887–1902.

[18] MedlinePlus. (USA), [online];. (Accessed 9 March 2008). `http://www.nlm.nih.gov/medlineplus/ency/imagepages/18072.htm`.

[19] Ernst CB. Abdominal Aortic Aneurysm. New England Journal of Medicine. 1993;328(16):1167.

[20] Rehders TC, Ince H, Nienaber CA. Aortic dissection: from aetiology to therapeutic management. Medicine. 2006;34(8):296–301.

[21] Leveson S, Guillou P, Terry H, Glanville J, Kester R. Pulse pressure wave analysis in the diagnosis of aorto-iliac disease. Ann Surg. 1978;187(2):161–165.

[22] Vorp DA, Raghavan M, Webster MW. Mechanical wall stress in abdominal aortic aneurysm: influence of diameter and asymmetry. J Vasc Surg. 1998;27(4):632–639.

[23] Raghavan M, Vorp DA, Federle MP, Makaroun MS, Webster MW. Wall stress distribution on three-dimensionally reconstructed models of human abdominal aortic aneurysm. Journal of Vascular Surgery. 2000;31(4):760–769.

[24] Finol E, Di Martino E, Vorp D, Amon C. Biomechanics of patient specific abdominal aortic aneurysms: computational analysis of fluid flow. Bioengineering Conference, 2002 Proceedings of the IEEE $28^{th}$ Annual Northeast. 2002;p. 191–192.

[25] Raghavan ML, Kratzberg JA, Golzarian J. Introduction to Biomechanics Related to Endovascular Repair of Abdominal Aortic Aneurysm. Techniques in Vascular and Interventional Radiology. 2005;8(1):50–55.

[26] Truijers M, Pol J, SchultzeKool L, van Sterkenburg S, Fillinger M, Blankensteijn J. Wall Stress Analysis in Small Asymptomatic, Symptomatic and Ruptured Abdominal Aortic Aneurysms. European Journal of Vascular & Endovascular Surgery. 2007;33(4):401–407.

[27] Vorp DA, Schiro BJ, Ehrlich MP, Juvonen TS, Ergin MA, Griffith BP. Effect of aneurysm on the tensile strength and biomechanical behavior of the ascending thoracic aorta. The Annals of thoracic surgery. 2003;75(4):1210–1214.

[28] Wassef M, Baxter BT. Pathogenesis of abdominal aortic aneurysms: a multidisciplinary research program supported by the National Heart, Lung, and Blood Institute. Journal of vascular surgery. 2001;34(4):730–8.

[29] Pereira L, Lee SY, Gayraud B, Andrikopoulos K, Shapiro SD, Bunton T, et al. Pathogenetic sequence for aneurysm revealed in mice underexpressing fibrillin-1. Proceedings of the National Academy of Sciences of the United States of America. 1999;96(7):3819.

[30] Hellenthal FA, Geenen ILA, Teijink JAW, Heeneman S, Schurink GWH. Histological features of human abdominal aortic aneurysm are not related to clinical characteristics. Cardiovascular Pathology. 2009;18(5):286–293.

[31] Mao D, Lee JK, VanVickle SJ, Thompson RW. Expression of Collagenase-3 (MMP-13) in Human Abdominal Aortic Aneurysms and Vascular Smooth Muscle Cells in Culture. Biochemical and biophysical research communications. 1999;261(3):904–910.

[32] Lopez-Candales A, Holmes DR, Liao S, Scott MJ, Wickline SA, Thompson RW. Decreased vascular smooth muscle cell density in medial degeneration of human abdominal aortic aneurysms. The American journal of pathology. 1997;150(3):993.

[33] Chen J, Zhuo S, Luo T, Liu D, Zhao J. Simultaneous observation of collagen and elastin based on the combined nonlinear optical imaging technique coupled with two-channel synchronized detection method. Optik - International Journal for Light and Electron Optics. 2008;119(11):519–522.

[34] O'Connell MK, Murthy S, Phan S, Xu C, Buchanan JA, Spilker R, et al. The three-dimensional micro-and nanostructure of the aortic medial lamellar unit measured using 3D confocal and electron microscopy imaging. Matrix Biology. 2007;.

[35] de Figueiredo Borges L, Gibin Jaldin R, Ribeiro Dias R, Groppo Stolf NA, Michel JB, Sampaio Gutierrez P. Collagen is reduced and disrupted in human aneurysms and dissections of ascending aorta. Human pathology. 2008 March;39(3):437–443.

[36] Hammer C, Linke R, Wagner F, Diefenbeck M. Organs from animals for man. International archives of allergy and immunology. 2009;116(1):5–21.

[37] Siepe M, Martin J, Sarai K, Ihling C, Sommer P, Beyersdorf F. Anatomical study on the surgical technique used for xenotransplantation: porcine hearts into humans. Journal of Surgical Research. 2007;143(2):211–215.

[38] Hughes GC, Post MJ, Simons M, Annex BH. Translational physiology: porcine models of human coronary artery disease: implications for preclinical trials of therapeutic angiogenesis. Journal of applied physiology. 2003;94(5):1689.

[39] Johnson G, Griggs T, Badimon L, et al. The utility of animal models in the preclinical study of interventions to prevent human coronary artery restenosis: analysis and recommendations. THROMBOSIS AND HAEMOSTASIS-STUTTGART-. 1999;81:835–843.

[40] Burton AC. Physical principles of circulatory phenomena: the physical equilibria of the heart and blood vessels. Handbook of Physiology: Circulation (3 v). 1959;p. 85.

[41] Biodidac. (Canada), [online];. (Accessed 9 March 2008). `http://biodidac.bio.uottawa.ca/thumbnails/filedet.htm?File_name=MAMM036B&File_type=GIF`.

[42] Shadwick RE. Mechanical design in arteries. Journal of Experimental Biology. 1999;202(23):3305–3313.

[43] Kalita P, Schaefer R. Mechanical Models of Artery Walls. Archives of Computational Methods in Engineering. 2008;15(1):1–36.

[44] Vito RP, Dixon SA. Blood Vessel Constitutive Models –1995–2002. Annual Reviews in Biomedical Engineering. 2003;5(1):413–439.

[45] Holzapfel GA. Nonlinear solid mechanics: a continuum approach for engineering. John Wiley & Sons, Chichester; 2000.

[46] Fung Y. Biomechanics: Mechanical Properties of Living Tissues. Springer; 1993.

[47] Holzapfel GA, Weizsäcker HW. Biomechanical behavior of the arterial wall and its numerical characterization. Computers in Biology and Medicine. 1998;28(4):377–392.

[48] Lally C, Reid A, Prendergast P. Elastic Behavior of Porcine Coronary Artery Tissue Under Uniaxial and Equibiaxial Tension. Annals of Biomedical Engineering. 2004;32(10):1355–1364.

[49] Holzapfel GA, Gasser TC, Stadler M. A structural model for the viscoelastic behavior of arterial walls: Continuum formulation and finite element analysis. European Journal of Mechanics/A Solids. 2002;21(3):441–463.

[50] Holzapfel GA, Stadler M, Schulze-Bauer CAJ. A Layer-Specific Three-Dimensional Model for the Simulation of Balloon Angioplasty using Magnetic Resonance Imaging and Mechanical Testing. Annals of Biomedical Engineering. 2002;30(6):753–767.

[51] Gasser TC, Schulze-Bauer CAJ, Holzapfel GA. A Three-dimensional Finite Element Model for Arterial Clamping. Journal of Biomechanical Engineering. 2002;124:355.

[52] Gasser T, Holzapfel G. A rate-independent elastoplastic constitutive model for biological fiber-reinforced composites at finite strains: continuum basis, algorithmic formulation and finite element implementation. Computational Mechanics. 2002;29(4):340–360.

[53] Gasser TC, Ogden RW, Holzapfel GA. Hyperelastic modelling of arterial layers with distributed collagen fibre orientations. Journal of The Royal Society Interface. 2006;3(6):15–35.

[54] Quapp MK, Weiss JA. Material chatacterization of human medial collateral ligament. Journal of Biomechanical Engineering. 1997;.

[55] Baek S, Gleason R, Rajagopal K, Humphrey J. Theory of small on large: Potential utility in computations of fluid–solid interactions in arteries. Computer Methods in Applied Mechanics and Engineering. 2007;196(31-32):3070–3078.

[56] Wicker B. Normal basilar artery structure and biaxial mechanical behaviour. Computer Methods in Biomechanics and Biomedical Engineering. 2008;11(5):539–551.

[57] Holzapfel GA. Determination of material models for arterial walls from uniaxial extension tests and histological structure. Journal of Theoretical Biology. 2006;238(2):290–302.

[58] Veress AI, Weiss JA, Gullberg GT, Vince DG, Rabbitt RD. Strain Measurement in Coronary Arteries Using Intravascular Ultrasound and Deformable Images. Journal of Biomechanical Engineering. 2002;124:734.

[59] Weiss JA. A Constitutive Model And Finite Element Representation For A Transversely Isotropic Soft Tissue. University of Utah, Department of Bioengineering; 1994.

[60] Holzapfel GA, Sommer G, Gasser CT, Regitnig P. Determination of layer-specific mechanical properties of human coronary arteries with nonatherosclerotic intimal thickening and related constitutive modeling. American Journal of Physiology- Heart and Circulatory Physiology. 2005;289(5):2048–2058.

[61] Holzapfel GA, Gasser TC. Computational stress-deformation analysis of arterial walls including high-pressure response. International journal of cardiology. 2007;116(1):78–85.

[62] Holzapfel GA, Ogden R. Constitutive modelling of arteries. Proceedings of the Royal Society A. 2010;(466):1551–1597.

[63] Holzapfel GA, Sommer G, Regitnig P. Anisotropic Mechanical Properties of Tissue Components in Human Atherosclerotic Plaques. Journal of Biomechanical Engineering. 2004;126:657.

[64] Sacks MS. Biaxial mechanical evaluation of planar biological materials. Journal of Elasticity. 2000;61(1):199–246.

[65] Stemper BD, Yoganandan N, Stineman MR, Gennarelli TA, Baisden JL, Pintar FA. Mechanics of Fresh, Refrigerated, and Frozen Arterial Tissue. Journal of Surgical Research. 2007;139(2):236–242.

[66] Hartnell GG, et al. Imaging of aortic aneurysms and dissection: CT and MRI. J Thorac Imaging. 2001;16(1):35–46.

[67] Ruehm SG, Goyen M, Barkhausen J, Kroger K, Bosk S, Ladd ME, et al. Rapid magnetic resonance angiography for detection of atherosclerosis. The Lancet. 2001;357(9262):1086–1091.

[68] Blondel C, Vaillant R, Devernay F, Malandain G, Ayache N. Automatic trinocular 3D reconstruction of coronary artery centerlines from rotational X-ray angiography. In: Proc. of CARS. Citeseer;. p. 832–837.

[69] Golzarian J, Murgo S, Dussaussois L, Guyot S, Said KA, Wautrecht JC, et al. Evaluation of abdominal aortic aneurysm after endoluminal treatment: comparison of color Doppler sonography with biphasic helical CT. American Journal of Roentgenology. 2002;178(3):623.

[70] Fayad ZA, Fuster V, Nikolaou K, Becker C. Computed tomography and magnetic resonance imaging for noninvasive coronary angiography and plaque imaging: current and potential future concepts. Circulation. 2002;106(15):2026.

[71] Toussaint JF, LaMuraglia GM, Southern JF, Fuster V, Kantor HL. Magnetic resonance images lipid, fibrous, calcified, hemorrhagic, and thrombotic components of human atherosclerosis in vivo. Circulation. 1996;94(5):932.

[72] Mudry KM, Plonsey R, Bronzino JD. Biomedical Imaging. CRC press; 2003.

[73] Shellock FG, Crues JV. MR Procedures: Biologic Effects, Safety, and Patient Care. Radiology. 2004;232(3):635–652.

[74] Nayak KS, Pauly JM, Kerr AB, Hu BS, Nishimura DG. Real-time color flow MRI. Magnetic Resonance in Medicine. 2000;43(2):251–258.

[75] Basser PJ, Pierpaoli C. Microstructural and Physiological Features of Tissues Elucidated by Quantitative-Diffusion-Tensor MRI. Journal of Magnetic Resonance, Series B. 1996;111(3):209–219.

[76] Kingsley PB. Introduction to Diffusion Tensor Imaging Mathematics: Part I. Tensors, Rotations, and Eigenvectors. Concepts in Magnetic Resonance Part A. 2006;28(2):101.

[77] Mori S, Zhang J. Principles of Diffusion Tensor Imaging and Its Applications to Basic Neuroscience Research. Neuron. 2006;51(5):527–539.

[78] Haacke ME. Magnetic Resonance Imaging. Wiley-Liss; 2005.

[79] Koay CG, Carew JD, Alexander AL, Basser PJ, Meyerand ME. Investigation of anomalous estimates of tensor-derived quantities in diffusion tensor imaging. Magn Reson Med. 2006;55:930–936.

[80] Kingsley PB. Introduction to diffusion tensor imaging mathematics: Part II. Anisotropy, diffusion-weighting factors, and gradient encoding schemes. Concepts in Magnetic Resonance Part A. 2006;28(2):123–154.

[81] Andreisek G, White LM, Kassner A, Tomlinson G, Sussman MS. Diffusion tensor imaging and fiber tractography of the median nerve at 1.5 T: optimization of b value. Skeletal radiology. 2009;38(1):51–59.

[82] Mukherjee P, Berman J, Chung S, Hess C, Henry R. Diffusion tensor MR imaging and fiber tractography: theoretic underpinnings. American Journal of Neuroradiology. 2008;29(4):632.

[83] Basser PJ, Jones DK. Diffusion-tensor MRI: theory, experimental design and data analysis- a technical review. NMR in Biomedicine. 2002;15(7-8):456–467.

[84] Marenco S, Rawlings R, Rohde GK, Barnett AS, Honea RA, Pierpaoli C, et al. Regional distribution of measurement error in diffusion tensor imaging. Psychiatry Research: Neuroimaging. 2006;147(1):69–78.

[85] Capuani S, Rossi C, Alesiani M, Maraviglia B. Diffusion tensor imaging to study anisotropy in a particular porous system: The trabecular bone network. Solid State Nuclear Magnetic Resonance. 2005;28(2-4):266–272.

[86] Basser PJ, Pajevic S, Pierpaoli C, Duda J, Aldroubi A. In vivo fiber tractography using DT-MRI data. Magnetic Resonance in Medicine. 2000;44(4):625–632.

[87] Kim S, Jeong JW, Singh M. Estimation of Multiple Fiber Orientations From Diffusion Tensor MRI Using Independent Component Analysis. IEEE Transations on Nuclear Science. 2005;52(1).

[88] Jun Z, Hao J, Ning K, Ning C. Fiber Tractography in Diffusion Tensor Magnetic Resonance Imaging: A Survey and Beyond. Laboratory for high performance scientific computing and computer simulation, Department of computer science, University of Kentucky, Lexington, KY. 2005;p. 40506–0046.

[89] Fillard P, Toussaint N, Pennec X. MedInria: DT-MRI Processing and Visualization Software. In: Similar NoE Tensor Workshop. Las Palmas de Gran Canaria, Spain; 2006. .

[90] Bonekamp D, Nagae LM, Degaonkar M, Matson M, Abdalla WMA, Barker PB, et al. Diffusion tensor imaging in children and adolescents: Reproducibility, hemispheric, and age-related differences. Neuroimage. 2007;34(2):733–742.

[91] Fletcher PT, Tao R, Jeong WK, Whitaker RT. A Volumetric Approach to Quantifying Region–to–Region White Matter Connectivity in Diffusion Tensor MRI. Information Processing in Medical Imaging 2007 Conference Proceedings. 2007;p. 346–358.

[92] Shiraishi A, Hasegawa Y, Okada S, Kimura K, Sawada T, Mizusawa H, et al. Highly Diffusion-Sensitized Tensor Imaging of Unilateral Cerebral Arterial Occlusive Disease. American Journal of Neuroradiology. 687;26(6):1498–1504.

[93] Sun SW, Neil JJ, Liang HF, He YY, Schmidt RE, Hsu CY, et al. Formalin fixation alters water diffusion coefficient magnitude but not anisotropy in infarcted brain. Magn Reson Med. 2005;53(6):1447–51.

[94] Reese TG, Weisskoff RM, Smith RN, Rosen BR, Dinsmore RE, Wedeen VJ. Imaging myocardial fiber architecture in vivo with magnetic resonance. Magn Reson Med. 1995;34(6):786–91.

[95] Buckberg GD, Mahajan A, Jung B, Markl M, Hennig J, Ballester-Rodes M. MRI myocardial motion and fiber tracking: a confirmation of knowledge from different imaging modalities. European Journal of Cardio-Thoracic Surgery. 2006;29:165–177.

[96] Dou J, Reese TG, Tseng WYI, Wedeen VJ. Cardiac diffusion MRI without motion effects. Magnetic Resonance in Medicine. 2002;48(1):105–114.

[97] Dou J, Tseng WYI, Reese TG, Wedeen VJ. Combined diffusion and strain MRI reveals structure and function of human myocardial laminar sheets in vivo. Magnetic Resonance in Medicine. 2003;50(1):107–113.

[98] Ennis DB. Assessment Of Myocardial Structure And Function Using Magnetic Resonance Imaging. John Hopkins University. Baltimore, Maryland, USA; 2004.

[99] Helm PA, Tseng HJ, Younes L, McVeigh ER, Winslow RL. Ex vivo 3D diffusion tensor imaging and quantification of cardiac laminar structure. Magn Reson Med. 2005;54(4):850–9.

[100] Hsu EW, Henriquez CS. Myocardial Fiber Orientation Mapping Using Reduced Encoding Diffusion Tensor Imaging. Journal of Cardiovascular Magnetic Resonance. 2001;3(4):339–347.

[101] Tseng W, Reese TG, Weisskoff RM, Brady TJ, Wedeen VJ. Myocardial fiber shortening in humans: initial results of MR imaging. Radiology. 2000;216(1):128–39.

[102] Tseng WYI, Wedeen VJ, Reese TG, Smith RN, Halpern EF. Diffusion tensor MRI of myocardial fibers and sheets: Correspondence with visible cut-face texture. Journal of Magnetic Resonance Imaging. 2003;17(1):31–42.

[103] Walker JC, Guccione JM, Jiang Y, Zhang P, Wallace AW, Hsu EW, et al. Helical myofiber orientation after myocardial infarction and left ventricular surgical restoration in sheep. The Journal of Thoracic and Cardiovascular Surgery. 2005;129(2):382–390.

[104] Heemskerk AM, Strijkers GJ, Vilanova A, Drost MR, Nicolay K. Determination of mouse skeletal muscle architecture using three-dimensional diffusion tensor imaging. Magn Reson Med. 2005;53(6):1333–40.

[105] Gilbert R, Wedeen V, Magnusson L, Benner T, Wang R, Dai G, et al. Three-dimensional myoarchitecture of the bovine tongue demonstrated by diffusion spectrum magnetic resonance imaging with tractography. Anat Rec A Discov Mol Cell Evol Biol. 2006;.

[106] Weiss S, Jaermann T, Schmid P, Staempfli P, Boesiger P, Niederer P, et al. Three-dimensional fiber architecture of the nonpregnant human uterus determined ex vivo using magnetic resonance diffusion tensor imaging. Anat Rec A Discov Mol Cell Evol Biol. 2006;288:84–90.

[107] Rossi C, Capuani S, Fasano F, Alesiani M, Maraviglia B. DTI of trabecular bone marrow. Magnetic Resonance Imaging. 2005;23(2):245–248.

[108] Van Wedeen J. Magnetic resonance imaging of myocardial kinematics. techniques to detect, localize and quantify strain rates of the active human myocardium. Magnetic Resonance in Medicine. 1992;27(1):52–67.

[109] Pelc NJ, Drangova M, Pelc LR, Zhu Y, Noll DC, Bowman BS, et al. Tracking of cyclic motion with phase-contrast cine MR velocity data. Journal of Magnetic Resonance Imaging. 2005;5(3):339–345.

[110] Srichai MB, Lim RP, Wong S, Lee VS. Cardiovascular applications of phase-contrast MRI. American Journal of Roentgenology. 2009;192(3):662.

[111] Brown M, Semelka R, Nishino TK. MRI: basic principles and applications. Medical Physics. 2004;31:170.

[112] Unterhinninghofen R, Stehle T, Albers J, Hosch W, Vahl C, Dillmann R. Analysis of left-ventricular pathological flow via phase-contrast magnetic resonance imaging. In: International Congress Series. vol. 1268. Elsevier; 2004. p. 1138–1143.

[113] Hoyos MH, Orlowski P, Pikatkowska-Janko E, Bogorodzki P, Orkisz M. Vascular centerline extraction in 3D MR angiograms for phase contrast MRI blood flow measurement. International Journal of Computer Assisted Radiology and Surgery. 2006;1(1):51–61.

[114] Jeays A, Lawford P, Gillott R, Spencer P, Barber D, Bardhan K, et al. Characterisation of the haemodynamics of the superior mesenteric artery. Journal of biomechanics. 2007;40(9):1916–1926.

[115] Enzmann D, Pelc N. Brain motion: measurement with phase-contrast MR imaging. Radiology. 1992;185(3):653.

[116] Asakawa D, Pappas G, Blemker S, Drace JE, Delp S. Cine phase-contrast magnetic resonance imaging as a tool for quantification of skeletal muscle motion. In: Seminars in Musculoskeletal Radiology. vol. 7. THIEME; 2003. p. 287–296.

[117] Finni T, Hodgson JA, Lai AM, Edgerton VR, Sinha S. Muscle synergism during isometric plantarflexion in Achilles tendon rupture patients and in normal subjects revealed by velocity-encoded cine phase-contrast MRI. Clinical Biomechanics. 2006;21(1):67–74.

[118] Felton SM, Gaige TA, Reese TG, Wedeen VJ, Gilbert RJ. Mechanical basis for lingual deformation during the propulsive phase of swallowing as determined by phase-contrast magnetic resonance imaging. Journal of applied physiology. 2007;103(1):255.

[119] Zhu Y, Drangova M, Pelc N. Estimation of deformation gradient and strain from cine-PC velocitydata [cardiac magnetic resonance imaging]. IEEE transactions on medical imaging. 1997;16(6):840–851.

[120] Wedding KL, Draney MT, Herfkens RJ, Zarins CK, Taylor CA, Pelc NJ. Measurement of vessel wall strain using cine phase contrast MRI. Journal of Magnetic Resonance Imaging. 2002;15(4):418–428.

[121] Draney MT, Herfkens RJ, Hughes TJR, Pelc NJ, Wedding KL, Zarins CK, et al. Quantification of vessel wall cyclic strain using cine phase contrast magnetic resonance imaging. Annals of Biomedical Engineering. 2002;30(8):1033–1045.

[122] Draney MT, Arko FR, Alley MT, Markl M, Herfkens RJ, Pelc NJ, et al. Quantification of vessel wall motion and cyclic strain using cine phase contrast MRI: in vivo validation in the porcine aorta. Magnetic Resonance in Medicine. 2004;52(2):286–295.

[123] Robson MD, Constable RT. Three-dimensional strain-rate imaging. Magnetic Resonance in Medicine. 2005;36(4):537–546.

[124] Epstein FH, Arai AE, Gaither CC, Wolff SD. Method for Extracting Deformations From Velocity Encoded Magnetic Resonance Images of the Heart. US Patent; 2000. 6,031,347.

[125] Filidoro L, Dietrich O, Weber J, Rauch E, Oerther T, Wick M, et al. High–resolution diffusion tensor imaging of human patellar cartilage: feasibility and preliminary findings. Magnetic Resonance in Medicine. 2005;53(5):993–998.

[126] Khalil C, Hancart C, Le Thuc V, Chantelot C, Chechin D, Cotten A. Diffusion tensor imaging and tractography of the median nerve in carpal tunnel syndrome: preliminary results. European radiology. 2008;18(10):2283–2291.

[127] Chen J, Song SK, Liu W, McLean M, Allen JS, Tan J, et al. Remodeling of cardiac fiber structure after infarction in rats quantified with diffusion tensor MRI. American Journal of Physiology- Heart and Circulatory Physiology. 2003;285(3):H946.

[128] Fillard P, Souplet JC, N T. Medical Image Navigation and Research Tool by INRIA (MedINRIA). INRIA Sophia Antipolis, Sophia Antipolis, France; 2007.

[129] Mori S, van Zijl PCM. Fiber tracking: principles and strategies-a technical review. NMR in Biomedicine. 2002;15(7-8):468–480.

[130] Berens P. CircStat: A MATLAB toolbox for circular statistics. Journal of Statistical Software. 2009;31(10).

[131] Petersen S, Peto V, Rayner M, Leal J, Luengo-Fernandez R, Gray A. European cardiovascular disease statistics: 2005 edition. London: British Heart Foundation. 2005;p. 1–100.

[132] Kassab GS. Biomechanics of the cardiovascular system: the aorta as an illustratory example. Journal of the Royal Society Interface. 2006;3(11):719.

[133] Clark JM, Glagov S. Transmural organization of the arterial media. The lamellar unit revisited. Arteriosclerosis, Thrombosis, and Vascular Biology. 1985;5(1):19.

[134] Farand P, Garon A, Plante GE. Structure of large arteries: Orientation of elastin in rabbit aortic internal elastic lamina and in the elastic lamellae of aortic media. Microvascular research. 2007;73(2):95–99.

[135] Stergiopulos N, Vulliemoz S, Rachev A, Meister JJ, Greenwald S. Assessing the homogeneity of the elastic properties and composition of the pig aortic media. Journal of vascular research. 2000;38(3):237–246.

[136] Driessen N, Wilson W, Bouten C, Baaijens F. A computational model for collagen fibre remodelling in the arterial wall. Journal of theoretical biology. 2004;226(1):53–64.

[137] Tang G, Liu Y, Li W, Yao J, Li B, Li P. Optimization of b value in diffusion-weighted MRI for the differential diagnosis of benign and malignant vertebral fractures. Skeletal radiology. 2007;36(11):1035–1041.

[138] Chao HS, Chang KH, Na DG, Kwon BJ, Lee DH. High b-Value Diffusion (b = 3000 s/mm$^2$) MR Imaging in Cerebral Gliomas at 3T: Visual and Quantitative Comparisons with b = 1000s/mm$^2$. American Journal of Neuroradiology. 2008;29:458–463.

[139] Delgadillo JOV. Mechanical Properties of Arterial Wall. University of British Columbia. Vancouver, Canada; 2008.

[140] Venkatasubramanian RT, Grassl ED, Barocas VH, Lafontaine D, Bischof JC. Effects of freezing and cryopreservation on the mechanical properties of arteries. Annals of Biomedical engineering. 2006;34(5):823–832.

[141] Tang PCY, Coady MA, Lovoulos C, Dardik A, Aslan M, Elefteriades JA, et al. Hyperplastic cellular remodeling of the media in ascending thoracic aortic aneurysms. Circulation. 2005;112(8):1098.

[142] Sakalihasan N, Limet R, Defawe O. Abdominal aortic aneurysm. The Lancet. 2005;365(9470):1577–1589.

[143] Nichols W, O'rourke M, Kenney WL. McDonald's Blood Flow in Arteries: Theoretical, Experimental and Clinical Principles, ed. 3. Journal of Cardiopulmonary Rehabilitation and Prevention. 1991;11(6341):407.

[144] Morrison TM, Choi G, Zarins CK, Taylor CA. Circumferential and longitudinal cyclic strain of the human thoracic aorta: Age-related changes. Journal of vascular surgery: official publication, the Society for Vascular Surgery [and] International Society for Cardiovascular Surgery, North American Chapter. 2009;49(4):1029.